frontiers | Research Topics

Vaccines and therapeutics utilizing new adjuvants and potential inhibitors to target emerging infectious diseases

Edited by
Jiae Kim, Ousman Jobe and
Mara Jana Broadhurst

Published in
Frontiers in Immunology

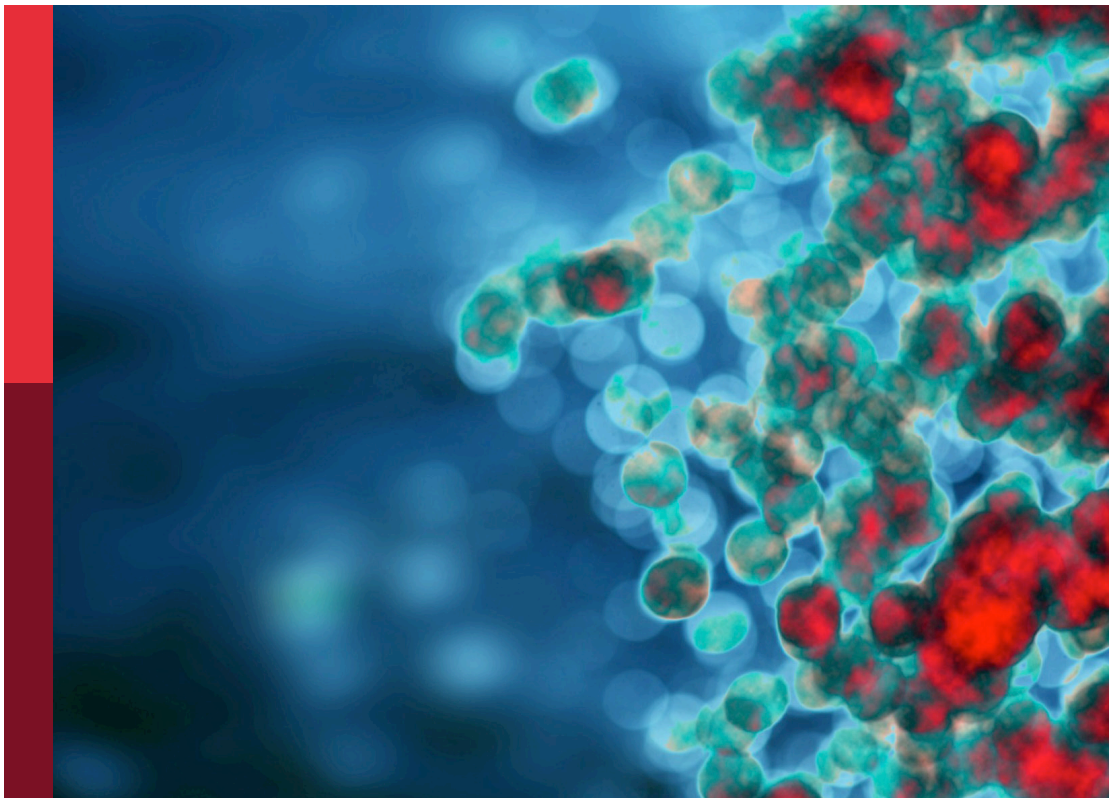

ISSN 1664-8714
ISBN 978-2-8325-6918-4
DOI 10.3389/978-2-8325-6918-4

Generative AI statement
Any alternative text (Alt text) provided alongside figures in the articles in this ebook has been generated by Frontiers with the support of artificial intelligence and reasonable efforts have been made to ensure accuracy, including review by the authors wherever possible. If you identify any issues, please contact us.

About Frontiers

Frontiers is more than just an open access publisher of scholarly articles: it is a pioneering approach to the world of academia, radically improving the way scholarly research is managed. The grand vision of Frontiers is a world where all people have an equal opportunity to seek, share and generate knowledge. Frontiers provides immediate and permanent online open access to all its publications, but this alone is not enough to realize our grand goals.

Frontiers journal series

The Frontiers journal series is a multi-tier and interdisciplinary set of open-access, online journals, promising a paradigm shift from the current review, selection and dissemination processes in academic publishing. All Frontiers journals are driven by researchers for researchers; therefore, they constitute a service to the scholarly community. At the same time, the *Frontiers journal series* operates on a revolutionary invention, the tiered publishing system, initially addressing specific communities of scholars, and gradually climbing up to broader public understanding, thus serving the interests of the lay society, too.

Dedication to quality

Each Frontiers article is a landmark of the highest quality, thanks to genuinely collaborative interactions between authors and review editors, who include some of the world's best academicians. Research must be certified by peers before entering a stream of knowledge that may eventually reach the public - and shape society; therefore, Frontiers only applies the most rigorous and unbiased reviews. Frontiers revolutionizes research publishing by freely delivering the most outstanding research, evaluated with no bias from both the academic and social point of view. By applying the most advanced information technologies, Frontiers is catapulting scholarly publishing into a new generation.

What are Frontiers Research Topics?

Frontiers Research Topics are very popular trademarks of the *Frontiers journals series*: they are collections of at least ten articles, all centered on a particular subject. With their unique mix of varied contributions from Original Research to Review Articles, Frontiers Research Topics unify the most influential researchers, the latest key findings and historical advances in a hot research area.

Find out more on how to host your own Frontiers Research Topic or contribute to one as an author by contacting the Frontiers editorial office: frontiersin.org/about/contact

Vaccines and therapeutics utilizing new adjuvants and potential inhibitors to target emerging infectious diseases

Topic editors

Jiae Kim — Henry M Jackson Foundation for the Advancement of Military Medicine (HJF), United States

Ousman Jobe — Henry M Jackson Foundation for the Advancement of Military Medicine (HJF), United States

Mara Jana Broadhurst — University of Nebraska Medical Center, United States

Citation

Kim, J., Jobe, O., Broadhurst, M. J., eds. (2025). *Vaccines and therapeutics utilizing new adjuvants and potential inhibitors to target emerging infectious diseases*. Lausanne: Frontiers Media SA. doi: 10.3389/978-2-8325-6918-4

Table of contents

frontiers | Frontiers in Immunology

TYPE Editorial
PUBLISHED 11 November 2025
DOI 10.3389/fimmu.2025.1716739

OPEN ACCESS

EDITED AND REVIEWED BY
Lee Mark Wetzler,
Boston University, United States

*CORRESPONDENCE
Jiae Kim
jakim@hivresearch.org

RECEIVED 30 September 2025
ACCEPTED 30 October 2025
PUBLISHED 11 November 2025

CITATION
Kim J, Jobe O and Broadhurst MJ (2025) Editorial: Vaccines and therapeutics utilizing new adjuvants and potential inhibitors to target emerging infectious diseases. *Front. Immunol.* 16:1716739. doi: 10.3389/fimmu.2025.1716739

Editorial: Vaccines and therapeutics utilizing new adjuvants and potential inhibitors to target emerging infectious diseases

Jiae Kim[1,2]*, Ousman Jobe[1,2] and Mara Jana Broadhurst[3]

[1]United States Military HIV Research Program, Henry M. Jackson Foundation for the Advancement of Military Medicine, Bethesda, MD, United States, [2]Laboratory of Adjuvant and Antigen Research, United States Military HIV Research Program, Center for Infectious Disease Research, Walter Reed Army Institute of Research, Silver Spring, MD, United States, [3]Department of Pathology, Microbiology, and Immunology, College of Medicine, University of Nebraska Medical Center, Omaha, NE, United States

KEYWORDS

emerging infectious diseases (EIDs), food and water borne diseases, viral infections, in silico, adjuvants, vaccine delivery platforms, computational approach and techniques, bacterial infections

Editorial on the Research Topic
Vaccines and therapeutics utilizing new adjuvants and potential inhibitors to target emerging infectious diseases

Infectious diseases that are persistent or increasing in incidence continue to have a broad impact on populations worldwide. Emerging infectious diseases often pose an outsized burden on health systems due to limited medical countermeasures and minimal population immunity. The catastrophic health burdens of emerging infectious diseases highlight the need for innovative strategies to develop effective preventive and therapeutic interventions.

This Research Topic "*Vaccines and therapeutics utilizing new adjuvants and potential inhibitors to target emerging infectious diseases*" comprises 10 articles that address critical emerging pathogens including SARS-CoV-2 (Sui et al., Xu et al., Neville et al.), influenza A virus (Zhang et al.), *Neisseria gonorrhoeae* (Lu et al.), *Salmonella enterica serovar Rissen* (Cuomo et al.), novel adjuvant effect on immune responses (Shamseldin et al.), and *in silico* and computational approaches for vaccine development and targeting (Panda et al.).

We have seen the impact of innovative vaccine platforms against emerging viruses with the implementation and utilization of SARS-CoV-2 vaccines. Xu et al. performed a prospective, longitudinal study of a healthcare worker immunization program in China, demonstrating short-lived neutralizing antibodies following COVID-19 booster immunization with incomplete protection from breakthrough infection. Therefore, although these vaccines are indeed effective, further improvements in the boosting strategy are warranted. Sui et al. examined whether boosting intranasally (i.n.) with an adjuvanted subunit vaccine would protect against a SARS-CoV-2 challenge. Their work demonstrated the efficacy of boosting with an i.n. formulation, showing that lower oral and lung viral loads were correlated with mucosal ACE2 inhibition activity. Neville et al.

examined the utilization of a peptidomimetic of complement C5a, EP67, with inactivated SARS-CoV-2, which resulted in enhanced immune responses. This work also demonstrated the possible utility of EP67 on its own as a potential antiviral agent.

Emerging avian influenza viruses pose persistent public health threats. Zhang et al. developed a vaccine against Eurasian avian-like H1N1 (EA H1N1) influenza. This subunit influenza vaccine formulation contained adjuvant gram-positive enhancer matrix (GEM) particles derived from *Lactococcus lactis*. Intranasal administration or co-administration via the i.n. and intramuscular (i.m.) routes generated mucosal and Th1-biased immune responses that were inferior to the responses induced by i.m. alone and displayed undetectable viral titers in the lungs after challenge. This study provides information on possible platforms and routes of administration for vaccination that are not only applicable to the viruses examined but perhaps other viral infections.

Bacterial infections are the cause of a wide range of pathogenic infections, from sexually transmitted diseases to foodborne illnesses. The emergence of multidrug resistance makes these emerging pathogens of importance in public health. Lu et al. examined the immunogenicity and efficacy of a trivalent vaccine targeting *Neisseria gonorrhoeae*. This formulation induced stronger circulating IgG and IgA antibody responses in mice compared to monovalent vaccine formulations. The serum from the vaccinees killed various strains of *N. gonorrhoeae in vitro*; however, it was only moderately effective in a mouse intravaginal challenge model. These results indicate the potential utility of a multivalent vaccine formulation strategy, especially against multidrug-resistant strains. Cuomo et al. examined modifications to the lipid A of *Salmonella enterica* serovar Rissen (S. Rissen) that render the bacteria phage-resistant. The modifications to lipid A were utilized in a potential lipopolysaccharide (LPS)-based vaccine, which was demonstrated to be less toxic and could be effective against salmonellosis.

In silico and computational work are new approaches to generating and developing novel vaccine formulations. Panda et al. utilized these approaches to develop a potential vaccine targeting Scrub typhus, which is a life-threatening illness caused by the gram-negative bacterium *Orientia tsutsugamushi*. The research group used a reverse vaccinology approach by taking subunit candidates and determining a possible formulation for a vaccine. Through molecular docking and simulations, the final construct was found to show high antigenicity, stability, and solubility. Sethi et al. also utilized an immunoinformatics approach to develop a vaccine formulation against *Leptospira*. This formulation was designed to be a multi-epitope subunit vaccine (MESV) with an adjuvant, and when tested *in silico*, it was shown to elicit robust B and T cell responses. An immunoinformatics approach to designing a multi-epitope subunit vaccine may provide additional tools to enhance vaccine development. It will be interesting to see if these two promising candidates can be effective not only *in silico* but experimentally on the bench.

Adjuvants are a critical component of vaccines, and there is a requirement for the development and understanding of new adjuvants. Shamseldin et al. provided more mechanistic insight into a potential adjuvant, Bordetella colonization factor (BcfA), an outer membrane protein. This adjuvant has been demonstrated to activate Th1/Th17 immune responses. The work examined BcfA in the context of antigen-presenting cells, bone marrow-derived dendritic cells, and human PBMCs. Informing the vaccinology field on the mechanism of adjuvant action and how an adjuvant activates immune responses is critical in aiding the development of vaccine formulations that target emerging infectious diseases.

Finally, a review written by Thom and D'Elia introduced and described the idea of Host-Directed Therapies (HDTs) as an alternative approach to pathogen-targeting therapeutics against emerging infectious diseases. This work explores the notion of targeting pathways to diminish the host response to a pathogen.

New technologies and approaches are necessary for both preventative vaccines and therapeutics against emerging infectious diseases, which continue to impact populations on a global scale. By utilizing bench-side and *in silico* approaches, these various platforms could make it to the clinic in the future. The contributions to this Research Topic highlight several new possible platforms and opportunities for targeting these diseases. We thank the authors of the articles for their contributions.

Author contributions

JK: Writing – original draft, Writing – review & editing. OJ: Writing – original draft, Writing – review & editing. MB: Writing – original draft, Writing – review & editing.

Conflict of interest

The authors declare that the research was conducted in the absence of any commercial or financial relationships that could be construed as a potential conflict of interest.

Generative AI statement

The author(s) declare that no Generative AI was used in the creation of this manuscript.

Any alternative text (alt text) provided alongside figures in this article has been generated by Frontiers with the support of artificial intelligence and reasonable efforts have been made to ensure accuracy, including review by the authors wherever possible. If you identify any issues, please contact us.

Publisher's note

Author disclaimer

The material has been reviewed by the Walter Reed Army Institute of Research. There is no objection to its presentation and/or publication. The opinions or assertions contained herein are the private views of the author, and are not to be construed as official, or as reflecting the true views of the Department of the Army, the Department of Defense, or HJF.

frontiers | Frontiers in Immunology

TYPE Original Research
PUBLISHED 29 August 2024
DOI 10.3389/fimmu.2024.1439418

OPEN ACCESS

EDITED BY
Jiae Kim,
Henry M Jackson Foundation for the Advancement of Military Medicine (HJF), United States

REVIEWED BY
Erica Louise Stewart,
Royal Prince Alfred Hospital, Australia
Oscar Badillo-Godinez,
Faculty of Medicine, Uppsala University, Sweden

*CORRESPONDENCE
Purnima Dubey
purnima.dubey@osumc.edu

†These authors share first authorship

RECEIVED 27 May 2024
ACCEPTED 09 August 2024
PUBLISHED 29 August 2024

CITATION
Shamseldin MM, Read KA, Hall JM, Tuazon JA, Brown JM, Guo M, Gupta YA, Deora R, Oestreich KJ and Dubey P (2024) The adjuvant BcfA activates antigen presenting cells through TLR4 and supports T_{FH} and T_H1 while attenuating T_H2 gene programming.
Front. Immunol. 15:1439418.
doi: 10.3389/fimmu.2024.1439418

The adjuvant BcfA activates antigen presenting cells through TLR4 and supports T_{FH} and T_H1 while attenuating T_H2 gene programming

Mohamed M. Shamseldin[1,2,3†], Kaitlin A. Read[1†], Jesse M. Hall[1†], Jasmine A. Tuazon[1], Jessica M. Brown[1], Myra Guo[1], Yash A. Gupta[1], Rajendar Deora[1,2], Kenneth J. Oestreich[1,4] and Purnima Dubey[1,4,5*]

[1]Departments of Microbial Infection and Immunity, The Ohio State University, Columbus, OH, United States, [2]Departments of Microbiology, The Ohio State University, Columbus, OH, United States, [3]Department of Microbiology and Immunology, Faculty of Pharmacy, Helwan University-Ain Helwan, Helwan, Egypt, [4]Pelotonia Institute for Immuno-Oncology, The Ohio State University, Columbus, OH, United States, [5]Comprehensive Cancer Center, The Ohio State University, Columbus, OH, United States

Introduction: Adjuvants added to subunit vaccines augment antigen-specific immune responses. One mechanism of adjuvant action is activation of pattern recognition receptors (PRRs) on innate immune cells. *Bordetella* colonization factor A (BcfA); an outer membrane protein with adjuvant function, activates T_H1/T_H17-polarized immune responses to protein antigens from *Bordetella pertussis* and SARS CoV-2. Unlike other adjuvants, BcfA does not elicit a T_H2 response.

Methods: To understand the mechanism of BcfA-driven T_H1/T_H17 vs. T_H2 activation, we screened PRRs to identify pathways activated by BcfA. We then tested the role of this receptor in the BcfA-mediated activation of bone marrow-derived dendritic cells (BMDCs) using mice with germline deletion of TLR4 to quantify upregulation of costimulatory molecule expression and cytokine production in vitro and in vivo. Activity was also tested on human PBMCs.

Results: PRR screening showed that BcfA activates antigen presenting cells through murine TLR4. BcfA-treated WT BMDCs upregulated expression of the costimulatory molecules CD40, CD80, and CD86 and produced IL-6, IL-12/23 p40, and TNF-α while TLR4 KO BMDCs were not activated. Furthermore, human PBMCs stimulated with BcfA produced IL-6. BcfA-stimulated murine BMDCs also exhibited increased uptake of the antigen DQ-OVA, supporting a role for BcfA in improving antigen presentation to T cells. BcfA further activated APCs in murine lungs. Using an *in vitro* T_H cell polarization system, we found that BcfA-stimulated BMDC supernatant supported T_{FH} and T_H1 while suppressing T_H2 gene programming.

Conclusions: Overall, these data provide mechanistic understanding of how this novel adjuvant activates immune responses.

KEYWORDS

adjuvants, antigen presenting cells, BcfA, T cell polarization, pattern recognition receptors

Introduction

Many approved vaccines are comprised of purified antigens admixed with an adjuvant, referred to as subunit vaccines. The inclusion of immune stimulatory adjuvants in vaccine formulations bolsters immune responses versus antigens alone, supports dose sparing, reduced frequency of administration (1, 2), and improves the stability and pharmacokinetics of the antigens leading to an increased *in vivo* half-life (2). Another notable advantage is the ability of the adjuvant to shape the phenotype of the resulting cellular and humoral responses (1).

Alum (aluminum hydroxide or aluminum phosphate) was the first adjuvant to be licensed for human use more than a century ago. For seven decades, it was the only adjuvant used in FDA- and EMA-approved vaccines administered to protect against a multitude of infectious diseases including hepatitis, pertussis, and diphtheria (3, 4). In the late 1990s, other adjuvants were approved for addition to previously licensed human vaccines (3). The first of these was the oil-in-water emulsion MF59 added to a trivalent influenza vaccine, FLUAD (5, 6). The more recently described AS01-AS04 family of adjuvants are TLR4 ligands and aim to maximize the immune response while maintaining tolerability using a mix of classical adjuvants and other immunostimulatory molecules (3). These are included in vaccines against shingles (7), malaria (8), pandemic influenza (9), HBV and HPV (10). The oligonucleotide cytosine phosphoguanosine 1018 (CpG 1018), is a TLR9 agonist included in a hepatitis B vaccine (11–13).

These approved adjuvants have different mechanisms of action and are safe and effective at generating T cell and antibody-mediated responses. Notably, however, they all elicit mixed T_H1/T_H2-polarized immunity (14). In contrast, natural immune responses to infection with most viral and bacterial pathogens elicit T_H1/T_H17-polarized T cell and antibody responses, which are correlated with sustained protection against disease and infections in both humans and mouse models (15–19). Recent studies (20) also highlight the importance of tissue-resident memory T (T_{RM}) and B cell responses which provide sustained protection at barrier sites (21–24). Therefore, there is a need for safe novel adjuvants that elicit T_H1/T_H17-polarized immune responses, and also generate tissue-resident memory. To rationally design such adjuvants, it is critical to understand their mechanism of action. We previously identified *Bordetella* colonization factor A (BcfA), a bacterial protein of the Gram-negative pathogen *Bordetella bronchiseptica*, and we have reported that it functions as an adjuvant *in vivo* (25). Systemic administration of BcfA-containing vaccines elicited T_H1- and T_H17-polarized $CD4^+$ and T_H1-polarized $CD8^+$ T cell responses (25), T follicular helper (T_{FH}) cells, and T_H1-skewed antibody responses (20) alone and in combination with alum. Mucosal immunization with antigens mixed with BcfA elicited $CD4^+IL\text{-}17^+$ T_{RM} cells in the lungs and nose (20, 26). Importantly, when BcfA was mixed with alum-containing approved and experimental vaccines, T_H2 responses were attenuated while T_H1 and T_H17 responses were sustained or amplified (20, 25), suggesting that BcfA can override the T_H2 polarized responses elicited by alum. This unique property therefore supports the potentially broad applicability of BcfA as an adjuvant for bacterial and viral pathogens where T_H1 and T_H17 responses are important for protection against infection and disease.

Here, we investigated the mechanism of BcfA activation of immune responses. We report that BcfA activates bone marrow-derived dendritic cells (BMDCs) through the pattern-recognition receptor TLR4. We observed dose-dependent upregulation of costimulatory molecules CD40, CD80 and CD86 on wildtype (WT) BMDCs and the production of innate cytokines IL-6, TNFα and IL-12/23 p40. BcfA-activated BMDCs more efficiently processed and presented the model antigen DQ-OVA. Furthermore, BcfA-stimulated BMDC conditioned medium supported differentiation of T_{FH}-like and T_H1 $CD4^+$ T cells in an *in vitro* culture system, demonstrating the ability of BcfA to shape therapeutically beneficial T cell responses. These results provide insight regarding the TLR-dependent mechanism of action of this novel adjuvant and suggest that inclusion of BcfA in next-generation vaccine formulations may represent a promising avenue to enhance protective long-term immunity.

Materials and methods

BcfA formulation

BcfA was produced and purified as described previously (27). Residual LPS was removed using MustangQ filters (Cytiva Life Sciences, Inc, Marlborough, MA, catalog no. MSTGXT25Q16) or polymyxin B agarose (Sigma-Aldrich, St. Louis MO, catalog no. P1411). Endotoxin was quantified [(LAL Chromogenic Endotoxin Quantitation Kit, Thermo Fisher Scientific, catalog no. 88282) and was ≤150 pg/μg protein.

PRR screening

HEK-Blue cells overexpressing murine TLR4 (catalog no. hkb-mtlr4) or murine TLR2 (catalog no. hkb-mtlr2) (InvivoGen, Inc. San Diego, CA) were stimulated with 1 or 5 μg/mL BcfA for 24hr in duplicate wells. Production of the co-expressed secreted embryonic alkaline phosphatase (SEAP) reporter was quantified. Minimal LPS (minLPS, 0.2ng/mL) in the BcfA preparation was used as negative control and purified LPS (100 μg/mL) (eBioscience, San Diego, CA catalog. no 00-4976-93) was used as positive control for stimulation.

Mice

All experiments were reviewed and approved by The Ohio State University (OSU) Institutional Animal Care and Use Committee (Protocol number 2017A00000090). C57BL/6J, TLR4 knockout mice on the C57BL/6 background were obtained from Jackson Laboratories and bred in our facility. Tail DNA from mice was genotyped by Transnetyx, Inc. (Cordova, TN) using validated probe sets to confirm genotypes.

Differentiation of murine bone marrow derived dendritic cells

Murine BMDCs were prepared according to published protocols (28). Briefly, bone marrow was isolated, dissociated into a single cell suspension, and red blood cells were lysed with ACK lysing buffer (Gibco Ref A10492). The cell suspension was resuspended in RPMI1640 (Gibco) + 10% fetal bovine serum (FBS, Sigma-Aldrich F4220), 10μg/mL gentamicin, $5x10^{-5}$M ß-mercaptoethanol and 40 ng/mL GM-CSF (R&D Systems, Minneapolis, MN, catalog no. 415-ML-020)) and seeded in 10 cm^2 non-tissue culture treated petri dishes (VWR catalog no. 25384-342) at a density of 5-10 $x10^6$ cells/plate. Half of the medium was replaced every 2 days with the addition of fresh GM-CSF. On day 6-7 post-differentiation, BMDCs were transferred to 6-well tissue culture-treated plates (Falcon catalog no. 353046) at a density of 0.5-1 $x10^6$ cells/well. The next day, the cells were stimulated with various concentrations of BcfA for 20-24hr. Supernatant was collected for ELISA analysis and the cells were harvested for flow cytometry.

Collection of human PBMCs and stimulation with BcfA

Peripheral blood was collected from adult human donors under a protocol approved by The Ohio State University Institutional Review Board (Protocol numbers 2020H0404 and 2021H0179). Whole blood was collected in EDTA treated tubes. PBMCs were separated from whole blood on a Percoll gradient (Cytiva, catalog no. 17144003), and cryo-preserved at -80°C. Cells were thawed and cultured in RPMI + 10% human AB serum (Sigma Aldrich, catalog no. H4522). To determine TLR4 expression, PBMCs were stained with α-human TLR4 (Thermo Fisher Scientific catalog no. 12-9041-80) antibody. Cells were analyzed on a Cytek Aurora spectral flow cytometer. Fluorescence minus one (FMO) controls were used for gating. To test cytokine production, 1-$2x10^6$ cells from individual donors were stimulated for 20-24hr and the supernatant was tested by ELISA.

Enzyme-linked immunosorbent assay for innate cytokines

The production of murine TNF-α, IL-6, IL-12/23 p40 common γ chain and IL-12 was quantified by a sandwich ELISA according to the manufacturer's instructions (Life Technologies or BioLegend). Human cytokines IL-6 and TNF-α were quantified using Quantikine ELISA kits (R&D Systems). Plates were read at A_{450} on a SpectraMax i3x® plate reader and concentrations were calculated based on the standard curve.

DQ-OVA uptake and processing

BMDCs were plated in 6 well plates at 1 $x10^6$ cells/well and stimulated with BcfA or cultured with medium alone. At 24 hr post-stimulation, DQ-OVA (InvivoGen, Inc. catalog no. D12053) was added at a concentration of 10 μg/mL for 45 min. The cells were then washed and harvested to quantify expression of CD11c, MHC-Class II and DQ-OVA by flow cytometry.

Immunization of mice

Mice were lightly anesthetized with 2.5% isoflurane/O_2 for immunization. To stimulate APCs in the lungs, mice were immunized intranasally with 10 μg BcfA or LPS-EB VacciGrade™ (InvivoGen, catalog no. vac-3pelps) (a TLR4 agonist used as a positive control) in 50 μL divided between both nares. Lungs were harvested 24 hr post-inoculation.

Tissue dissociation and flow cytometry

BMDCs were harvested at 20-24hr post-stimulation and were washed with cold PBS prior to staining with Live/Dead Zombie NIR fixable viability dye (BioLegend, catalog no. 423105) for 30 min at 4°C. Cells were then washed twice with PBS supplemented with 1% heat-inactivated FBS (1% FBS) (FACS buffer) and resuspended in Fc Block (α-CD16/CD32 antibody, clone 93) (eBioscience, catalog no. 14-0161-86) at 4°C for 5 min before staining with a mixture of the following Abs for 20 min at 4°C: CD11c e450 (clone N418; Invitrogen, catalog no.48-0114-82), MHC Class II I-A/I-E BV785 (clone M5/114.15.2; Biolegend, catalog no.107645), CD40-APC (clone 1C10), CD80 PerCP-Cy5.5 (clone 16-10A1; Biolegend, catalog no.104722) and CD86 FITC (clone GL1; eBioscience, catalog no.11-0862-85).

Lungs were processed, digested (mouse lung dissociation kit, Miltenyi Biotec, catalog no. 130-095-927), and mechanically disrupted (gentleMACS) into a single-cell suspension followed by RBC lysis.Cells were washed with cold PBS and stained with Live/Dead Zombie NIR fixable viability dye (BioLegend, catalog no. 423105) for 30 min at 4°C, then washed with PBS/1% FBS and resuspended in Fc Block at 4°C for 5 min. Lung cells were stained with a mixture of the following antibodies for 20 min at 4°C: CD11b APC (clone M1/70; Invitrogen, catalog no.17-0112-82), CD11c e450 (clone N418; Invitrogen, catalog no.48-0114-82), MHC Class II I-A/I-E BV785 (clone M5/114.15.2; Biolegend, catalog no.107645), CD45 PE (clone 30-F11; BD Biosciences, catalog no.553081), CD40 PE-CF594 (clone 3/23; BD Biosciences, catalog no.562847), CD80 PerCP-Cy5.5 (clone 16-10A1; Biolegend, catalog no.104722) and CD86 FITC (clone GL1; eBioscience, catalog no.11-0862-85).

For intracellular cytokine staining, cells were first incubated in complete IMDM (cIMDM; IMDM [Life Technologies], 10% FBS [26140079, Life Technologies], 1% Penicillin-Streptomycin [Life Technologies], and 0.05% (50 mM) 2-ME [Sigma-Aldrich]) with eBioscience protein transport inhibitors (PTI; catalog no. 00-4980-93, Invitrogen) for 4 hr. For cell surface marker staining, samples were pre-incubated for 5 min at 4°C with TruStain FcX™ (α-mouse CD16/32) Fc block (clone 93; catalog no. 101320, BioLegend). Samples were then stained for extracellular markers in the

presence of Fc block for 30 min at 4°C protected from light using the following antibodies: α-CD4 (PerCP-Cy5.5; 1:100; clone GK1.5; catalog no. 100434, BioLegend) and Ghost Dye (V510; 1:400; catalog no. 50-105-2992, Tonbo Biosciences). Cells were then washed twice with FACS buffer and were fixed and permeabilized using the eBioscience Foxp3 transcription factor staining kit (Thermo Fisher Scientific, catalog no. 00-8333-56) overnight at 4°C.

Following fixation, cells were washed once with the 1X eBioscience permeabilization buffer (Thermo Fisher Scientific). Recombinant Mouse IL-21R Fc Chimera primary antibody (catalog no. 596-MR, R&D) was diluted 1:5 in 1X eBioscience permeabilization buffer and 100 µL was added per well to incubate for 30 min at 4°C protected from light. Cells were washed once with 1X eBioscience permeabilization buffer. Goat F(ab')2 Anti-Human IgG - Fc secondary antibody (PE, catalog no. ab98596, Abcam) was diluted 1:31.25 in 1X eBioscience permeabilization buffer and 100 µL was added per well to incubate for 30 min at 4°C protected from light. For staining the remaining intracellular markers, cells were washed once with 1X eBioscience permeabilization buffer and then stained with the following antibodies in 1X eBioscience permeabilization buffer for 1hr at room temperature protected from light: α-Bcl6 (AF488; 1:20; clone K112-91; catalog no. BDB561524, BD Biosciences); α-Gata3 (PE-Cy7; 1:20; clone TWAJ; catalog no. 25-9966-42, Invitrogen); α-IL-4 (APC; 1:50; clone 11B11; catalog no. 504106, BioLegend); α-IFN-γ (APC-Cy7; 1:300; clone XMG1.2; catalog no. 505850, BioLegend), and α-T-bet (PacBlue; 1:50; clone 4B10; catalog no. 644808, BioLegend). Cells were washed twice with 1X permeabilization buffer and resuspended in FACS buffer for analysis.

Fluorescence minus one or isotype control antibodies were used as negative controls. After two washes, cells were resuspended in PBS/1% FBS and samples were collected on or BD FACS Symphony or Cytek Aurora spectral flow cytometer (Cytek Biosciences).

Analysis was performed using FlowJo software version 10.8.0. The number of cells within each population was calculated by multiplying the frequency of live singlets in the population of interest by the total number of cells in each sample.

Preparing and assaying CD4$^+$ T cells for lineage-defining transcription factors and effector cytokines

Naïve CD4$^+$ T cells were purified from the spleen and lymph nodes of 5-8-week-old WT C57BL/6J mice using the BioLegend Mojosort kit. Cells were plated in 24-well plates on plate-bound anti-CD3 (5 µg/mL) and anti-CD28 (2µg/mL) in the presence or absence of IL-4 neutralizing antibody (11B11, BioLegend, 5µg/mL). After 16-20hr, medium from non-stimulated control (NS Ctrl) or BcfA-treated BMDCs was added to the well, with or without IL-4-neutralizing antibody. Where indicated, IL-6-neutralizing antibody (MP5-20F3, BioLegend, 10µg/mL) was also added. Cells were cultured for an additional 48hr before harvest and subsequent analysis.

RNA was isolated using the Macherey-Nagel Nucleospin kit per the manufacturer's instructions, and complementary DNA (cDNA) was synthesized using the SYBR Superscript IV First Strand Synthesis System with oligo dT primers (Thermo Fisher). qRT-PCR reactions were run on the CFX Connect (BioRad) with 5-20ng of cDNA, using the SYBR Select Mastermix for CFX (ThermoFisher) and the following primers:

Bcl6 forward: 5'-CCAACCTGAAGACCCACACTC-3', *Bcl6* reverse: 5'-GCGGACATGGCTCTTCAGAGTC-3'; *Il21* forward: 5'-TGGATCCTGAACTTCTATCAGCTCC -3', *Il21* reverse: 5'- A GGCAGCCTCCTCCTGAGC -3'; *Tbx21* forward: 5'- GTG ACTGCCTACCAGAACGC -3', *Tbx21* reverse: 5'- AGGG GACACTCGTATCAACAG -3'; *Ifng* forward: 5'- CTACCT TCTTCAGCAACAGC -3', *Ifng* reverse: 5'- GCTCATTGA ATGCTTGGCGC -3'. Data were normalized to *Rps18* and are presented relative to either *Rps18* or the control sample, as noted.

Statistical analysis

Data were analyzed using GraphPad Prism by the methods described in each figure legend.

Results

Activation of murine BMDCs by BcfA is dependent on TLR4

We hypothesized that BcfA activates antigen-presenting cells (APCs) through a PRR and conducted an empirical PRR screening using the HEK-Blue system, where human embryonic kidney (HEK) cells were transfected with the SEAP (secreted embryonic alkaline phosphatase) reporter gene under the control of a promoter inducible by NF-κB and activator protein-1 (AP-1) and expressing murine TLR (mTLR) or NOD receptors. SEAP reporter production was quantified using a colorimetric assay. The screen showed activation of mTLR4 and mTLR2 (Supplementary Figure S1A). We then stimulated cells expressing TLR4 (HEK-mTLR4) and TLR2 (HEK-mTLR2) with 1 or 5 µg/mL BcfA. Maximal SEAP release was detected from HEK cells expressing murine TLR4 (HEK-mTLR4) following stimulation with 1 µg/mL BcfA (Supplementary Figure S1B) at levels comparable to purified LPS used as a positive control. SEAP production from HEK-mTRL2 cells was nearly maximal at 5 µg/mL BcfA stimulation (Supplementary Figure S1C) with lower SEAP production detected with 1 µg/mL BcfA stimululation. To mitigate any confounding effects of BcfA produced in *E. coli* as a bacterial recombinant protein, we utilized a stringent purification procedure to remove LPS (27). HEK-mTLR4 or HEK-mTLR2 cells incubated with this minimal LPS (≤150 pg/µg protein) (min LPS) did not produce SEAP.

We then evaluated the BcfA stimulatory activity in a more physiologically relevant system. We isolated bone marrow from WT C57BL/6 mice and TLR4 KO mice and differentiated BMDCs *in vitro*. The immature DCs were treated with BcfA (1 or 5 µg/mL) for 24 hr and analyzed for the expression of costimulatory molecules by flow cytometry. BMDCs were identified as a CD11c$^+$ MHC-II^{hi} population (Supplementary Figure S2) (29) and were evaluated for the expression of costimulatory molecules by flow cytometry. Representative flow plots are shown in Figure 1A. The mean fluorescence intensity (MFI) expression of CD40 (Figure 1B),

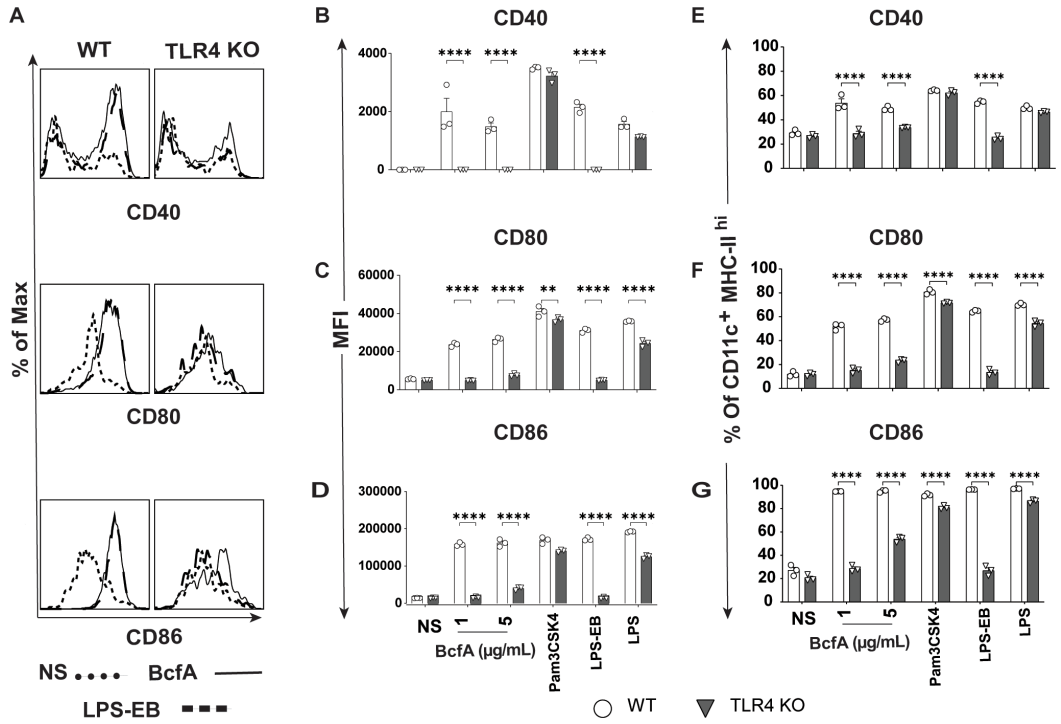

FIGURE 1
Costimulatory molecule expression is upregulated on BMDCs following BcfA stimulation. **(A)**. Representative overlays of CD40, CD80 and CD86 expression on WT and TLR4 KO BMDCs stimulated with 5 μg/mL BcfA. Median fluorescence intensity (MFI) expression of **(B)**. CD40, **(C)**. CD80 and **(D)**. CD86 and percentage of cells expressing **(E)**. CD40, **(F)**. CD80 and **(G)**. CD86 on WT and TLR4 KO BMDCs stimulated with 1 μg/mL and 5 μg/mL BcfA for 20-24 hr. LPS, Pam3CSK4 and LPS-EB were used as positive controls. Mean ± SEM of triplicate wells is shown. *, p<0.05, **, p<0.01, ***, p<0.001, ****, p<0.0001 by ANOVA. One experiment of 2.

CD80 (Figure 1C), and CD86 (Figure 1D) and percentage of cells expressing CD40 (Figure 1E) CD80 (Figure 1F) and CD86 (Figure 1G) was upregulated in response to BcfA stimulation compared to no stimulation (NS) control. LPS-EB (de-O-acelylated lipooligosaccharide) (5 μg/mL) that has been used as an adjuvant *in vivo* (30) and purified *E. coli* LPS (100 ng/mL) were included as positive controls for TLR4, and PAM3Csk was used as a positive control to confirm that TLR4 KO BMDCs respond to stimulation. Both the MFI and percentage of cells that upregulated costimulatory molecule expression was reduced to background in BcfA-stimulated TLR4 KO BMDCs, suggesting that BcfA primarily functions through this PRR. We also tested activation of TLR2 KO BMDCs which showed that costimulatory molecule expression was not reduced by the absence of TLR2 (Supplementary Figure S3), suggesting that BcfA primarily functions through TLR4. Thus, we focused on TLR4 mediated activity of BcfA in the following studies.

BcfA induces the production of T_{FH}/T_H1/T_H17-polarizing cytokines by BMDCs

To determine the T cell responses that may be supported by APCs activated by BcfA, we quantified cytokine production from BcfA-stimulated BMDCs by ELISA. WT BMDCs produced IL-6 (Figure 2A), TNF-α (Figure 2B), IL-12/23 p40 (Figure 2C) and IL-12 (Figure 2D) at levels comparable to the positive control LPS. Production of all four cytokines was significantly reduced in TLR4 KO BMDCs. These results show that innate immune responses elicited by BcfA are mediated through TLR4 and may support T_H1/T_H17-polarized immune responses.

We then tested whether BcfA activated human PBMCs. First, we confirmed expression of TLR4 on adult human PBMCs by flow cytometry (Figure 3A). We then stimulated PBMCs *in vitro* with BcfA and measured the levels of innate cytokines IL-6 and TNF-α present in the cell culture supernatant after 24 hr. We found that IL-6 was significantly induced in response to stimulation with 5 μg/mL or 25 μg/mL of BcfA (Figure 3B). Although TNF-α production was substantially increased upon stimulation with BcfA, differences were not statistically significant compared to unstimulated cells (Figure 3C). These data show that BcfA stimulation elicits T_H1/T_H17-polarizing innate cytokines by human cells.

BcfA stimulation of BMDCs supports antigen uptake and processing

Next, we evaluated whether BcfA stimulation of BMDCs would increase antigen uptake and processing of DQ-OVA, a chicken ovalbumin (OVA) conjugate that displays a bright green fluorescence only after proteolytic processing. We stimulated BMDCs with 5 μg/mL BcfA or media alone as a negative control for 24 hr at 37°C. The next day, cells were treated with DQ-OVA for 60 min. at 37°C. The level of

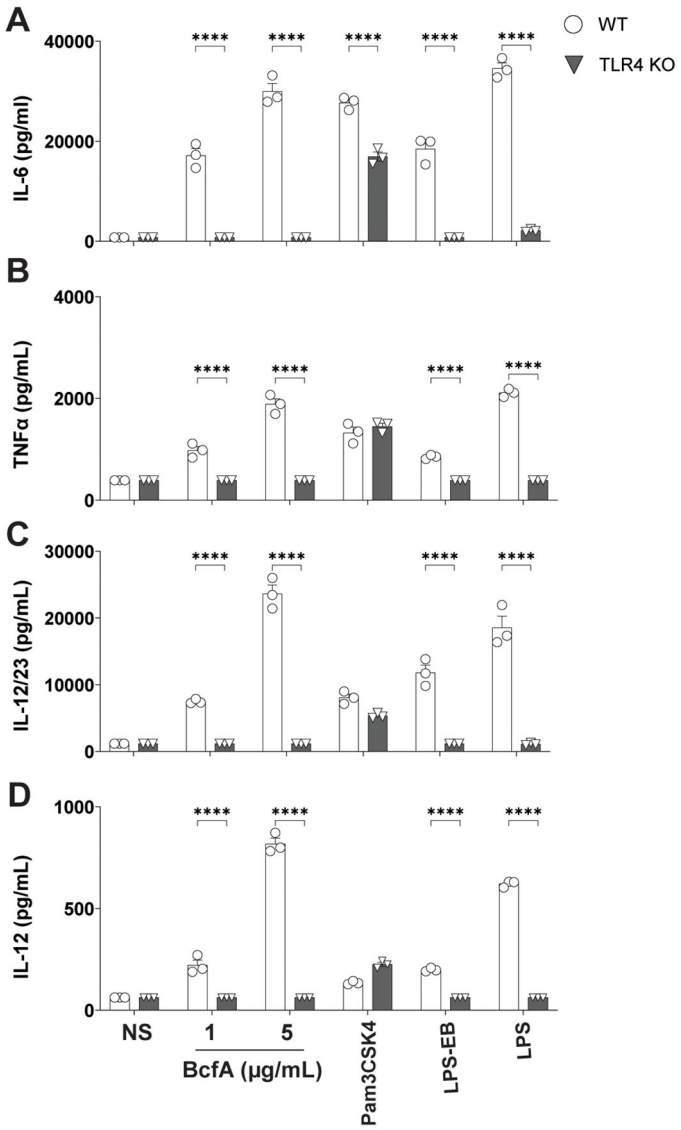

FIGURE 2
Production of T_{FH}/T_H1-polarizing innate cytokines following BcfA stimulation is dependent on TLR4. Expression of **(A)**. IL-6, **(B)**. TNF-α, **(C)**. IL-12/23 p40 and **(D)**. IL-12 by WT and TLR4 KO BMDCs stimulated with BcfA for 20-24 hr. LPS, Pam3CSK4 and LPS-EB were used as positive controls. Mean ± SEM of triplicate wells is shown. *, p<0.05, ***, p<0.001, ****, p<0.0001 by ANOVA. One experiment of 2.

green fluorescence was then quantified by flow cytometry as a proxy for antigen uptake and processing. BcfA-treated BMDCs took up more DQ-OVA than unstimulated BMDCs (Figure 4A). We also observed an increase in the percentage of BMDCs with green fluorescence (Figure 4B) compared to NS controls. Together, these data suggest that BcfA-activated BMDCs have an increased ability to uptake and process antigen.

BcfA upregulates costimulatory molecule expression on $CD11b^+CD11c^+$ cells via TLR4 *in vivo*

To test whether BcfA stimulates lung cells, we administered 10 µg BcfA or LPS-EB intranasally to C57BL/6 and TLR4 KO mice. Lungs were harvested 24 hr later and evaluated for the expression of MHC Class II, CD40, CD80, and CD86 on the $CD11b^+$ $CD11c^+$ population (31) (Figure 5A). The gating strategy is shown in Supplementary Figure S4. MFI expression of MHC Class II (Figure 5B), CD40 (Figure 5C), CD80 (Figure 5D) and CD86 (Figure 5E) and the percentage of cells that upregulated expression of MHC Class II (Figure 5F), CD40 (Figure 5G), CD80 (Figure 5H) and CD86 (Figure 5I) increased on this cell population, demonstrating that BcfA efficiently activates putative antigen presented cells in the lungs. The MFI of costimulatory molecule expression was not upregulated on $CD11b^+$ $CD11c^+$ cells in TLR4 KO lungs (Figures 5B–E). The percentage of cells expressing MHC Class II compared to no stimulation increased in WT and TLR4 KO lungs (Figure 5F). In contrast the percentage of TLR4 KO lung cells expressing the costimulatory molecules CD40 (Figure 5G), CD80 (Figure 5H) and

10.3389/fimmu.2024.1439418

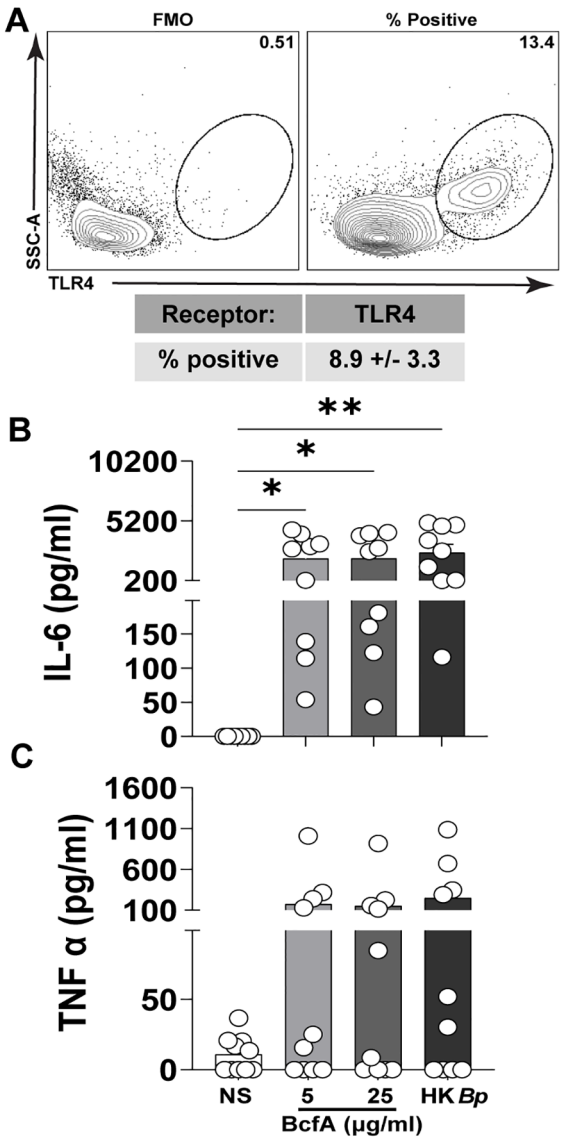

FIGURE 3
Human PBMCs produce IL-6 following stimulation with BcfA. **(A)**. The percentage of live PBMCs expressing TLR4 (N=5 adult donors) **(B)**. PBMCs from 10 adult donors were stimulated for 24 hr with the indicated concentrations of BcfA or heat-killed *B. pertussis* control (HK *Bp*). IL-6 and **(C)**. TNF-α in culture supernatant was evaluated by ELISA). *, p<0.05, **, p<0.01 by ANOVA.

CD86 (Figure 5I) did not increase compared to no stimulation. These data further confirm TLR4 as the primary *bona fide* PRR for BcfA mediated activity.

BcfA-stimulated BMDC-conditioned medium supports T_{FH} and T_H1 cell programming

As part of pathogen-specific immune responses, naïve $CD4^+$ T cells differentiate into effector subsets which perform specialized activities to orchestrate immune-mediated clearance of infection. Particularly critical for responses to intracellular pathogens like SARS-CoV-2 and primarily extracellular pathogens like *B. pertussis* are T helper 1 (T_H1) and T follicular helper (T_{FH}) populations. Of these, T_H1 cells activate other immune populations by secreting pro-inflammatory cytokines such as IFN-γ, while T_{FH} cells produce IL-21 and provide help to B cells to promote antibody generation and humoral immunity (32, 33). We previously reported that intramuscular (i.m.) immunization with an acellular pertussis vaccine (aPV) containing BcfA elicited systemic T_H1 responses *in vivo* (25). In our recent work (20), we established that immunization of mice with BcfA-adjuvanted SARS-CoV-2 spike protein supported production of IFN-γ-driven IgG2c spike protein-specific antibodies. Thus, we hypothesized that BcfA may support both T_H1 and T_{FH} cell differentiation programs, and consequently productive anti-bacterial and anti-viral cell-mediated and humoral immune responses.

Effector $CD4^+$ T cell differentiation is directed by a coordinated interplay between cell-intrinsic transcriptional networks and environmental cytokine signals that are often produced by antigen-

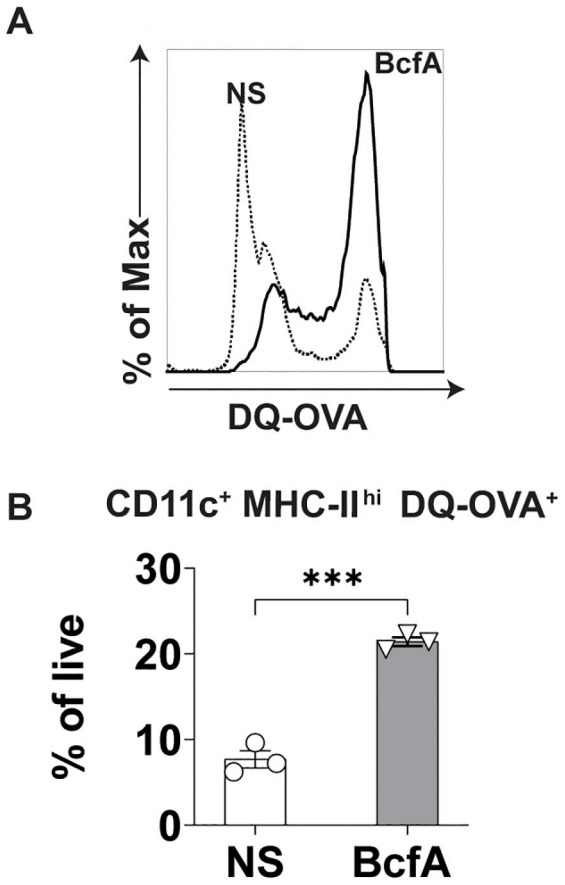

FIGURE 4
Increased uptake of DQ-OVA by BcfA-stimulated BMDCs. **(A)**. Representative overlays of non-stimulated (NS) and BMDCs stimulated with 5 μg/mL BcfA. **(B)**. $CD11c^+$ $MHC\text{-}II^+$ $DQ\text{-}OVA^+$ BMDCs as % of live cells. Mean ± SEM of triplicate wells is shown. ***, $p<0.001$ by paired Student's t-test. One experiment of 2.

presenting cells (34). To test whether the IL-6, IL-12, and IL-12/23 common chain cytokines in BcfA-stimulated supernatants would be sufficient to induce T_{FH} and/or T_H1 differentiation, we stimulated naïve $CD4^+$ T cells on plate-bound α-CD3/α-CD28 in the presence of cell-free supernatant from untreated BMDCs (NS) or those treated with 5 μg/mL BcfA for 72 hr. We then assessed the expression of key T_{FH} and T_H1/ genes via qRT-PCR. Consistent with our hypothesis, expression of genes for lineage-defining transcription factors and effector cytokines associated with T_{FH} (*Bcl6, Il21*; Figure 6A) and T_H1 (*Tbx21* (T-bet), *Ifng*; Figure 6B) cells were elevated in cells cultured in the presence of BcfA-conditioned medium relative to NS controls.

As IL-6/STAT3 signaling is an established driver of T_{FH} differentiation, we determined whether the IL-6 in the culture medium was responsible for driving T_{FH} differentiation. We cultured cells in BcfA-treated or NS control medium in the presence or absence of IL-6-neutralizing antibody. Consistent with a role for IL-6 in promoting T_{FH} gene expression, we observed a significant reduction in the expression of both *Bcl6* and *Il21* when IL-6 was neutralized (Figure 6C).

As standard T_{FH}-like and T_H1 culture conditions include the addition of anti-IL-4 neutralizing antibody which prevents inherent T_H2 polarization (35), we also tested whether BcfA elicited T_{FH} or T_H1 gene programming in the absence of IL-4-neutralization. Naïve T cells were differentiated *in vitro* without the addition of anti-IL-4 blocking antibody. We evaluated the expression of T cell subset-specific lineage-defining transcription factors and key cytokines by qRT-PCR and flow cytometry. Interestingly, BcfA reduced the RNA (Figure 7A) expression of the T_H2 lineage-defining transcription factor Gata-3, while the protein level was unchanged (Figure 7B). Similarly, the RNA (Figure 7C) level of the T_H2 effector cytokine IL-4 was reduced, while the protein (Figure 7D) expression was unchanged. In contrast, while transcript abundance for the T_{FH} lineage-defining transcription factor Bcl-6 was unchanged (Figure 7E), its protein expression was elevated (Figure 7F). Yet, transcript levels for the T_{FH} cytokine IL-21 were significantly elevated (Figure 7G), while protein expression was not significantly increased (Figure 7H). Finally, T_H1 differentiation was elevated, as the RNA expression of the T_H1-defining factor *Tbx21* (T-bet) was increased (Figure 7I), and the protein level was slightly but not significantly elevated (Figure 7J). RNA for the T_H1 cytokine IFN-γ was unchanged (Figure 7K) while protein expression was increased (Figure 7L). Overall, these data suggest that BcfA both negatively regulates T_H2 differentiation and positively regulates T_{FH} and T_H1 programming.

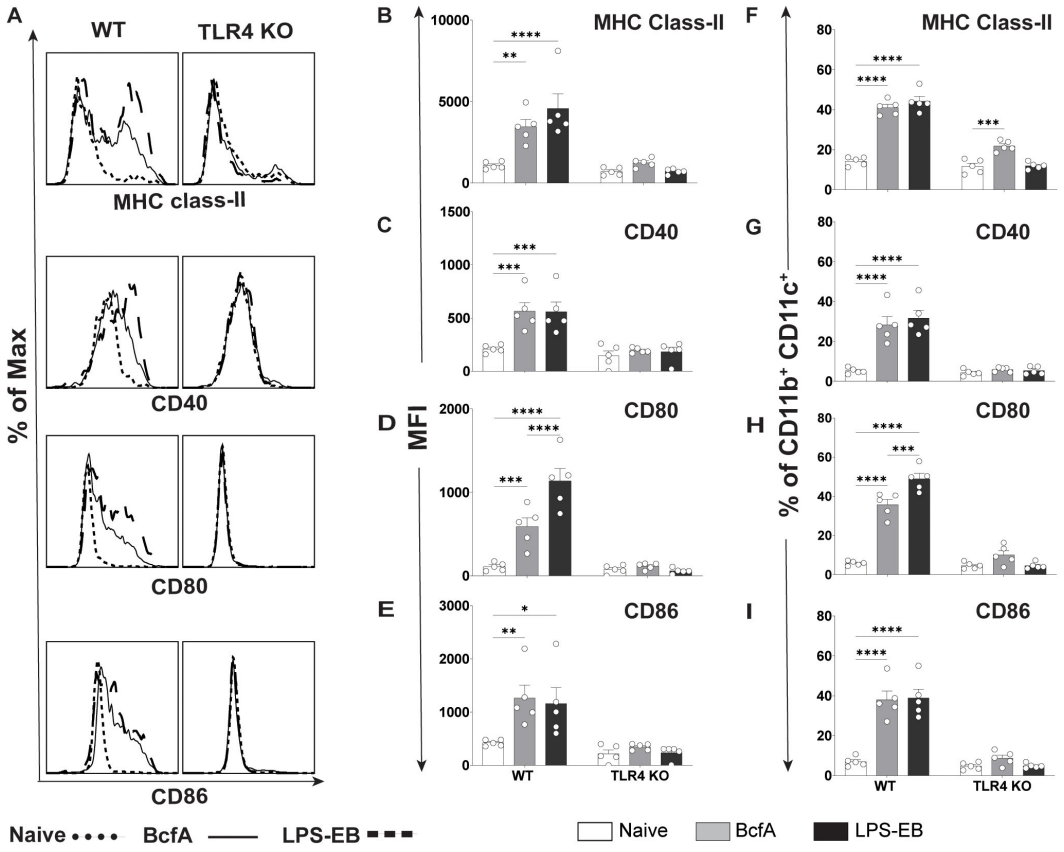

FIGURE 5
Upregulation of costimulatory molecule expression on lung CD11b$^+$CD11c$^+$ cells by BcfA is dependent on TLR4. **(A)**. Representative overlays of MHC class-II, CD40, CD80 and CD86 expression on lung cells from WT and TLR4 KO mice. Median fluorescence intensity (MFI) of **(B)**. MHC class-II, **(C)**. CD40, **(D)**. CD80 and **(E)**. CD86 and percentage of cells expressing **(F)**. MHC class-II, **(G)**. CD40, **(H)**. CD80, and **(I)**. CD86 on CD11b$^+$ CD11c$^+$ lung cells from WT and TLR4 KO mice, analyzed 24 hr post intranasal immunization with 10 µg of BcfA or LPS-EB. Mean ± SEM of 5 mice is shown. *, p<0.05, **, p<0.01, ***, p<0.001, ****, p<0.0001 by ANOVA. One experiment of 2.

Discussion

The development and characterization of novel adjuvants is an active area of research, with the goal of defining adjuvants that elicit strong, sustained vaccine-mediated immune responses. Despite the decades-long use of alum as an adjuvant and the recent development of newer formulations, there remains a need for safe and effective adjuvants that elicit systemic and mucosal immunity.

Here, we investigated the mechanism of action of the adjuvant BcfA, which was discovered by our group and has demonstrated adjuvant activity in experimental vaccines against respiratory pathogens *B. pertussis* (25, 26) and SARS CoV-2 (20). The hallmark feature of BcfA that distinguishes it from FDA-approved and other experimental adjuvants is the absence of T_H2 responses when BcfA is used as the single adjuvant (25) and strong attenuation of T_H2 responses when BcfA is added to alum-adjuvanted vaccines (20, 26).

Furthermore, BcfA elicits T_H1 and T_H17 responses which are critical for protection against both bacterial and viral pathogens. Attenuation of T_H2 immune responses may also reduce the risk of vaccine related adverse events such as antibody dependent enhancement of disease (ADE) and vaccine associated enhancement of respiratory disease (VAERD).

As BcfA is a protein, we hypothesized that it may activate immune responses through PRRs expressed on APCs. A PRR/NOD receptor screen identified both murine TLR4 and TLR2 as the receptors triggered on HEK-293 reporter cell lines following BcfA stimulation (Supplementary Figure S1). When the activity of BcfA was tested in murine BMDCs as a more physiological system, upregulation of costimulatory molecule expression (Figure 1) and production of innate cytokines (Figure 2) was significantly reduced in TLR4 KO BMDCs compared with WT BMDCs, but not in TLR2 KO BMDCs (Supplementary Figure S3). These data show that BcfA acts primarily through TLR4. BcfA-stimulated BMDCs showed uptake and processing of the model antigen DQ-OVA (Figure 4), suggesting that BcfA may also support T cell activation by amplifying antigen presentation. We pretreated BMDCs with BcfA prior to testing uptake of DQ-OVA. Coadministration of antigen and adjuvant may change the kinetics or magnitude of antigen uptake and processing and is a limitation of our experimental design.

To determine the potential utility of BcfA as an adjuvant for human vaccines, we tested cytokine production by human PBMCs stimulated with BcfA for 24 hr (Figure 3). Production of IL-6 was detected in supernatants of all samples tested, suggesting that

10.3389/fimmu.2024.1439418

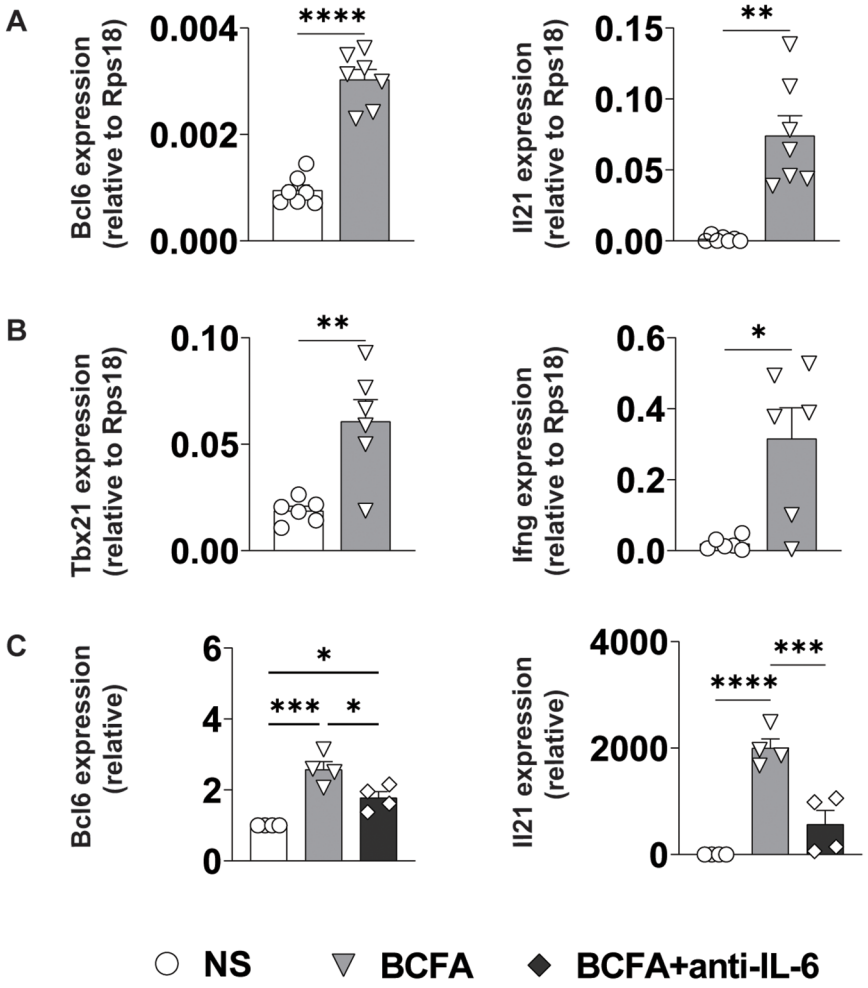

FIGURE 6
BcfA conditioned medium supports T_{FH} and T_H1 cell polarization *in vitro*. qRT-PCR of T cells that were unstimulated (NS) or stimulated with BcfA conditioned medium with the addition of IL-4-neutralizing antibody. Data are presented relative to housekeeping gene *Rps18*. Data pooled from individual experiments with 4-7 samples per group. **(A)**. Bcl6 and IL21 expression, **(B)**. Tbx21 and IFN-γ expression, **(C)**. Bcl6 and IL21 expression alone or with anti-IL-6 neutralizing antibody. Mean ± SEM of 4 experiments is shown. *, p<0.05, **, p<0.01, ***, p<0.001, ****, p<0.0001 by paired Student's t-test.

human PBMCs stimulated with BcfA may support T_{FH} polarization of $CD4^+$ T cells. Expression of the inflammatory cytokine TNF-α was variable between donors, and not significantly increased compared with unstimulated cells. It is important to note that we collected supernatant at 24 hr post-stimulation, which may be beyond the time of maximal TNF-α production in this context. Alternately, there may be autocrine consumption of TNF-α produced by the monocytes (36). Thus, the ability of BcfA to activate human cells suggests that BcfA will have adjuvant function when included in human vaccines.

Although bacterial LPS is the canonical ligand for TLR4, this PRR may also be activated by a wide array of bacterial proteins (37). Interestingly, triggering of the same receptor may elicit disparate immune phenotypes. The pneumococcal proteins DnaJ and Ply (38, 39) and the *M. tuberculosis* derived proteins RpfE and Rv0652 are TLR4 ligands that activate DCs and polarize the immune response towards the T_H1/T_H17 phenotype (40, 41), but elicit different innate cytokines. Collectively, these findings suggest that the type of immune response elicited by adjuvants depends both on the responding PRR as well as the properties of the ligand.

Adjuvants also activate the adaptive immune response by directly triggering PRRs on lymphocytes (42). Murine and human T cells express TLR4 (43). Thus, BcfA may directly activate T cells when delivered *in vivo* as part of a vaccine formulation, and thereby amplify the vaccine-elicited response. This potential function of BcfA is an area of future study for our group.

Using an *in vitro* T cell polarization system, we showed that the innate cytokines produced by BcfA-stimulated BMDCs support the differentiation of T_H1 and T_{FH} cells while preventing T_H2 differentiation in parallel (Figure 6 and Figure 7). This result is in accordance with our previous report of the ability of BcfA to attenuate alum-induced T_H2 responses when combined *in vivo* (20, 26). In addition, the IL-6-dependent polarization of T_{FH} cells we observed also provides a potential mechanistic explanation for the induction of IgG2c antibody production we observed in the serum and lungs of mice immunized with BcfA-containing vaccines.

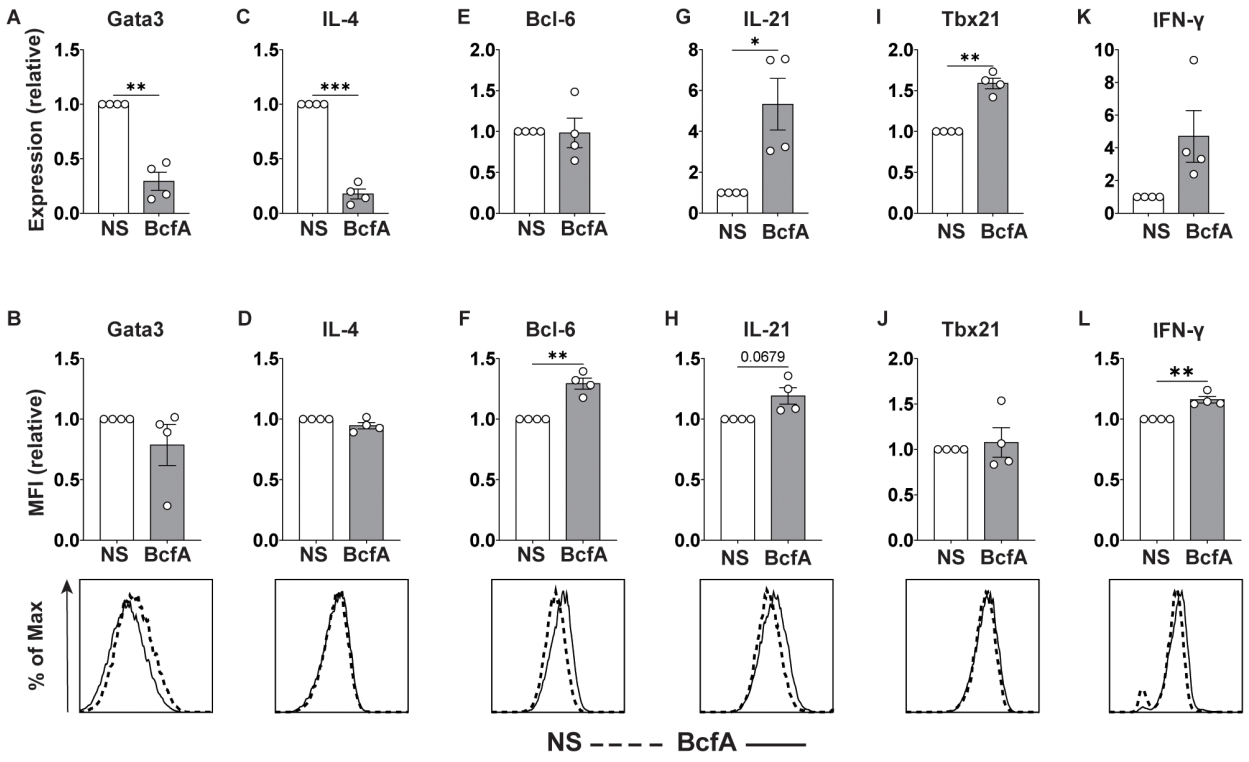

FIGURE 7
BcfA conditioned medium represses T_H2 cell polarization *in vitro*. qRT-PCR and flow cytometry analysis of unstimulated (NS) T cells or stimulated with BcfA conditioned medium in the absence of IL-4-neutralizing antibody. qRT-PCR data are presented relative to housekeeping gene *Rps18*. Mean ± SEM of 4 experiments is shown. Expression of Gata3 **(A, B)**, IL-4 **(C, D)**, Bcl-6 **(E, F)**, IL-21 **(G, H)**, T-bet **(I, J)**, and IFN-γ **(K, L)**. *, p<0.05, **, p<0.01, ***, p<0.001 by paired Student's t-test.

Generation of mucosal immunity to respiratory pathogens is critical for providing sustained protection against infection (44, 45) and preventing subsequent transmission (46). For *B. pertussis*, the $CD4^+IL\text{-}17^+$ T cells generated during natural infection are essential for reducing bacterial colonization of the nose (45, 46). Immunization of baboons with the whole cell pertussis vaccine (wPV) also clears the infection from the nose (47). In contrast, acellular pertussis (aPV) vaccine immunization does not reduce nasal bacterial burden (48). Our recent paper (26) showed that mucosal delivery of BcfA-adjuvanted acellular pertussis vaccines elicited $CD4^+IL\text{-}17^+$ tissue-resident memory T cells (T_{RM}) in the nose and reduced nasal bacterial burden. Although we detected production of the IL-12/23 p40 common γ chain by BcfA-stimulated BMDCs, suggesting that IL-17 may also be produced, we did not detect T_H17 polarization *in vitro* (data not shown), suggesting that either the amount of IL-12/23 produced in BcfA supernatant is insufficient, or that additional factors such as such as TGF-β (49) that support T_H17 generation are not replicated in the culture system.

In summary, this work provides a mechanistic understanding of the function of BcfA as an adjuvant and supports the utility of BcfA for use in human vaccines. Continued identification and validation of novel adjuvants that are safe, effective, and generate mucosal immunity is key to improving vaccine-mediated protection against infectious diseases.

Data availability statement

The original contributions presented in the study are included in the article/Supplementary Material. Further inquiries can be directed to the corresponding author.

Ethics statement

The studies involving humans were approved by Ohio State University Institutional Review Board. The studies were conducted in accordance with the local legislation and institutional requirements. The participants provided their written informed consent to participate in this study. The animal study was approved by Ohio State University Institutional Animal Care and Use Committee. The study was conducted in accordance with the local legislation and institutional requirements.

Author contributions

MS: Writing – original draft, Investigation, Methodology. KR: Investigation, Writing – review & editing. JH: Investigation, Writing – review & editing, Writing – original draft. JT: Investigation, Writing –

review & editing. JB: Investigation, Writing – review & editing. MG: Investigation, Writing – review & editing. YG: Investigation, Writing – review & editing. RD: Writing – review & editing, Funding acquisition. KO: Funding acquisition, Writing – review & editing, Supervision. PD: Writing – review & editing, Conceptualization, Funding acquisition, Project administration, Writing – original draft.

Funding

The author(s) declare financial support was received for the research, authorship, and/or publication of this article. This work was supported by 1R01AI125560 and 1R01AI153829 (to PD and RD) and 1R01AI134972 (to KO). MS was supported by a doctoral fellowship from the Egyptian Bureau of Higher Education. KR was supported by The Ohio State University College of Medicine Advancing Research in Infection and Immunity Fellowship Program. JH is supported by NIAID 1T32AI165391-01. JT is supported by NIAID 1F30AI172189-01A1.

Conflict of interest

The authors declare that the research was conducted in the absence of any commercial or financial relationships that could be construed as a potential conflict of interest.

The author(s) declared that they were an editorial board member of Frontiers, at the time of submission. This had no impact on the peer review process and the final decision.

Publisher's note

Supplementary material

The Supplementary Material for this article can be found online at: https://www.frontiersin.org/articles/10.3389/fimmu.2024.1439418/full#supplementary-material

SUPPLEMENTARY FIGURE 1
BcfA activates BMDCs and TLR2 and TLR4 expressing reporter cell lines. **(A)**. HEK-Blue™ cells expressing murine TLRs, and NOD1/2 were stimulated with BcfA (1μg/mL). SEAP reporter expression was detected using HEK-Blue™ Detection media. The average of duplicate wells is shown. **(B)**. HEK-Blue-mTLR4 and **(C)**. HEK-Blue-mTLR2 cells were stimulated with 1 and 5μg/mL of BcfA. NT = no treatment; min LPS = minimal LPS present in the BcfA preps. PAM3CSK4 and LPS were used as positive controls for TLR2 and TLR4 respectively. Mean ± SEM of triplicate wells is shown. ****, p<0.0001 by ANOVA. One experiment of 2.

SUPPLEMENTARY FIGURE 2
Gating strategy to identify activated BMDCs. Differentiated BMDCs were stained with antibodies specific for CD11c, MHC Class II, CD40, CD80 and CD86. Live, single cells were gated as $CD11c^{+}MHC\text{-}II^{high}$ cells. This double positive population from WT and TLR4 KO cells was evaluated for expression of CD40, CD80 and CD86 as shown.

SUPPLEMENTARY FIGURE 3
Upregulation of costimulatory molecule expression is unchanged in TLR2 KO BMDCs. **(A).** Representative overlays of CD40, CD80 and CD86 expression on WT and TLR2 KO BMDCs stimulated with 5 μg/mL BcfA. Median fluorescence intensity (MFI) expression of **(B)**. CD40, **(C)**. CD80 and **(D)**. CD86 and percentage of cells expressing **(E)**. CD40, **(F)**. CD80 and **(G)**. CD86 on WT and TLR2 KO BMDCs stimulated with 1 μg/mL and 5 μg/mL BcfA for 20-24 hr. Heat-killed *B. pertussis* (HKBp) were used as positive controls. Mean ± SEM of triplicate wells is shown. *, p<0.05, ** by ANOVA. One experiment of 2.

SUPPLEMENTARY FIGURE 4
Gating strategy to identify lung $CD11b^{+}CD11c^{+}$ cells. Single cell suspensions from lungs were stained with antibodies specific for CD11b, CD11c, MHC Class II, CD40, CD80 and CD86. Live, single cells were gated as $CD11b^{+}CD11c^{+}$. This double positive population from WT and TLR4 KO lungs was evaluated for expression of MHC Class II, CD40, CD80 and CD86 as shown.

References

1. Coffman RL, Sher A, Seder RA. Vaccine adjuvants: putting innate immunity to work. *Immunity*. (2010) 33:492–503. doi: 10.1016/j.immuni.2010.10.002

2. Facciola A, Visalli G, Lagana A, Di Pietro A. An overview of vaccine adjuvants: current evidence and future perspectives. *Vaccines (Basel)*. (2022) 10:819. doi: 10.3390/vaccines10050819

3. Pulendran B, S Arunachalam P, O'Hagan DT. Emerging concepts in the science of vaccine adjuvants. *Nat Rev Drug Discovery*. (2021) 20:454–75. doi: 10.1038/s41573-021-00163-y

4. Ghimire TR. The mechanisms of action of vaccines containing aluminum adjuvants: an in *vitro* vs in *vivo* paradigm. *Springerplus*. (2015) 4:181. doi: 10.1186/s40064-015-0972-0

5. Ott G, Barchfeld GL, Chernoff D, Radhakrishnan R, van Hoogevest P, Van Nest G. MF59. Design and evaluation of a safe and potent adjuvant for human vaccines. *Pharm Biotechnol*. (1995) 6:277–96.

6. De Donato S, Granoff D, Minutello M, Lecchi G, Faccini M, Agnello M, et al. Safety and immunogenicity of MF59-adjuvanted influenza vaccine in the elderly. *Vaccine*. (1999) 17:3094–101. doi: 10.1016/S0264-410X(99)00138-3

7. Chlibek R, Bayas JM, Collins H, de la Pinta ML, Ledent E, Mols JF, et al. Safety and immunogenicity of an AS01-adjuvanted varicella-zoster virus subunit candidate vaccine against herpes zoster in adults >=50 years of age. *J Infect Dis*. (2013) 208:1953–61. doi: 10.1093/infdis/jit365

8. Laurens MB. RTS,S/AS01 vaccine (Mosquirix): an overview. *Hum Vaccin Immunother*. (2020) 16:480–9. doi: 10.1080/21645515.2019.1669415

9. Canelle Q, Dewe W, Innis BL, van der Most R. Evaluation of potential immunogenicity differences between Pandemrix and Arepanrix. *Hum Vaccin Immunother*. (2016) 12:2289–98. doi: 10.1080/21645515.2016.1168954

10. Ebensen T, Delandre S, Prochnow B, Guzman CA, Schulze K. The combination vaccine adjuvant system alum/c-di-AMP results in quantitative and qualitative enhanced immune responses post immunization. *Front Cell Infect Microbiol*. (2019) 9:31. doi: 10.3389/fcimb.2019.00031

11. Krieg AM. An innate immune defense mechanism based on the recognition of CpG motifs in microbial DNA. *J Lab Clin Med*. (1996) 128:128–33. doi: 10.1016/S0022-2143(96)90004-9

12. Chatzikleanthous D, O'Hagan DT, Adamo R. Lipid-based nanoparticles for delivery of vaccine adjuvants and antigens: Toward multicomponent vaccines. *Mol Pharm*. (2021) 18:2867–88. doi: 10.1021/acs.molpharmaceut.1c00447

13. Wagner H. Bacterial CpG DNA activates immune cells to signal infectious danger. *Adv Immunol*. (1999) 73:329–68. doi: 10.1016/S0065-2776(08)60790-7

14. Del Giudice G, Rappuoli R, Didierlaurent AM. Correlates of adjuvanticity: A review on adjuvants in licensed vaccines. *Semin Immunol*. (2018) 39:14–21. doi: 10.1016/j.smim.2018.05.001

15. Bermejo-Martin JF, Ortiz de Lejarazu R, Pumarola T, Rello J, Almansa R, Ramirez P, et al. Th1 and Th17 hypercytokinemia as early host response signature in severe pandemic influenza. *Crit Care*. (2009) 13:R201. doi: 10.1186/cc8208

16. Khader SA, Gaffen SL, Kolls JK. Th17 cells at the crossroads of innate and adaptive immunity against infectious diseases at the mucosa. *Mucosal Immunol*. (2009) 2:403–11. doi: 10.1038/mi.2009.100

17. Lin L, Ibrahim AS, Xu X, Farber JM, Avanesian V, Baquir B, et al. Th1-Th17 cells mediate protective adaptive immunity against Staphylococcus aureus and Candida albicans infection in mice. *PLoS Pathog*. (2009) 5:e1000703. doi: 10.1371/journal.ppat.1000703

18. Lyadova IV, Panteleev AV. Th1 and th17 cells in tuberculosis: Protection, Pathology, and Biomarkers. *Mediators Inflammation*. (2015) 2015:854507. doi: 10.1155/2015/854507

19. Ross PJ, Sutton CE, Higgins S, Allen AC, Walsh K, Misiak A, et al. Relative contribution of Th1 and Th17 cells in adaptive immunity to Bordetella pertussis: towards the rational design of an improved acellular pertussis vaccine. *PLoS Pathog*. (2013) 9:e1003264. doi: 10.1371/journal.ppat.1003264

20. Shamseldin MM, Kenney A, Zani A, Evans JP, Zeng C, Read KA, et al. Prime-Pull immunization of mice with a bcfA-adjuvanted vaccine elicits sustained mucosal immunity that prevents SARS-CoV-2 infection and pathology. *J Immunol*. (2023) 210:1–15. doi: 10.4049/jimmunol.2200297

21. Lee CM, Oh JE. Resident memory B cells in barrier tissues. *Front Immunol*. (2022) 13:953088. doi: 10.3389/fimmu.2022.953088

22. Mettelman RC, Allen EK, Thomas PG. Mucosal immune responses to infection and vaccination in the respiratory tract. *Immunity*. (2022) 55:749–80. doi: 10.1016/j.immuni.2022.04.013

23. Poon MML, Rybkina K, Kato Y, Kubota M, Matsumoto R, Bloom NI, et al. SARS-CoV-2 infection generates tissue-localized immunological memory in humans. *Sci Immunol*. (2021) 6:eabl9105. doi: 10.1126/sciimmunol.abl9105

24. Zazara DE, Belios I, Lucke J, Zhang T, Giannou AD. Tissue-resident immunity in the lung: a first-line defense at the environmental interface. *Semin Immunopathol*. (2022) 44:827–54. doi: 10.1007/s00281-022-00964-2

25. Jennings-Gee J, Quataert S, Ganguly T, D'Agostino R Jr., Deora R, Dubey P. The adjuvant bordetella colonization factor A attenuates alum-induced th2 responses and enhances bordetella pertussis clearance from mouse lungs. *Infect Immun*. (2018) 86. doi: 10.1128/IAI.00935-17

26. Yount KS, Hall JM, Caution K, Shamseldin MM, Guo M, Marion K, et al. Systemic priming and intranasal booster with a BcfA-adjuvanted acellular pertussis vaccine generates CD4+ IL-17+ nasal tissue resident T cells and reduces B. pertussis nasal colonization. *Front Immunol*. (2023) 14:1181876. doi: 10.3389/fimmu.2023.1181876

27. Sukumar N, Love CF, Conover MS, Kock ND, Dubey P, Deora R. Active and passive immunizations with Bordetella colonization factor A protect mice against respiratory challenge with Bordetella bronchiseptica. *Infect Immun*. (2009) 77:885–95. doi: 10.1128/IAI.01076-08

28. Inaba K, Inaba M, Romani N, Aya H, Deguchi M, Ikehara S, et al. Generation of large numbers of dendritic cells from mouse bone marrow cultures supplemented with granulocyte/macrophage colony-stimulating factor. *J Exp Med*. (1992) 176:1693–702. doi: 10.1084/jem.176.6.1693

29. Wang W, Li J, Wu K, Azhati B, Rexiati M. Culture and identification of mouse bone marrow-derived dendritic cells and their capability to induce T lymphocyte proliferation. *Med Sci Monit*. (2016) 22:244–50. doi: 10.12659/MSM.896951

30. Han JE, Wui SR, Kim KS, Cho YJ, Cho WJ, Lee NG. Characterization of the structure and immunostimulatory activity of a vaccine adjuvant, de-O-acylated lipooligosaccharide. *PLoS One*. (2014) 9:e85838. doi: 10.1371/journal.pone.0085838

31. Suzuki Y, Suda T, Furuhashi K, Shibata K, Hashimoto D, Enomto N, et al. Mouse CD11bhigh lung dendritic cells have more potent capability to induce IgA than CD103+ lung dendritic cells in *vitro*. *Am J Respir Cell Mol Biol*. (2012) 46:773–80. doi: 10.1165/rcmb.2011-0329OC

32. Crotty S. T follicular helper cell differentiation, function, and roles in disease. *Immunity*. (2014) 41:529–42. doi: 10.1016/j.immuni.2014.10.004

33. Zhu J, Paul WE. CD4 T cells: fates, functions, and faults. *Blood*. (2008) 112:1557–69. doi: 10.1182/blood-2008-05-078154

34. Zhu J, Yamane H, Paul WE. Differentiation of effector CD4 T cell populations (*). *Annu Rev Immunol*. (2010) 28:445–89. doi: 10.1146/annurev-immunol-030409-101212

35. Moser M, Murphy KM. Dendritic cell regulation of TH1-TH2 development. *Nat Immunol*. (2000) 1:199–205. doi: 10.1038/79734

36. Gane JM, Stockley RA, Sapey E. TNF-alpha autocrine feedback loops in human monocytes: The pro- and anti-inflammatory roles of the TNF-alpha receptors support the concept of selective TNFR1 blockade *in vivo*. *J Immunol Res*. (2016) 2016:1079851. doi: 10.1155/2016/1079851

37. Kumar S, Sunagar R, Gosselin E. Bacterial protein toll-like-receptor agonists: A novel perspective on vaccine adjuvants. *Front Immunol*. (2019) 10:1144. doi: 10.3389/fimmu.2019.01144

38. Su Y, Li D, Xing Y, Wang H, Wang J, Yuan J, et al. Subcutaneous immunization with fusion protein DnaJ-DeltaA146Ply without additional adjuvants induces both humoral and cellular immunity against pneumococcal infection partially depending on TLR4. *Front Immunol*. (2017) 8:686. doi: 10.3389/fimmu.2017.00686

39. Wu Y, Cui J, Zhang X, Gao S, Ma F, Yao H, et al. Pneumococcal DnaJ modulates dendritic cell-mediated Th1 and Th17 immune responses through Toll-like receptor 4 signaling pathway. *Immunobiology*. (2017) 222:384–93. doi: 10.1016/j.imbio.2016.08.013

40. Choi HG, Kim WS, Back YW, Kim H, Kwon KW, Kim JS, et al. Mycobacterium tuberculosis RpfE promotes simultaneous Th1- and Th17-type T-cell immunity via TLR4-dependent maturation of dendritic cells. *Eur J Immunol*. (2015) 45:1957–71. doi: 10.1002/eji.201445329

41. Lee SJ, Shin SJ, Lee MH, Lee MG, Kang TH, Park WS, et al. A potential protein adjuvant derived from Mycobacterium tuberculosis Rv0652 enhances dendritic cells-based tumor immunotherapy. *PLoS One*. (2014) 9:e104351. doi: 10.1371/journal.pone.0104351

42. Fan J, Jin S, Gilmartin L, Toth I, Hussein WM, Stephenson RJ. Advances in infectious disease vaccine adjuvants. *Vaccines (Basel)*. (2022) 10. doi: 10.3390/vaccines10071120

43. Kabelitz D. Expression and function of Toll-like receptors in T lymphocytes. *Curr Opin Immunol*. (2007) 19:39–45. doi: 10.1016/j.coi.2006.11.007

44. Cheon IS, Son YM, Sun J. Tissue-resident memory T cells and lung immunopathology. *Immunol Rev*. (2023). doi: 10.1111/imr.13201

45. Wilk MM, Mills KHG. CD4 T(RM) cells following infection and immunization: implications for more effective vaccine design. *Front Immunol*. (2018) 9:1860. doi: 10.3389/fimmu.2018.01860

46. Chasaide CN, Mills KHG. Next-generation pertussis vaccines based on the induction of protective T cells in the respiratory tract. *Vaccines (Basel)*. (2020) 316 (1):63–83. doi: 10.3390/vaccines8040621

47. Warfel JM, Zimmerman LI, Merkel TJ. Comparison of three whole-cell pertussis vaccines in the baboon model of pertussis. *Clin Vaccine Immunol*. (2016) 23:47–54. doi: 10.1128/CVI.00449-15

48. Warfel JM, Zimmerman LI, Merkel TJ. Acellular pertussis vaccines protect against disease but fail to prevent infection and transmission in a nonhuman primate model. *Proc Natl Acad Sci U.S.A*. (2014) 111:787–92. doi: 10.1073/pnas.1314688110

49. Veldhoen M, Hocking RJ, Atkins CJ, Locksley RM, Stockinger B. TGFbeta in the context of an inflammatory cytokine milieu supports *de novo* differentiation of IL-17-producing T cells. *Immunity*. (2006) 24:179–89. doi: 10.1016/j.immuni.2006.01.001

frontiers | Frontiers in Immunology

TYPE Review
PUBLISHED 01 October 2024
DOI 10.3389/fimmu.2024.1436557

OPEN ACCESS

EDITED BY
Ousman Jobe,
Henry M Jackson Foundation for the Advancement of Military Medicine (HJF), United States

REVIEWED BY
Elizabeth Clarke,
Los Alamos National Laboratory (DOE), United States
Diego Luis Costa,
University of São Paulo, Brazil

*CORRESPONDENCE
Ruth E. Thom
reholloway@dstl.gov.uk

RECEIVED 22 May 2024
ACCEPTED 06 September 2024
PUBLISHED 01 October 2024

CITATION
Thom RE and D'Elia RV (2024) Future applications of host direct therapies for infectious disease treatment.
Front. Immunol. 15:1436557.
doi: 10.3389/fimmu.2024.1436557

Future applications of host direct therapies for infectious disease treatment

Ruth E. Thom[1]* and R V. D'Elia[2]

[1]Chemical, Biological and Radiological Division, Defence Science and Technology Laboratory, Porton Down, Salisbury, United Kingdom, [2]Strathclyde Institute of Pharmacy & Biomedical Sciences, University of Strathclyde, Glasgow, United Kingdom

New and emerging pathogens, such as SARS-CoV2 have highlighted the requirement for threat agnostic therapies. Some antibiotics or antivirals can demonstrate broad-spectrum activity against pathogens in the same family or genus but efficacy can quickly reduce due to their specific mechanism of action and for the ability of the disease causing agent to evolve. This has led to the generation of antimicrobial resistant strains, making infectious diseases more difficult to treat. Alternative approaches therefore need to be considered, which include exploring the utility of Host-Directed Therapies (HDTs). This is a growing area with huge potential but difficulties arise due to the complexity of disease profiles. For example, a HDT given early during infection may not be appropriate or as effective when the disease has become chronic or when a patient is in intensive care. With the growing understanding of immune function, a new generation of HDT for the treatment of disease could allow targeting specific pathways to augment or diminish the host response, dependent upon disease profile, and allow for bespoke therapeutic management plans. This review highlights promising and approved HDTs that can manipulate the immune system throughout the spectrum of disease, in particular to viral and bacterial pathogens, and demonstrates how the advantages of HDT will soon outweigh the potential side effects.

KEYWORDS

host-directed, therapeutic, STING, pyroptosis, itaconate, infection

1 Introduction to host-directed therapies

Since the beginning of the 20th century and the advent of antibiotics the premise to treat infectious disease is the use of antimicrobial agents that directly target the pathogen. To our detriment, now in the 21st century we are still heavily reliant on this approach and we are continually facing new strains of bacteria and viruses that are resistant to our available armament. Furthermore, lessons learnt from the coronavirus disease 2019 (COVID-19) global pandemic mean we need to become better equipped for the emergence of new infectious disease.

Research and development into alternative solutions for the treatment of infectious disease has accelerated and one such approach is to identify drugs that modulate the host pathways in a growing area of research known as Host-Directed Therapies (HDTs). HDTs are showing success in the field of cancer with a number of licenced products (1, 2). For infectious disease, momentum is building to develop HDTs and it is becoming a promising area of drug discovery. HDTs are much less prone to the generation of drug-resistant pathogen strains because the therapeutic strategy is to target evolutionary conserved host factors. The pathogen would require considerable evolutionary changes to overcome these targeted host pathways (3). HDT could also offer a broad-spectrum of therapy and would be beneficial where rapid treatment is required such as during epidemics and pandemics as well for the preparedness of new pathogens.

The advantages of HDT do need to be caveated for the potential of toxicity. Indeed targeting host-specific pathways could have devastating effects on the host as seen in the first phase 1 clinical trial of an agonistic anti-CD28 monoclonal antibody, which led to an incapacitating cytokine storm in the volunteers (4). Furthermore, the therapeutic window for HDT is critical in the treatment strategy. For example, it was reported that the early treatment of COVID-19 patients with exogenous IFNα was beneficial (5, 6), but was detrimental when administered later in disease (7, 8). To overcome this careful monitoring of the host and understanding of the time course of infection is critical. This can be achieved with the use of diagnostic biomarkers which can differentiate between bacterial and viral infection (9) as well as pre-symptomatic diagnosis of cytokine storms including biomarkers of sepsis (10).

HDT encompass a continually growing arsenal of agents, which includes repurposed drugs, small molecules, synthetic nucleic acids, biologics, cytokines, cellular therapy, recombinant proteins and micronutrients (11). Here we describe a range of HDT strategies, which is not exhaustive, but provides a representation of the research and development in this field focussing on infectious disease caused by bacterial and viral pathogens. The application of HDT for fungal and parasitic infections are reviewed in detail elsewhere (12–15). An area that will not be discussed will be therapeutic and prophylactic vaccination and the overview will focus on alternative methods to modify the host response. We have compartmentalised the course of disease into specific phases to describe the potential beneficial uses for HDT: (i) Early phase, referring to pathogen entry and establishment of infection. (ii) Middle phase, including disease progression leading to either convalescence or acute infection. (iii) Late phase, which describes persistency and latency. However, some therapies or targets may have applicability across more than one phase of infectious disease. For instance, it may also be advantageous to boost the immune response when the disease has reached latency and not just early in infection; such examples will be discussed. Further, we conclude that with increased depth of knowledge of immune function across the time course of infection, the same HDT pathway could be manipulated to either agonise or antagonise host defence responses supporting a protective outcome over the spectrum of disease.

2 Early intervention using HDT to treat infectious disease

The earliest point to target the host upon pathogen infection is to block or inhibit cellular entry thus rendering the host cell non-permissive (Figure 1A). With advancements in the understanding of host-pathogen interactions, novel HDT strategies targeting pathogen entry are currently being pursued. The most progress has been achieved with the treatment of Human immunodeficiency virus (HIV)-1 by targeting CC-chemokine receptor 5 (CCR5). CCR5 is a cofactor for the entry of the virus and antagonists of CCR5 inhibit its function and can block viral entry (16). Maraviroc was the first CCR5 antagonist to be licenced in 2007 and has now become part of the therapeutic schedule for HIV positive patients (17). Additionally entry inhibitors for hepatitis B and D viruses are also now licenced, such as myrcludex B (18); illustrating the promise that entry inhibitors are successful HDT targets (19, 20). The identification of other early entry molecules for harmful viruses such Ebola virus (21) and Lassa virus (22) is a starting point for potential HDTs. In the case for Ebola, a number of small molecules have been identified that can affect various stages of Ebola virus uptake from cell attachment, internalisation by macropinocytosis and fusion of the viral envelope (23). Madrid et al. (24) demonstrated that the chloroquine (an approved antimalarial treatment) can inhibit the trafficking of the Ebola virus through the endosomal pathway and prevents viral fusion thus aborting infection. Using a murine model of Ebola infection, treatment with chloroquine led to 80-90% survival (24). Inhibiting pathogen entry pathway could be beneficial as a pre-exposure therapy for instance during an epidemic or pandemic. They could also be utilized to negate subsequent rounds of pathogen entry and replication thus alleviating the infectious cycle.

Another attractive approach for HDT development is to target cellular pathways that the pathogen is dependent upon for replication and infection but are dispensable to the host (Figure 1B). Targeting host pathogen-dependent pathways, instead of individual factors, is a more promising HDT approach for bacterial infections owning to its higher autonomy compared to viruses. The majority of research has focused on kinases and lipid biosynthesis. There are over 500 kinases identified by the Human Genome Project, which are involved in a range of physiological processes and cellular homeostasis (25). Kinases are also associated with all stages of viral replication, however, a number of cellular kinases have been identified to be non-essential for the host but are required for viral infection (26). Such kinases represent potentially valuable drug targets. Kinase inhibitors are small chemical molecules and the screening of kinase inhibitor libraries has identified some promising HDT candidates that are required for pathogen replication but are non-essential to the host. Inhibitors to two receptor tyrosine kinases have been discovered that block the replication of a range of DNA (herpes simplex virus) and RNA (influenza A virus, Sendai virus, mouse hepatitis virus and rhesus rotavirus) viruses (27). A whole range of kinase inhibitors have been licenced for the treatment of cancer therapy (28) and these compounds are now been examined for use as HDT. For

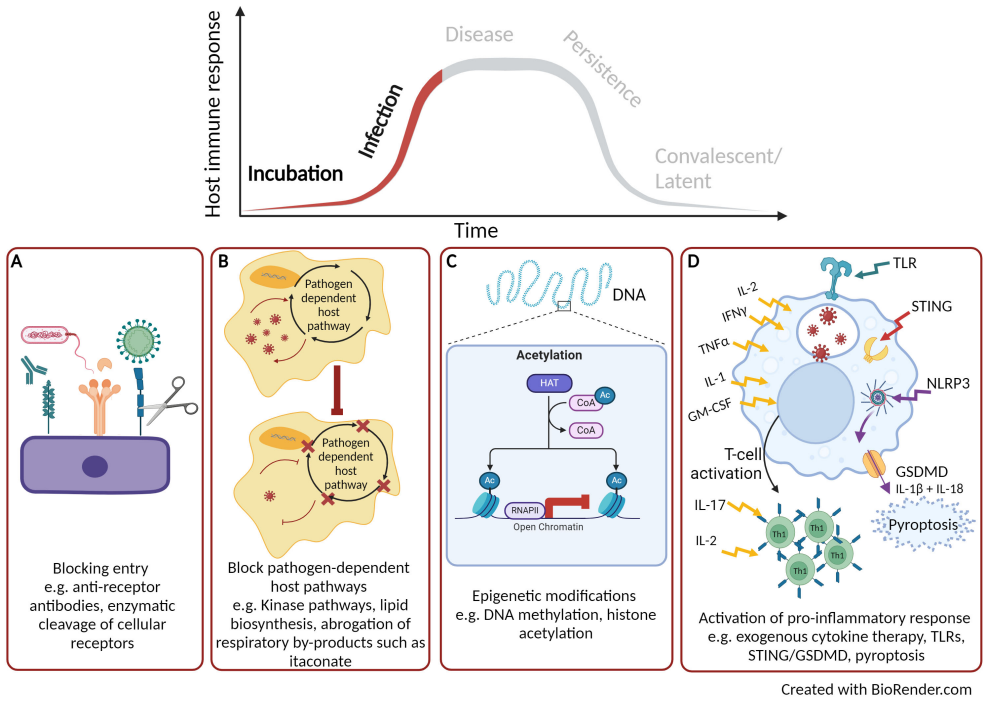

FIGURE 1
Early targets for host directed therapies. **(A)** Blocking pathogen entry. **(B)** Blocking pathogen-dependent host pathways. **(C)** Host or pathogen epigenetic modification. **(D)** Activation of pro-inflammatory cytokine response. Created with BioRender.com.

example, dasatinib, a potent inhibitor of the SCR kinases, is used in the treatment of chronic myeloid leukaemia. However, repurposing of dasatinib has also shown beneficial effects in preventing dengue virus replication by inhibition of viral RNA replication and particle secretion (29). During the COVID-19 pandemic, a number of licenced kinase inhibitors were identified for both inhibition of viral life cycle [e.g. tyrosine kinase inhibitor, imatinib (30)] as well as those that could reduce host immuno-pathology [e.g. Janus kinase inhibitor, baricitinib (31)]; further demonstrating the potential broad-range activity of kinase inhibitors as HDTs (32). Fatty acids are required for pathogens to replicate and they can gain these host factors by reprogramming cellular metabolism, including lipid synthesis (33). Blocking lipid synthesis with chemical inhibitors has been shown to decrease the production of flaviviruses (34). Chu et al. (35) screened 22 fatty acid inhibitors to identify compounds that could inhibit replication of SARS-CoV2 and demonstrated that half of the compounds could significantly reduce replication *in vitro*. The most prominent was orlistat, which is a licenced anti-obesity drug that reduces the absorption of dietary fat through the inhibition of lipases. Chu et al. (35), demonstrated in a SARS-CoV2 murine model that following treatment with orlistat there was reduced viral loads within the lungs, reduced lung pathology and increased survival (35). *Mycobacterium tuberculosis* resides in macrophages and requires fatty acids derived from lipid bodies as an essential source of energy. The lipid sensing nuclear receptor, peroxisome proliferator-activated gamma (PPARγ), can be activated by mycobacteria to form lipid bodies (36). Pre-treatment of macrophages with a PPARγ antagonist followed by mycobacterial infection leads to a decrease in lipid body formation as well effective mycobactericidal activity (37).

Bacterial pathogens have also been reported to utilise by-products of the host cellular respiration cycle to support growth. For instance, itaconate, a small metabolic molecule that is a by-product of the tricarboxylic acid (TCA) cycle, is known to have direct links to immune function (38) and has a range of anti-inflammatory and anti-oxidant functions (39, 40). Despite the antimicrobial properties of itaconate, intracellular bacteria have developed strategies to benefit from endogenous itaconate (41). For example, *Klebsiella pneumoniae*, can induce metabolic oxidative stress responses through lipopolysaccharide binding to toll-like receptor (TLR) 4 leading to the accumulation of itaconate. This bacterial defence mechanism has been shown to promote an anti-inflammatory response and induce a disease-tolerant immune response (42). Furthermore, some bacterial pathogens such as *Psuedomonas aeruginosa* and *Staphylococcus aureus* utilise itaconate as a carbon source to establish a persistent infection and support the development of biofilms (43, 44). The production of itaconate can be controlled by the immune response gene 1 (IRG1) and the utilization of itaconate by pathogens to tolerate the host response and to support growth is achieved through the activation of the IRG1 pathway (39). Further research is required to unravel the host-pathogen link with IRG1-itaconate, but there is potential for HDT to target this pathway and abrogate the utilization of itaconate by pathogens (Figure 1B).

As well as targeting pathogen-dependent host factors, directing HDTs towards DNA-modifying enzymes is an alternative approach

under development (Figure 1C). Phenotypic modification of genomic DNA caused by DNA methylation and histone acetylation leads to altered structures and stability of the DNA which can regulate gene expression and cell division (45). These DNA-modifying enzymes have been used in the successful treatment of cancers (46). For example, vorinostat was the first approved histone deacetylase inhibitor to be used as a therapy to treat cutaneous T-cell lymphoma (47). Human macrophages infected with *Salmonella enterica* alongside treatment with an inhibitor of histone deacetylase have shown to promote intracellular bacterial clearance through the induction of mitochondrial reactive oxygen species (ROS) (48). Additional studies have demonstrated the inhibition of histone deacetylase can subvert the cytotoxic effects of bacterial toxins, such as those produced by *Bacillus anthracis*. Macrophages treated with a histone deacetylase inhibitor following exposure to *B. anthracis* lethal toxin showed a marked increase in pro-inflammatory cytokines signalling pathways such as IL-1β as well as pyroptosis, a pro-inflammatory programmed cell death pathway (49). Conversely, pathogens can also target these host enzymes to modify the host genome and become permissive to infection. For example *B. anthracis* and *M. tuberculosis* have both been reported to modulate histone phosphorylation of down-stream inflammatory pathways resulting in alterations in macrophage and epithelial cell activation (50, 51); thus efforts to develop inhibitors to these pathogen DNA modification pathways are also on going (52, 53).

The HDT approaches described above have focussed on enhancing underlying antimicrobial cellular pathways that aim to control and clear infection. An alternative strategy is to target the early host immune response (Figure 1D). Since the second half of the 20th Century, there have been numerous examples of the use of exogenous cytokine therapy for the treatment of viral infections such as influenza (54), hepatitis C (55) and HIV-1 (56) right up until the present day with the treatment of COVID-19 (57). A number of successful recombinant interferons have been licenced, such as IFN-alpha2b (licenced as Intron A) for the treatment of hepatitis B and C, as well as human papillomavirus (58) and early infection to SARS-CoV2 (57). The use of exogenous cytokines have been well documented for the treatment of tuberculosis, for example cytokines TNFα, IFNγ and IL-1α are known to stimulate antimicrobial properties of mycobacterial infected macrophages (59). The delivery of IFNγ via the aerosol route, in combination with standard therapy, demonstrated promising results for patients with multi-drug resistant pulmonary *M. tuberculosis* infection. The study reported that the combinational therapy led to enhanced mycobacterial killing, reduced lung lesions and improved clinical outcome (60). Exogenous cytokine therapy can have diverse effects on the host immune response including the activation and recruitment of immune cells as well as down-stream signalling to amplify the antimicrobial immune response. However, there can be severe side effects to cytokine-based therapy and timing is critical to when they should be administered. Cytokine therapy remains a key research interest in cancer therapy, with an IFNα (Peginterferon-α 2b) and IL-2 (Aldesleukin) therapies approved for specific cancers (61). Recent advancements in cytokine-based therapeutics, such as improving half-life, targeted delivery and reduced toxicity, still make them an appealing HDT. New technology and improved understanding of pharmacodynamics/pharmacokinetics has led to bio-engineered cytokines that can be directed to the site of immunopathology in a timely manner (62). Furthermore, advances in the individual treatment of patients can lead to bespoke individual management plans (63). Alternatively, endogenous cytokines can be induced by the activation of TLRs (64), for example, imiquimod is a TLR7 agonist that is used to treat human papillomavirus. When it is applied topically to warts, imiquimod activates IFNα, IL-1, IL-6, and TNFα leading to the reduction of viral load (65).

Early innate immune responses rely on the detection of conserved structural features of the pathogen, known as pathogen-associated molecular patterns (PAMPs) by binding to host pattern-recognition receptors (PRRs), present on the cell surface or within the cells. Over the last decade DNA and RNA sensing PPRs have been described which are typically activated through viral infection leading to a potent antiviral host immune response. Such PPRs include; TLRs, RIG-1 like receptors (RLRs), NOD-like receptors (NLRs) and cyclic GMP-AMP synthase (cGAS) protein families, all of which have been extensively reviewed (66, 67). More recently it has been identified that these nucleic acid sensing pathways could be a potential target for HDTs (68). Indeed, cGAS which senses both self and foreign double-stranded DNA activates the cGAS-stimulator of interferon genes (STING) signalling pathway resulting in the expression of type 1 IFNs (69, 70). The cGAS-STING signalling pathway is critical in the activation of the innate immune response, but in addition, an increasing number of immune roles have been described (71). Conversely, RNA viruses (including Dengue virus, Influenza A Virus, Zika virus and SARS-CoV2) have been reported to antagonise cGAS-STING and block DNA-dependent IFN-1 activation (72). Thus, during infection with RNA viruses, the release of host genomic or mitochondrial DNA within the cytoplasm would not be detected and cGAS-STING-induced anti-viral immune responses will be inhibited. STING agonists have been identified that induce cGAS-STING signalling prior to and during early infection of RNA viruses (Figure 1D). Humpries et al. (73) administered the STING agonist, diABZI-4 intranasally to a SARS-CoV2 murine model and demonstrated transient activation of STING. They reported a pro-inflammatory response, with cytokine production, lymphocyte activation and inhibition of viral replication (73).

Exploitation of pyroptosis, a rapid and lytic pro-inflammatory programmed cell death pathway, has been shown to be another effective early HDT for infectious disease (Figure 1D). Upon activation of either PAMPs (e.g. bacterial derived molecules and viral nucleic acid) or damage-associated molecular pattern (DAMPs, host molecular makers of disease e.g. ATP, IL-1α, DNA) leads to a cascade of events resulting in the assembly of cytosolic pro-inflammatory complexes such as the NOD-, LRR- and pyrin domain-containing protein 3 (NLRP3) inflammasome (74). NLRP3 activates the inflammatory cytokines IL-1β and IL-18 as well as the pore-forming protein, gasdermin D (GSDMD). Initially, the GSDMD pore allows the release of these cytokines from macrophages and dendritic cells but ultimately leads to pyroptosis

through osmotic cell lysis and disruption of the plasma membrane (75). GSDMD has an essential role in innate immunity; inducing a pro-inflammatory response, promoting effective pathogen clearance and preventing replication (76). Indeed, the induction of pyroptosis by GSDMD has been shown to protect a melioidosis murine model following infection with the intracellular bacteria, *Burkholderia thaliandensis* (77). Furthermore, antibody-opsonised SARS-CoV2 infection of human blood monocytes and macrophages activates the NLRP3 inflammasome, inducing pyroptosis, as demonstrated by increased levels of GSDMD and IL-18. Pyroptosis occurs rapidly preventing the replication and assembly of infectious viral progeny thus rendering myeloid cells a dead end for infection (78). In some cases, a pathogen can hijack the process of pyroptosis, such as the case for intracellular *M. tuberculosis* infection, where the cellular membrane is disrupted and impairs GSDMD-mediated pyroptosis (79). Exploiting this rapid innate immune-regulated form of cell death through activation of NLRP3 signalling via DAMPs or PAMPs could be an effective early HDT to protect from infectious disease. Pre-clinical cancer therapies targeting pyroptosis is currently leading the way in this approach with several different therapy strategies (80). Alternative licenced drugs such as metformin (for diabetic treatment) and ivermectin (an anti-parasitic agent) have been demonstrated to induce pyroptosis and exert anti-tumour activity *in vitro* and *in vivo* (81, 82). These studies are examples of how licenced drugs have the potential to be repurposed for other diseases.

3 The use of HDT to induce immune homeostasis and minimise immunopathology during disease progression

As disease-causing pathogens establish infection and evade the early innate host immune response, the adaptive immune response begins to develop, initiating an antigen-specific cellular and/or humoral infiltration. During disease progression, the innate and adaptive immune responses are not mutually exclusive but are complementary in the resolution of disease. Strategies to enhance the adaptive immune response can prevent the establishment of latent or persistent infection and support the immune cells in eliminating infectious pathogens. Such strategies include vaccination, cytokine therapy, adoptive cell transfer and immune checkpoint blockade (the later discussed below) (83). If these two arms of the immune response are not aligned then the host response can become dysregulated resulting in tissue damage caused by immunopathology, acute disease status and morbidity. In this section, we discuss HDTs that can rebalance the host immune response thus reducing disease severity and eliminate infectious pathogens.

It is well reported that during some acute and severe infections, a cytokine storm can be activated which correlates with increased disease severity and mortality (84). Over 150 cytokines have been reported to be involved in a cytokine storm but primarily the key cytokines are TNFα, IL-6 and IFN's (85). In some cases, treatment with a monoclonal antibody directed towards one of these cytokines can have beneficial therapeutic effect (Figure 2A). During the COVID-19 pandemic monoclonal antibodies targeting IL-6, IL-1β, IL-23 and GM-CSF, or their receptors, went through clinical trials and demonstrated varying levels of therapeutic efficacy by reducing morbidity and mortality (86). A number of clinical trials have demonstrated the use of tocilizumab, an anti-IL-6 compound, as a COVID-19 therapeutic (87). The largest of these clinical trials, (RECOVERY), reported the most compelling evidence of the benefit to treat patients with acute infection with tocilizumab, leading to improved clinical outcome and an increase likelihood to be discharged from hospital within 28 days (88). To block the down-stream signalling pathways that activate pro-inflammatory cytokines and cytokine storms maybe a more effective HDT approach (Figure 2B). The transcription factor nuclear factor-kappa beta (NF-κβ) is critical in the regulation and downstream signalling pathways of cytokines involved in both the innate and adaptive immune response. Targeting this transcription factor has been shown to have therapeutic advantages in a mouse model of influenza strain H5N1 leading to a drastic reduction in NF-κβ regulated cytokines (89). The inhibition of NF-κβ signalling has also been an effective target to reduce the inflammatory response during critical stages of SARS-CoV-2 infection (90). As part of the COVID-19 RECOVERY trial, the therapeutic benefits of the anti-inflammatory corticosteroid dexamethasone were assessed using either a high or a low dose to treat patients on respiratory support (91). Dexamethasone is used for a broad range of inflammatory conditions and is known to supress NF-κβ (92). The COVID-19 patients on respiratory support that received the lower dose of dexamethasone demonstrated significant protection with 20-30% reduced mortality (91). However, the study was stopped due to an increase in mortality seen in patients receiving the high-dose therapy. It was hypothesised that due to an excessive dampening of the of the immune response, there was an increase opportunity for secondary infections (91). Inflammatory responses have also been demonstrated to be dampened by treatment of the DNAzyme Dz13 which is known to cleave the transcription factor c-Jun (93). c-Jun is activated during the early stages of influenza A and is involved in viral replication as well as induction of the inflammatory response. Administration of Dz13 *in vivo* following influenza A infection resulted in significantly improved survival, as well as decreased viral titres and reduced production of pro-inflammatory cytokines in lung tissues (94). In the field of cancer therapy, a number of approved proteasome inhibitors (such as bortezomib, carfilzomib and ixazomib) are known to be strong suppressors of down-stream signalling pathways, such as NF-κβ (95). It is plausible that such therapies could be used in down-regulating acute cytokine storms induced by bacterial or viral infections. An alternative to blocking pro-inflammatory cytokine responses is to activate the Th2 immune response through exogenous Th2 cytokine therapy (Figure 2C), leading to immune homeostasis, protective immunity and tissue repair (96, 97). IL-10 therapy has had success for the treatment of inflammatory conditions, such as rheumatoid arthritis, psoriasis and inflammatory bowl disease (98). The most advanced IL-10 therapy has been the treatment of cancer patients with a PEGylated recombinant human IL-10 (PEG-rHuIL-10), which

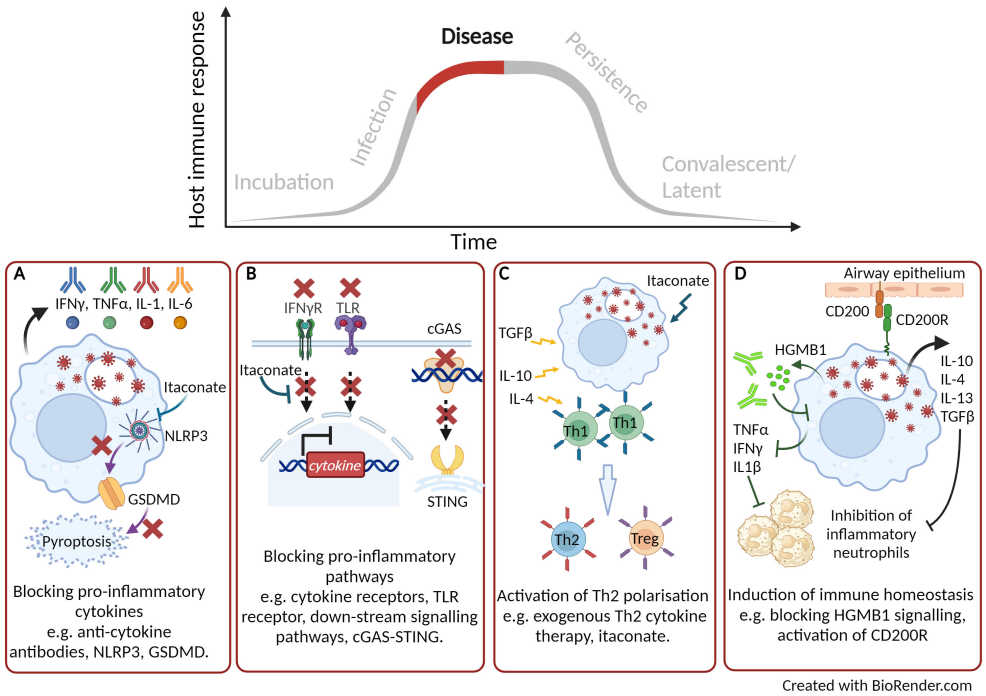

FIGURE 2
Targeting host directed therapies to treat and reduce disease progression. **(A)** Blocking pro-inflammatory cytokines. **(B)** Blocking down-stream signalling pathways. **(C)** Activation of Th2 immune response. **(D)** Induction of immune homeostasis. Created with BioRender.com.

has been shown to suppress tumour-associated immunity, improve clinical outcome (99). Indeed IL-10 or agonists of the down-stream signalling pathways have been proposed as a therapeutic for acute lung infection with *Streptococcus pneumonia* (100), chronic mycobacterial infection (101) as well for COVID-19 therapy (102).

As described earlier, nucleic acid sensing pathways are critical in the activation of anti-viral innate immune response. However, these pathways can become dysregulated and depending on the intensity of the signal, a protective pathway could lead to a pathological outcome. Using a murine SARS-CoV2 infection model, Domizio et al. (70) demonstrated that the RNA virus promoted mitochondrial damage leading to mitochondrial DNA leakage. The presence of mitochondrial DNA within the cytosol of infected cells activated the cGAS-STING signalling pathway leading to inflammation and extensive lung pathology (70). They further demonstrated that treatment with the STING inhibitor, H151, in their murine model showed a decrease in lung inflammation at late time points and a reduction of viral loads. A number of high-throughput screening studies have identified antagonists of the cGAS-STING pathway which have been demonstrated to either inhibit cGAS (103) or STING though competitively binding at the substrate binding sites (104) or induce conformation change (105) (Figure 2B).

Pyroptosis, although a critical early innate host response that can prevent infection and replication of both bacteria and virus, can become a double-edged sword. Recent studies have revealed examples where chronic activation can have a detrimental role resulting in immunopathogenesis. In a murine model of severe influenza A infection, mice typically succumb to fatal pulmonary disease due to a hyper-inflammatory response and tissue damage (106). Using a *gsdmd* $^{-/-}$ modified mouse model of severe influenza A infection, Rosli et al. (106), demonstrated a significantly improved outcome with increased survival, reduced viral burden and reduced tissue pathology compared to infection in wild type mice (106). Additionally, pyroptosis was shown to be a major cause of inflammatory sequelae in patients with critical COVID-19 symptoms, resulting in severe lung damage and multi-organ failure (78). HDTs are emerging which can target the NLRP3 inflammasome pathway (107). Pre-clinical studies using compounds that can inhibit either GSDMD and NLRP3 have been successful in the treatment of a range of immunopathological disease models, (108). The most widely researched NLRP3 inhibitor is a small molecule, MCC950, known to bind and lock the inflammasome in an inactive conformation (109). Using a murine infection model of influenza A, Tate et al. (110) demonstrated the timely importance of administering the NLRP3 inhibitor. When MCC950 was administered early after influenza A challenge, mice succumbed to fatal infection. However, when the inhibitor was used to treat mice later in infection, there was reduced inflammation within the lungs and prolonged survival (110). Targeting the pyroptotic cell death pathway such that GSDMD pores are reduced or inhibited, could be a potential new HDT to protect against disease caused by infectious pathogens (Figure 2A).

It is now becoming clear that cellular metabolic process, essential for biological function, can directly effect the outcome to infectious disease and inflammation (38). As described earlier the TCA by-product, itaconate, is known to have immuno-modulatory properties. In recent studies, itaconate has been shown to reduce inflammation by modification of pro-inflammatory inflammasomes, such as the

NLRP3 inflammasome. Itaconate can modify the NLRP3 complex and ameliorate NLRP3 induced cascade of pro-inflammatory cytokines IL-1β and IL-18 (111) (Figure 2A). Itaconate has also been described to modulate immune responses though the activation or suppression of a range of transcriptions factors to limit pro-inflammatory cytokines (Figure 2B), induce antioxidant responses and regulate macrophage polarization (Figure 2C). For instance, the induction of the activating transcription factor (AFT3) through itaconate is reported to inhibit the production of pro-inflammatory cytokines (112). Furthermore, the nuclear factor erythroid 2-related factor 2 (NRF2) induces antioxidant and anti-inflammatory responses. The use of the itaconate derivative, 4-octyl itaconate, was shown to induce NRF2 and promoted a successful wound healing phenotype leading to a topical treatment for chronic wounds (113). Itaconate role in the regulation of macrophage polarization was also demonstrated through the suppression of Janus kinase 1 (JAK1) signalling (112, 114). Owning to the broad range of immunological function of itaconate, using a chemically synthesised derivative of the metabolite has demonstrated huge potential as a HDT therapy across both viral (Herpes Simplex Virus-1 and-2, Vaccinia virus, Zika virus and SARS-CoV2 (115)) and bacterial (*M. tuberculosis* (116), *Francisella tularensis* (117), *Brucella abortus* (118) and *Coxellia burnettii* (119) infections. Furthermore, there have been no known reports of pathogen utilization of these synthetic itaconate compounds unlike their endogenous counterparts (41).

In our laboratory, we are interested in immunomodulatory drugs that target the host and we have reported promising immunomodulatory data when reducing high mobility group B protein 1 (HMGB1). HMGB1 is a DAMP molecule and induces signalling of a pro-inflammatory cytokine response. It is released from damaged or infected cells and has been correlated to poor prognosis in human melioidosis patients (120). Using our *Burkholderia pseudomallei* mouse model, we have demonstrated that blocking HMGB1 signalling with a monoclonal antibody led to reduced bacterial burden in organ tissues which correlated to a reduction in pro-inflammatory cytokines (121). Similar findings were also reported in our *F. tularensis* mouse model (122) highlighting the potential of broad-range spectrum use of these immunomodulatory compounds.

Our more recent research investigating the immunomodulator CD200-Fc has also demonstrated effective treatment in mouse models of *F. tularensis* LVS (123) as well as in our murine aerosol models of CDC category A threat agents, such as *B. pseudomallei* (124). We hypothesised that CD200-Fc binds to its receptor and activates immune homeostasis through Th1 and Th2 cytokine profiles as well as inducing antimicrobial activity through the induction of ROS (Figure 2D). This work is further supported by data published demonstrating the importance of CD200 receptor in the lung macrophage following severe influenza infection by reducing lung inflammation and inducing immune homeostasis (125).

As discussed earlier, an overactive immune response can contribute to disease lethality. Even if the host is able to survive, it is likely that damage to cells and tissues has occurred leading to short or long-term immunopathology. Aiding the body to recover from tissue damage can significantly reduce morbidity and decrease the risk of secondary infections. Resolvins are a class of lipid metabolites that have been extensively studied which promote the resolution of chronic infection and used to treat a range of chronic inflammatory diseases, as previously reviewed (126, 127). The use of resolvins alongside the other HDT strategies discussed above could have a double benefit by reduce disease progression as well as protecting the host from immunopathology.

4 The use of HDT to treat persistent infection

Persistent infections are described as those in which the pathogen is not cleared during the primary infection and can remain viable within the host. There are three overlapping types of persistence, defined as chronic, slow and latent infection. Here we described the potential use of HDTs to target the various stages of persistency. *M. tuberculosis*, is well adapted to persist infection and resides in phagosomes of the infected macrophage. Here the pathogen inhibits phagosomal fusion and slowly replicates, evading the host response, leading to chronic infection and tissue pathology if left untreated (128, 129). HDTs have been identified to activate autophagy and is an area of interest for the treatment of intracellular bacterial pathogens including mycobacteria (Figure 3A) (130). A number of small compounds can be used to induce autophagy, for example activation of ROS, blocking ion channels and maturation of the phagosome. Autophagy allows the release of infectious particles, which can then be taken up by activated phagocytic cells (131). Rapamycin is a broad range anti-inflammatory drug originally approved for the use of organ transplant rejection (132). Rapamycin has been extensively studied as an inducer of autophagy (133) and *in vivo M. tuberculosis* infection models have demonstrated reduced mycobacterial lung immunopathology, the formation of necrotic lesions within the lung (134) and clearance of mycobacteria, including multi-drug resistant strains (135). Similar autophagy inducing drugs, such as ridaforolimus (approved for use in the treatment of solid tumours and haematological malignancies (136)) and temsirolimus [approved for use in renal cell carcinoma therapy (137)] have demonstrated potential therapeutic benefits for the treatment of tuberculosis (138). Furthermore, the repurposing of metformin has also been shown to support macrophage control through the induction of ROS and has been shown to improve the resolution of lung cavities in patients with tuberculosis (139). Itaconate, as described earlier is a broad-ranging anti-inflammatory host molecule that has also been shown to regulate autophagy through activation of the transcription factor EB (TFEB). Antimicrobial activity of the induced endogenous metabolite has been reported to limit infection of intracellular bacteria *Salmonella typhimurium* infection *in vitro* and *in vivo* (140, 141).

Immune checkpoints are signalling pathways that regulate the host immune response. They are critical for self-tolerance but are also activated during chronic inflammatory responses, such as sepsis and during persistent infection. Once activated, the

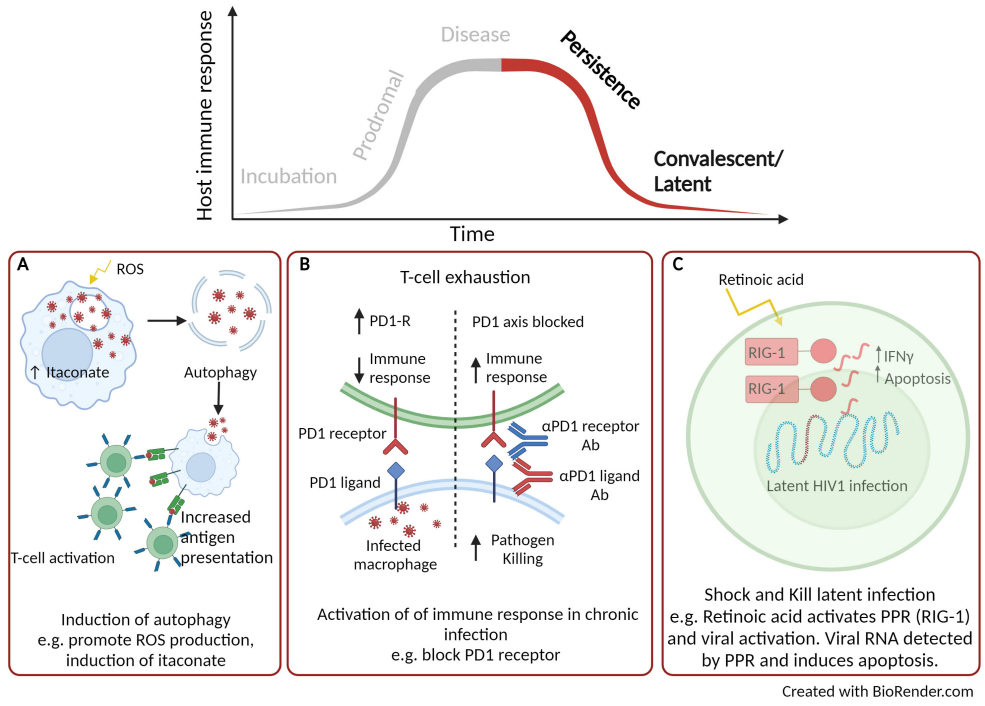

FIGURE 3
Using host directed therapy to treat persistence and latent infection. **(A)** Activation of autophagy. **(B)** Inhibition of immune checkpoints. **(C)** Shock and kill therapy. Created with BioRender.com.

immune response is dampened which can alleviate immune-directed tissue damage but can also reduce the effectiveness of clearing the infection (142). There are a variety of interactions between antigen presenting cells and T-cells that can promote T-cell exhaustion leading to inhibitory effects of the immune response and these are illustrated in a previous review (142). Once such interaction is that of the co-inhibitory receptor, programmed death-1 (PD1) expressed on T-cells and its corresponding ligand (PDL-1) found on dendritic cells. A number of approved inhibitors targeting these checkpoint proteins are in use for cancer immunotherapy such as PD-1 inhibitors (Nivolumab, Pembrolizumab and Cemiplimab), PDL-1 inhibitors (Atezolizumab, Durvalumab and Avelumab) (143) and are now being considered for the treatment of viral infections (Figure 3B). In simian immunodeficiency viruses (SIV)-infected macaques, treatment with a humanised anti-PD1 antibody led to improved functionality of $CD8^+$ T cells, reduced amounts of SIV RNA and increased survival of the macaques (144). Further beneficial efficacy has been described using anti-PD1 or anti-PDL-1 for the treatment of hepatitis B and C in pre-clinical infection models (145, 146). When blocking the PD1/PD1-L interaction, IFNγ production was no longer suppressed, anti-viral T-cell phenotypes were restored and there was significant clearance of viral persistence (145, 146). While blocking immune checkpoints for viral infection has shown beneficial therapeutic effects, these effects can be detrimental in chronic bacterial disease, such as tuberculosis. Using PD1 deficient murine model infected with *M. tuberculosis* led to significantly reduced survival (147, 148), uncontrolled bacterial proliferation with areas necrotic foci (149), compared to infection of wild-type mice. Further, there was increased number of neutrophils and high levels of TNFα and IL-6 which corresponded to a discordant inflammatory response (149). These studies highlight that such HDT is not necessarily appropriate for intracellular bacterial infection and that consideration and understanding of immunopathology is a critical consideration.

Latent infection is another area of research where HDT could be utilised to treat disease, in particular this has been described for HIV-1. The approach used is termed "Shock and Kill", where latency reversal agents actively induce replication of latent HIV-1 and thus making the infectious viral particles more susceptible to clearance through the host immune response (Figure 3C) (150). Retinoids (a derivative of Vitamin A) have been long approved for the treatment of a number of cancers as well as various skin conditions (151) and are now been considered for latent HIV-1 therapy. Retinoids have been shown to re-activate virus replication by activating the PRR, RIG-1 (152), which detects viral RNA (153). Once viral RNA is detected by PRRs, $CD8^+$ cytotoxic T-cells are induced which have enhanced anti-viral properties and can eliminate infected cells (154). Although there is concern that the "Shock and Kill" approach may increase permissiveness of HIV-1 infection, used in combination with standard HIV-1 therapy may make this a beneficial therapeutic approach (155). The unique use

of retinoids as latency reversal agents which can activate viral replication alongside anti-viral activity could also have the potential to treat a range of quiescence viral infections.

5 Summary of the use of HDT for infectious disease and future direction

HDTs represent a novel solution for the treatment of infectious disease. Their immunomodulatory action make them ideal for combatting the spread of antimicrobial resistance as well as emerging new pathogens. Cancer HDTs are leading the way; where in 2021 there were 14 immunomodulators, 20 cellular and gene therapies and 98 antibody therapies currently approved by the United States Food and Drug Administration (156). These compounds have huge potential to be repurposed for the treatment of infectious disease. Currently much of the focus has been on discovering HDTs for tuberculosis, hepatitis B and C and HIV-1 but due to their pleiotropic functions, HDTs have huge promise for the treatment of a broad range of infectious disease. Throughout the review, examples of clinically approved licenced drugs for the treatment of immune related diseases have been described and these have been summarised in Figure 4. The summary is not exhaustive but lists a number or approved therapies that could be repurposed. The repurposing of such drugs have huge potential as they already have well established safety and pharmokinetic profiles as well as known manufacturing and distribution networks. The use of such therapies mean they could become quickly available for alternative indications. Although HDTs have many advantages over pathogen-directed anti-microbial treatment, (for example, reduced likelihood of the development of resistant microbial strains and potential broad-spectrum use), it is more likely that these therapies would be used as part of a layered defence strategy in combination with other anti-microbial therapies.

In this review, we described potential targets for HDT over the trajectory of infection, from entry of pathogen, through disease and followed by persistence and latency. Over the time course of disease there are a range of immune related pathways that could be targeted, and typically a HDT is targeted to a specific phase of infection. The downstream effect of the therapy is dependent on whether a pathway is being blocked or activated. An agonist or an antagonist to particular receptors can completely alter the response and therefore outcome of disease. To avoid inadvertently manipulating an immune response pathway that would be detrimental to the host, it is highly likely that immune-profiling diagnostics would be required to help identify and characterise the patient's stage of disease. Indeed, these time dependent HDT approaches are limited as they do not allow flexibility to manage disease through the course of an infection.

In more recent years, the understanding of immune function pathways are now becoming well characterised and offer some of the most exciting opportunities for HDT development. Alongside the use of companion diagnostics, emerging therapies have been identified that could either augment or dampen a specific pathway depending on the stage of infection and inflammatory response. For

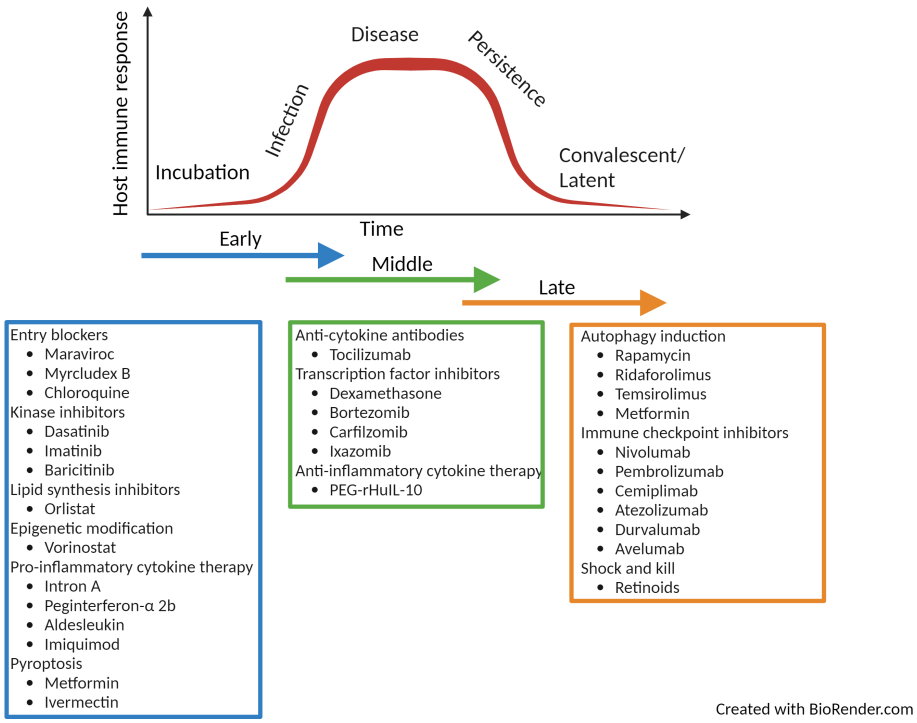

FIGURE 4
Summary of licenced drugs approved for clinical use in the treatment of immune-related diseases. The summary of drugs listed is not comprehensive but highlights a range of therapies that could be repurposed as HDT for infectious disease over the time-course of infection. Created with BioRender.com.

instance, activation of down-stream PAMP signalling such as that described for cGAS-STING could support an early innate host response (Figure 1D), but later in the disease profile, antagonists of this pathway may reduce immune-pathological tissue damage (Figure 2B). Similarly, HDTs that can induce inflammasomes, pro-inflammatory cytokine release and rapid programmed cell death (e.g. pyroptosis) are beneficial in the early stages of infection (Figure 1D), but as disease progresses it would be more beneficial to inhibit such pathways (Figure 2A). Furthermore, the increased understanding of the intricate link between cellular metabolism and immune function reveals potential pathways that could be targeted by HDT. For example, inhibition of the TCA metabolite, itaconate, prevents both the utilization as a carbon source to support bacterial growth as well as the induction of an early anti-inflammatory immune response (Figure 1B). However, the immune-modulatory properties of itaconate can be of benefit later in disease where enhancing this pathway would support the host response (Figures 2A–C, 3A). Research of such immune functions in healthy and disease state are still in their infancy and it is critical to understand the pharmacokinetics of such compounds that can enhance or reduce such pathways. The ability to refine and modify an immune-regulated pathway to manage infection across the disease profile would be incredibly beneficial.

Looking forward, in a generation of systems biology and the huge advances in "omics" technology (for example, transcriptomics, epigenetics, metabolomics and proteomics), high-throughput immune profiling has the potential to identify an individual's susceptibility to infection (157) and long term-prognosis (158). The use of patient specific "omic" data alongside microbial whole-genome sequencing and machine learning would be indispensable for the future of evidence-based management of infectious disease and precision medicine. The bespoke application of HDT to modulate a patient's immune response in combination with antimicrobial drug therapy is the future to treating infectious disease and the management of drug-resistant pathogens.

Author contributions

RT: Writing – original draft. RD'E: Writing – review & editing.

Funding

The author(s) declare financial support was received for the research, authorship, and/or publication of this article. The research and writing of this manuscript was funded by the Ministry of Defence, UK.

Acknowledgments

We acknowledge Chris Jenkins and BioRender.com for the icons, templates and original artwork that were used to complete the graphics for this review.

Conflict of interest

The authors declare that the research was conducted in the absence of any commercial or financial relationships that could be construed as a potential conflict of interest.

Publisher's note

References

1. Pennock GK, Chow LQ. The evolving role of immune checkpoint inhibitors in cancer treatment. *Oncologist*. (2015) 20:812–22. doi: 10.1634/theoncologist.2014-0422

2. Wolchok JD, Hodi FS, Weber JS, Allison JP, Urba WJ, Robert C, et al. Development of ipilimumab: A novel immunotherapeutic approach for the treatment of advanced melanoma. *Ann N Y Acad Sci*. (2013) 1291:1–13. doi: 10.1111/nyas.12180

3. Chiang CY, Uzoma I, Moore RT, Gilbert M, Duplantier AJ, Panchal RG. Mitigating the impact of antibacterial drug resistance through host-directed therapies: current progress, outlook, and challenges. *mBio*. (2018) 9(1):e01932–17. doi: 10.1128/mBio.01932-17

4. Suntharalingam G, Perry MR, Ward S, Brett SJ, Castello-Cortes A, Brunner MD, et al. Cytokine storm in A phase 1 trial of the anti-cd28 monoclonal antibody tgn1412. *N Engl J Med*. (2006) 355:1018–28. doi: 10.1056/NEJMoa063842

5. Zhou Q, Chen V, Shannon CP, Wei XS, Xiang X, Wang X, et al. Interferon-alpha2b treatment for covid-19. *Front Immunol*. (2020) 11. doi: 10.3389/fimmu.2020.01061

6. Meng Z, Wang T, Chen L, Chen X, Li L, Qin X, et al. The effect of recombinant human interferon alpha nasal drops to prevent covid-19 pneumonia for medical staff in an epidemic area. *Curr Top Med Chem*. (2021) 21:920–7. doi: 10.2174/1568026621666210429083050

7. Zhou Z, Ren L, Zhang L, Zhong J, Xiao Y, Jia Z, et al. Heightened innate immune responses in the respiratory tract of covid-19 patients. *Cell Host Microbe*. (2020) 27:883–890.E2. doi: 10.1016/j.chom.2020.04.017

8. Laing AG, Lorenc A, Del Molino Del Barrio I, Das A, Fish M, Monin L, et al. A dynamic covid-19 immune signature includes associations with poor prognosis. *Nat Med*. (2020) 26:1623–35. doi: 10.1038/s41591-020-1038-6

9. Halabi S, Shiber S, Paz M, Gottlieb TM, Barash E, Navon R, et al. Host test based on tumor necrosis factor-related apoptosis-inducing ligand, interferon gamma-induced protein-10 and C-reactive protein for differentiating bacterial and viral respiratory tract infections in adults: diagnostic accuracy study. *Clin Microbiol Infect*. (2023) 29:1159–65. doi: 10.1016/j.cmi.2023.05.033

10. Lukaszewski RA, Jones HE, Gersuk VH, Russell P, Simpson A, Brealey D, et al. Presymptomatic diagnosis of postoperative infection and sepsis using gene expression signatures. *Intensive Care Med*. (2022) 48:1133–43. doi: 10.1007/s00134-022-06769-z

11. Zumla A, Rao M, Wallis RS, Kaufmann SH, Rustomjee R, Mwaba P, et al. Host-directed therapies for infectious diseases: current status, recent progress, and future prospects. *Lancet Infect Dis*. (2016) 16:E47–63. doi: 10.1016/S1473-3099(16)00078-5

12. Armstrong-James D, Brown GD, Netea MG, Zelante T, Gresnigt MS, Van De Veerdonk FL, et al. Immunotherapeutic approaches to treatment of fungal diseases. *Lancet Infect Dis*. (2017) 17:E393–402. doi: 10.1016/S1473-3099(17)30442-5

13. Goncalves SM, Ferreira AV, Cunha C, Carvalho A. Targeting immunometabolism in host-directed therapies to fungal disease. *Clin Exp Immunol*. (2022) 208:158–66. doi: 10.1093/cei/uxab014

14. Varikuti S, Jha BK, Volpedo G, Ryan NM, Halsey G, Hamza OM, et al. Host-directed drug therapies for neglected tropical diseases caused by protozoan parasites. *Front Microbiol*. (2018) 9. doi: 10.3389/fmicb.2018.02655

15. Adderley J, Grau GE. Host-directed therapies for malaria: possible applications and lessons from other indications. *Curr Opin Microbiol*. (2023) 71:102228. doi: 10.1016/j.mib.2022.102228

16. Latinovic OS, Reitz M, Heredia A. Ccr5 inhibitors and hiv-1 infection. *J AIDS HIV Treat*. (2019) 1:1–5. doi: 10.33696/AIDS.1.001

17. Woollard SM, Kanmogne GD. Maraviroc: A review of its use in hiv infection and beyond. *Drug Des Devel Ther*. (2015) 9:5447–68. doi: 10.2147/DDDT.S90580

18. Cheng D, Han B, Zhang W, Wu W. Clinical effects of ntcp-inhibitor myrcludex B. *J Viral Hepat*. (2021) 28:852–8. doi: 10.1111/jvh.13490

19. Bogomolov P, Alexandrov A, Voronkova N, Macievich M, Kokina K, Petrachenkova M, et al. Treatment of chronic hepatitis D with the entry inhibitor myrcludex B: first results of A phase ib/iia study. *J Hepatol*. (2016) 65:490–8. doi: 10.1016/j.jhep.2016.04.016

20. Lempp FA, Urban S. Inhibitors of hepatitis B virus attachment and entry. *Intervirology*. (2014) 57:151–7. doi: 10.1159/000360948

21. Wang H, Shi Y, Song J, Qi J, Lu G, Yan J, et al. Ebola viral glycoprotein bound to its endosomal receptor niemann-pick C1. *Cell*. (2016) 164:258–68. doi: 10.1016/j.cell.2015.12.044

22. Hulseberg CE, Fénéant L, Szymanska KM, White JM. Lamp1 increases the efficiency of lassa virus infection by promoting fusion in less acidic endosomal compartments. *mBio*. (2018) 9(1):e01818–17. doi: 10.1128/mBio.01818-17

23. Salata C, Calistri A, Alvisi G, Celestino M, Parolin C, Palù G. Ebola virus entry: from molecular characterization to drug discovery. *Viruses*. (2019) 11(3):274. doi: 10.3390/v11030274

24. Madrid PB, Chopra S, Manger ID, Gilfillan L, Keepers TR, Shurtleff AC, et al. A systematic screen of fda-approved drugs for inhibitors of biological threat agents. *PloS One*. (2013) 8:E60579. doi: 10.1371/journal.pone.0060579

25. Milanesi L, Petrillo M, Sepe L, Boccia A, D'agostino N, Passamano M, et al. Systematic analysis of human kinase genes: A large number of genes and alternative splicing events result in functional and structural diversity. *BMC Bioinf*. (2005) 6 Suppl 4:S20. doi: 10.1186/1471-2105-6-S4-S20

26. Meineke R, Rimmelzwaan GF, Elbahesh H. Influenza virus infections and cellular kinases. *Viruses*. (2019) 11(2):171. doi: 10.3390/v11020171

27. Kumar N, Sharma NR, Ly H, Parslow TG, Liang Y. Receptor tyrosine kinase inhibitors that block replication of influenza A and other viruses. *Antimicrob Agents Chemother*. (2011) 55:5553–9. doi: 10.1128/AAC.00725-11

28. Kannaiyan R, Mahadevan D. A comprehensive review of protein kinase inhibitors for cancer therapy. *Expert Rev Anticancer Ther*. (2018) 18:1249–70. doi: 10.1080/14737140.2018.1527688

29. De Wispelaere M, Lacroix AJ, Yang PL. The small molecules azd0530 and dasatinib inhibit dengue virus rna replication via fyn kinase. *J Virol*. (2013) 87:7367–81. doi: 10.1128/JVI.00632-13

30. Cagno V, Magliocco G, Tapparel C, Daali Y. The tyrosine kinase inhibitor nilotinib inhibits sars-cov-2 *in vitro*. *Basic Clin Pharmacol Toxicol*. (2021) 128:621–4. doi: 10.1111/bcpt.13537

31. Hoang TN, Pino M, Boddapati AK, Viox EG, Starke CE, Upadhyay AA, et al. Baricitinib treatment resolves lower-airway macrophage inflammation and neutrophil recruitment in sars-cov-2-infected rhesus macaques. *Cell*. (2021) 184 460-475:E21. doi: 10.1016/j.cell.2020.11.007

32. Naik RR, Shakya AK, Aladwan SM, El-Tanani M. Kinase inhibitors as potential therapeutic agents in the treatment of covid-19. *Front In Pharmacol*. (2022) 13. doi: 10.3389/fphar.2022.806568

33. Thaker SK, Ch'ng J, Christofk HR. Viral hijacking of cellular metabolism. *BMC Biol*. (2019) 17:59. doi: 10.1186/s12915-019-0678-9

34. Martin-Acebes MA, Vazquez-Calvo A, Saiz JC. Lipids and flaviviruses, present and future perspectives for the control of dengue, zika, and west nile viruses. *Prog Lipid Res*. (2016) 64:123–37. doi: 10.1016/j.plipres.2016.09.005

35. Chu J, Xing C, Du Y, Duan T, Liu S, Zhang P, et al. Pharmacological inhibition of fatty acid synthesis blocks sars-cov-2 replication. *Nat Metab*. (2021) 3:1466–75. doi: 10.1038/s42255-021-00479-4

36. Baindara P. Host-directed therapies to combat tuberculosis and associated non-communicable diseases. *Microb Pathog*. (2019) 130:156–68. doi: 10.1016/j.micpath.2019.03.003

37. Almeida PE, Silva AR, Maya-Monteiro CM, Torocsik D, D'avila H, Dezso B, et al. Mycobacterium bovis bacillus calmette-guerin infection induces tlr2-dependent peroxisome proliferator-activated receptor gamma expression and activation: functions in inflammation, lipid metabolism, and pathogenesis. *J Immunol*. (2009) 183:1337–45. doi: 10.4049/jimmunol.0900365

38. Chi H. Immunometabolism at the intersection of metabolic signaling, cell fate, and systems immunology. *Cell Mol Immunol*. (2022) 19:299–302. doi: 10.1038/s41423-022-00840-x

39. Michelucci A, Cordes T, Ghelfi J, Pailot A, Reiling N, Goldmann O, et al. Immune-responsive gene 1 protein links metabolism to immunity by catalyzing itaconic acid production. *Proc Natl Acad Sci U.S.A*. (2013) 110:7820–5. doi: 10.1073/pnas.1218599110

40. Lampropoulou V, Sergushichev A, Bambouskova M, Nair S, Vincent EE, Loginicheva E, et al. Itaconate links inhibition of succinate dehydrogenase with macrophage metabolic remodeling and regulation of inflammation. *Cell Metab*. (2016) 24:158–66. doi: 10.1016/j.cmet.2016.06.004

41. Yuk JM, Park EJ, Kim IS, Jo EK. Itaconate family-based host-directed therapeutics for infections. *Front Immunol*. (2023) 14:1203756. doi: 10.3389/fimmu.2023.1203756

42. Wong Fok Lung T, Charytonowicz D, Beaumont KG, Shah SS, Sridhar SH, Gorrie CL, et al. Klebsiella pneumoniae induces host metabolic stress that promotes tolerance to pulmonary infection. *Cell Metab*. (2022) 34:761–774.E9. doi: 10.1016/j.cmet.2022.03.009

43. Tomlinson KL, Lung TWF, Dach F, Annavajhala MK, Gabryszewski SJ, Groves RA, et al. Staphylococcus aureus induces an itaconate-dominated immunometabolic response that drives biofilm formation. *Nat Commun*. (2021) 12(1):1399. doi: 10.1038/s41467-021-21718-y

44. Riquelme SA, Liimatta K, Wong Fok Lung T, Fields B, Ahn D, Chen D, et al. Pseudomonas aeruginosa utilizes host-derived itaconate to redirect its metabolism to promote biofilm formation. *Cell Metab*. (2020) 31:1091–1106. E6. doi: 10.1016/j.cmet.2020.04.017

45. Bannister S, Messina NL, Novakovic B, Curtis N. The emerging role of epigenetics in the immune response to vaccination and infection: A systematic review. *Epigenetics*. (2020) 15:555–93. doi: 10.1080/15592294.2020.1712814

46. Kim HJ, Bae SC. Histone deacetylase inhibitors: molecular mechanisms of action and clinical trials as anti-cancer drugs. *Am J Transl Res*. (2011) 3:166–79.

47. Grant S, Easley C, Kirkpatrick P. Vorinostat. *Nat Rev Drug Discovery*. (2007) 6:21–2. doi: 10.1038/nrd2227

48. Ariffin JK, Das Gupta K, Kapetanovic R, Iyer A, Reid RC, Fairlie DP, et al. Histone deacetylase inhibitors promote mitochondrial reactive oxygen species production and bacterial clearance by human macrophages. *Antimicrob Agents Chemother*. (2015) 60:1521–9. doi: 10.1128/AAC.01876-15

49. Ha SD, Reid C, Meshkibaf S, Kim SO. Inhibition of interleukin 1beta (Il-1beta) expression by anthrax lethal toxin (Letx) is reversed by histone deacetylase 8 (Hdac8) inhibition in murine macrophages. *J Biol Chem*. (2016) 291:8745–55. doi: 10.1074/jbc.M115.695809

50. Pennini ME, Pai RK, Schultz DC, Boom WH, Harding CV. Mycobacterium tuberculosis 19-kda lipoprotein inhibits ifn-gamma-induced chromatin remodeling of mhc2ta by tlr2 and mapk signaling. *J Immunol*. (2006) 176:4323–30. doi: 10.4049/jimmunol.176.7.4323

51. Raymond B, Batsche E, Boutillon F, Wu YZ, Leduc D, Balloy V, et al. Anthrax lethal toxin impairs il-8 expression in epithelial cells through inhibition of histone H3 modification. *PloS Pathog*. (2009) 5:E1000359. doi: 10.1371/journal.ppat.1000359

52. Choi SJ, Shin YS, Kang BW, Kim JG, Won KJ, Lieberman PM, et al. Dna hypermethylation induced by epstein-barr virus in the development of epstein-barr virus-associated gastric carcinoma. *Arch Pharm Res*. (2017) 40:894–905. doi: 10.1007/s12272-017-0939-5

53. Courtney DG, Kennedy EM, Dumm RE, Bogerd HP, Tsai K, Heaton NS, et al. Epitranscriptomic enhancement of influenza A virus gene expression and replication. *Cell Host Microbe*. (2017) 22 377-386:E5. doi: 10.1016/j.chom.2017.08.004

54. Isaacs A, Burke DC. Viral interference and interferon. *Br Med Bull*. (1959) 15:185–8. doi: 10.1093/oxfordjournals.bmb.a069760

55. Reichard O, Norkrans G, Fryden A, Braconier JH, Sonnerborg A, Weiland O. Randomised, double-blind, placebo-controlled trial of interferon alpha-2b with and without ribavirin for chronic hepatitis C. The swedish study group. *Lancet*. (1998) 351:83–7. doi: 10.1016/S0140-6736(97)06088-1

56. Kovacs JA, Baseler M, Dewar RJ, Vogel S, Davey RTJr., Falloon J, et al. Increases in cd4 T lymphocytes with intermittent courses of interleukin-2 in patients with human immunodeficiency virus infection. A preliminary study. *N Engl J Med*. (1995) 332:567–75. doi: 10.1056/NEJM199503023320904

57. Wang N, Zhan Y, Zhu L, Hou Z, Liu F, Song P, et al. Retrospective multicenter cohort study shows early interferon therapy is associated with favorable clinical responses in covid-19 patients. *Cell Host Microbe*. (2020) 28:455–464.E2. doi: 10.1016/j.chom.2020.07.005

58. Kumar N, Sharma S, Kumar R, Tripathi BN, Barua S, Ly H, et al. Host-directed antiviral therapy. *Clin Microbiol Rev*. (2020) 33(3):e00168–19. doi: 10.1128/CMR.00168-19

59. Kaufmann SHE, Dorhoi A, Hotchkiss RS, Bartenschlager R. Host-directed therapies for bacterial and viral infections. *Nat Rev Drug Discov*. (2018) 17:35–56. doi: 10.1038/nrd.2017.162

60. Suarez-Mendez R, Garcia-Garcia I, Fernandez-Olivera N, Valdes-Quintana M, Milanes-Virelles MT, Carbonell D, et al. Adjuvant interferon gamma in patients with drug - resistant pulmonary tuberculosis: A pilot study. *BMC Infect Dis*. (2004) 4:44. doi: 10.1186/1471-2334-4-44

61. Conlon KC, Miljkovic MD, Waldmann TA. Cytokines in the treatment of cancer. *J Interferon Cytokine Res*. (2019) 39:6–21. doi: 10.1089/jir.2018.0019

62. Deckers J, Anbergen T, Hokke AM, De Dreu A, Schrijver DP, De Bruin K, et al. Engineering cytokine therapeutics. *Nat Rev Bioeng*. (2023) 1:286–303. doi: 10.1038/s44222-023-00030-y

63. Saxton RA, Glassman CR, Garcia KC. Emerging principles of cytokine pharmacology and therapeutics. *Nat Rev Drug Discovery*. (2023) 22:21–37. doi: 10.1038/s41573-022-00557-6

64. Hernandez A, Patil NK, Stothers CL, Luan L, Mcbride MA, Owen AM, et al. Immunobiology and application of toll-like receptor 4 agonists to augment host

resistance to infection. *Pharmacol Res*. (2019) 150:104502. doi: 10.1016/j.phrs.2019.104502

65. Bilu D, Sauder DN. Imiquimod: modes of action. *Br J Dermatol*. (2003) 149 Suppl 66:5–8. doi: 10.1046/j.0366-077x.2003.05628.x

66. Zahid A, Ismail H, Li B, Jin T. Molecular and structural basis of dna sensors in antiviral innate immunity. *Front Immunol*. (2020) 11:613039. doi: 10.3389/fimmu.2020.613039

67. Guy C, Bowie AG. Recent insights into innate immune nucleic acid sensing during viral infection. *Curr Opin Immunol*. (2022) 78:102250. doi: 10.1016/j.coi.2022.102250

68. Kong LZ, Kim SM, Wang C, Lee SY, Oh SC, Lee S, et al. Understanding nucleic acid sensing and its therapeutic applications. *Exp Mol Med*. (2023) 55:2320–31. doi: 10.1038/s12276-023-01118-6

69. Dobbs N, Burnaevskiy N, Chen D, Gonugunta VK, Alto NM, Yan N. Sting activation by translocation from the er is associated with infection and autoinflammatory disease. *Cell Host Microbe*. (2015) 18:157–68. doi: 10.1016/j.chom.2015.07.001

70. Domizio JD, Gulen MF, Saidoune F, Thacker VV, Yatim A, Sharma K, et al. The cgas-sting pathway drives type I ifn immunopathology in covid-19. *Nature*. (2022) 603:145–51. doi: 10.1038/s41586-022-04421-w

71. Ou L, Zhang A, Cheng Y, Chen Y. The cgas-sting pathway: A promising immunotherapy target. *Front Immunol*. (2021) 12:795048. doi: 10.3389/fimmu.2021.795048

72. Webb LG, Fernandez-Sesma A. Rna viruses and the cgas-sting pathway: reframing our understanding of innate immune sensing. *Curr Opin Virol*. (2022) 53:101206. doi: 10.1016/j.coviro.2022.101206

73. Humphries F, Shmuel-Galia L, Jiang Z, Wilson R, Landis P, Ng SL, et al. A diamidobenzimidazole STING agonist protects against SARS-CoV-2 infection. *Sci Immunol*. (2021) 6(59):eabi9002. doi: 10.1126/sciimmunol.abi9002

74. Zheng D, Liwinski T, Elinav E. Inflammasome activation and regulation: toward A better understanding of complex mechanisms. *Cell Discov*. (2020) 6:36. doi: 10.1038/s41421-020-0167-x

75. Zheng Z, Li G. Mechanisms and therapeutic regulation of pyroptosis in inflammatory diseases and cancer. *Int J Mol Sci*. (2020) 21(4):1456. doi: 10.3390/ijms21041456

76. Magnani L, Colantuoni M, Mortellaro A. Gasdermins: new therapeutic targets in host defense, inflammatory diseases, and cancer. *Front Immunol*. (2022) 13:898298. doi: 10.3389/fimmu.2022.898298

77. Wang J, Deobald K, Re F. Gasdermin D protects from melioidosis through pyroptosis and direct killing of bacteria. *J Immunol*. (2019) 202:3468–73. doi: 10.4049/jimmunol.1900045

78. Junqueira C, Crespo A, Ranjbar S, De Lacerda LB, Lewandrowski M, Ingber J, et al. Fcgammar-mediated sars-cov-2 infection of monocytes activates inflammation. *Nature*. (2022) 606:576–84. doi: 10.1038/s41586-022-04702-4

79. Chai Q, Yu S, Zhong Y, Lu Z, Qiu C, Yu Y, et al. A bacterial phospholipid phosphatase inhibits host pyroptosis by hijacking ubiquitin. *Science*. (2022) 378: Eabq0132. doi: 10.1126/science.abq0132

80. Jia Y, Wang X, Deng Y, Li S, Xu X, Qin Y, et al. Pyroptosis provides new strategies for the treatment of cancer. *J Cancer*. (2023) 14:140–51. doi: 10.7150/jca.77965

81. Draganov D, Gopalakrishna-Pillai S, Chen YR, Zuckerman N, Moeller S, Wang C, et al. Modulation of P2x4/P2x7/pannexin-1 sensitivity to extracellular atp via ivermectin induces A non-apoptotic and inflammatory form of cancer cell death. *Sci Rep*. (2015) 5:16222. doi: 10.1038/srep16222

82. Wang L, Li K, Lin X, Yao Z, Wang S, Xiong X, et al. Metformin induces human esophageal carcinoma cell pyroptosis by targeting the mir-497/pelp1 axis. *Cancer Lett*. (2019) 450:22–31. doi: 10.1016/j.canlet.2019.02.014

83. Kim TK, Vandsemb EN, Herbst RS, Chen L. Adaptive immune resistance at the tumour site: mechanisms and therapeutic opportunities. *Nat Rev Drug Discovery*. (2022) 21:529–40. doi: 10.1038/s41573-022-00493-5

84. D'elia RV, Harrison K, Oyston PC, Lukaszewski RA, Clark GC. Targeting the "Cytokine storm" For Therapeutic Benefit. *Clin Vaccine Immunol*. (2013) 20:319–27. doi: 10.1128/CVI.00636-12

85. Tisoncik JR, Korth MJ, Simmons CP, Farrar J, Martin TR, Katze MG. Into the eye of the cytokine storm. *Microbiol Mol Biol Rev*. (2012) 76:16–32. doi: 10.1128/MMBR.05015-11

86. Deb P, Molla MMA, Saif-Ur-Rahman KM. An update to monoclonal antibody as therapeutic option against covid-19. *Biosaf Health*. (2021) 3:87–91. doi: 10.1016/j.bsheal.2021.02.001

87. Gupta S, Leaf DE. Tocilizumab in covid-19: some clarity amid controversy. *Lancet*. (2021) 397:1599–601. doi: 10.1016/S0140-6736(21)00712-1

88. Group RC. Tocilizumab in patients admitted to hospital with covid-19 (Recovery): A randomised, controlled, open-label, platform trial. *Lancet*. (2021) 397:1637–45. doi: 10.1016/S0140-6736(21)00676-0

89. Droebner K, Reiling SJ, Planz O. Role of hypercytokinemia in nf-kappab P50-deficient mice after H5n1 influenza A virus infection. *J Virol*. (2008) 82:11461–6. doi: 10.1128/JVI.01071-08

90. Kircheis R, Haasbach E, Lueftenegger D, Heyken WT, Ocker M, Planz O. Nf-kappab pathway as A potential target for treatment of critical stage covid-19 patients. *Front Immunol*. (2020) 11:598444. doi: 10.3389/fimmu.2020.598444

91. Narasaraju T, Ravi Y, Jonsson CB, Chow VTK. High-dose corticosteroid therapy in covid-19: the recovery trial. *Lancet*. (2024) 403:1338–9. doi: 10.1016/S0140-6736(23)02884-2

92. Meduri GU, Muthiah MP, Carratu P, Eltorky M, Chrousos GP. Nuclear factor-kappab- and glucocorticoid receptor alpha- mediated mechanisms in the regulation of systemic and pulmonary inflammation during sepsis and acute respiratory distress syndrome. Evidence for inflammation-induced target tissue resistance to glucocorticoids. *Neuroimmunomodulation*. (2005) 12:321–38. doi: 10.1159/000091126

93. Xie J, Zhang S, Hu Y, Li D, Cui J, Xue J, et al. Regulatory roles of C-jun in H5n1 influenza virus replication and host inflammation. *Biochim Biophys Acta*. (2014) 1842:2479–88. doi: 10.1016/j.bbadis.2014.04.017

94. Zhang Z, Zhang S, Wang S. Dnazymes dz13 target the C-jun possess antiviral activity against influenza A viruses. *Microb Pathog*. (2017) 103:155–61. doi: 10.1016/j.micpath.2016.12.024

95. Richardson PG, Briemberg H, Jagannath S, Wen PY, Barlogie B, Berenson J, et al. Frequency, characteristics, and reversibility of peripheral neuropathy during treatment of advanced multiple myeloma with bortezomib. *J Clin Oncol*. (2006) 24:3113–20. doi: 10.1200/JCO.2005.04.7779

96. Walker JA, Mckenzie ANJ. T(H)2 cell development and function. *Nat Rev Immunol*. (2018) 18:121–33. doi: 10.1038/nri.2017.118

97. Al-Qahtani AA, Alhamlan FS, Al-Qahtani AA. Pro-inflammatory and anti-inflammatory interleukins in infectious diseases: A comprehensive review. *Trop Med Infect Dis*. (2024) 9(1):13. doi: 10.3390/tropicalmed9010013

98. Saraiva M, Vieira P, O'garra A. Biology and therapeutic potential of interleukin-10. *J Exp Med*. (2020) 217(1):e20190418. doi: 10.1084/jem.20190418

99. Autio K, Oft M. Pegylated interleukin-10: clinical development of an immunoregulatory cytokine for use in cancer therapeutics. *Curr Oncol Rep*. (2019) 21:19. doi: 10.1007/s11912-019-0760-z

100. Gonzalez LA, Melo-Gonzalez F, Sebastian VP, Vallejos OP, Noguera LP, Suazo ID, et al. Characterization of the anti-inflammatory capacity of il-10-producing neutrophils in response to streptococcus pneumoniae infection. *Front Immunol*. (2021) 12:638917. doi: 10.3389/fimmu.2021.638917

101. Redford PS, Murray PJ, O'garra A. The role of il-10 in immune regulation during M. Tuberculosis infection. *Mucosal Immunol*. (2011) 4:261–70. doi: 10.1038/mi.2011.7

102. Islam H, Chamberlain TC, Mui AL, Little JP. Elevated interleukin-10 levels in covid-19: potentiation of pro-inflammatory responses or impaired anti-inflammatory action? *Front Immunol*. (2021) 12:677008. doi: 10.3389/fimmu.2021.677008

103. Lama L, Adura C, Xie W, Tomita D, Kamei T, Kuryavyi V, et al. Development of human cgas-specific small-molecule inhibitors for repression of dsdna-triggered interferon expression. *Nat Commun*. (2019) 10(1):2261. doi: 10.1038/s41467-019-08620-4

104. Zhao W, Xiong M, Yuan X, Li M, Sun H, Xu Y. In silico screening-based discovery of novel inhibitors of human cyclic gmp-amp synthase: A cross-validation study of molecular docking and experimental testing. *J Chem Inf Model*. (2020) 60:3265–76. doi: 10.1021/acs.jcim.0c00171

105. Hong Z, Mei J, Li C, Bai G, Maimaiti M, Hu H, et al. STING inhibitors target the cyclic dinucleotide binding pocket. *Proc Natl Acad Sci USA*. (2021) 118(24): e2105465118. doi: 10.1073/pnas.2105465118

106. Rosli S, Harpur CM, Lam M, West AC, Hodges C, Mansell A, et al. Gasdermin D promotes hyperinflammation and immunopathology during severe influenza A virus infection. *Cell Death Dis*. (2023) 14:727. doi: 10.1038/s41419-023-06258-1

107. He W, Dong H, Wu C, Zhong Y, Li J. The role of nlrp3 inflammasome in sepsis: A potential therapeutic target. *Int Immunopharmacol*. (2023) 115:109697. doi: 10.1016/j.intimp.2023.109697

108. Coll RC, Schroder K, Pelegrin P. Nlrp3 and pyroptosis blockers for treating inflammatory diseases. *Trends Pharmacol Sci*. (2022) 43:653–68. doi: 10.1016/j.tips.2022.04.003

109. Dekker C, Mattes H, Wright M, Boettcher A, Hinniger A, Hughes N, et al. Crystal structure of nlrp3 nacht domain with an inhibitor defines mechanism of inflammasome inhibition. *J Mol Biol*. (2021) 433:167309. doi: 10.1016/j.jmb.2021.167309

110. Tate MD, Ong JDH, Dowling JK, Mcauley JL, Robertson AB, Latz E, et al. Reassessing the role of the nlrp3 inflammasome during pathogenic influenza A virus infection via temporal inhibition. *Sci Rep*. (2016) 6:27912. doi: 10.1038/srep27912

111. Hooftman A, Angiari S, Hester S, Corcoran SE, Runtsch MC, Ling C, et al. The immunomodulatory metabolite itaconate modifies nlrp3 and inhibits inflammasome activation. *Cell Metab*. (2020) 32:468–478.E7. doi: 10.1016/j.cmet.2020.07.016

112. Runtsch MC, Angiari S, Hooftman A, Wadhwa R, Zhang Y, Zheng Y, et al. Itaconate and itaconate derivatives target jak1 to suppress alternative activation of macrophages. *Cell Metab*. (2022) 34:487–501.E8. doi: 10.1016/j.cmet.2022.02.002

113. Maassen S, Coenen B, Ioannidis M, Harber K, Grijpstra P, Van Den Bossche J, et al. Itaconate promotes A wound resolving phenotype in pro-inflammatory macrophages. *Redox Biol*. (2023) 59:102591. doi: 10.1016/j.redox.2022.102591

114. Li Z, Zheng W, Kong W, Zeng T. Itaconate: A potent macrophage immunomodulator. *Inflammation*. (2023) 46:1177–91. doi: 10.1007/s10753-023-01819-0

115. Olagnier D, Farahani E, Thyrsted J, Blay-Cadanet J, Herengt A, Idorn M, et al. SARS-CoV2-mediated suppression of NRF2-signaling reveals potent antiviral and anti-inflammatory activity of 4-octyl-itaconate and dimethyl fumarate. *Nat Commun*. (2020) 11(1):4938. doi: 10.1038/s41467-020-18764-3. Erratum in: Nat Commun. 2020 Oct 21;11(1):5419. doi: 10.1038/s41467-020-19363-y

116. Nair S, Huynh JP, Lampropoulou V, Loginicheva E, Esaulova E, Gounder AP, et al. Irg1 expression in myeloid cells prevents immunopathology during M. Tuberculosis infection. *J Exp Med*. (2018) 215:1035–45. doi: 10.1084/jem.20180118

117. Roberts LM, Leighton I, Schwarz B, Wehrly TD, Evans TJ, Bosio CM. Itaconate indirectly influences expansion of effector T cells following vaccination with francisella tularensis live vaccine strain. *Cell Immunol*. (2022) 373:104485. doi: 10.1016/j.cellimm.2022.104485

118. Lacey CA, Ponzilacqua-Silva B, Chambers CA, Dadelahi AS, Skyberg JA. Myd88-dependent glucose restriction and itaconate production control brucella infection. *Infect Immun*. (2021) 89:E0015621. doi: 10.1128/IAI.00156-21

119. Kohl L, Siddique M, Bodendorfer B, Berger R, Preikschat A, Daniel C, et al. Macrophages inhibit coxiella burnetii by the acod1-itaconate pathway for containment of Q fever. *EMBO Mol Med*. (2023) 15:E15931. doi: 10.15252/emmm.202215931

120. Charoensup J, Sermswan RW, Paeyao A, Promakhejohn S, Punasee S, Chularari C, et al. High hmgb1 level is associated with poor outcome of septicemic melioidosis. *Int J Infect Dis*. (2014) 28:111–6. doi: 10.1016/j.ijid.2014.07.025

121. Laws TR, Clark GC, D'elia RV. Immune profiling of the progression of A balb/C mouse aerosol infection by burkholderia pseudomallei and the therapeutic implications of targeting hmgb1. *Int J Infect Dis*. (2015) 40:1–8. doi: 10.1016/j.ijid.2015.09.003

122. D'elia RV, Laws TR, Carter A, Lukaszewski R, Clark GC. Targeting the "Rising damp" During A francisella tularensis infection. *Antimicrob Agents Chemother*. (2013) 57:4222–8. doi: 10.1128/AAC.01885-12

123. Casulli J, Fife ME, Houston SA, Rossi S, Dow J, Williamson ED, et al. CD200R deletion promotes A neutrophil niche for francisella tularensis and increases infectious burden and mortality. *Nat Commun*. (2019) 10(1):2121. doi: 10.1038/s41467-019-10156-6

124. Thom RE, Williamson ED, Casulli J, Butcher WA, Burgess G, Laws TR, et al. Assessment of cd200r activation in combination with doxycycline in A model of melioidosis. *Microbiol Spectr*. (2023) 11:E0401622. doi: 10.1128/spectrum.04016-22

125. Snelgrove RJ, Goulding J, Didierlaurent AM, Lyonga D, Vekaria S, Edwards L, et al. A critical function for cd200 in lung immune homeostasis and the severity of influenza infection. *Nat Immunol*. (2008) 9:1074–83. doi: 10.1038/ni.1637

126. Liu C, Fan D, Lei Q, Lu A, He X. Roles of resolvins in chronic inflammatory response. *Int J Mol Sci*. (2022) 23(23):14883. doi: 10.3390/ijms232314883

127. Centanni D, Henricks PAJ, Engels F. The therapeutic potential of resolvins in pulmonary diseases. *Eur J Pharmacol*. (2023) 958:176047. doi: 10.1016/j.ejphar.2023.176047

128. Rohde K, Yates RM, Purdy GE, Russell DG. Mycobacterium tuberculosis and the environment within the phagosome. *Immunol Rev*. (2007) 219:37–54. doi: 10.1111/j.1600-065X.2007.00547.x

129. Alsayed SSR, Gunosewoyo H. Tuberculosis: pathogenesis, current treatment regimens and new drug targets. *Int J Mol Sci*. (2023) 24(6):5202. doi: 10.3390/ijms24065202

130. Adikesavalu H, Gopalaswamy R, Kumar A, Ranganathan UD, Shanmugam S. Autophagy induction as A host-directed therapeutic strategy against mycobacterium tuberculosis infection. *Medicina (Kaunas)*. (2021) 57(6):522. doi: 10.3390/medicina57060522

131. Zhang S, Zhou X, Ou M, Fu X, Lin Q, Tao X, et al. Berbamine promotes macrophage autophagy to clear mycobacterium tuberculosis by regulating the ros/ca(2+) axis. *Mbio*. (2023) 14:E0027223. doi: 10.1128/mbio.00272-23

132. Saunders RN, Metcalfe MS, Nicholson ML. Rapamycin in transplantation: A review of the evidence. *Kidney Int*. (2001) 59:3–16. doi: 10.1046/j.1523-1755.2001.00460.x

133. Mugume Y, Kazibwe Z, Bassham DC. Target of rapamycin in control of autophagy: puppet master and signal integrator. *Int J Mol Sci*. (2020) 21(21):8259. doi: 10.3390/ijms21218259

134. Bhatt K, Bhagavathula M, Verma S, Timmins GS, Deretic VP, Ellner JJ, et al. Rapamycin modulates pulmonary pathology in A murine model of mycobacterium tuberculosis infection. *Dis Model Mech*. (2021) 14(10):dmm049018. doi: 10.1242/dmm.049018

135. Singh DK, Bhaskar A, Pahuja I, Shaji A, Moitra B, Shi Y, et al. Cotreatment with clofazimine and rapamycin eliminates drug-resistant tuberculosis by inducing polyfunctional central memory T-cell responses. *J Infect Dis*. (2023) 228:1166–78. doi: 10.1093/infdis/jiad214

136. Huang Z, Wu Y, Zhou X, Qian J, Zhu W, Shu Y, et al. Clinical efficacy of mtor inhibitors in solid tumors: A systematic review. *Future Oncol*. (2015) 11:1687–99. doi: 10.2217/fon.15.70

137. Boni JP, Hug B, Leister C, Sonnichsen D. Intravenous temsirolimus in cancer patients: clinical pharmacology and dosing considerations. *Semin Oncol*. (2009) 36 Suppl 3:S18–25. doi: 10.1053/j.seminoncol.2009.10.009

138. Singh P, Subbian S. Harnessing the mtor pathway for tuberculosis treatment. *Front Microbiol*. (2018) 9:70. doi: 10.3389/fmicb.2018.00070

139. Padmapriydarsini C, Mamulwar M, Mohan A, Shanmugam P, Gomathy NS, Mane A, et al. Randomized trial of metformin with anti-tuberculosis drugs for early sputum conversion in adults with pulmonary tuberculosis. *Clin Infect Dis*. (2022) 75:425–34. doi: 10.1093/cid/ciab964

140. Schuster EM, Epple MW, Glaser KM, Mihlan M, Lucht K, Zimmermann JA, et al. Tfeb induces mitochondrial itaconate synthesis to suppress bacterial growth in macrophages. *Nat Metab*. (2022) 4:856–66. doi: 10.1038/s42255-022-00605-w

141. Zhang Z, Chen C, Yang F, Zeng YX, Sun P, Liu P, et al. Itaconate is A lysosomal inducer that promotes antibacterial innate immunity. *Mol Cell*. (2022) 82:2844–2857.E10. doi: 10.1016/j.molcel.2022.05.009

142. Wykes MN, Lewin SR. Immune checkpoint blockade in infectious diseases. *Nat Rev Immunol*. (2018) 18:91–104. doi: 10.1038/nri.2017.112

143. Shiravand Y, Khodadadi F, Kashani SMA, Hosseini-Fard SR, Hosseini S, Sadeghirad H, et al. Immune checkpoint inhibitors in cancer therapy. *Curr Oncol*. (2022) 29:3044–60. doi: 10.3390/curroncol29050247

144. Velu V, Titanji K, Zhu B, Husain S, Pladevega A, Lai L, et al. Enhancing siv-specific immunity *in vivo* by pd-1 blockade. *Nature*. (2009) 458:206–10. doi: 10.1038/nature07662

145. Tzeng HT, Tsai HF, Liao HJ, Lin YJ, Chen L, Chen PJ, et al. Pd-1 blockage reverses immune dysfunction and hepatitis B viral persistence in A mouse animal model. *PloS One*. (2012) 7:E39179. doi: 10.1371/journal.pone.0039179

146. Fuller MJ, Callendret B, Zhu B, Freeman GJ, Hasselschwert DL, Satterfield W, et al. Immunotherapy of chronic hepatitis C virus infection with antibodies against programmed cell death-1 (Pd-1). *Proc Natl Acad Sci U.S.A*. (2013) 110:15001–6. doi: 10.1073/pnas.1312772110

147. Tousif S, Singh Y, Prasad DV, Sharma P, Van Kaer L, Das G. T cells from programmed death-1 deficient mice respond poorly to mycobacterium tuberculosis infection. *PloS One*. (2011) 6:E19864. doi: 10.1371/journal.pone.0019864

148. Barber DL, Mayer-Barber KD, Feng CG, Sharpe AH, Sher A. Cd4 T cells promote rather than control tuberculosis in the absence of pd-1-mediated inhibition. *J Immunol*. (2011) 186:1598–607. doi: 10.4049/jimmunol.1003304

149. Lazar-Molnar E, Chen B, Sweeney KA, Wang EJ, Liu W, Lin J, et al. Programmed death-1 (Pd-1)-deficient mice are extraordinarily sensitive to tuberculosis. *Proc Natl Acad Sci U.S.A*. (2010) 107:13402–7. doi: 10.1073/pnas.1007394107

150. Kim Y, Anderson JL, Lewin SR. Getting the "Kill" Into "Shock and kill": strategies to eliminate latent hiv. *Cell Host Microbe*. (2018) 23:14–26. doi: 10.1016/j.chom.2017.12.004

151. Jin Y, Teh SS, Lau HLN, Xiao J, Mah SH. Retinoids as anti-cancer agents and their mechanisms of action. *Am J Cancer Res*. (2022) 12:938–60.

152. Huang SL, Shyu RY, Yeh MY, Jiang SY. Cloning and characterization of A novel retinoid-inducible gene 1(Rig1) deriving from human gastric cancer cells. *Mol Cell Endocrinol*. (2000) 159:15–24. doi: 10.1016/S0303-7207(99)00207-5

153. Berg RK, Melchjorsen J, Rintahaka J, Diget E, Soby S, Horan KA, et al. Genomic hiv rna induces innate immune responses through rig-I-dependent sensing of secondary-structured rna. *PloS One*. (2012) 7:E29291. doi: 10.1371/journal.pone.0029291

154. Li P, Kaiser P, Lampiris HW, Kim P, Yukl SA, Havlir DV, et al. Stimulating the rig-I pathway to kill cells in the latent hiv reservoir following viral reactivation. *Nat Med*. (2016) 22:807–11. doi: 10.1038/nm.4124

155. Purssell A MM, Vulesevic B, Angel Jb. Retinoids: novel potential therapeutics in the pursuit of hiv-1 cure. *Front Virol*. (2022) 2. doi: 10.3389/fviro.2022.957124

156. Nash A, Aghlara-Fotovat S, Hernandez A, Scull C, Veiseh O. Clinical translation of immunomodulatory therapeutics. *Adv Drug Delivery Rev*. (2021) 176:113896. doi: 10.1016/j.addr.2021.113896

157. Ward RA, Aghaeepour N, Bhattacharyya RP, Clish CB, Gaudilliere B, Hacohen N, et al. Harnessing the potential of multiomics studies for precision medicine in infectious disease. *Open Forum Infect Dis*. (2021) 8:Ofab483. doi: 10.1093/ofid/ofab483

158. Epsi NJ, Powers JH, Lindholm DA, Mende K, Malloy A, Ganesan A, et al. A machine learning approach identifies distinct early-symptom cluster phenotypes which correlate with hospitalization, failure to return to activities, and prolonged covid-19 symptoms. *PloS One*. (2023) 18:E0281272. doi: 10.1371/journal.pone.0281272

frontiers | Frontiers in Immunology

TYPE Original Research
PUBLISHED 26 November 2024
DOI 10.3389/fimmu.2024.1473193

OPEN ACCESS

EDITED BY
Jiae Kim,
Henry M Jackson Foundation for the Advancement of Military Medicine (HJF), United States

REVIEWED BY
Tarek A. Ahmad,
Bibliotheca Alexandrina, Egypt
Sanjay Ram,
University of Massachusetts Medical School, United States
Peter A. Rice,
University of Massachusetts Medical School/ UMass Memorial Medical Center, United States

*CORRESPONDENCE
Jian Huang
81537648@qq.com
Meirong Huang
277792461@qq.com

†These authors have contributed equally to this work

RECEIVED 30 July 2024
ACCEPTED 12 November 2024
PUBLISHED 26 November 2024

CITATION
Lu Q, Yang H, Peng Y, Dong Z, Nie P, Wang G, Luo S, Min X, Huang J and Huang M (2024) Intranasal trivalent candidate vaccine induces strong mucosal and systemic immune responses against *Neisseria gonorrhoeae*. *Front. Immunol.* 15:1473193. doi: 10.3389/fimmu.2024.1473193

Intranasal trivalent candidate vaccine induces strong mucosal and systemic immune responses against *Neisseria gonorrhoeae*

Qin Lu[1†], Hui Yang[1,2†], Yanfeng Peng[1,2], Zeling Dong[1,2], Pujing Nie[1,2], Guangli Wang[1,2], Shilu Luo[1,2], Xun Min[1,2], Jian Huang[1,2*] and Meirong Huang[3*]

[1]School of Laboratory Medicine, Zunyi Medical University, Zunyi, Guizhou, China, [2]Department of Laboratory Medicine, Affiliated Hospital of Zunyi Medical University, Zunyi, Guizhou, China, [3]Department of Blood Transfusion, Affiliated Hospital of Zunyi Medical University, Zunyi, Guizhou, China

The spread of multidrug-resistant strains of *Neisseria gonorrhoeae* poses a great challenge in gonorrhea treatment. At present, vaccination is the best strategy for gonorrhea control. However, given the extensive antigenic variability of *N. gonorrhoeae*, the effectiveness of monovalent vaccines is limited. Therefore, increasing the coverage of vaccination by using a multivalent vaccine may be more effective. In this study, a trivalent vaccine comprising three conserved antigens, namely, the App passenger domain, MetQ, and neisserial heparin binding antigen (NHBA), was constructed, and its protective effect was evaluated. Trivalent vaccines induced stronger circulating IgG and IgA antibody responses in mice than monovalent vaccines, in addition to eliciting Th1, Th2, and Th17 immune responses. Antiserum generated by the trivalent vaccine killed *N. gonorrhoeae* strains (homologous FA1090 and heterologous FA19), exhibiting superior bactericidal capacity than NHBA and MetQ vaccine antisera against *N. gonorrhoeae*, but similar capacities to those of the App vaccine antiserum. In addition, the trivalent vaccine antiserum achieved greater inhibition of *N. gonorrhoeae* FA1090 strain adherence to ME-180 cells compared to that elicited by the monovalent vaccine antiserum. In a mouse vaginal infection model, the trivalent vaccine was modestly effective (9.2% decrease in mean area under curve compared to the pCold-TF control mice), which was somewhat better than the protection seen with the monovalent vaccines. Our findings suggest that recombinant multivalent vaccines targeting *N. gonorrhoeae* exhibit advantages in protective efficacy compared to monovalent vaccines, and future research on multivalent vaccines should focus on optimizing different antigen combinations.

KEYWORDS

***Neisseria gonorrhoeae*, MetQ, neisserial heparin binding antigen, adhesion and penetration protein, nasal immunization**

1 Introduction

Neisseria gonorrhoeae causes the sexually transmitted disease gonorrhea, threatening global health (1). Each year, 87 million people are estimated to be infected with *N. gonorrhoeae* globally (2), with the infection leading mainly to urethritis in men and cervicitis in women. In women, untreated infections may result in pelvic inflammatory diseases and infertility (3). Additionally, gonorrhea increases the risk of contracting and transmitting the human immunodeficiency virus (4). *N. gonorrhoeae* has been reported to be resistant to all antimicrobials recommended for gonorrhea treatment (5). Extensively drug-resistant strains of *N. gonorrhoeae* with high levels of resistance to ceftriaxone and azithromycin have been developed in the United Kingdom and Australia (6, 7). The *N. gonorrhoeae* FC428 strain, which is resistant to first-line therapeutic agents such as ceftriaxone and azithromycin, has spread worldwide (8). Thus, the World Health Organization has identified drug-resistant *N. gonorrhoeae* as an urgent threat to public health (9). As treatment failure due to antibiotic resistance is common, an effective vaccine is required to prevent and treat gonorrhea (1).

Since the 1970s, the protective efficacy of several *N. gonorrhoeae* vaccines have been explored in clinical trials, including a partially inactivated whole-cell vaccine, a gonococcal pilus vaccine, and a gonococcal outer membrane (OM) vaccine enriched in gonococcal porin. However, none of these vaccines have been successful. In recent years, novel strategies, such as reverse vaccinology (10), "omics", and bioinformatics have been employed to discover *N. gonorrhoeae* vaccine antigens. As a result, *N. gonorrhoeae* candidate vaccine antigens have been evaluated in preclinical settings, including the gonococcal lipooligosaccharide epitope 2C7 (11) and some surface membrane proteins (1). For example, MetQ, the methionine-binding component of an ATP-binding cassette transporter system, is a highly conserved lipoprotein in different strains of *N. gonorrhoeae* (12–14). In addition to its function in methionine transportation, MetQ also affects *N. gonorrhoeae* adhesion to epithelial cells, invasion, and survival in primary monocytes, macrophages, and human serum (15). The rMetQ-CpG vaccine significantly accelerates the clearance rate of gonococcal infections in immunized mice and reduces the bacterial load (16). Recent studies have reported that serum group B *N. menigitidis* OM vesicle (OMV) vaccines, including MeNZB, 4CMenB, MenVA-MENGOC-BC, and MenBvac, elicit moderate cross-protection against *N. gonorrhoeae* (1, 17, 18), which has reignited interest in *N. gonorrhoeae* multivalent OMV vaccines. A gonococcal vaccine composed of OMVs and microencapsulating IL-12 elicits Th1-driven immunity, generates both circulating and local antibodies in the genital tract, and confers resistance to vaginal gonococcal infections upon intravaginal immunization (19). Additionally, the nasal immunization route likewise elicits immune responses in the genital tract and confers resistance to vaginal infection with multiple *N. gonorrhoeae* strains (20). However, OMVs are derived from the bacterial OM and contain a variety of protein components, which are highly variable during production and expensive to extract (21). Increasing vaccine coverage through co-vaccination with multiple key surface antigens to minimize the likelihood of immune escape and the selection of resistant mutants may be effective for developing an efficient gonorrhea vaccine (22). Gulati et al. showed that a chimeric molecule comprising NGO0265 and FtsN adjuvanted with GLA-SE elicits an IgG response with broad anti-gonococcal bactericidal activity and attenuates gonococcal colonization in a complement-dependent manner (23). In addition, Zhu et al. found that the killing ability of anti-NGO0690 and anti-NGO1701 mixed serum against *N. gonorrhoeae* F62 strain was significantly improved compared with a single serum, with an additive effect (24). They further constructed a trivalent vaccine consisting of recombinant proteins NGO0690, NGO0948, and NGO1701 that strongly induced serum bactericidal antibodies against several *N. gonorrhoeae* strains (22). Consequently, multivalent vaccines may be a promising research direction for gonorrhea prevention.

The adhesion and penetration protein (App), an autotransporter with serine protease activity in *N. gonorrhoeae*, is a conserved virulence factor localized on the bacterial surface and involved in bacterial adhesion, invasion and colonization (14, 25). Our previous study suggested that, within the intranasal mucosa, the passenger domain of the App protein is immunoprotected against gonococcal infections (26). Neisserial heparin binding antigen (NHBA) is a surface-exposed lipoprotein that binds to heparin and heparan sulfate proteoglycans on the surface of host epithelial cells (27). Recombinant NHBA is highly immunogenic, and antibodies against NHBA mediate the killing of gonococci through serum bactericidal and opsonophagocytic activities. These antibodies also prevent the functional activity of NHBA by reducing heparin binding and adherence to cervical and urethral epithelial cells (28). Since research on gonococcal multivalent recombinant vaccines remains in its infancy, it is essential to explore and optimize more antigen combinations. Based on the important roles of MetQ, App, and NHBA in the adhesion and invasion of *N. gonorrhoeae*, this study aimed to explore the protective effects of these three protein combinations against gonorrhea.

N. gonorrhoeae usually colonizes the genitourinary system (3). However, most current gonorrhoeae vaccines are systemic and do not elicit mucosal immunity to effectively prevent or reduce transmission (29, 30). Therefore, in the present study, we evaluated the *in vivo* immune response and protection against gonococcal infections induced by a trivalent combined-protein vaccine consisting of the App passenger domain, NHBA, and MetQ proteins in combination with the mucosal adjuvant cholera toxin B subunit (CTB), delivered via nasal immunization. Our findings provide a foundation for developing multivalent vaccines and for further characterization of these antigens.

2 Materials and methods

2.1 Bacterial strains and growth conditions

N. gonorrhoeae standard strains FA1090 (ATCC700825) and FA19 (BAA-1838) and two *N. gonorrhoeae* strains from clinical isolates (Department of Medical Laboratory, Affiliated Hospital of Zunyi Medical University) were plated overnight on gonococcal base (GCB) agar (Oxoid, Basingstoke, UK) at 37°C with 5% CO_2. To obtain sialylation of *N. gonorrhoeae*, a final concentration of 50 μg/

mL CMP-N-acetylneuraminic acid (CMP-NANA) (Sigma) was added to gonococcal base liquid (GCBL) medium and grown at 37°C for 18 h in an atmosphere of 5% (v/v) CO_2 (30, 31). In some experiments, bacteria grown for 18–24 h were resuspended in phosphate-buffered saline (PBS) using a Sensititre nephelometer to prepare the corresponding bacterial suspensions.

2.2 Vaccine design and construction

Sequences of the App passenger domain (*ngo*2105), NHBA protein (*ngo*1958), and MetQ protein (*ngo*2139) were obtained from the NCBI database (GenBank: NC_002946.2). Genes encoding the passenger domain (43–1190 aa), NHBA protein (1–429 aa), and MetQ protein (23–288 aa) fragments were amplified from *N. gonorrhoeae* FA1090 through polymerase chain reaction using the primers listed in Supplementary Table S1. The above gene fragments were amplified and cloned into the pCold-TF vector (plasmid map is shown in Supplementary Figure S1) to obtain template plasmids pCold-TF-*passenger*, pCold-TF-*nhba*, and pCold-TF-*metQ*.

2.3 Expression and purification of target proteins

The pCold-TF-*passenger*, pCold-TF-*nhba*, and pCold-TF-*metQ*, and pCold-TF plasmids were transformed into *E. coli* BL21 (DE3) cells using heat shock. Bacterial strains transformed with recombinant plasmids were cultured on Luria–Bertani agar plates supplemented with ampicillin (100 μg/mL) and then incubated at 37°C for 12–15 h. A single colony was inoculated into Luria–Bertani broth supplemented with ampicillin in a conical flask and then incubated at 37°C for 12–15 h with shaking at 250 *rpm*. When the bacterial culture reached an optical density of 0.60 at 600 nm (OD_{600}), 0.05 mM isopropyl beta-D-thiogalactoside was added to induce recombinant protein expression, which continued for 10 h at 15°C. Recombinant proteins were purified using a Ni^{2+}-nitrilotriacetic acid column, and imidazole was removed. Lipopolysaccharide was removed from the recombinant protein preparations using an EtEraser™ Endotoxin Removal Kit (Xiamen Bioendo Technology Co. Ltd, Xiamen, China). After the recombinant protein was treated with endotoxin removal, LPS content in the recombinant protein was detected using a gram-negative lipopolysaccharide detection kit (Xinuo Biopharmaceutical Co, LTD, Tianjin, China), which was lower than 0.5 EU/mL. Protein purity was analyzed via 10% sodium dodecyl sulfate-polyacrylamide gel electrophoresis (SDS-PAGE) and Coomassie Blue Fast staining (Epizyme, China). The protein concentration was determined using a BCA kit (Solarbio, Beijing, China), followed by storage at −80°C until use.

2.4 Immunization of mice

Female BALB/c mice (6–8 weeks old) of specific-pathogen-free (SPF) grade were purchased from the Experimental Animal Center of Zunyi Medical University (Zunyi, China). The mice (n = 6) were randomly divided into six groups: App + CTB, NHBA + CTB, MetQ + CTB, App + NHBA + MetQ (trivalent + CTB), pCold-TF + CTB, and PBS + CTB. Mice were immunized intranasally on days 0, 14, 28, and 42 (32). Then, 10 μg of App, NHBA, MetQ, or pCold-TF protein or 10 μg each of App, NHBA, MetQ, or their mixture (App + NHBA + MetQ) were suspended in 20 μL of PBS and mixed with 10 μg of CTB adjuvant (Absin, Shanghai, China) to a total volume of 30 μL for mouse immunization. Tail vein blood was collected from the mice 1 week after each vaccination, and vaginal secretions were collected on days 35 and 49. For vaginal secretions, 50 μL of sterile PBS was aspirated into the posterior vaginal fornix three to five times, repeated twice, and the fluids were combined. Finally, after centrifugation, the supernatants of the serum and vaginal secretions were stored at −80°C until further analysis.

2.5 Native target protein expression in different *N. gonorrhoeae* strains

N. gonorrhoeae FA1090, FA19, and the two clinical strains were inoculated on GCB plates and incubated at 37°C for 24 h. Colonies were picked and placed in PBS and adjusted to 0.5 McFarland units. The bacterial precipitates were washed with PBS and added to 1× loading buffer, then boiling at 100°C for 15 min. Bacterial lysates were separated via SDS-PAGE and transferred to polyvinylidene fluoride membranes. The expression of App passenger, NHBA, and MetQ in different *N. gonorrhoeae* strains were analyzed through immunoblotting using App, NHBA, or MetQ antisera as the primary antibodies (1:2,000) and horseradish peroxidase-labelled goat anti-mouse IgG (ZSGB-Bio, China) as the secondary antibody (1:5,000). Finally, a high-sensitivity chemiluminescent substrate detection kit (Epizyme, Cambridge, MA, USA) was used to analyze App, NHBA, and MetQ expression in different *N. gonorrhoeae* strains.

2.6 Mouse antibody titers and antibody typing

Antibody titers in serum and vaginal secretions were assessed using enzyme-linked immunosorbent assays (ELISAs). Nunc-Immuno plates were coated with purified antigen (96 wells of purified antigen for App, NHBA, MetQ, or pCold-TF at 10 μg/mL), incubated overnight at 4°C, and washed with PBS-T (PBS containing 0.1% Tween 20). Antisera from the immunized groups were diluted with blocking buffer (100 μL/well) and incubated at 37°C for 1 h in the wells. The plates were then washed three times with PBS-T. Horseradish-peroxidase-labelled goat anti-mouse IgG, IgG1, IgG2a, IgG2b, IgG3, and IgA were diluted at 1:5,000 and added to the plates, which were left to stand for 1 h at 37°C. The plates were washed three times, and a 3,3',5,5'-tetramethylbenzidine solution (Solarbio) was added for 30 min for color development. The reaction was terminated by adding a termination solution (Solarbio). Absorbance was recorded at 450 nm, and the antibody titer was defined as the highest dilution of the sample with an absorbance value 2.1 times that of the negative control.

2.7 Serum bactericidal activity

For the serum bactericidal assay (SBA) (33), *N. gonorrhoeae* FA1090 and FA19 were inoculated into GCB plates and incubated for 18–24 h at 37°C with 5% CO_2. To obtain sialylation of *N. gonorrhoeae* strain FA1090 was cultured in GCBL medium (containing 50 μg/mL CMP-NANA) in 5% (v/v) CO_2 at 37°C for 18 h. The number of selected colonies was adjusted to 4×10^4 colony-forming units (CFU)/45 μL. Then, 45 μL of heat-inactivated antisera at different dilution titers (mixture of three mouse sera samples) was added, and the plates were incubated at 37°C with 5% CO_2 for 15 min. Thereafter, 25% human serum was added as a complement source, followed by incubation at 37°C, 5% CO_2 for 30 min. The entire reaction mixture was diluted and spread onto GCB plates, with the CFU counted on the following day. The SBA bactericidal titers had the highest antibody dilutions, which resulted in more than 50% *N. gonorrhoeae* killing. The untreated group (0, without serum and complement), the lowest dilution of PBS-immunized group antiserum (PBS, with complement) and pCold-TF-immunized group antiserum (pCold-TF, with complement) were set as controls. The bacterial survival rate of the untreated group (0, without serum and complement) was set to 100%, and the bacterial survival rate of each group was calculated by the number of colonies in each serum group/number of colonies in the untreated group ×100%.

2.8 Antibody adherence inhibition assay

As described previously (26), an antibody-mediated adhesion inhibition assay was performed using human cervical cancer epithelial cells (ME-180, ATCC HTB33, Fenghui Biotechnology Co, Ltd, Hunan, China). ME-180 cells were cultured in RPMI 1640 with 10% fetal bovine serum for 24 h to form a monolayer of fused cells in 24-well tissue culture plates. Bacterial suspensions were prepared by inoculating *N. gonorrhoeae* FA1090 onto GCB plates and incubating overnight. Colonies with pili were then selected. The bacteria were pre-incubated with heat-inactivated antiserum in RPMI 1640 medium (HyClone, Logan, UT, USA) for 30 min at 37°C. ME-180 cells were washed three times with PBS, and the antiserum-pre-treated bacterial suspension was added at a multiplicity of infection of 10:1 to the ME-180 cells. This was followed by co-incubation at 37°C and 5% CO_2 for 3 h. To remove the non-adherent bacteria, we washed the solution three times with PBS. The ME-180 cells were lysed with 1% saponin. The lysates were serially diluted and plated on GCB plates to determine the bacterial number of CFU. Adhesion rates were calculated as the ratio of the number of CFU that adhered to the cells to the initial number of CFU.

2.9 Whole-cell ELISA

Whole-cell ELISA experiments were carried out as described (15). The ELISA was conducted using 96-well MaxiSorp plates (Nunc) coated with *N. gonorrhoeae* FA1090 strains (1×10^7 CFU). After coating, the plates were washed with PBS and blocked with PBS containing 1% bovine serum albumin (BSA) for 1 hour. Following blocking, the plates were incubated with antibody (diluted 1:1,000) for 1 hour at 37°C, 5% CO_2. After washing three times with PBS, the plates were incubated with a secondary antibody (HRP-conjugated anti-mouse, diluted 1:2,000) for 1 hour. After additional washes, the plates were developed using tetramethylbenzidine (TMB) solution (Solarbio). The reaction was terminated by adding 1 volume of 1 M HCl. Absorbance was measured at 450 nm using a Victor3 plate reader. Relative binding capacity was calculated as $A450_{sialylation}$/$A450_{non\text{-}sialylation}$ for each antiserum.

2.10 Assay of cytokine levels

One week after the last immunization, three mice were randomly selected from each group. Mouse spleens were crushed and resuspended through filtration in RPMI 1640 to prepare splenocyte suspensions that were supplemented with 10% fetal bovine serum, 10 kU/mL penicillin, 10 mg/mL streptomycin, and 25 μg/mL amphotericin B. The suspension was incubated at room temperature for 24 h. The cells were added to 24-well cell culture plates (1 mL/well) at 5×10^6 cells/mL. Finally, splenocytes from immunocompetent mice were stimulated by adding 10 μg of purified App, NHBA, MetQ, App + NHBA + MetQ (Trivalent), or pCold-TF proteins to PBS and cultured for 72 h at 37°C and 5% CO_2. The culture medium supernatant was collected, and the levels of IL-17A and IFN-γ were determined using cytokine assay kits (Proteintech, Rosemont, IL, USA).

2.11 Mouse immunity and challenge studies

SPF-grade female BALB/c mice aged 6 to 8 weeks (Experimental Animal Centre, Zunyi Medical University) were randomly divided into the following six groups (n = 6): App, NHBA, MetQ, App + NHBA + MetQ (Trivalent), pCold-TF, and PBS. Mice were vaccinated via intranasal inoculation on days 0, 14, 28, and 42. The vaccine contained 10 μg of antigen and 10 μg of CTB (CTB adjuvant:antigen = 1:1; total volume 30 μL). After the final immunization, pro-estrus mice were administered subcutaneous injections of 0.5 mg of sesame-oil-soluble estradiol on days −2, 0 (day of bacterial challenge), and +2 to increase their susceptibility. Mice were treated with antibiotics to prevent the overgrowth of commensal flora. FA1090 (1×10^8 CFU/mL) was prepared, and mice were infected with 20 μL of this solution to achieve an infective dose of approximately 2×10^6 CFU/mouse. Each group of mice was vaginally inoculated with vaginal secretions (vaginal rinse with 50 μL of normal saline, repeated twice), which were collected daily to dilute the smear for colony counting and observe the clearance of *N. gonorrhoeae* colonization.

2.12 Statistical analysis

Comparisons between two independent groups were performed using the Student's t-test. Antibody titers were analyzed using Šídák's multiple comparison test. Kaplan–Meier plots were used

to analyze the time needed for infection clearance. The log-rank (Mantel–Cox) test was used to compare the Kaplan–Meier curves of the groups. The AUC comparisons should be made by One-way ANOVA and Dunn's multiple comparisons test.

3 Results

3.1 Preparation and characterization of the trivalent vaccine

To construct the trivalent vaccine, we used the App protein passenger domain, full-length NHBA, and truncated MetQ with the signal peptide region removed as vaccine components (Figure 1A). These components were expressed in *E. coli* BL21 with the tag protein "trigger factor" in the pCold-TF vector, resulting in pure bands of the target proteins at relative molecular masses of 180, 130, 90, and 55 kDa, respectively (Figure 1B). Polyclonal antibodies were prepared by immunizing mice with the three tagged recombinant proteins. Western blotting showed that the polyclonal antibodies specifically recognized natively expressed App, NHBA, and MetQ in two laboratory strains, FA1090 and FA19, as well as in randomly selected clinical isolates (Figure 1C). The genetic sequences of 100 strains of *N. gonorrhoeae* showed 99.93% 96.37%, and 99.88% conservation of *app*, *nhba* and *metQ* genes, respectively (Supplementary Tables S2–S4), suggesting that App, NHBA, and MetQ are conserved among different strains.

3.2 Circulating and genital antibody responses

Mice were immunized with tagged recombinant proteins intranasally on days 0, 14, 28, and 35, with serum and vaginal secretions collected to determine antibody titers 1 week after each immunization (Figure 2A). Overall, mice immunized with the trivalent vaccine tended to exhibit stronger circulating IgG and IgA antibody responses than those immunized with the monovalent vaccine (Figures 2B–G). Both IgG and IgA antibodies were significantly induced in vaginal washes (Figures 3A–F). Except for anti-NHBA IgG, the trivalent vaccine group had significantly higher IgG and IgA antibody titers in the vaginal washes after the fourth immunization than those in the monovalent vaccine group.

3.3 Th1, Th2, and Th17 immune responses

The IgG isotype indirectly reflects changes in the Th1/Th2 balance (26). In mice, Th1-type cytokines induce lgG2a, whereas Th2-type cytokines induce lgG1 antibody production. After the final immunization, higher titers of each IgG isotype were observed in the trivalent vaccine group than in the monovalent vaccine group (Figures 4A–C). All groups generated high titers of IgG1 antibody responses (IgG1 > IgG2b > IgG2a > IgG3) and had IgG1/IgG2a ratios > 1. These results suggest that mice in all groups exhibited a bias toward Th2-type humoral immune responses. The IFN-γ and IL-17A levels were significantly higher in spleen leukocyte supernatants from trivalent vaccine-, App-, NHBA-, and MetQ-immunized mice compared to those in control mice (Figures 4D, E). IL-17A levels were significantly higher in the trivalent vaccine group than in the monovalent vaccine group. These results suggested that the trivalent vaccine elicited strong Th1, Th2, and Th17 immune responses.

3.4 Bactericidal activity against diverse gonococcal strains

To further investigate the putative protective immune responses, we characterized the functions of antibodies elicited by

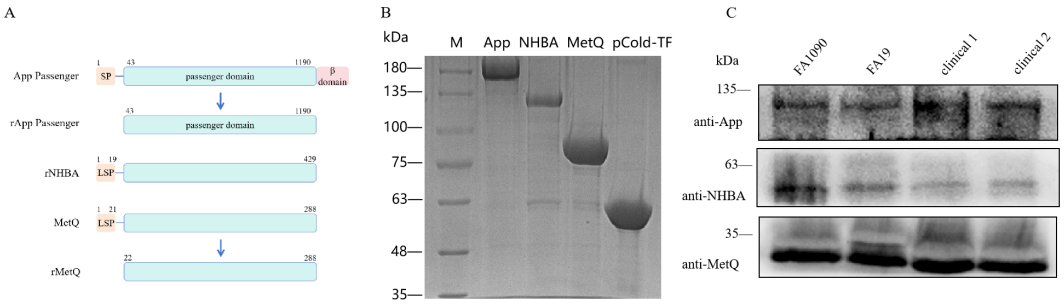

FIGURE 1
Expression and identification of trivalent vaccine component proteins. **(A)** Schematic of the protein domains. To generate rApp passenger antigen, which lacks the signal peptide (SP) and β domain, we engineered a partial passenger domain (43–1190 aa). To generate rNHBA antigen, the lipoprotein signal peptide (LSP)-containing *nhba* gene was engineered to produce a full-length NHBA recombinant protein. To generate rMetQ antigen, the *metQ* gene, encoding a full-length MetQ protein, was engineered to produce a recombinant protein that lacks the LSP. **(B)** Recombinant proteins were separated using 7.5% sodium dodecyl sulfate-polyacrylamide gel electrophoresis. Lane M: Marker, lane 1: App passenger domain, lane 2: full-length NHBA protein, lane 3: truncated MetQ protein, lane 4: pCold-TF-tagged protein. These recombinant proteins were expressed as a fusion that comprised Trigger factor plus three peptides that contained cleavage sites for HRV3C protease, Thrombin, and Factor Xa. **(C)** Western blotting analysis of App, NHBA, and MetQ protein expression in different gonococcal strains using antibodies generated against the recombinant proteins.

10.3389/fimmu.2024.1473193

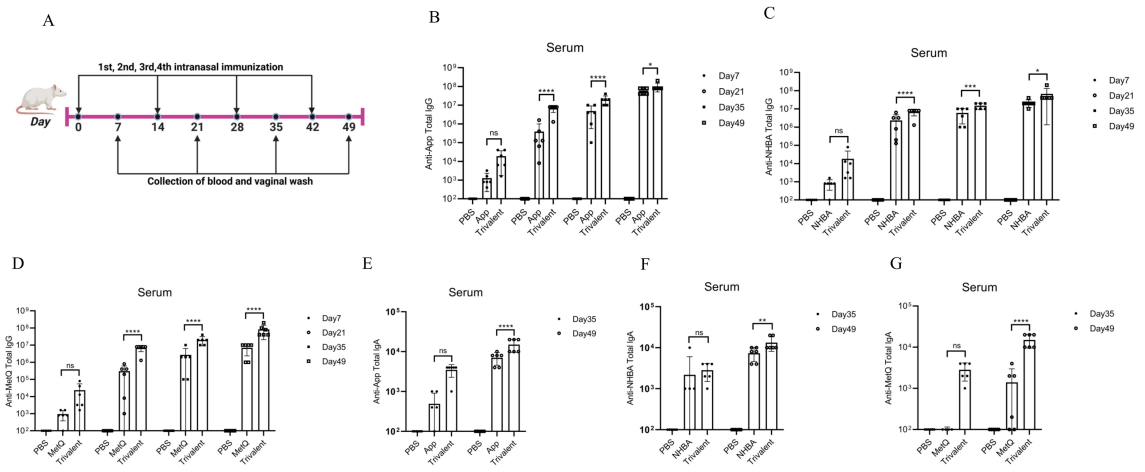

FIGURE 2
Comparison of serum antibody responses to nasal immunization in mice. **(A)** Timeline of mouse immunity. **(B–D)** On days 7, 21, 35, and 49 post-immunization, the serum titers of anti-App, anti-NHBA, and anti-MetQ IgG antibodies in each group were determined using enzyme-linked immunosorbent assay (ELISA). **(E–G)** On days 35 and 49 of immunization, anti-App, anti-NHBA, and anti-MetQ IgA serum antibody titers were determined using ELISAs. Data are presented as the mean ± standard error of the mean (SEM), n = 6, compared to the monovalent group (Šídák's multiple comparisons test), ns: non-significant, $P > 0.05$; *$P \leq 0.05$; **$P \leq 0.01$; ***$P \leq 0.001$; ****$P \leq 0.0001$.

the trivalent vaccines. We evaluated the bactericidal efficacy of antisera from various immunization groups against three strains, including homologous *N. gonorrhoeae* FA1090 and heterologous FA19. SBA showed that the antiserum from the trivalent vaccine group had stronger bactericidal activity against the three strains than that of the NHBA and MetQ groups, with bactericidal activity range of 100–800 dilution titers (Figures 5A, B and Supplementary Figure S2). To examine whether sialylation has an effect on bactericidal activity, we cultured strain FA1090 in the presence of CMP-NANA and tested the bactericidal activity of antiserum against both sialylated and non-sialylated gonococci. The results showed that the bactericidal efficiency of several antisera against sialylated gonococci was lower than that of non-sialylated gonococci (Figure 5C). We investigated whether sialylation affected the binding of antiserum to *N. gonorrhoeae* FA1090 by whole bacteria ELISA. The results showed no significant differences

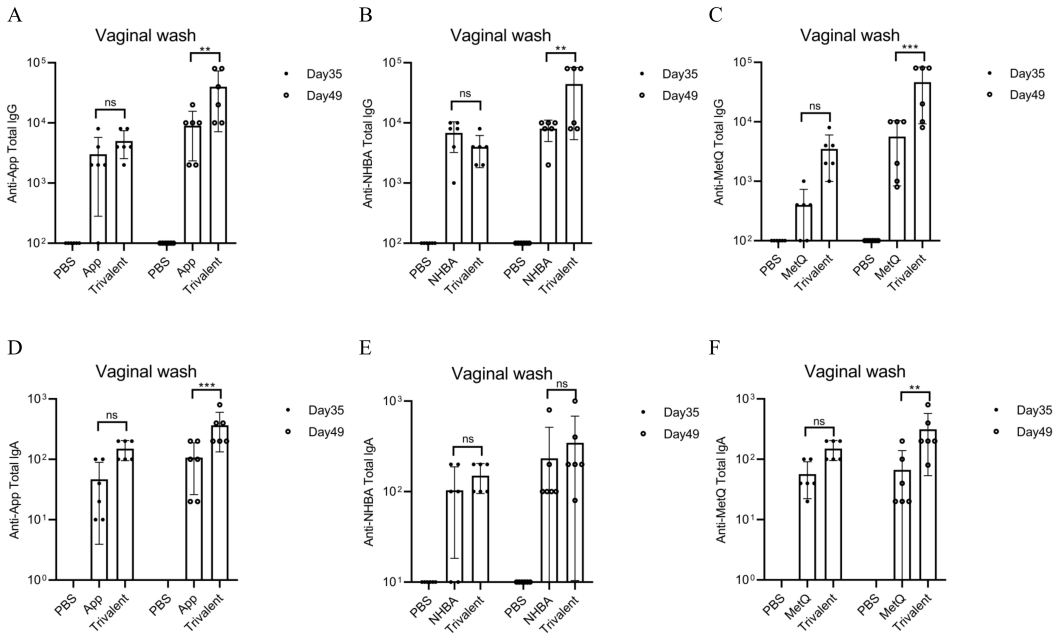

FIGURE 3
Comparison of vaginal antibody responses after nasal immunization in mice. On days 35 and 49 post-immunization, anti-App, anti-NHBA, anti-MetQ IgG **(A–C)**, and IgA **(D–F)** antibody titers in vaginal wash fluid from each group were determined using ELISAs. Data are presented as the mean ± SEM, n = 6, compared to the monovalent group (Šídák's multiple comparisons test), ns, non-significant, $P > 0.05$; **$P \leq 0.01$; ***$P \leq 0.001$.

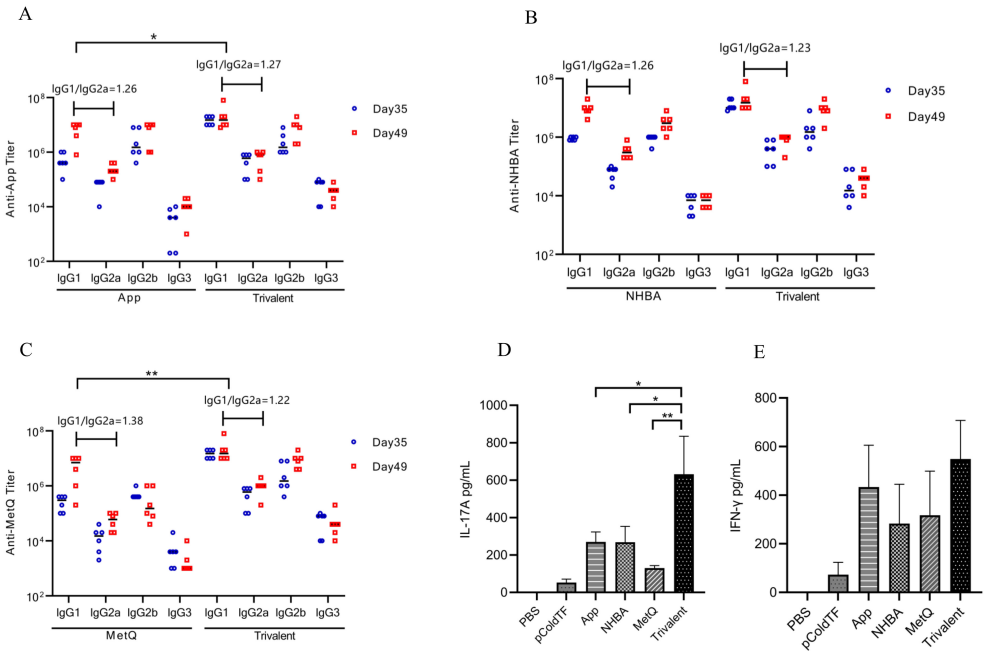

FIGURE 4
Serum antibody subtype and spleen cytokine analysis. **(A–C)** Antigen-specific IgG1, IgG2a, IgG2b, and IgG3 titers in serum were analyzed on days 39 and 49 post-immunization, and the IgG1/IgG2a ratio was calculated using antibody titer data from day 49 post-immunization (n = 6). **(D, E)** On day 49 post-immunization, three mice in each group were randomly selected for the isolation of splenocytes, which were stimulated with 10 μg of the corresponding recombinant proteins for 72 h, whereafter the supernatant was analyzed for IL-17A and IFN-γ levels. Data are presented as the mean ± SEM, compared to the monovalent group (unpaired Student's t-test), $*P \leq 0.05$, $**P \leq 0.01$.

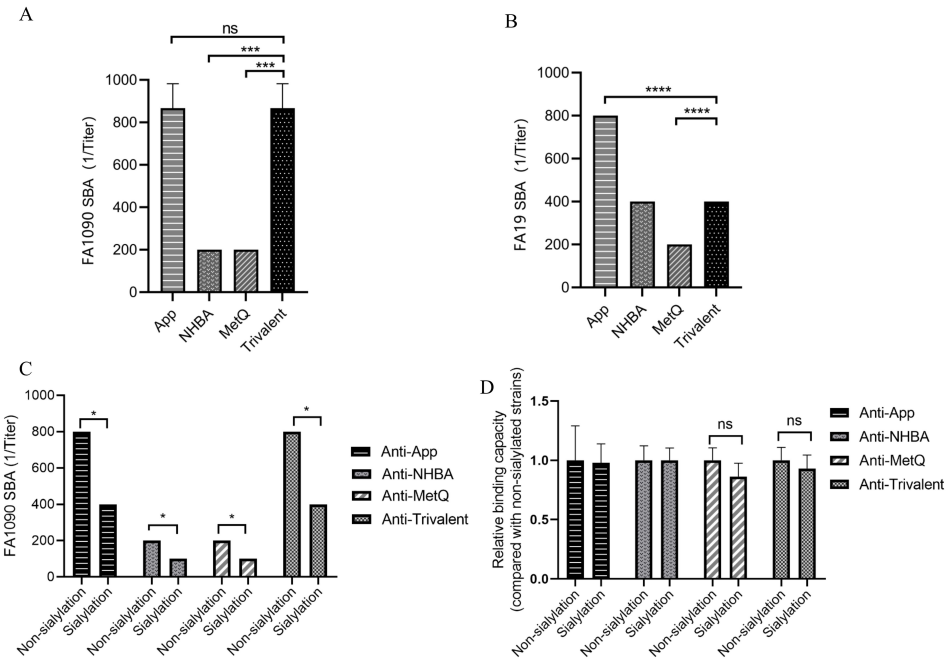

FIGURE 5
Analysis of antisera for bactericidal activity against *N. gonorrhoeae* strains FA1090 andFA19. For the serum bactericidal experiment, heat-inactivated sera of different dilutions from each immune group were co-incubated with strains FA1090 **(A)** and FA19 **(B)**. **(C)** Bactericidal effect of antiserum on sialylated and non-sialylated *N. gonorrhoeae* FA1090 strains. **(D)** Whole-cell ELISA of sialylated and non-sialylated *N. gonorrhoeae* FA1090 strains. Data are shown as mean ± standard deviation (n ≥ 3), some with identical results, so there were no Error bars. ns, non-significant, $P > 0.05$; $*P \leq 0.05$; $***P \leq 0.001$; $****P \leq 0.0001$.

10.3389/fimmu.2024.1473193

in the binding ability of the different antisera to sialylated and non-salialylated gonococci (Figure 5D).

3.5 Gonococcal adhesion to ME-180 cells

The adhesion of gonococci to epithelial cells is a key mechanism in the establishment of infection (34). Therefore, adhesion experiments were performed on ME-180 cells with strain FA1090 in the presence of antiserum. Our results showed that the antisera from each immunized group inhibited the adhesion of gonococci to ME-180 cells in a concentration-dependent manner (Figure 6). When the antisera of the App, NHBA, and MetQ groups were diluted to 1:80, gonococcal adhesion was reduced by 36.76% ($P < 0.001$), 31.37% ($P < 0.0001$), and 38.74% ($P < 0.01$), respectively, whereas the antisera of the trivalent vaccine group reduced gonococcal adhesion by 60.22% at this dilution ($P < 0.0001$). These results showed that the antiserum from the trivalent vaccine group inhibited the gonococcal adhesion rate to a significantly greater extent than antisera from the monovalent vaccine groups.

3.6 Clearance of *N. gonorrhoeae* in the vaginal tract

The efficacy of the trivalent and monovalent vaccines was tested in a mouse model of vaginal gonococcal infection by assessing the daily bacterial loads in vaginal washes and the time to clearance of the infection. There was no significant difference in the number of colonized bacteria between the PBS and pCold-TF controls, whereas the number of colonized bacteria in the monovalent vaccine group was lower than that in the control group (Figure 7A). Importantly, the number of colonized bacteria was significantly less in the trivalent vaccine group than in the monovalent vaccine group (Figure 7A). The area under the curve (AUC) was significantly lower in the trivalent vaccine group than in the pCold-TF group (Figure 7B). Although the AUC of the trivalent vaccine group exhibited a downward tendency when compared with the App, NHBA, and MetQ groups, no statistically significant difference was observed. In terms of the time to infection clearance, mice in the monovalent vaccine group were completely cleared of gonococcal infection on day 9, while for those in the PBS and

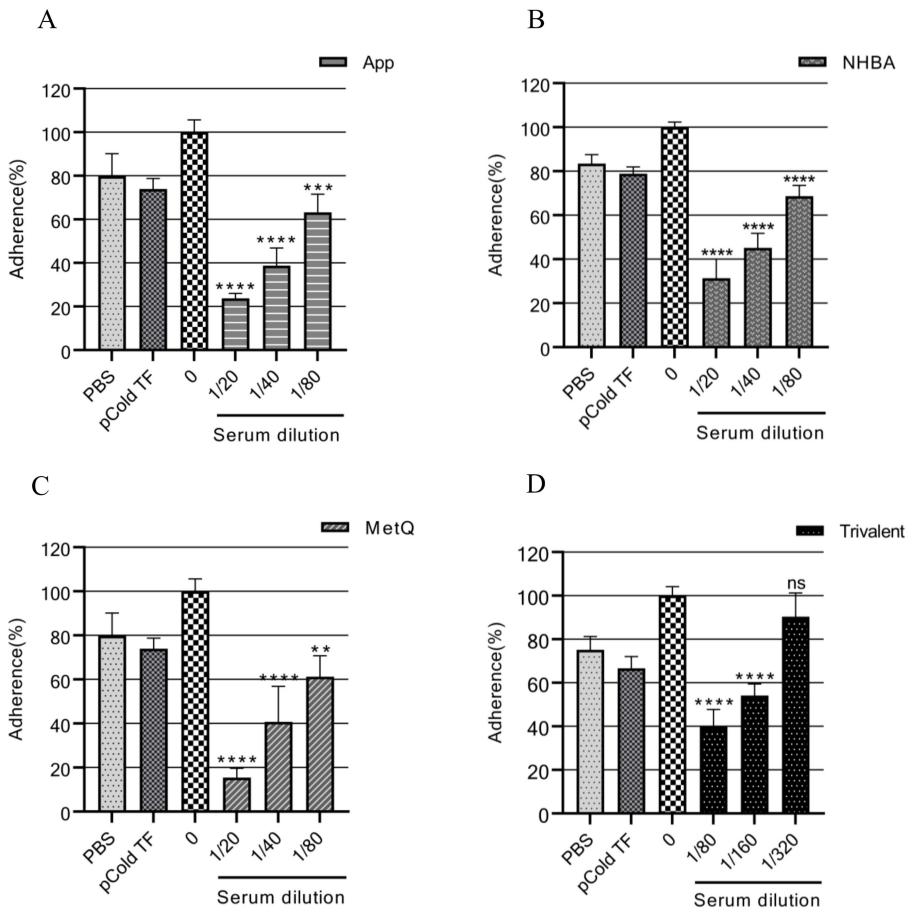

FIGURE 6
Analysis of the adhesion inhibition effect of antiserum on gonorrhea. FA1090 was pre-incubated with heat-inactivated antiserum of different dilutions in each group for 30 min and then co-incubated with ME-180 cells for 3 h. Antisera from the heat-inactivated PBS and pCold-TF groups were used as controls. The dilution of the PBS and pCold-TF control sera was the lowest dilution of the corresponding experimental group sera. The adhesion rate of *N. gonorrhoeae* in each group was calculated and compared with that in the untreated group (0, 100%). Data are presented as the mean ± SEM (n = 3). ns, non-significant, $P > 0.05$; $^{**}P \leq 0.01$; $^{***}P \leq 0.001$; $^{****}P \leq 0.0001$ (unpaired Student's t-test).

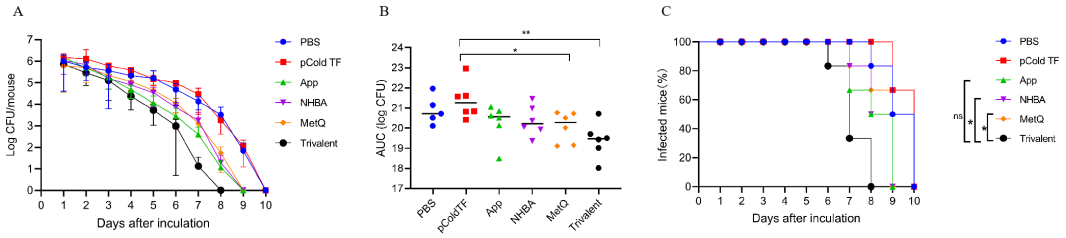

FIGURE 7
Resistance of each immune group to gonococcal FA1090 infection in the mouse vaginal colonization model. One week after the fourth immunization, pre-estrous mice (n = 6/group) were infected with 2×10^6 colony-forming units (CFU) of the gonococcal FA1090 strain through the vagina, and vaginal secretions were collected every day to count the gonococcal colony number. **(A)** The calculated log10 of CFU per day and plot of the relationship with time. **(B)** Graph displaying the individual area under the curve (AUC) for the daily CFU counts from the colonized mice. **(C)** Graph displaying the removal time curve of gonorrhoeae for each group. Data are presented as the mean ± SEM compared with the monovalent group. Kaplan–Meier curves were analyzed using the Mantel-Cox log-rank test, and AUCs were analyzed using One-way ANOVA and Dunn's multiple comparisons test, ns, non-significant, $P > 0.05$; *$P \leq 0.05$; **$P \leq 0.01$.

pCold-TF control groups, clearance was achieved on day 10 ($P < 0.01$, Figure 7C). Mice in the trivalent vaccine group were completely cleared of gonococcal infection on day 8, which was significantly faster than clearance in the NHBA and MetQ groups ($P < 0.01$), but not significantly different from that in the App group ($P = 0.0548$, Figure 7C). Overall, these results suggest that the trivalent vaccine is somewhat better than the monovalent vaccine in protecting mice against gonococcal infections of the genital tract.

4 Discussion

The widespread emergence of antibiotic resistance in *N. gonorrhoeae* poses considerable challenges for the treatment of gonorrhea, with the demand for an effective vaccine becoming increasingly urgent (35). At present, gonorrhea vaccine development is at the level of antigen discovery and the validation of protective immune responses (36, 37). However, given the extensive antigenic variability of *N. gonorrhoeae*, it may be difficult to achieve satisfactory protection using a monovalent vaccine (21, 22). Multivalent vaccines against bacterial and viral pathogens, and even cancer, may provide broader and potentially stronger protection than monovalent vaccines, and targeting multiple epitopes in antigens can also increase strain coverage (38–40). However, multicomponent gonococcal vaccines are relatively understudied (16, 28).

OMV vaccines are multicomponent vaccines (41) that mainly comprise bacterial OM components, which contain key antigens required to induce protective immune responses (42). The OMV-based MeNZB and 4CMenB vaccines can prevent *Neisseria meningitidis* infection (43, 44). *N. meningitidis* and *N. gonorrhoeae* share high genomic homology, with the MeNZB and 4CMenB vaccines being cross-protective against gonorrhea (45, 46). Thus, multivalent vaccines hold promise for protecting against gonorrhea.

In the present study, three antigens were found to be highly conserved among *N. gonorrhoeae* strains. The trivalent vaccine elicited earlier and higher circulating and vaginal IgG and IgA antibody titers than the monovalent vaccine, suggesting stronger immune activation. Serum bactericidal activities reflect immune function (33). Our results showed that antisera from the trivalent vaccine group were able to kill homologous and heterologous *N. gonorrhoeae* strains. However, the bactericidal activities of antisera from trivalent and monovalent vaccine groups differed against different strains (28). This may be caused by the different sensitivities of strains to complement, as well as by possible differences in antigen expression among strains. The bactericidal activities of antisera from the trivalent vaccine group were higher than those of NHBA and MetQ antisera but similar to those of the App group antiserum. Antisera from the trivalent vaccine group did not show additive or synergistic effects on bactericidal activities. A similar phenomenon was observed in the study of Menon et al., when Pfs25 was administered together with Pfs28 or Pfs230C as a mixed-malaria vaccine antigen. The antibody response of each antigen in the mixed vaccine was similar to that of the monovalent vaccine (47). However, the mixed-antigen vaccine did not show a cumulative effect of the two antigens in reducing malaria transmission. In multivalent vaccines, and possibly even in OMV vaccines, when increasing the number of antigens, the possibility of antagonism between antibodies should be considered, as this can diminish the protective effects. For example, the reduction modifiable protein (Rmp) antibody has been shown to suppress the bactericidal activity of other antibodies (48). Therefore, it is necessary to optimize and screen the antigen combinations in subsequent research of multivalent vaccines to obtain the best protective effect and ensure no interference between antibodies. In addition, since the majority of *N. gonorrhoeae* strains exist *in vivo* as sialylated bacteria and the salivated *N. gonorrhoeae* develops resistance to the bactericidal activity of normal human serum (30, 49), which may be related to the addition of sialic acid residues that block the binding of anti-LOS antibodies present in normal human serum to bacteria. Salivated gonococci have also been found to be resistant to bactericidal effects of immune sera in addition to LOS (50). Our results show that sialylated gonococci are able to resist killing by several antisera to a certain extent, but sialylation did not affect the binding of antisera to bacteria. Wetzler et al. also found no difference in the binding of anti-PI monoclonal antibodies against surface exposed cyclic epitopes to sialylated and non-sialylated *N. gonorrhoeae* (50). Therefore, we speculate that the attenuation of antiserum bactericidal activity by sialylation may have affected the

activation of the complement pathway. LOS sialylation is thought to potentially interfere with the ability of Ab to bind C1q (51). Sialic acids present on glycolipids or bacterial capsules can inhibit the complement cascade (52, 53), the bactericidal effect of anti-gonococcal antibodies is dependent on the complement cascade, and LOS sialylation may have an impact on their bactericidal effect. Moreover, sialylation of gonococcal LOS enhances factor H binding, thereby inhibiting alternative pathways (31, 51). LOS sialylation also inhibited the binding of serum mannose-binding lectin (MBL) to *N. gonorrhoeae*, thereby inhibiting the MBL pathway (51, 54). However, the complement can only be activated when *N. gonorrhoeae* is co-incubated with purified MBL-MASP prior to serum addition; MBL is not involved in complement activation of *N. gonorrhoeae* in the presence of complete serum containing C1-inhibitor and α_2-macroglobulin (55). In this study, we used complete serum as a complement source, so the role of the MBL pathway may be limited.

Adhesion to host cells is a key link between bacterial colonization, subsequent invasion, and infection (56). The colonization ability of bacteria largely depends on their resistance mechanisms to host mechanical and immune clearance (57). Therefore, bacterial adherence inhibition should be a goal when developing vaccines (58). For example, anti-NanAT1-TufT1-PlyD4 antisera can inhibit the adhesion of *Streptococcus pneumoniae* to A549 cells, and *in vivo* experiments have shown that it reduces *S. pneumoniae* colonization in the lungs (38). We found that when approximately 5×10^4 N. *gonorrhoeae* cells were added to a monolayer of ME-180 cells in the presence of antiserum, the trivalent vaccine antiserum inhibited gonococcal adhesion to ME-180 cells significantly better than the monovalent vaccine antiserum. The bacterial dose was close to the estimated infective dose of *N. gonorrhoeae* in humans. Our results showed that the vaccine effectiveness for clearing gonococcal infections in animal experiments was in agreement with the results of *in vitro* antibody adhesion inhibition assays compared to those of bactericidal assays. This suggests that vaccine-induced antibodies can reduce the initial level of gonococcal colonization in the host.

T helper (Th) cells play a key role in gonococcal infections (59). In the present study, antibody subtype analysis suggested that the trivalent vaccine significantly induced lgG1-type antibody responses, suggesting the indirect induction of a Th2-type immune response bias, which may be related to the CTB adjuvant used. The use of a CTB adjuvant induces a Th2-type response bias (60, 61). Splenocyte cytokine analysis revealed that splenocytes in the trivalent vaccine group secreted significantly more IFN-γ and IL-17A, suggesting the activation of Th1 and Th17 cellular immune responses. The clearance of *N. gonorrhoeae* is associated with Th1 and Th17 responses. Blocking IL-17 leads to prolonged gonorrhea, indicating that the Th17 response is involved in *N. gonorrhoeae* clearance (62). Gonococcal infection experiments in IL-12-knockout (Th1-deficient) mice have revealed that accelerated *N. gonorrhoeae* clearance is Th1-dependent (19). An effective gonorrhea vaccine should, therefore, induce a Th1 polarization response in the genital tract of mice, which may confer greater protection (29). However, the Th17 response is less protective against gonococci than the Th1 response, which does not produce protective immunity (63). Song et al. screened several adjuvant types to identify the optimal Th1-polarizing adjuvant, CpG1826, which triggered a strong Th1-polarizing antigen-specific immune response and provided excellent protection against gonococcal infection in a mouse model of vaginal infection (29). Therefore, it is necessary to screen and optimize adjuvants in subsequent studies to better activate the Th1 polarization response against gonorrhea.

In conclusion, the trivalent vaccine was highly immunogenic and broadly protective compared to monovalent vaccines, with the trivalent-vaccine-specific antiserum inhibiting *N. gonorrhoeae* adhesion to ME-180 cells and effectively clearing *N. gonorrhoeae* from the genital tract of mice. There are some limitations of our study. For example, although the monovalent and trivalent vaccines induced a strong antibody response, they did not show a surprising advantage in gonococcal infection clearance compared with controls. The possible reason is that Th1-biased IgG2a and IgG2b antibodies can activate complement more effectively than Th2-biased IgG1 antibodies, thereby enhancing the bactericidal activity of serum against *N. gonorrhoeae* (64). Hence, subsequent studies should also be carried out to evaluate the protective effect of multivalent vaccines using Th1-biased adjuvants.

Data availability statement

The original contributions presented in the study are included in the article/Supplementary Material. Further inquiries can be directed to the corresponding author/s.

Ethics statement

The studies involving humans were approved by The Ethics Committee of Zunyi Medical University. The studies were conducted in accordance with the local legislation and institutional requirements. The human samples used in this study were acquired from a by- product of routine care or industry. Written informed consent for participation was not required from the participants or the participants' legal guardians/next of kin in accordance with the national legislation and institutional requirements. The animal study was approved by The Animal Ethics Committee of Zunyi Medical University. The study was conducted in accordance with the local legislation and institutional requirements.

Author contributions

QL: Methodology, Writing – original draft. HY: Methodology, Writing – original draft. YP: Methodology, Writing – original draft. ZD: Formal analysis, Funding acquisition, Writing – review & editing. PN: Writing – review & editing, Methodology. GW: Methodology, Writing – review & editing. SL: Writing – review & editing, Formal analysis. XM: Writing – review & editing, Conceptualization. JH: Conceptualization, Writing – review & editing, Data curation, Funding acquisition, Project administration. MH: Conceptualization, Data curation, Funding acquisition, Project administration, Writing – review & editing.

Funding

The author(s) declare financial support was received for the research, authorship, and/or publication of this article. This work was supported by grants from the National Natural Science Foundation of China (82260330), the Science and Technology Fund Project of Guizhou Provincial Health Commission (gzwkj2024-044), and the Future Talent Program of Zunyi Medical University (Rc220211223).

Conflict of interest

The authors declare that the research was conducted in the absence of any commercial or financial relationships that could be construed as a potential conflict of interest.

Publisher's note

Supplementary material

The Supplementary Material for this article can be found online at: https://www.frontiersin.org/articles/10.3389/fimmu.2024.1473193/full#supplementary-material.

References

1. Williams E, Seib KL, Fairley CK, Pollock GL, Hocking JS, McCarthy JS, et al. Neisseria gonorrhoeae vaccines: A contemporary overview. *Clin Microbiol Rev*. (2024) 37:e0009423. doi: 10.1128/cmr.00094-23

2. Rowley J, Vander Hoorn S, Korenromp E, Low N, Unemo M, Abu-Raddad LJ, et al. Chlamydia, gonorrhoea, trichomoniasis and syphilis: global prevalence and incidence estimates, 2016. *Bull World Health Organ*. (2019) 97:548–62P. doi: 10.2471/BLT.18.228486

3. Lenz JD, Dillard JP. Pathogenesis of neisseria gonorrhoeae and the host defense in ascending infections of human fallopian tube. *Front Immunol*. (2018) 9:2710. doi: 10.3389/fimmu.2018.02710

4. Galvin SR, Cohen MS. The role of sexually transmitted diseases in hiv transmission. *Nat Rev Microbiol*. (2004) 2:33–42. doi: 10.1038/nrmicro794

5. Unemo M, Shafer WM. Antimicrobial resistance in neisseria gonorrhoeae in the 21st century: past, evolution, and future. *Clin Microbiol Rev*. (2014) 27:587–613. doi: 10.1128/CMR.00010-14

6. Whiley DM, Jennison A, Pearson J, Lahra MM. Genetic characterisation of neisseria gonorrhoeae resistant to both ceftriaxone and azithromycin. *Lancet Infect Dis*. (2018) 18:717–8. doi: 10.1016/S1473-3099(18)30340-2

7. Eyre DW, Sanderson ND, Lord E, Regisford-Reimmer N, Chau K, Barker L, et al. Gonorrhoea treatment failure caused by a neisseria gonorrhoeae strain with combined ceftriaxone and high-level azithromycin resistance, england, february 2018. *Euro Surveill*. (2018) 23:1800323. doi: 10.2807/1560-7917.ES.2018.23.27.1800323

8. Chen SC, Han Y, Yuan LF, Zhu XY, Yin YP. Identification of internationally disseminated ceftriaxone-resistant neisseria gonorrhoeae strain fc428, China. *Emerg Infect Dis*. (2019) 25:1427–9. doi: 10.3201/eid2507.190172

9. Nekahiwot S, Debela N. Multi-drug resistant gonorrhea: an emerging global threat. *Int J Infect Dis Ther*. (2024) 9:17–25. doi: 10.11648/j.ijidt.20240901.13

10. Seib KL, Zhao X, Rappuoli R. Developing vaccines in the era of genomics: A decade of reverse vaccinology. *Clin Microbiol Infect*. (2012) 18 Suppl 5:109–16. doi: 10.1111/j.1469-0691.2012.03939.x

11. Gulati S, Pennington MW, Czerwinski A, Carter D, Zheng B, Nowak NA, et al. Preclinical efficacy of a lipooligosaccharide peptide mimic candidate gonococcal vaccine. *mBio*. (2019) 10:e02552-19. doi: 10.1128/mBio.02552-19

12. Zielke RA, Wierzbicki IH, Baarda BI, Gafken PR, Soge OO, Holmes KK, et al. Proteomics-driven antigen discovery for development of vaccines against gonorrhea. *Mol Cell Proteomics*. (2016) 15:2338–55. doi: 10.1074/mcp.M116.058800

13. Zielke RA, Wierzbicki IH, Weber JV, Gafken PR, Sikora AE. Quantitative proteomics of the neisseria gonorrhoeae cell envelope and membrane vesicles for the discovery of potential therapeutic targets. *Mol Cell Proteomics*. (2014) 13:1299–317. doi: 10.1074/mcp.M113.029538

14. El-Rami FE, Zielke RA, Wi T, Sikora AE, Unemo M. Quantitative proteomics of the 2016 who neisseria gonorrhoeae reference strains surveys vaccine candidates and antimicrobial resistance determinants. *Mol Cell Proteomics*. (2019) 18:127–50. doi: 10.1074/mcp.RA118.001125

15. Semchenko EA, Day CJ, Seib KL. Metq of neisseria gonorrhoeae is a surface-expressed antigen that elicits bactericidal and functional blocking antibodies. *Infect Immun*. (2017) 85:e00898-16. doi: 10.1128/IAI.00898-16

16. Sikora AE, Gomez C, Le Van A, Baarda BI, Darnell S, Martinez FG, et al. A novel gonorrhea vaccine composed of metq lipoprotein formulated with cpg shortens experimental murine infection. *Vaccine*. (2020) 38:8175–84. doi: 10.1016/j.vaccine.2020.10.077

17. Abara WE, Jerse AE, Hariri S, Kirkcaldy RD. Planning for a gonococcal vaccine: A narrative review of vaccine development and public health implications. *Sex Transm Dis*. (2021) 48:453–7. doi: 10.1097/OLQ.0000000000001332

18. Wang B, Mohammed H, Andraweera P, McMillan M, Marshall H. Vaccine effectiveness and impact of meningococcal vaccines against gonococcal infections: A systematic review and meta-analysis. *J Infect*. (2024) 89:106225. doi: 10.1016/j.jinf.2024.106225

19. Liu Y, Hammer LA, Liu W, Hobbs MM, Zielke RA, Sikora AE, et al. Experimental vaccine induces th1-driven immune responses and resistance to neisseria gonorrhoeae infection in a murine model. *Mucosal Immunol*. (2017) 10:1594–608. doi: 10.1038/mi.2017.11

20. Liu Y, Hammer LA, Daamen J, Stork M, Egilmez NK, Russell MW. Microencapsulated il-12 drives genital tract immune responses to intranasal gonococcal outer membrane vesicle vaccine and induces resistance to vaginal infection with diverse strains of neisseria gonorrhoeae. *mSphere*. (2023) 8:e0038822. doi: 10.1128/msphere.00388-22

21. Petousis-Harris H, Radcliff FJ. Exploitation of neisseria meningitidis group B omv vaccines against N. Gonorrhoeae to inform the development and deployment of effective gonorrhea vaccines. *Front Immunol*. (2019) 10:683. doi: 10.3389/fimmu.2019.00683

22. Roe SK, Felter B, Zheng B, Ram S, Wetzler LM, Garges E, et al. *In vitro* pre-clinical evaluation of a gonococcal trivalent candidate vaccine identified by transcriptomics. *Vaccines (Basel)*. (2023) 11:1846. doi: 10.3390/vaccines11121846

23. Gulati S, Mattsson AH, Schussek S, Zheng B, DeOliveira RB, Shaughnessy J, et al. Preclinical efficacy of a cell division protein candidate gonococcal vaccine identified by artificial intelligence. *mBio*. (2023) 14:e0250023. doi: 10.1128/mbio.02500-23

24. Zhu T, McClure R, Harrison OB, Genco C, Massari P. Integrated bioinformatic analyses and immune characterization of new neisseria gonorrhoeae vaccine antigens expressed during natural mucosal infection. *Vaccines (Basel)*. (2019) 7:153. doi: 10.3390/vaccines7040153

25. Huang J, Zhang Q, Chen J, Zhang T, Chen Z, Chen Z, et al. Neisseria gonorrhoeae ngo2105 is an autotransporter protein involved in adhesion to human cervical epithelial cells and in vivo colonization. *Front Microbiol*. (2020) 11:1395. doi: 10.3389/fmicb.2020.01395

26. Xia L, Lu Q, Wang X, Jia C, Zhao Y, Wang G, et al. Characterization of protective immune responses against neisseria gonorrhoeae induced by intranasal immunization with adhesion and penetration protein. *Heliyon*. (2024) 10:e25733. doi: 10.1016/j.heliyon.2024.e25733

27. Esposito V, Musi V, de Chiara C, Veggi D, Serruto D, Scarselli M, et al. Structure of the C-terminal domain of neisseria heparin binding antigen (Nhba), one of the main antigens of a novel vaccine against neisseria meningitidis. *J Biol Chem*. (2011) 286:41767–75. doi: 10.1074/jbc.M111.289314

28. Semchenko EA, Day CJ, Seib KL. The neisseria gonorrhoeae vaccine candidate nhba elicits antibodies that are bactericidal, opsonophagocytic and that reduce gonococcal adherence to epithelial cells. *Vaccines (Basel)*. (2020) 8:219. doi: 10.3390/vaccines8020219

29. Song S, Wang S, Jiang X, Yang F, Gao S, Lin X, et al. Th1-polarized mtre-based gonococcal vaccines display prophylactic and therapeutic efficacy. *Emerg Microbes Infect*. (2023) 12:2249124. doi: 10.1080/22221751.2023.2249124

30. Almonacid-Mendoza HL, Humbert MV, Dijokaite A, Cleary DW, Soo Y, Hung MC, et al. Structure of the recombinant neisseria gonorrhoeae adhesin complex protein (Rng-acp) and generation of murine antibodies with bactericidal activity against gonococci. *mSphere*. (2018) 3:e00331-18. doi: 10.1128/mSphere.00331-18

31. Ram S, Sharma AK, Simpson SD, Gulati S, McQuillen DP, Pangburn MK, et al. A novel sialic acid binding site on factor H mediates serum resistance of sialylated neisseria gonorrhoeae. *J Exp Med*. (1998) 187:743–52. doi: 10.1084/jem.187.5.743

32. Hartwell BL, Melo MB, Xiao P, Lemnios AA, Li N, Chang JYH, et al. Intranasal vaccination with lipid-conjugated immunogens promotes antigen transmucosal uptake to drive mucosal and systemic immunity. *Sci Transl Med*. (2022) 14:eabn1413. doi: 10.1126/scitranslmed.abn1413

33. Semchenko EA, Jen FE, Jennings MP, Seib KL. Assessment of serum bactericidal and opsonophagocytic activity of antibodies to gonococcal vaccine targets. *Methods Mol Biol*. (2022) 2414:363–72. doi: 10.1007/978-1-0716-1900-1_19

34. Tramont EC. Adhesion of neisseria gonorrhoeae and disease. *Ciba Found Symp*. (1981) 80:188–201. doi: 10.1002/9780470720639.ch12

35. Lin EY, Adamson PC, Klausner JD. Epidemiology, treatments, and vaccine development for antimicrobial-resistant neisseria gonorrhoeae: current strategies and future directions. *Drugs*. (2021) 81:1153–69. doi: 10.1007/s40265-021-01530-0

36. Baarda BI, Zielke RA, Holm AK, Sikora AE. Comprehensive bioinformatic assessments of the variability of neisseria gonorrhoeae vaccine candidates. *mSphere*. (2021) 6:e00977-20. doi: 10.1128/mSphere.00977-20

37. Edwards JL, Jennings MP, Seib KL. Neisseria gonorrhoeae vaccine development: hope on the horizon? *Curr Opin Infect Dis*. (2018) 31:246–50. doi: 10.1097/QCO.0000000000000450

38. Cui Y, Miao C, Chen W, Shang W, Qi Q, Zhou W, et al. Construction and protective efficacy of a novel streptococcus pneumoniae fusion protein vaccine nanat1-tuft1-plyd4. *Front Immunol*. (2022) 13:1043293. doi: 10.3389/fimmu.2022.1043293

39. Song SJ, Shin GI, Noh J, Lee J, Kim DH, Ryu G, et al. Plant-based, adjuvant-free, potent multivalent vaccines for avian influenza virus via lactococcus surface display. *J Integr Plant Biol*. (2021) 63:1505–20. doi: 10.1111/jipb.13141

40. Porebska N, Ciura K, Chorazewska A, Zakrzewska M, Otlewski J, Opalinski L. Multivalent protein-drug conjugates - an emerging strategy for the upgraded precision and efficiency of drug delivery to cancer cells. *Biotechnol Adv*. (2023) 67:108213. doi: 10.1016/j.bioteChadv.2023.108213

41. Sartorio MG, Pardue EJ, Feldman MF, Haurat MF. Bacterial outer membrane vesicles: from discovery to applications. *Annu Rev Microbiol*. (2021) 75:609–30. doi: 10.1146/annurev-micro-052821-031444

42. Micoli F, MacLennan CA. Outer membrane vesicle vaccines. *Semin Immunol*. (2020) 50:101433. doi: 10.1016/j.smim.2020.101433

43. Kelly C, Arnold R, Galloway Y, O'Hallahan J. A prospective study of the effectiveness of the New Zealand meningococcal B vaccine. *Am J Epidemiol*. (2007) 166:817–23. doi: 10.1093/aje/kwm147

44. Castilla J, Garcia Cenoz M, Abad R, Sanchez-Cambronero L, Lorusso N, Izquierdo C, et al. Effectiveness of a meningococcal group B vaccine (4cmenb) in children. *N Engl J Med*. (2023) 388:427–38. doi: 10.1056/NEJMoa2206433

45. Wang B, Giles L, Andraweera P, McMillan M, Almond S, Beazley R, et al. 4cmenb Sustained Vaccine Effectiveness against Invasive Meningococcal B Disease and Gonorrhoea at Three Years Post Programme Implementation. *J Infect*. (2023) 87:95–102. doi: 10.1016/j.jinf.2023.05.021

46. Leduc I, Connolly KL, Begum A, Underwood K, Darnell S, Shafer WM, et al. The serogroup B meningococcal outer membrane vesicle-based vaccine 4cmenb induces cross-species protection against neisseria gonorrhoeae. *PloS Pathog*. (2020) 16: e1008602. doi: 10.1371/journal.ppat.1008602

47. Menon V, Kapulu MC, Taylor I, Jewell K, Li Y, Hill F, et al. Assessment of antibodies induced by multivalent transmission-blocking malaria vaccines. *Front Immunol*. (2017) 8:1998. doi: 10.3389/fimmu.2017.01998

48. Rice PA, Vayo HE, Tam MR, Blake MS. Immunoglobulin G antibodies directed against protein iii block killing of serum-resistant neisseria gonorrhoeae by immune serum. *J Exp Med*. (1986) 164:1735–48. doi: 10.1084/jem.164.5.1735

49. de la Paz H, Cooke SJ, Heckels JE. Effect of sialylation of lipopolysaccharide of neisseria gonorrhoeae on recognition and complement-mediated killing by monoclonal antibodies directed against different outer-membrane antigens. *Microbiol (Reading)*. (1995) 141:913–20. doi: 10.1099/13500872-141-4-913

50. Wetzler LM, Barry K, Blake MS, Gotschlich EC. Gonococcal lipooligosaccharide sialylation prevents complement-dependent killing by immune sera. *Infect Immun*. (1992) 60:39–43. doi: 10.1128/iai.60.1.39-43.1992

51. Ram S, Shaughnessy J, de Oliveira RB, Lewis LA, Gulati S, Rice PA. Gonococcal lipooligosaccharide sialylation: virulence factor and target for novel immunotherapeutics. *Pathog Dis*. (2017) 75:ftx049. doi: 10.1093/femspd/ftx049

52. Markham RB, Nicholson-Weller A, Schiffman G, Kasper DL. The presence of sialic acid on two related bacterial polysaccharides determines the site of the primary immune response and the effect of complement depletion on the response in mice. *J Immunol*. (1982) 128:2731–3. doi: 10.4049/jimmunol.128.6.2731

53. Okada N, Yasuda T, Okada H. Restriction of alternative complement pathway activation by sialosylglycolipids. *Nature*. (1982) 299:261–3. doi: 10.1038/299261a0

54. Devyatyarova-Johnson M, Rees IH, Robertson BD, Turner MW, Klein NJ, Jack DL. The lipopolysaccharide structures of salmonella enterica serovar typhimurium and neisseria gonorrhoeae determine the attachment of human mannose-binding lectin to intact organisms. *Infect Immun*. (2000) 68:3894–9. doi: 10.1128/IAI.68.7.3894-3899.2000

55. Gulati S, Sastry K, Jensenius JC, Rice PA, Ram S. Regulation of the mannan-binding lectin pathway of complement on neisseria gonorrhoeae by C1-inhibitor and alpha 2-macroglobulin. *J Immunol*. (2002) 168:4078–86. doi: 10.4049/jimmunol.168.8.4078

56. Freter R. Mechanisms of association of bacteria with mucosal surfaces. *Ciba Found Symp*. (1981) 80:36–55. doi: 10.1002/9780470720639.ch4

57. Microbial adhesion, colonisation, and virulence. *Lancet*. (1981) 2:508–9.

58. Krachler AM, Orth K. Targeting the bacteria-host interface: strategies in anti-adhesion therapy. *Virulence*. (2013) 4:284–94. doi: 10.4161/viru.24606

59. Belcher T, Rollier CS, Dold C, Ross JDC, MacLennan CA. Immune responses to neisseria gonorrhoeae and implications for vaccine development. *Front Immunol*. (2023) 14:1248613. doi: 10.3389/fimmu.2023.1248613

60. Sun P, Li X, Pan C, Liu Z, Wu J, Wang H, et al. A short peptide of autotransporter ata is a promising protective antigen for vaccination against acinetobacter baumannii. *Front Immunol*. (2022) 13:884555. doi: 10.3389/fimmu.2022.884555

61. Holmgren J, Adamsson J, Anjuere F, Clemens J, Czerkinsky C, Eriksson K, et al. Mucosal adjuvants and anti-infection and anti-immunopathology vaccines based on cholera toxin, cholera toxin B subunit and cpg DNA. *Immunol Lett*. (2005) 97:181–8. doi: 10.1016/j.imlet.2004.11.009

62. Feinen B, Jerse AE, Gaffen SL, Russell MW. Critical role of th17 responses in a murine model of neisseria gonorrhoeae genital infection. *Mucosal Immunol*. (2010) 3:312–21. doi: 10.1038/mi.2009.139

63. Liu Y, Russell MW. Diversion of the immune response to neisseria gonorrhoeae from th17 to th1/th2 by treatment with anti-transforming growth factor beta antibody generates immunological memory and protective immunity. *mBio*. (2011) 2:e00095–11. doi: 10.1128/mBio.00095-11

64. Michaelsen TE, Kolberg J, Aase A, Herstad TK, Hoiby EA. The four mouse igg isotypes differ extensively in bactericidal and opsonophagocytic activity when reacting with the P1.16 epitope on the outer membrane pora protein of neisseria meningitidis. *Scand J Immunol*. (2004) 59:34–9. doi: 10.1111/j.0300-9475.2004.01362.x

frontiers | Frontiers in Immunology

TYPE Original Research
PUBLISHED 11 December 2024
DOI 10.3389/fimmu.2024.1450600

OPEN ACCESS

EDITED BY
Jiae Kim,
Henry M Jackson Foundation for the Advancement of Military Medicine (HJF), United States

REVIEWED BY
Ho Seong Seo,
Korea Atomic Energy Research Institute (KAERI), Republic of Korea
Daniela Eletto,
University of Salerno, Italy

*CORRESPONDENCE
Rosanna Capparelli
capparel@unina.it

†These authors have contributed equally to this work and share first authorship

RECEIVED 17 June 2024
ACCEPTED 22 November 2024
PUBLISHED 11 December 2024

CITATION
Cuomo P, Medaglia C, Casillo A, Gentile A, Fruggiero C, Corsaro MM and Capparelli R (2024) Phage-resistance alters Lipid A reactogenicity: a new strategy for LPS-based conjugate vaccines against *Salmonella* Rissen. *Front. Immunol.* 15:1450600. doi: 10.3389/fimmu.2024.1450600

Phage-resistance alters Lipid A reactogenicity: a new strategy for LPS-based conjugate vaccines against *Salmonella* Rissen

Paola Cuomo[1,2†], Chiara Medaglia[3†], Angela Casillo[4], Antonio Gentile[1,2], Carmine Fruggiero[1], Maria Michela Corsaro[4] and Rosanna Capparelli[1,2*]

[1]Department of Agricultural Sciences, University of Naples Federico II, Portici, Italy, [2]Task Force on Microbiome Studies, University of Naples Federico II, Naples, Italy, [3]Functional Genomics Research Center, Fondazione Human Technopole, Milan, Italy, [4]Department of Chemical Sciences, University of Naples Federico II, Naples, Italy

Salmonella enterica serovar Rissen (*S.* Rissen) is an emerging causative agent of foodborne diseases. The current emergence of antibiotic resistance makes necessary alternative therapeutic strategies. In this study, we investigated the potential of a phage-resistant strain of *S.* Rissen (R^R) as a tool for developing an effective lipopolysaccharide (LPS)-based vaccine. The LPS O-antigen is known to play critical roles in protective immunity against *Salmonella*. However, the high toxicity of the LPS lipid A moiety limits its use in vaccines. Here, we demonstrated that the acquisition of bacteriophage resistance by *S.* Rissen leads to structural modifications in the LPS structure. Using NMR and mass spectrometry, we characterized the LPS from phage-resistant strains as a smooth variant bearing under-acylated Lipid A portions (penta- and tetra-acylated forms). We then combined RT-qPCR and NMR-based metabolomics to explore the effects of phage resistance and LPS modification on bacterial fitness and virulence. Finally, we conducted *in vivo* studies to determine whether lysogeny-induced remodeling of LPS affects the host immune response. Results revealed that the under-acylated variant of LPS from R^R attenuates the inflammatory response in BALB/c mice, while eliciting a specific antibody response that protects against *S.* Rissen (R^W) infection. In conclusion, our findings suggest that phage resistance, through lipid A modification, may offer a novel strategy for reducing LPS toxicity, highlighting its potential as a promising biological approach for developing LPS-based vaccines against *Salmonella* infections.

KEYWORDS

bacteriophages, host immune response, lipid A, salmonella infection, vaccine

Introduction

Salmonellosis is a major enteric infection causing a high rate of mortality worldwide every year (1, 2). The limited treatment options due to antimicrobial resistance and the absence of an effective prophylactic therapy, have contributed to increase the annual morbidity and mortality, positioning salmonellosis as a serious public health concern (3). In the last few years, *S.* Rissen has emerged as a notable serovar causing salmonellosis in various regions of the world (4), making the development of a successful vaccine a pressing challenge.

To date, only three categories of vaccine are licensed for protection against *Salmonella* infection, and specifically *S.* typhi (5). These are the live attenuated vaccine Ty21a, a subunit vaccine based on the Vi capsular polysaccharide (Vi CPS) and the Vi typhoid conjugate vaccine (TCV) (6). Despite their different approaches, both Ty21a and unconjugated Vi CPS vaccines have severe limitations. Neither Ty21a nor unconjugated Vi CPS provide protection for young children, and they offer limited efficacy in adults (7). Additionally, Ty21a contains a mixture of antigens which makes difficult to determine which specific antigen confers protection or increases the risk of adverse effects (8). These difficulties have been successfully overcome by TCV, which promises long-lasting immunity and protection in infants while maintaining a favorable safety profile (9). However, TCV also has a limitation as it confers protection only against a selected subset of *Salmonella* species expressing the Vi capsular polysaccharide. Consequently, the growing interest in developing *Salmonella* vaccines has led to the exploration of alternative vaccine strategies. Most of these strategies, including the Generalized Modules for Membrane Antigens (GMMA), focus on targeting the O-antigen of the lipopolysaccharide (LPS) (10, 11).

LPS, also known as endotoxin, is a glycolipid located in the outer membrane of Gram-negative bacteria (12). It consists of a conserved Lipid A, a core oligosaccharide and a variable O-polysaccharide (OPS) (13). For many years, the polysaccharide component of LPS was thought to lack antigenicity. This assumption was definitively disproved by André Boivin, who demonstrated that isolated polysaccharide moieties can act as haptens, retaining antigenic properties without stimulating antibody production (14). Boivin also showed that smooth bacteria, which possess a "complete antigen", composed of a complete OPS and Lipid A, stimulate robust immune responses by activating the Toll-like receptor 4 (TLR4) and producing polysaccharide-specific antibodies that neutralize pathogenic bacteria (15). As a result, smooth LPS (sLPS) is a virulence factor and a valid target for vaccine development, compared to rough LPS (rLPS) - which lack OPS or contain only a single subunit (16).

sLPS has been proven to be particularly effective in preventing infections caused by various *Enterobacteriaceae*, such as *Klebsiella pneumoniae*, *Shigella flexneri* and *Salmonella* (17–19). However, due to the diversity of O-antigens among Enterobacteria, sLPS is expected to induce an immune response with restricted specificity. Interestingly, the high similarity of surface molecules among *Salmonella* strains makes sLPS an attractive candidate for broader-spectrum vaccines capable of cross-reactive immunity and protection against closely related *Salmonella* serotypes sharing analogous O-antigen profiles (20). Despite this, the high toxicity of sLPS, due to Lipid A component, makes it challenging to develop safe vaccines.

To address this concern and develop safe and immunogenic vaccines, several approaches have been attempted. Among these, genetic manipulation for silencing genes encoding acyl transferases, such as *msbB*, *htrB* and *pagP*, has been the most successful (21, 22). This results in mutant strains that - compared to the parent strain - synthetize LPS molecules with different lengths or numbers of fatty acyl chains in Lipid A, leading to attenuation of the LPS signaling pathway and reduced LPS toxicity (23, 24).

In a previous study, we demonstrated that LPS from the bacteriophage-resistant strain of *S.* Rissen (R^R) induces a reduced inflammatory response *in vitro* compared to the LPS produced by the bacteriophage-sensitive strain of *S.* Rissen (R^W) (25, 26), and attributed this result to Lipid A modification.

The goal of the present study was to validate our hypothesis, proposing bacteriophage-resistance as an alternative strategy to traditional chemical, enzymatic, or genetic manipulations, to obtain under-acylated variants of Lipid A, useful for producing LPS-based vaccines.

Lysogenic phages play an influential role in shaping various aspects of bacterial lifestyle, significantly contributing to both micro- and macro-diversity observed within bacterial species (27). Of note, prophage Φ1 has been found to introduce variability between R^R and R^W strains. Unlike R^W, the R^R strain demonstrated a propensity to spontaneously lose the phage Φ1 without generating phage particle. Yet, the acquisition of phage-resistance has been found to supply the R^R strain with additional virulence factors (26). To realize the above transformations, the phage Φ1 provides the host new genetic material which confers several advantages (25).

Morons are prophage genes encoding proteins that enhance bacterial fitness through different mechanisms (28). They can increase bacterial virulence, promote resistance to environmental stressors, and contribute to phage resistance via Superinfection exclusion (Sie) proteins (25, 28). These proteins prevent further infections by the same or closely related phages, inhibiting phage genome entry into bacterial cell (29).

Salmonella phages use LPS to enter host cells and establish a successful infection. Therefore, as part of the Sie mechanism, *Salmonella* may acquire prophage genes that modify the LPS structure (30).

Based on these considerations, we tested the potential of R^R to reduce the LPS reactogenicity through Lipid A modification, proposing it as an alternative approach for developing LPS-based vaccines against *Salmonella* infections. We found that the acquisition of the phage-resistant phenotype induces metabolic and physiological changes in R^R, which alter the host-pathogen interaction by remodeling the LPS acylation pattern. Furthermore, we demonstrated that Lipid A modification in R^R-LPS impairs the TLR4 signaling, weakening the innate immune response while mediating early protection in BALB/C mice infected with *S.* Rissen.

In conclusion, our findings offer a promising strategy for developing effective LPS-based vaccine to prevent *Salmonella* infection and may pave the way for the development of broad-spectrum vaccines against other Gram-negative bacteria.

Materials and methods

Ethics statement

All mouse experiments were carried out in accordance with the guidelines for the Care and Use of Laboratory Animals of the European Community (Legislative Decree n. 116/92). The Animal Use Protocol (AUP, Number: 86/609/CEE) was approved by the Committee on the Ethics of Animal Experiments of the University of Naples and authorized from the Italian Ministry of Health.

Salmonella Rissen strains and culture conditions

The bacteriophage-sensitive *S. enterica ssp. enterica* serovar Rissen (R^W) was isolated from food products and characterized by Istituto Zooprofilattico Sperimentale del Mezzogiorno (Portici, Naples, Italy), using standard conventional methods (31). The bacteriophage-resistant *S.* Rissen (R^R), instead, was obtained from the R^W strain following selection for resistance to phage Φ1, as described by Papaianni et al. (25). Both R^R and R^W strains were grown in Luria-Bertani (LB) medium (ThermoFisher Scientific, Waltham, Massachusetts, USA) at 37°C, with shaking at 200 rpm.

Phage Φ1 isolation

As previously reported by Papaianni et al. (25), bacteriophage Φ1 was isolated from the R^W strain upon induction with mitomycin C. Briefly, the overnight culture of the R^W strain was inoculated in 5 mL of fresh LB medium (2 x 10^8 CFU/5 mL) containing 1 µg/mL mitomycin C (Merck, Darmstadt, Germany) and incubated for 1 hour at 37°C with shaking. After incubation, the induced culture was centrifugated at 5,700 x g for 10 minutes. The supernatant was collected and stored at +4°C, while pellet was resuspended in 5 mL of fresh LB medium and incubated for further 4 hours at 37°C with shaking. After 4 hours, lysate was centrifugated again and the supernatant collected. Supernatants from both the centrifugations were pooled and filtered by 0.22 µm filters (Millipore, Darmstadt, Germany) (25).

The enumeration of phage particles, expressed as plaques forming colony (PFU/mL), was determined by performing the Double Agar Layer (DAL) method (32). Plaques were re-isolated, propagated and stored in SM buffer (NaCl 100 mM, Tris-HCl 50 mM, $MgSO_4$ 8 mM; pH 7.5) at + 4°C, or in liquid nitrogen with DMSO 5% (v/v) to avoid loss of phage titer (33).

Bacteriophage-resistant and sensitive *Salmonella* Rissen genome comparison

Genotyping differences between bacteriophage-resistant and sensitive *S.* Rissen strains were explored using circular genome visualization methods. Protein Basic Local Alignment Search Tool (BLASTp) was used to match the sequence similarities between the SieB protein of *Salmonella* Typhimurium phage 22 (GenBank: AF217253, Protein ID: AAF75022) and the Superinfection exclusion protein of *S.* Rissen phage 29485 (Φ1, GenBank: KY709687, Protein ID: ARB10858). Genome visualization of *SieB* gene in both *S.* Rissen strains was performed using BLAST Ring Image Generator (BRIG) software (34) (v0.95). Both R^R and R^W complete genome sequence were reported by Papaianni et al. (25). *S.* Rissen phage 29485 was selected as reference genome. The raw sequence data are available via the European Nucleotide Archive (ENA; http://www.ebi.ac.uk/ena) and are accessible through the accession number PRJEB69481. The genome assembly and annotation of the RR strain can be accessed via European Nucleotide Archive under the following accession number GCA_963679805.

Cell culture

The human gastric adenocarcinoma cell line AGS was kindly provided by Prof. Alessandra Tosco from the University of Salerno (Fisciano, SA, Italy). Cells were grown in Dulbecco's Modified Eagle Medium (DMEM) high glucose (Microtech), supplemented with 10% fetal bovine serum (FBS; Microtech), 1% penicillin/streptomycin (Microtech) and 1% L-glutamine (Microtech) and maintained at 37°C, in a humidified atmosphere of 5% CO_2. The cell line was authenticated through the short tandem repeat (STR) analysis and periodically tested for mycoplasma contamination.

Superinfection exclusion gene transcriptional changes

To better investigate genome differences between the bacteriophage-resistant and sensitive *Salmonella* Rissen strains, due to prophage gene integration, the presence of the *SieB* gene was analyzed by end-point PCR and electrophoretic run on an automated qiaxcel instrument (Qiagen, Hilden, Germany) as described by Capparelli et al. (26). In addition, transcriptional changes in *SieB* gene were examined by real-time quantitative PCR experiment (RT-qPCR), using StepOne (Applied Biosystem) Real-Time PCR system. As reported by Capparelli et al., AGS cells were infected with R^R or R^W strains for 2, 4 and 6 hours and *SieB* gene expression level was evaluated by qRT-PCR, following the protocol described by Capparelli et al. (26). The primers for detecting *SieB* gene were: reverse primer 5'-CAAACAA ATCCCGAACGACT-3'; forward primer 5'-ATGGTGGCAGGA GTTAATGC-3'.

LPSs isolation and chemical analyses

Dried cells of R^R and R^W *S.* Rissen strains were extracted by PCP (phenol:chloroform:petroleum ether 2:5:8) and by water/phenol method as already reported (35).

PolyAcrylamide Gel Electrophoresis (PAGE) was performed using the system of Laemmli (36) with sodium deoxycholate (DOC) as detergent. Purified LPS from *S.* Rissen R^R and R^W and

the LPS from *Escherichia coli* O111:B4 were prepared at the concentration of 1 mg/mL, and denaturated with sample buffer (2% DOC and 60 mM Tris/HCl pH 6.8, 25% glycerol, 14.4 mM 2-mercaptoethanol, and 0.1% bromophenol blue). Then, 8 µL of each sample was loaded on a 14% DOC gel with a 5% stacking gel and separated using a mini-PROTEAN electrophoresis instrument (Bio-Rad Laboratories). The electrophoresis was conducted at a constant amperage of 30 mA. The gel was fixed in an aqueous solution of 40% ethanol and 5% acetic acid, and finally visualized after silver nitrate staining (37). Precision Plus Protein Dual Color Standards (4 µL, MW size range 10–250 kDa) were used for molecular weight estimation. Glycosyl and fatty acids composition were obtained after derivatization as acetylated methyl glycosides (AMGs) and fatty acid methyl esters (FAMEs), as already described (38).

The linkage positions of the monosaccharides were determined by GC-MS analysis of the partially methylated alditol acetates (PMAAs). Samples (1 mg) were methylated with CH_3I (100 µL) and NaOH powder in DMSO (300 µL) for 20 h (39). The products were totally hydrolyzed with 2 M TFA at 120°C for 2 h, reduced with $NaBD_4$, and acetylated with Ac_2O and pyridine (50 µL each, 100°C for 30 min).

All the derivatives were analyzed on Agilent Technologies gas chromatograph 7820A equipped with a mass selective detector 5977B and an HP-5 capillary column (Agilent, 30 m × 0.25 mm i.d.; flow rate, 1 mL/min). AMGs and FAMEs analyses were performed using different temperature programs. In detail, the AMGs analysis started at 140°C for 3 min, followed by an increase from 140°C to 240°C at 3°C/min; while the FAMEs analysis started at 140°C for 3 min, followed by an increase from 140°C to 280°C at 10°C/min. PMAA analysis was performed using a temperature program that began at 90°C for 1 minute, then increased from 90°C to 140°C at 25°C/min, 140°C to 200°C at 5°C/min, and 200°C to 280°C at 10°C/min, with a final hold at 280°C for 10 minutes.

OPSs isolation, purification, and structural characterization

The supernatants obtained after mild acid hydrolysis of the entire LPSs (19.5 mg and 15 mg from R^R-LPS and R^W-LPS, respectively) were fractionated on a Biogel P-10 column (Biorad, 0.75 x 112 cm) eluted with water. The collected fractions were pooled, freeze-dried, and analyzed by ^1H NMR spectroscopy.

The molecular weight determination for OPSs was obtained through a calibration curve by using an Agilent 1100 HPLC system, with a TSK G-5000 PWXL size exclusion column (30 cm × 7.8 mm) equilibrated with NH_4HCO_3 50 mM as eluent (flow = 0.7 mL/min). The column was calibrated by injecting dextran standards (50 µL of a 1 mg/mL solution) of known molecular weight (12, 50, 150, and 670 kDa). The eluate was monitored with a refractive index detector (40).

Lipid A isolation and characterization

The Lipid A fraction was obtained from crude LPSs of both R^R and R^W *S.* Rissen by mild acid hydrolysis, as reported (38). After centrifugation at 3000 rpm for 15 min, the supernatants were removed and the pellet suspended in water and freeze-dried (3 mg and 4mg, for R^R and R^W respectively). MALDI TOF mass spectrometry was performed in the reflectron negative ions mode using a ABSCIEX TOF/TOF^{TM}5800 (AB SCIEX, Darmstadt, Germany) instrument, equipped with an Nd: YLF laser with a λ of 345 nm, and a delayed extraction technology. A solution of 2,4,6-trihydroxyacetophenone (THAP) in MeOH:H_2O (v/v 1:1, 10 mg/mL) was used as the matrix. After desalting on a Dowex 50WX8 (H^+ form) the samples with a concentration of 2 mg mL^{-1} were dissolved using $CHCl_3$:MeOH (v/v 2:1). The matrix solution (0.5 µL) and Lipid A solutions (0.5 µL) were spotted on a MALDI plate. Each spectrum was a result of 2000 laser shots. The spectra were calibrated by using an ABSciex calibration mixture, and processed under computer control by using the Data Explorer software (v0.2.0) (41). Fatty acids analyses were obtained as already described (38). In few words, 0.5 mg of each sample was treated with 1 mL of 1.25 M HCl/CH_3OH for 20 h at 80°C. The crude mixtures were extracted twice with hexane, and injected into GC-MS. The analyses were performed on Agilent Technologies gas chromatograph 7820A equipped with a mass selective detector 5977B and an HP-5 capillary column (Agilent, 30 m × 0.25 mm i.d.; flow rate, 1 mL/min). A temperature program starting at 140°C for 3 min and followed by an increase from 140°C to 280°C at 10°C/min was used for fatty acid analyses.

LPS purification for biological studies

LPS isolated from both R^R and R^W (38) were purified according to Stephens et al. (42). Briefly, LPSs were resuspended in endotoxin-free water containing triethylamine (TEA; 0.2%), deoxycholate (0.5%) and water-saturated phenol (500 µL). The obtained solution was vortexed for 5 minutes, incubated on ice for 5 minutes and then centrifugated (10,000 g for 2 minutes at 4°C). The upper phase (aqueous) was transferred into a fresh tube, supplemented with 75% ethanol and 30 mM sodium acetate, precipitated for 1 hour at -20°C and lastly resuspended in TEA.

LPS conjugation for mice immunization

The R^R and R^W-LPS were coupled to Rat Serum Albumin (RSA; purchased from Sigma Aldrich) using 1-ethyl-3-(3-dimethylaminopropyl) carbodiimide (EDC), following the protocol described by Masoud, 2007 (43). Briefly, purified LPSs (10 mg) were dissolved in sterile distilled water (1 mL), and the solution was mixed with 500 µL RSA (10 mg/ml), in the presence of EDC (40 mg). The mixture was stirred on an automatic shaker at room temperature for 3 h. After mixing, the pH was adjusted to 7 and the mixture was centrifuged (1000 rpm for 10 minutes). The supernatants were purified by using a Sephadex G-75 column and eluted with phosphate buffered saline (PBS). Eluates containing both LPS and protein were pooled and dialyzed against distilled water at 48°C, and finally lyophilized.

Bacterial growth culture preparation for metabolomics analysis

R^W and R^R strains were obtained as indicated above (see the *S.* Rissen strains and culture conditions paragraph). $R^W\Phi1$- and $R^S\Phi1$- strains were derived from the R^W and R^R strains as described by Papaianni et al. (25). All strains were grown in LB medium and centrifugated when bacteria reached the exponential growth phase and the same cell density. After centrifugation, the pellet was discarded, and the supernatant filtered by 0.22 µm filters (Millipore, Darmstadt, Germany). Sterile supernatants were quenched in liquid nitrogen for 10 minutes - in order to stop metabolic activities in the filtrates - and stored at -80°C, until NMR analysis. Ten biological replicates of growth culture of each strain were prepared. Uninoculated growth medium was used as negative control.

NMR sample preparation

To achieve the NMR-based footprinting metabolomics analysis, growth media from R^R, R^W, $R^S\Phi1$- and $R^W\Phi1$- were rapidly defrosted and 630 µL of each fluid sample were pipetted into eppendorfs containing 70 µL of D_2O, containing sodium 3-(trimethylsilyl)-2,2,3,3-tetradeuteropropionate (TSP) 0.1 mM (for chemical shift reference), and sodium azide 3 mM as antimicrobial agent, reaching 700 µL of total volume.

NMR spectra acquisition

NMR spectra were acquired as described by Papaianni et al. (44). In detail, all NMR experiments were performed on a Bruker Avance III-600 MHz spectrometer (Bruker BioSpin GmbH, Rheinstetten, Germany), equipped with a refrigerated autosampler and a TCI CryoProbe™ fitted with a gradient along the Z-axis, at a probe temperature of 300K (27°C). All spectra were recorded in H_2O 90%:D_2O 10% with 0.1 mM of TSP. ^{1}H-NMR spectra were acquired with water suppression using excitation sculpting with gradience sequence (45). Spectra were acquired for 32 scans, with an acquisition time of 5.2 s, a relaxation delay of 2 s, a pulse width of 8.000 µs, receiver gain of 101, dwell time of 61 µs, 4 dummy scans and a spectral width of 13.0180 ppm. Two-dimensional homonuclear (^{1}H-^{1}H; TOCSY) spectra were acquired with water suppression using excitation sculpting with gradients, DIPSI-2 sequence (46). Mixing time of 100 ms was applied for TOCSY experiments. TOCSY experiments were acquired with 256 FIDs of 2048 complex points with 80 scans, a relaxation delay of 1 s, a pulse width of 8.000 µs, receiver gain of 101, dwell time of 64 µs, 32 dummy scans and a spectral width of 13.6582 ppm. All data were zero-filled to 4,096 points in both dimensions, and prior to Fourier transformation, a Lorentz- to-Gauss window with different parameters was applied for both t_1 and t_2 dimensions for all the experiments. The resonances of both 1D and homonuclear 2D spectra were referenced to internal sodium 3-(trimethylsilyl)-2,2,3,3-tetradeuteropropionate (0.1 mM; TSP) which was assumed to resonate at δ_H = 0.00 ppm. Two-dimensional heteronuclear (^{1}H-^{13}C; HSQC) spectra were recorded on the spectrometer operating at 150.90 MHz for ^{13}C, using pre-saturation for water suppression (47, 48). HSQC resonances spectra were referenced to the lactate doublet (βCH_3), assumed to resonate at 1.33 ppm for ^{1}H and 20.76 ppm for ^{13}C.

^{1}H NMR spectra of the O-chains were recorded by using a Bruker 600 MHz spectrometer equipped with a cryo-probe, at 298K. The samples (3 mg) were dissolved in 550 µL of D_2O and the spectra were calibrated with external acetone (δ_H = 2.225 ppm; δ_C = 31.45 ppm). Spectra were acquired for 32 scans, with an acquisition time of 4.58 s, dwell time of 70 µs, and spectral width of 11.90 ppm.

NMR data analysis

To obtain bacteria growth culture datasets, a spectral area ranging from 9.50 to 0.50 ppm was selected. Prior the data analysis, each proton spectrum was manually phased, and the baseline corrected using Buker Tospin software (v.3.6.3). Successively, they were automatically segmented into integrated regions (buckets) of 0.02 ppm, using the AMIX 3.6 package (Bruker Biospin, Germany). The residual water resonance region (5.00-4.58 ppm) was excluded, and the binned regions were normalized to the total spectrum area. Multivariate statistical data analysis was applied to each dataset, to differentiate culture medium profiles of bacteriophage-sensitive or resistant *S.* Rissen, before and after lysogenic Φ1 excision (R^W or R^R and $R^W\Phi1$- or $R^S\Phi1$-, respectively), through NMR spectra, according to their different metabolic content. Therefore, each integrated dataset – containing information on metabolite concentration - was exported to excel and the derived data matrix imported into SIMCA-P17 package (Umetrics, Umea, Sweden) where unsupervised Principal Component Analysis (PCA), supervised Partial Least Squares Discriminant Analysis (PLS-DA) and Orthogonal Partial Least Squares Discriminant Analysis (OPLS-DA) analyses were performed. PCA was first applied to check outliers and uncover initial trends within the dataset by investigating the systematic variation in the data matrix, in order to identify trends and clusters. Once assessed data homogeneity, PLS-DA or OPLS-DA discriminant analysis was employed to improve group discrimination. The performance of each elaborated model was evaluated via the parameters R2 and Q2 (PCA: R2 = 0.879, Q2 = 0.769; OPLS-DA: R2 = 0.99, Q2 = 0.873), indicating the goodness of fit and the goodness of prediction, respectively. NMR variables with $|pcorr| \geq 0.7$, VIP >1 (Variable Importance in the Projection) were then considered for metabolite identification and univariate statistical analysis. Metabolites were identified through the chemical shift, according to both the literature (49) and metabolomics databases, such as the Human Metabolome Database (HMDB). Statistical significance was determined by one-way analysis of variance (ANOVA) followed by Bonferroni *post hoc* correction. p values < 0.05 were considered statistically significant.

Hemolytic activity

The susceptibility of erythrocytes to R^R or R^W-LPS was evaluated by performing the hemolysis assay on fresh human blood. Erythrocytes were isolated from blood of healthy donors (n=9), in accordance with the principles of good clinical practices reported in the Declaration of Helsinki and under the approval of the Ethics Committee of Villa Betania Hospital. Here, blood samples were obtained from the arm's peripheral vein and collected in heparin tubes. An informed consent was obtained from all participants.

As reported by Greco et al. (50), whole blood was centrifuged at 1,500 x g for 5 minutes and the supernatant (plasma) discarded. Cell pellet, instead, was washed with PBS and gently shacked. These operations were repeated 5 times. Aliquots of 5 x 10^7/mL red blood cells were resuspended in PBS containing different concentrations of R^R or R^W-LPS (from 1 to 500 µg/mL), incubated at 37°C for 1 hour and centrifuged at 1,500 x g for 5 minutes. The supernatant was removed, and the released hemoglobin measured at 405 nm, using a plate reader. The percentage of hemolysis was calculated as the ratio of the untreated control.

Animal experiments

Animal experiments were carried out on female BALB/c mice aged 8 to 10 weeks - purchased from Charles River Laboratories (Wilmington, Massachusetts, USA) - at the animal facility of the University of Naples "Federico II". Animal were housed in static microisolator cages, in order to handle them aseptically, and fed with sterile food and beverage. Mice were randomly assigned to the treatment groups. The sample group allocation was not blinded to the investigators.

Six mice per group were infected intraperitoneally with 100 µL of sterile phosphate-buffered saline (PBS), containing grown doses (10^3, 10^5, 10^7 and 10^9 CFU/animal) of R^R or R^W strains. Control group, instead, received 100 µL of PBS only. Mice were observed for 21 days, in order to evaluate clinical manifestations and death. Lethal Dose-50 (LD_{50}) was calculated according to the Reed and Muench method (51).

LPS purified from both R^R and R^W strains was administrated intraperitoneally in a dose responsible for endotoxemia (20 mg/Kg body weight) (52) and mice (6 per group) were observed 2, 8 and 24 hours after the LPS injection, in order to evaluate body temperature and weight. As for viable bacteria, LPS was dissolved in PBS (100 µL per animal) and the control group was injected with PBS only. Mice that lost more than 20% of their starting body weight or decreased their starting body temperature more than 4°C were euthanized.

Cytokine measurement by ELISA assay

Blood samples were collected from mice via tail vein bleeding, after application of a local anesthetic. Blood was collected 2-4-6-8- and 24-hours following R^R or R^W-derived LPS administration and was immediately centrifugated at 3,000 g for 10 minutes at + 4°C. Blood samples collected from mice injected with sterile PBS were used as control. After centrifugation, serum was separated and frozen at - 80°C, until cytokine measurement was performed. The concentration of IL-6, IL-10, TNF-α, G-CSF and IFN-γ cytokines was determined by multiplex ELISA assay, using the Bio-Plex pro-mouse cytokine 23-plex assay (Bio-Rad), according to the manufacturer's recommendations. Briefly, samples were diluted 1:4 with sample diluent and assayed as previously described by Verrillo et al. (53). Data were collected using the Bio-Plex 200 System (Bio-Rad) and analyzed by Bio-Plex Manager™ software. In addition, the concentration of IFN-β, was determined by the single target ELISA assay, using the mouse IFN-β ELISA kit (Elabscience), according to the manufacturer's instructions. Samples were read using the 96-well plate reader (NeoBiotech). Cytokines were measured at different times and their concentration was determined based on the automatically calculated standard curve.

Immunization

Mice were divided into three groups, each group containing 6 mice. The first group was injected intraperitoneally with the R^R-entire LPS, while the second one with the R^W-entire LPS. Both the antigens were extracted, purified and conjugated with Rat Serum Albumin (RSA) as reported above ("LPS purification for biological studies" and "LPS conjugation for mice immunization"). For the immunization, they were dissolved in sterile PBS (pH=7.4) and administrated twice at two-weeks interval at the final concentration of 10 µg (100 µL). The third group (control group) was injected with sterile PBS only (100 µL). On day 21, a secondary booster was administrated. Blood samples from the tail vein and feces were collected on day 4, 9, 14, 21 and 28 to determine the adaptive immune response and evaluate the cross-protective ability conferred by the R^R-LPS immunization, as described below.

Antibody response: IgG, IgA and IgM detection

To investigate the levels of adaptive immune response following animal immunization, the levels of IgG, IgM and IgA were detected. Serum was separated from whole blood by centrifugation (3,000 g, 10 minutes at + 4°C) and used to measure LPS-specific IgG and IgM, while feces were resuspended in protein extraction buffer (100 µL/10 mg), vortexed for 20 minutes and centrifugated 13,000 x g for 10 minutes. Supernatants were collected and used to detect LPS-specific IgA. First, the total antibody level for each Ig was detected using the mouse IgG Elisa kit (Abcam, Cambridge, United Kingdom), IgM ELISA kit (Abcam, Cambridge, United Kingdom) and IgA (Bethyl Laboratories, Montgomery, Texas, USA), according to the manufacturer's recommendations. Successively, the anti-LPS IgG, IgM or IgA titer was quantified using LPS coated microplates, according to the standard indirect ELISA protocol (54). Briefly, 96-well plate was coated with R^R or R^W purified LPS (5 µg/mL) in 100 µL/well coating buffer (Na_2CO_3 0.64 g and $NaHCO_3$ 3.7 $_g$) and incubated overnight at + 4°C. The next day, wells were

blocked with 200 µL/well of wash-buffer containing 2% bovine serum albumin (BSA) and the plate was incubated for 1h at 37°C. Sera or fecal supernatants were diluted 1:100 in blocking buffer (100 µL/well) and incubated at 37°C for 1 h. Following incubation, 100 µL of the HRP-conjugated goat anti-mouse IgG (1:2,000; Invitrogen), IgA (1:10,000; Abcam) or IgM (1:1,000; Invitrogen) were added to each well and incubated at 37°C for 30 min. Finally, the plate was filled with 100 µL/well of the indicator substrate (TMB; 1 mg/mL to each well) and incubated at room temperature for 10 min in the dark. After incubation the enzymatic reaction was stopped by adding 100 µL/well of stop solution (1M sulphuric acid) and 15-30 minutes later the optical density (OD) was recorded at 450 nm with an automatic ELISA reader (NeoBiotech). The assay was performed in triplicate and each incubation period was followed by multiple washings using PBS containing Tween 20 (0.05%). The standard curve was used to accurately determine the concentration of target LPS-immunoglobulins.

Evaluation of the R^R-LPS immunization efficacy

The efficacy of the R^R-LPS immunization was evaluated by using a mouse model of salmonellosis producing disseminated infection after intraperitoneal injection of the bacteriophage-sensitive *Salmonella* Rissen (*R*^{W}). In detail, mice immunized as detailed above (see the "Immunization" paragraph) were infected with the R^W strain (10^9 CFU/100 µL) two weeks after the last immunization via the intraperitoneal route and the bacterial burden in the spleens was determined. Therefore, mice were sacrificed 3 days post-infection and spleens were aseptically removed. Spleens (1 g) were homogenized in 1 mL of phosphate buffer saline (PBS) solution and serial dilutions were cultured on BHI agar for 24 hours, at 37°C. The next day, colony were counted, and results were expressed as colony forming unit (CFU) per gram of tissue (CFU/spleen).

Additionally, the protective efficacy of the R^R-LPS was also evaluated upon a single immunization. Mice (n=13 per group) were immunized intraperitoneally with pure conjugated LPS (10 µg dissolved in PBS 100 µL) isolated from the R^R or R^W strains or with vehicle (PBS 100 µL; control group). Two weeks post-immunization, each group was infected with the R^W strain (10^9 CFU/100 µL) via the intraperitoneal route and the bacterial burden in the spleens was determined 3 days post-infection.

Antibody bactericidal activity

To investigate the role of anti-R^R-LPS antibodies in imparting immune protection against *S.* Rissen infection, the bactericidal assay was performed. Mice were immunized as described above and four days after the last immunization, blood samples were collected, and serum separated by centrifugation. Polyclonal antibodies were purified by affinity chromatography, using protein A/G agarose beads as previously described (55, 56). 45 µL of antibody solution, antibody solution plus complement (BioMerieux, France), complement or LB broth (for control group) were mixed with 5 µL of viable R^W (final bacterial concentration 1 x 10^6 CFU/mL) in a 96-well plate and incubated at 37°C for 3 hours. After incubation, the absorbance at 600 nm was measured using a microplate reader. Data are reported as Log_{10} of CFU/mL.

Analysis of the cross-protective ability of anti-*R*^{R}-LPS antibodies

To evaluate whether the R^R-LPS immunization could confer cross-protection, serum samples from mice immunized with the R^R-LPS were tested for antibody reactivity against three different serovars of *Salmonella* (*S.* Choleraesuis, *S.* Infantis, *S.* Newport) by the agglutination test.

Mice were immunized as described above and four days following the last immunization, blood samples were collected, and the serum was separated by centrifugation (3,000 g, 10 minutes at + 4°C). Serum samples were used to measure IgG levels by the LPS-specific ELISA assay and animals giving the highest level of antibodies were selected for serum harvest. For the agglutination test, colonies of the selected *Salmonellae* were mixed with 100 µL of serum (undiluted or diluted 1:50 or 1:100 with sterile PBS) or with sterile PBS only (negative control). *S.* Rissen was used as positive control. The presence of cross-reaction was determined by observing the development of visible clumping of bacterial cells within 3 minutes.

Evaluation of the anti-R^R-LPS antibodies target determinant to *S.* Rissen LPS

To explore the target determinant of the anti-R^R-LPS antibodies to *S.* Rissen LPS, an Indirect ELISA assay was performed. We tested the antibody reactivity against both LPS and O-antigen from the R^R and R^W strains using serum samples from mice immunized with the R^R-LPS, as reported above. Briefly, a 96-well plate was coated with O-antigen (5 µg/mL) or LPS (5 µg/mL) in 100 µL/well coating buffer (Na_2CO_3 0.64 g and $NaHCO_3$ 3.7 g) for 16 h at 4°C. Sera were diluted 1:100 in 100 µL/well of wash-buffer containing 2% bovine serum albumin (BSA) and incubated at 37°C for 1 h. Following incubation, 100 µL of the HRP-conjugated goat anti-mouse IgG diluted 1:2,000 (Invitrogen) was added to each well and incubated at 37°C for 30 min. Finally, the plate was filled with 100 µL/well of the indicator substrate (TMB; 1 mg/mL to each well) and incubated at room temperature for 10 min in the dark. After incubation the enzymatic reaction was stopped by adding 100 µL/well of stop solution (1M sulphuric acid) and 15-30 minutes later the optical density (OD) was recorded at 450 nm with an automatic ELISA reader (NeoBiotech). The assay was performed in triplicate and each incubation period was followed by multiple washings using PBS containing Tween 20 (0.05%).

Statistical analysis

Statistical analysis was conducted using GraphPad Prism 9.0 software (San Diego, CA, USA). One-way ANOVA, followed by

10.3389/fimmu.2024.1450600

either Turkey or Bonferroni *post-hoc* correction, was utilized to compare two or more experimental groups. For simultaneous comparison of multiple groups with two or more factors, we used two-way ANOVA followed by Bonferroni *post-hoc* test. The Log-rank test was employed to compare Kaplan–Meier survival curves. A minimum of n = 6 mice per group was included, and no formal randomization procedure was implemented. The reported values represent the means ± SD of two or three biological replicates, as indicated in figure legends. A *p*-value of < 0.05 was considered statistically significant.

Results

Prophage genes promote the expression of a phage-resistance phenotype

The property of prophages to mediate phenotypic changes in bacterial host is widely known. Our previous studies demonstrated significant differences in virulence profiles between R^W and R^R (26). Importantly, R^R exhibited higher expression levels of prophage-related virulence genes (*sspH1, sodC1, gtgE, grvA*, and *gogB*) than R^W (26). In the present study, we also observed transcriptional changes in the *Superinfection exclusion* (*SieB*) gene, which affects the bacterial membrane integrity and inhibits phage infection (57). As expected, R^R expressed *SieB* at a level 300-fold higher than R^W (Figure 1), in a time-dependent manner.

To further investigate the genetic diversity between R^R and R^W, a genome comparison analysis, using the prophage Φ1 genome as a reference (*Salmonella* phage 29485, GenBank: KY709687), was performed. The circle plot revealed the insertion of the prophage derived *SieB* gene into the R^R genome (Supplementary Figure S1). The evidence that the gene under investigation was *SieB*, was provided by the Basic Local Alignment Search Toll (BLAST, https://blast.ncbi.nlm.nih.gov/Blast.cgi), showing robust sequence similarity between *Salmonella* phage 29485 superinfection exclusion protein (Protein Id: ARB10858) and *Salmonella* phage P22 SieB protein (Protein Id: AAF75022, Supplementary Figure S2).

In conclusion, these results suggest that R^R expresses the *SieB* gene, which confers immunity against secondary phage attack and contributes to the phage-resistance phenotype, likely through modifications of cell membrane elements, such as LPS (28). In addition, these results, along with previous reported results (26), prompted us to investigate whether the prophage-related virulence genes overexpressed by R^R confer advantages to the host response against *Salmonella*.

Phage-resistance alters the LPS structure by inducing the production of under-acylated Lipid A

To investigate whether phage-resistance alters the LPS structure and to assess the effects of these modifications on bacterial virulence and host immune responses, the chemical structure of the Lipid A and O-antigen portions was examined.

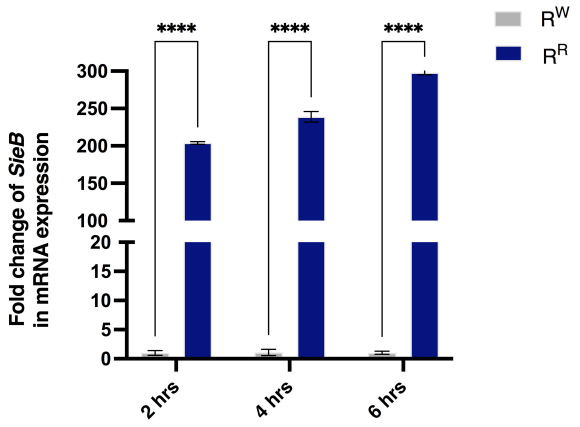

FIGURE 1
The R^R strain expresses the prophage *SieB* gene. Analysis of mRNA expression levels displayed increased levels of *SieB* gene in the R^R strain - following AGS cell line infection - compared to R^W strain. Results are reported as graph bars and represent mean ± SD of three biological replicates from two independent experiments. Two-way ANOVA followed by Turkey *post-hoc* correction was used to compare the *SieB* gene expression between R^R and/or R^W groups, according to different time points. ****$p < 0.0001$.

Dried cells from both R^R and R^W strains were extracted as previously described (35). Both R^R and R^W produced smooth LPS (Supplementary Figure S3A). Additionally, GC-MS chromatograms of the purified O-chain polysaccharides (OPSs) revealed no differences in the sugar content of the O-antigen between the R^R and R^W strains (Supplementary Figure S3B). Methylation analysis further indicated the presence of 2-substituted mannose units (2-Man), 2,3-disubstituted mannoses (2,3-Man), 3-substituted glucosamine (3-GlcN) and terminal non reducing glucose (t-Glc) in the O-chains of both strains (Supplementary Table S1). Finally, in line with chemical analyses, ^{1}H NMR spectra revealed an identical structure for the purified OPSs (Supplementary Figure S3C). In contrast, differences in the Lipid A portion were detected.

Pure Lipid A was analyzed through chemical techniques and mass spectrometry. GC-MS analysis of the fatty acid methyl esters (FAMEs) disclosed the presence of mainly C12:0, C14:0, C16:0, and C14:0(3-OH), in both the Lipid As. In addition, Lipid A from the R^W strain was found to contain C14:0(2-OH). The Lipid A samples were analyzed by negative ions MALDI- TOF in reflectron mode. The acquired spectrum of Lipid A from R^R revealed four clusters of signals corresponding to glycoforms with distinct acyl patterns (Figure 2). More in detail, the primary signal at m/z 1795.875 (calculated $[M\text{-}H]^-$ = 1796.229 Da) was assigned to the di-phosphorylated hexa-acylated glycoforms $HexN_2P_2$ $[C14:0(3\text{-}OH)]_4(C14:0)(C12:0)$. The spectrum also showed the presence of a signal at m/z 2034.034 corresponding to the di-phosphorylated hepta-acylated species (calculated $[M\text{-}H]^-$ =2034.462 Da), which differs from the hexa-acylated species for the additional presence of a C16:0 and, signals at m/z 1585.750 and 1359.630 corresponding to the di-phosphorylated penta- and tetra-acylated glycoforms, respectively. Finally, each cluster exhibited heterogeneity as proven by the occurrence of signals differing in 80 u, corresponding to the phosphate group, and in 14 u ($–CH_2–$ unit), which indicates Lipid A species differing in the length of their acyl chains.

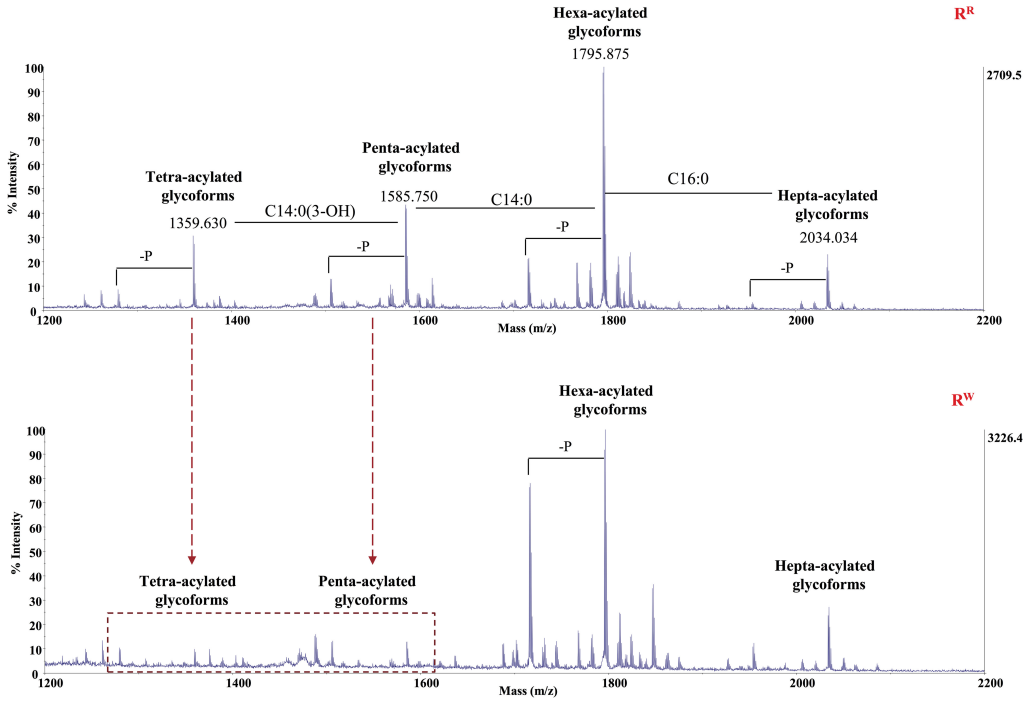

FIGURE 2
Reflectron negative MALDI-TOF MS spectra of *S.* Rissen R^R and R^W Lipid A.

In conclusion, these results suggest that R^R LPS contains highly variant Lipid A species, including di-phosphorylated hexa- and hepta-acylated species, along with under-acylated species (di-phosphorylated tetra- and penta-acylated variants). The same pattern was observed in the R^W LPS. Nevertheless, R^W LPS shows an extremely reduced presence of di-phosphorylated tetra- and penta-acylated species, compared to R^R LPS. It is well known that under-acylated variants of Lipid A compete with the hexa-acylated form for TLR4 activation, functioning as weak agonists of TLR4 signaling (58). Specifically, under-acylated Lipid A species destabilize the MD-2–TLR4 complex, leading to a reduced production of pro-inflammatory cytokines (59, 60). Based on these considerations, our findings suggest that R^R-LPS is a weak stimulator of the host innate immune response and elicits a mitigated inflammatory response.

Phage-resistance alters host metabolic profiles

In order to investigate the physiology of R^R and its capability to adapt to various host conditions and evade host innate immune attack, basic insights into bacterial metabolism are fundamental. Culture supernatants from R^R or R^W – before and after lysogenic Φ1 excision (R^R or R^W and R^SΦ1- or R^WΦ1, respectively) – were compared by untargeted NMR-based metabolomics analysis. NMR spectra of growth medium from the wild-type R^W strain and the selected R^R mutant displayed extensive differences. Conversely, growth medium from R^W and R^R, following phage excision (R^WΦ1- and R^SΦ1-, respectively) showed a considerable similarity in the NMR profiles (Supplementary Figure S4). NMR spectra were compared by performing multivariate analysis. The OPLS-DA scores plot revealed a clear separation of the R^R group (placed at negative coordinates of the first component t[1]) from R^W, R^WΦ1- and R^SΦ1- groups (placed at positive coordinates of the first component t[1], Figure 3A). This result might be attributable to metabolic alterations associated with phage-resistance. The second component t[2], instead, revealed a distinct separation of R^WΦ1- and R^SΦ1- groups (placed at positive coordinates) from the R^W group (placed at negative coordinates), likely due to phage-specific changes in the metabolism of the bacteriophage-sensitive strain (Figure 3A). Based on the first two principal components (t[1] and t[2]), R^WΦ1- and R^SΦ1- groups were found closely related each other, forming a single cluster in the hotteling's T2 plot (Figure 3A). A more evident separation between R^WΦ1- and R^SΦ1- groups was detected by the third component t[3], which positioned the R^WΦ1- group at t[3] positive coordinates and the R^SΦ1- group at t[3] negative coordinates (Figure 4A).

A total of 28 metabolites were identified as responsible for the above reported classes separation (Supplementary Table 2). In fact, significant differences in their concentration were detected. In detail, 14 amino acids and derivatives (arginine, lysine, isoleucine, proline, leucine, glutamate, methionine, aspartate, glycine, alanine, phenylalanine, tyrosine, N-acetyl-alanine and γ-aminobutyric acid), 1 sugar (glucose), the nucleic acid derivative hypoxanthine, the short chain fatty acid (SCFA) acetate, and 5 organic acid and derivatives (pyruvate hydrate, 5-aminopentanoic acid, lactate, succinate and formate) discriminated the R^W group from the R^R

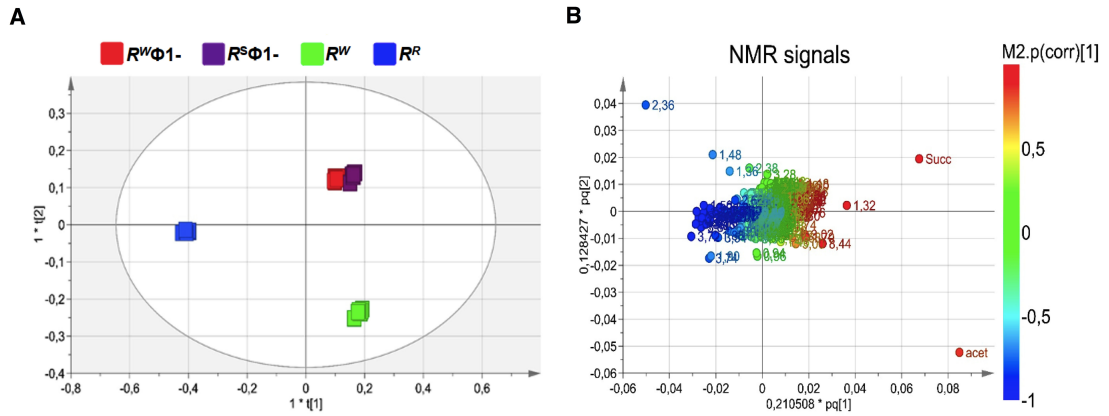

FIGURE 3
Orthogonal Projection to Latent Structure Discriminant Analysis (OPLS-DA) of bacteriophage-sensitive or resistant *S.* Rissen medium samples, before or after phage excision (R^W; R^R; $R^S\Phi1$-; $R^W\Phi1$-, respectively). **(A)** Scores plot showing a distinct separation of R^R group (blue squares) from R^W, $R^W\Phi1$- and $R^S\Phi1$- groups (green, red and purple squares, respectively) and of $R^W\Phi1$- and $R^S\Phi1$- groups (red and purple squares, respectively) from the R^W group (green squares). **(B)** Loading plot indicating NMR variables (chemical shift) of metabolites responsible for between-classes separation, characterized by |p(corr)| value > 0.7.

($p < 0.05$). Interestingly, $R^S\Phi1$- and $R^W\Phi1$- groups did not display significant differences ($p > 0.05$) in the concentration of succinate, lactate, 5-aminopentanoic acid, formate, arginine, lysine, proline and phenylalanine. This result suggests that the different concentration observed in the growth medium from R^W and R^R is ascribable to metabolic changes induced by the presence of the phage Φ1 and specifically to endogenous phage genome elements responsible for phage-resistance.

Similarly, phage infection altered the expression levels of 3 amino acids and derivatives (betaine, threonine and pyroglutamate), 1 sugar (myo-inositol) and other metabolites (nicotinate and imidazole). These metabolites were present in different concentrations ($p < 0.05$) in the growth medium from $R^W\Phi1$- compared to R^W. The same result was found in $R^S\Phi1$- compared to R^R. No significant differences ($p > 0.05$), instead, were detected between R^W and R^R groups or $R^S\Phi1$- and $R^W\Phi1$-, thus addressing the mentioned differences to phage metabolism. On the contrary, $R^S\Phi1$- and $R^W\Phi1$- groups were found to show significant differences ($p < 0.05$) in the concentration of the amino acid tyrosine, the alcohol ethanol and fatty acids, due to the different behavior of Φ1 when excised from the phage-resistant or sensitive strain.

These results suggest that lysogeny affects bacterial metabolism and confers to R^R biological advantages, which reflect both an increased fitness and the acquisition of virulence factors, implicated in modulating the host response (Supplementary Figure S5). Thus, taken together, genomics and metabolomics approaches allow for a complete understanding of the R^R physiology and its interplay with the host, providing essential information for the development of new candidate vaccines (61).

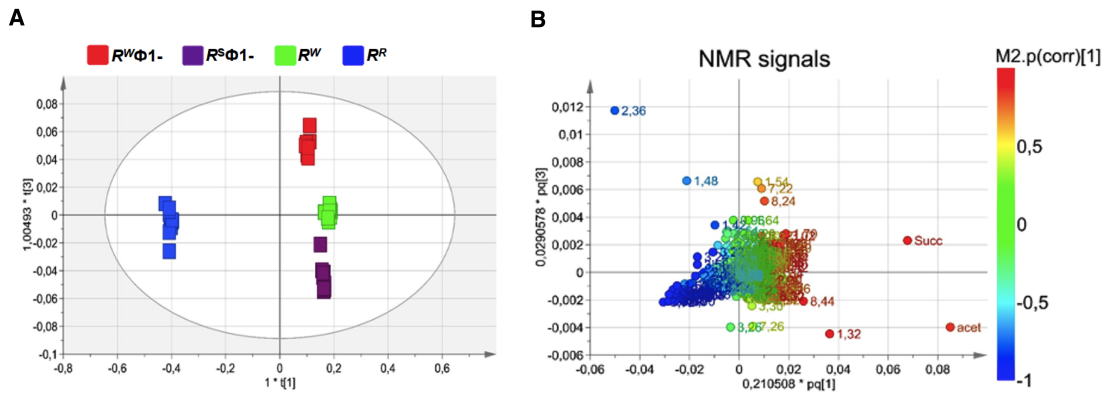

FIGURE 4
Orthogonal Projection to Latent Structure Discriminant Analysis (OPLS-DA) of bacteriophage-sensitive or resistant *S.* Rissen medium samples, before or after phage excision (R^W; R^R; $R^S\Phi1$-; $R^W\Phi1$-, respectively). **(A)** Scores plot showing a distinct separation of $R^S\Phi1$- group (purple squares) from $R^W\Phi1$- group (red squares). **(B)** Loading plot indicating NMR variables (chemical shift) of metabolites responsible for between-classes separation, characterized by |p(corr)| value> 0.7.

10.3389/fimmu.2024.1450600

Under-acylated LPS mitigates bacterial virulence in mice

To evaluate the effects of lysogeny on the virulence profile of *S.* Rissen, the lethal dose 50 (LD_{50}) of both R^R and R^W strains was determined in a mouse model of infection. Female BALB/c mice aged 10 weeks were infected intraperitoneally with a dose-range of viable R^R or R^W bacteria (10^3, 10^5, 10^7, 10^9 CFU/mouse) and survival was monitored for 21 days (Figure 5).

Results displayed that mice infected with lower doses (10^3 and 10^5 CFU/animal) of *S.* Rissen – R^R or R^W – survived throughout the study (Figure 5; Supplementary Table S3). On the contrary, mice infected with higher doses (10^7 and 10^9 CFU/animal) showed different survival rates (Figure 5; Supplementary Table S3). Compared to R^R-infected mice, a limited percentage (~30%) of mice infected with R^W (10^7 CFU/animal) began dying 4 days after infection (Figure 5B). Furthermore, while 30% of mice infected with R^R (10^9 CFU/animal) died 6 days after infection, almost all of the mice (~90%) were killed within 7 days following infection with the same amount of R^W (Figure 5A). These results show that the R^R strain displays a reduced virulence compared to R^W, with a LD_{50} significantly higher (1 x 10^9 CFU per mouse in R^R vs 5.25 x 10^7 CFU per mouse in R^W). This finding could find explanation in differences in the LPS-Lipid A structure between R^R and R^W (Figure 2). LPS is an endotoxin responsible for the host innate immune response activation, which can result in detrimental effects, such as the endotoxic shock (62). Due to its capacity to synthesize a LPS molecule lacking one or two acyl chains in the Lipid A portion, R^R only triggers a mitigated immune response with reduced risk for adverse secondary complications (63). This was confirmed by stimulating mice with a single intraperitoneal injection of LPS (20 mg/Kg body weight) purified from the R^R and R^W strains (R^R-LPS and R^W-LPS, respectively) and monitoring clinical signs of endotoxemia (Figure 6A). As expected, mice stimulated with R^W-LPS displayed more severe signs of disease (decreased body temperature and weight, diminution of appetite and apathy) compared to the R^R one (Figures 6B–E), suggesting that mice are hyporesponsive to R^R-LPS stimulation and hence, unable to mount an immediate defensive response. This property may reflect the unique organization of the R^R-LPS and its capacity to mitigate the host immune system.

Under-acylated LPS triggers a mitigated innate immune response in mice

To assess whether the biochemical diversity in R^R and R^W-derived LPS affects the host innate immune response, we measured the expression levels of pro-inflammatory cytokine (TNF-α, G-CSF, IL-6, IL-10, IFN-β, RANTES/CCL5 and IFN-γ) using an ELISA assay. LPS (20 mg/Kg body weight) was injected intraperitoneally in female BALB/c mice (n = 6 per group) and blood samples were collected both every 2 hours for a period of 8 hours and at 24 hours post injection. Results showed a much stronger increase in TNF-α, G-CSF and IL-6 levels in blood serum of mice stimulated with R^W-LPS compared to those stimulated with R^R-LPS (Figures 7A–C).

TNF-α and G-CSF increased rapidly during the first hours of stimulation and reached their highest level 4 hours post-stimulation, then started declining (Figures 7A, B). However, their concentration remained higher than the control group or mice stimulated with R^R-LPS (Figures 7A, B). INF-γ and IL-6, instead, were secreted later than TNF-α and G-CSF. The highest levels of these cytokines were observed 6- and 8-hours post-stimulation, respectively and, started decreasing after 24 hours of stimulation (Figures 7C, D). As expected, increased levels of IL-10 were detected at 24 hours, compared to control group (Figure 7E). These results show that R^W-LPS initiates sooner an acute inflammatory response via the MyD88-dependent pathway (64), aimed at controlling the injury, as indicated by IL-10 up-regulation at 24 hours after LPS stimulation (Figure 7E). On the contrary, R^R-LPS induced a milder inflammatory response. As illustrated in Figure 7, the secretion of the pro-inflammatory cytokines involved in the acute phase response (TNF-α and IL-6) was unaltered during the first hours post-LPS stimulation, compared to the control group (Figures 7A, C), while RANTES, IFN-β and IL-10 were found increased compared to both control group and mice injected with R^W-LPS (Figures 7E–G). However, IL-6 showed an increase at 24 hours (Figure 7C). These data indicate the capability of the R^R-LPS to selectively engage the TRIF-dependent pathway, while resulting a weaker elicitor of the MyD88-dependent pathway (65–67).

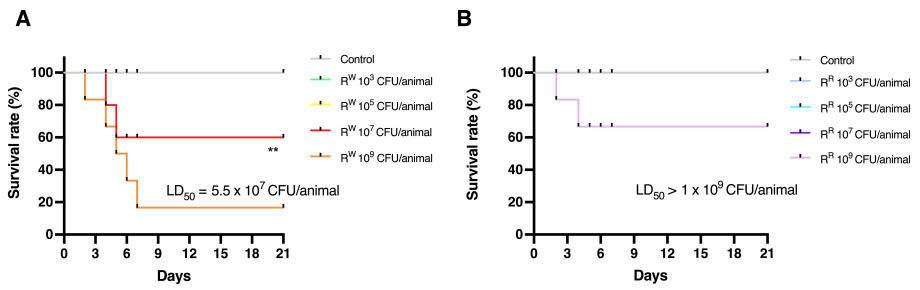

FIGURE 5
Determination of 50% Lethal Dose (LD_{50}) of R^R and R^W in BALB/c mice. Survival curves of mice infected with different concentrations of R^W strain **(A)** or R^R strain **(B)**. Uninfected control group included mice injected with PBS vehicle (n = 6/group). ** $p < 0.01$ (Long-rank Mentel-Cox test). Data are representative of two independent experiments. LD_{50} was calculated according to the Reed and Muench method. LD_{50} = Log_{10} end-point bacterial dose = Log_{10} (bacterial dose showing mortality next below 50%) + {[(50% - mortality at bacterial dose next below 50%)/(mortality at bacterial dose next above 50% - mortality at bacterial dose next below 50%)] x Log_{10} (differences between bacterial doses used in the assay)]}.

10.3389/fimmu.2024.1450600

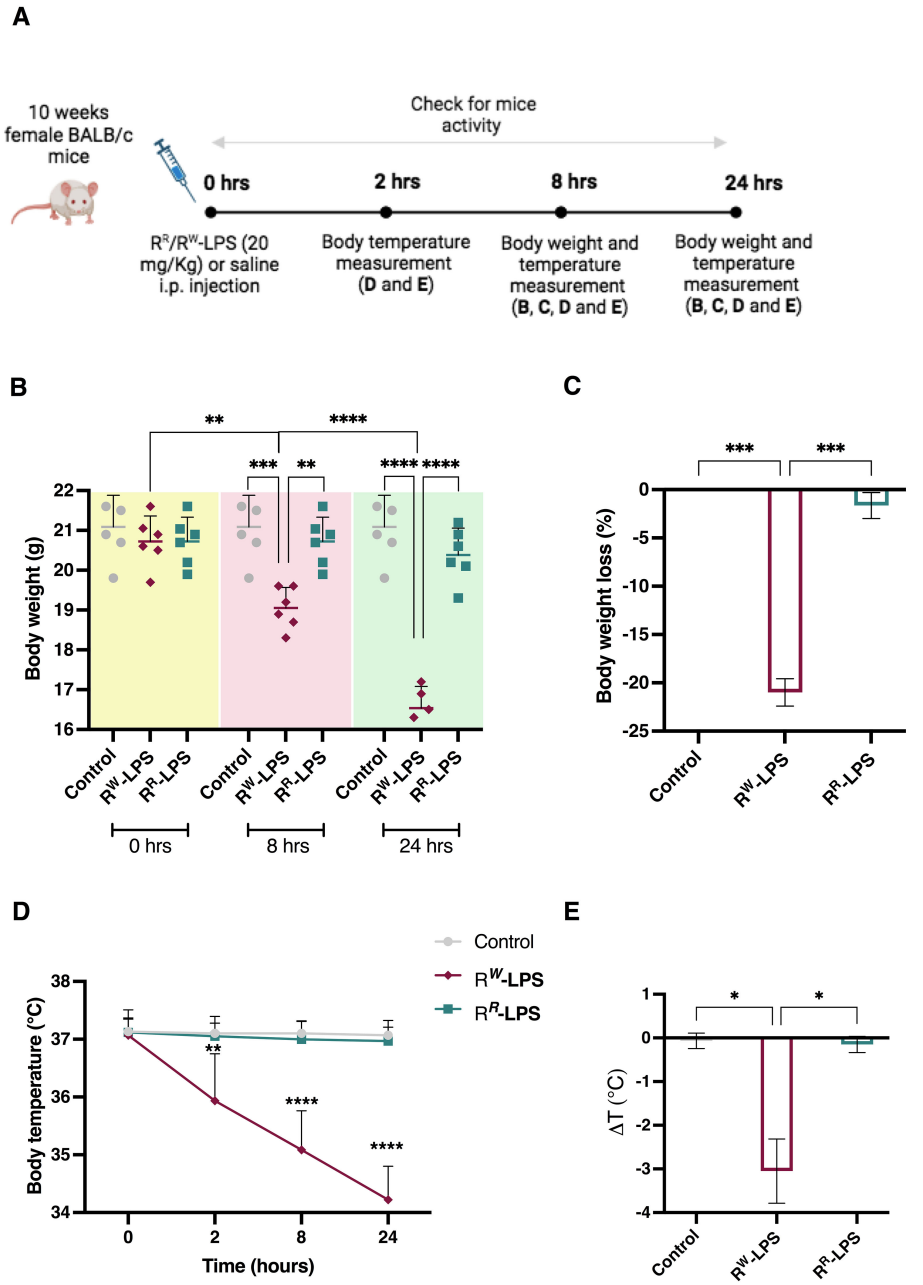

FIGURE 6
R^R-LPS does not induce endotoxemia. **(A)** Experimental design for the intraperitoneal (i.p.) injection of R^R or R^W-LPS. Ten-week-old, female BALB/c mice (n = 6 per group) were injected intraperitoneally with 20 mg/Kg of R^R or R^W-derived LPS (R^R-LPS and R^W-LPS, respectively) dissolved in PBS solution and then body weight and temperature were evaluated. Mice (n = 6) in the control group (Control) were injected intraperitoneally with the same volume of PBS solution. **(B)** Body weight was measured 0, 8 and 24 hours after LPS stimulation. Graph represents mean ± SD of values from individual mice (dots). **(C)** Bar graph represents changes (%) of body weight 24 hours after LPS injection. Data are representative of a single experiment. Two-way ANOVA followed by Turkey *post-hoc* correction was used to compare body weight among three groups (Control, R^R-LPS and R^W-LPS) at different times. One-way ANOVA followed by Turkey *post-hoc* correction was used to compare body weight changes among three groups. $^{**}p < 0.01$; $^{***}p < 0.001$; $^{****}p < 0.0001$. **(D)** Body temperature was measured 0, 2, 8 and 24 hours following LPS injection. **(E)** Bar graph represents change of temperature 24 hours after LPS injection. Data are representative of a single experiment. Two-way ANOVA followed by Turkey *post-hoc* correction was used to compare body temperature between R^R-LPS and R^W-LPS groups at different times following LPS injection. One-way ANOVA followed by Turkey *post-hoc* correction was used to compare the mean temperature among three groups. $^{*}p < 0.05$; $^{**}p < 0.01$; $^{****}p < 0.0001$.

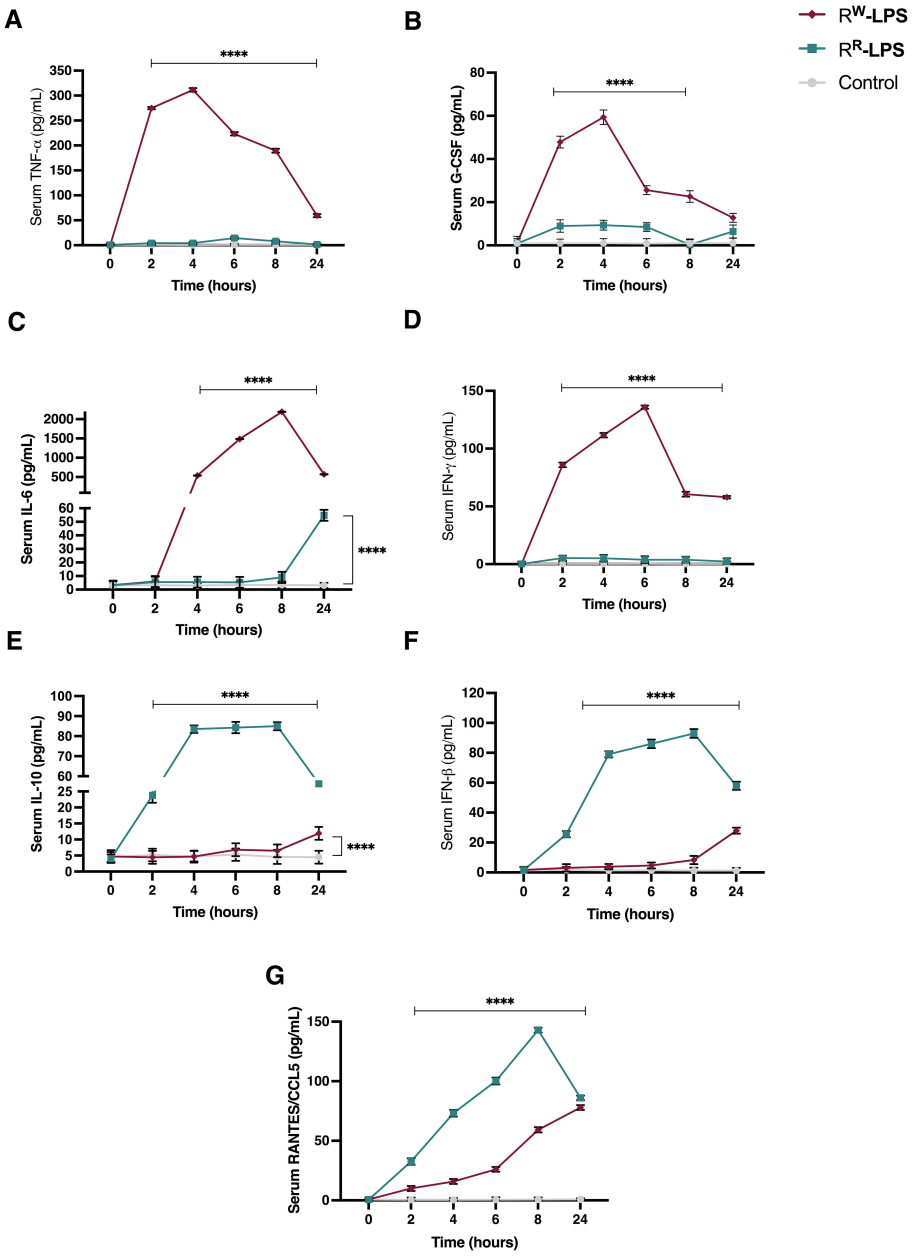

FIGURE 7
Cytokine levels in serum of BALB/c mice stimulated with R^R or R^W-LPS. Mice (n = 6 per group) were injected intraperitoneally with 20 mg/Kg of R^R or R^W-LPS dissolved in PBS solution. Mice in the control group (Control) were injected intraperiteonally with the same volume of PBS solution. Serum was collected every 2 hours for 8 hours and 24 hours following injection. The cytokines: **(A)** TNF-alpha; **(B)** G-CSF; **(C)** IL-6; **(D)** IFN-gamma; **(E)** IL-10; **(F)** IFN-beta and **(G)** RANTES/CCL5 were analyzed by ELISA. Data are representative of two independent experiments. Two-way ANOVA followed by Turkey *post-hoc* correction was used to compare cytokine levels among the three groups (control, R^R- and R^W-LPS groups). ****$p < 0.0001$.

Taken together, these results suggest a different capacity of R^R and R^W-LPS to stimulate the host immune response and a reduced toxicity of the R^R-LPS.

Under-acylated LPS stimulates a more efficient and safer antibody response

As a powerful antigen, LPS plays a pivotal role in immunological processes, stimulating antibody production (68). However, due to the Lipid A reactogenicity, LPS – in its native form - is not suitable as vaccine (69). Instead, the low toxicity of the R^R-LPS (Figure 7) – resulting from the deacylation of Lipid A (Figure 2) – could make it safe enough to develop antimicrobial vaccines.

To investigate the protective role of the R^R-LPS against *S.* Rissen infection, the immunization assay was performed. Therefore, we first explored the concentration of the whole LPS structure necessary for mice immunization, by evaluating the hemolytic effect (Supplementary Figure S6) of a wide range of doses (spanning from 1 to 500 µg). Results demonstrated that the minimum concentration of R^R-LPS showing

hemolytic effect < 8% was 10 µg. Thus, this concentration was selected to assess R^R-LPS as a potential vaccine candidate.

To evaluate the level of the antibody response, two groups of BALB/c mice (6 mice per group) were immunized intraperitoneally with RSA-conjugated R^R-LPS or R^W-LPS (10 µg/100 µL PBS) twice, at an interval of two weeks, while a third group received an intraperitoneal (i.p.) dose of PBS (control group). The secondary booster was administrated seven days after the primary one. Mice immunized with R^R-LPS exhibited higher levels of IgG and IgM (IgM > IgG) than those immunized with R^W-LPS (Figure 8A). Of note, 7 days after the last immunization, the IgG response prevailed on the IgM one, with a higher extent in mice immunized with R^R-LPS compared to those immunized with R^W-LPS (Figure 8B). This result reflects the capability of R^R-LPS to selectively engage the TLR4-TRIF-dependent pathway compared to R^W-LPS (70). We also analyzed the IgA titers, as the primary antibody produced in the intestinal mucosa (71), site of *Salmonella* infection. Significant LPS-specific IgA titers were detected in feces of mice immunized with R^R-LPS compared to both R^W-LPS immunized mice and control ones (Figure 8C). Additionally, similar to IgM, IgA levels were found to decrease after the boosting doses (Figure 8D).

These results clearly suggest R^R-LPS as a more effective and safer immunostimulant than the parent R^W-LPS, as it retains immunostimulatory properties while lacking most of its toxicity.

Under-acylated LPS protects mice against *Salmonella* Rissen infection

To evaluate the protective efficacy of the R^R-LPS induced immunity against *S.* Rissen infection, all mice were infected with a bacteremia-inducing dose of the R^W strain (10^9 CFU/animal) two weeks after the last immunization. The bacterial count in the splenic tissue was measured on day 4 post infection. Results revealed a significant reduction in bacterial burden in the spleens of mice immunized with R^R-LPS, compared to both control mice and mice immunized with R^W-LPS (Table 1).

Conversely, mice that received unconjugated R^R-LPS exhibited only a modest reduction in bacterial burden. Although bacterial burden was still higher than in those receiving PBS or a single dose of R^W-LPS, it was not lethal (Table 1).

Collectively, these findings suggest that LPS-specific antibodies significantly contribute to immune protection against *S.* Rissen

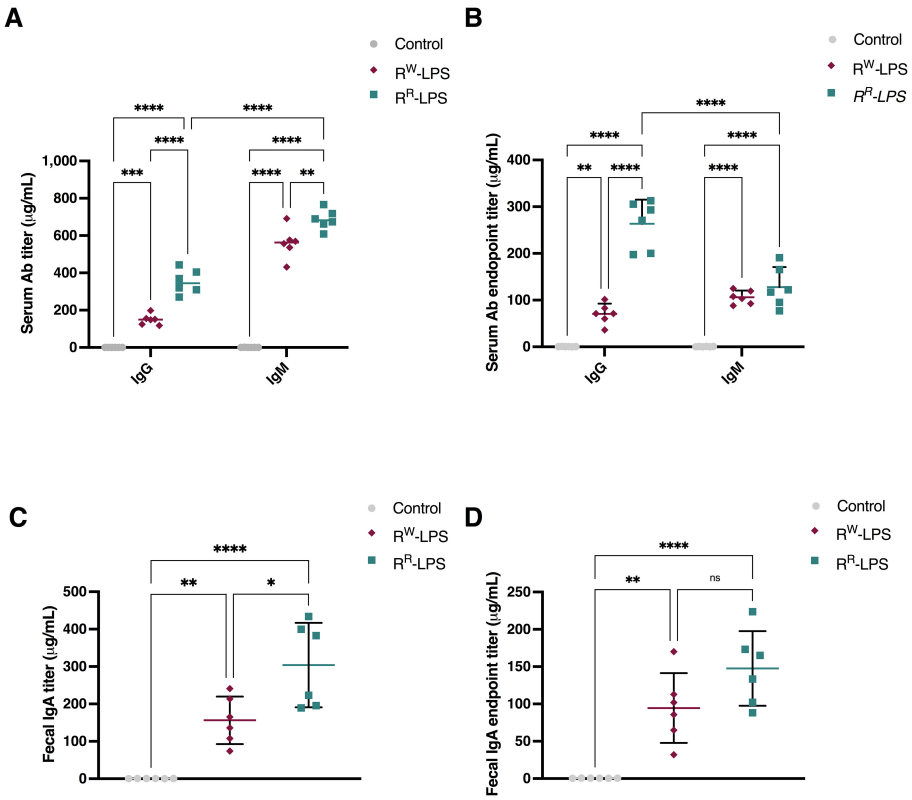

FIGURE 8
R^R-LPS favors antibody response. **(A, C)** Total IgM, IgG and IgA antibody response elicited after immunization with R^R-LPS or R^W-LPS. Results are represented as mean titers (µg/mL) in serum or feces ± SD from female BALB/c mice (n = 6 per group) immunized intraperitoneally three times with: 1) R^R-LPS (10 µg/100 µL PBS, teal green); 2) R^W-LPS (10 µg/100 µL PBS, amaranth red) or 3) vehicle (100 µL PBS, grey). Graph represents mean ± SD of values from individual mice (dots). Data are representative of a single experiment. Two-way ANOVA followed by Turkey *post-hoc* correction was used to compare total antibody levels among three groups. * p <0.05; ** p <0.01; **** p <0.0001. **(B, D)** IgM, IgG and IgA end-point anti-R^R-LPS or R^W-LPS antibody titers. Results represent the antibody response elicited on day 7 after last immunization and are represented as mean titers (µg/mL) in serum or feces ± SD. Data are representative of a single experiment. Two-way ANOVA followed by Turkey *post-hoc* correction was used to compare total antibody levels. ** p <0.01; **** p <0.0001. ns, not statistically significant.

10.3389/fimmu.2024.1450600

infection, as confirmed by serum bactericidal activity (Figure 9) and highlight R^R-LPS as a promising adjuvant for the development of vaccines against *Salmonella* infections.

Under-acylated LPS-specific antibodies mediate cross-reactivity

Salmonella species share a high degree of homology in genes encoding cell-surface molecules, including LPS, a major target of antibodies (20). As a result, immunization with LPS from one *Salmonella* serovar could confer immunity against related serovars.

To explore the potential of anti-R^R-LPS antibodies to confer cross-protective immunity to closely related *Salmonella* serovars, mice were intraperitoneally immunized at two-week intervals with 100 µL of R^R-LPS (10 µg) or vehicle (sterile PBS). Four days after the final immunization, blood samples were collected, and serum was separated by centrifugation. Serum samples were then used to test cross-reactivity between anti-R^R-LPS antibodies and LPSs from different *Salmonella* serovars through an agglutination test. As shown in Supplementary Table 4, serum samples (undiluted or diluted 1:50 and 1:100) exhibited variable agglutination with different selected *Salmonella* strains (*S.* Infantis, *S.* Newport and *S.* Choleresius). Specifically, undiluted serum showed strong agglutination with S. Choleraesuis and *S.* Infantis, which are both part of the *S.* Rissen serogroup C1. When diluted 1:50 or 1:100, serum also agglutinated the above *Salmonella* serovars, although the reaction required more time than the undiluted serum. Remarkably, a late agglutination activity of undiluted serum was observed against *S.* Newport, expressing O:6,8 antigens (C2 serogroup).

The strong interaction of anti-R^R-LPS antibodies with S. Choleraesuis and *S.* Infantis and, to a lesser extent with *S.* Newport, suggests the O-antigenic determinants O:6 and 7 as their major target. These results indicate that anti-R^R-LPS antibodies may confer cross-protection against related *Salmonella* serovars by targeting shared O-antigens.

Under-acylated LPS-specific antibodies mediate host protection by targeting the O-antigen

The O-antigen portion of LPS is widely recognized as the key target for immune defense against bacterial infections.

To further determine whether O-antigen is the primary antigenic determinant recognized by anti-R^R-LPS antibodies, an indirect ELISA assay was performed. Serum samples from mice immunized with R^R-LPS were tested for reactivity against both the O-antigen and LPS from the R^R and R^W strains. Results revealed that anti-R^R-LPS antibodies interacted with both LPS and O-antigen from the two *S.* Rissen strains (Supplementary Table 5). Specifically, the antibodies showed moderately stronger reactivity with LPS and O-antigen from the R^R strain than with those from the R^W strain. Notably, LPS exhibited slightly stronger reactivity than the purified O-antigen ($p < 0.05$, Supplementary Table 5).

These results demonstrate that O-antigen is the primary R^R-LPS epitope responsible for modulating the antibody-mediated host protection, supporting our previous findings (Supplementary Table 4). Furthermore, they suggest that other, poorly investigated portions of the LPS molecule may also contribute to the host defense and antibody reactivity.

TABLE 1 R^R-LPS reduces bacterial burden in mice infected with *S.* Rissen.

	R^W (CFU/spleen)	
	UNCONJUGATED ANTIGEN	CONJUGATED ANTIGEN
R^R-LPS	2×10^5	$< 10^3$
R^W-LPS	5×10^7	2.5×10^5

Discussion

In this study, we investigated the protective effect of an LPS-based vaccine against *S.* Rissen in BALB/c mice. LPS is a key immunogenic component of Gram-negative bacteria. It stimulates

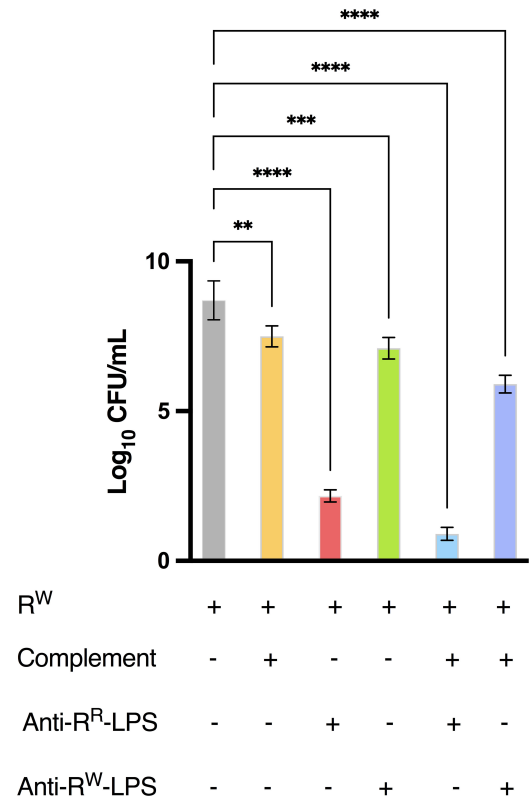

FIGURE 9
Antibodies from mice immunized with R^R-LPS display bactericidal activity against WT *S.* Rissen. The bacteriophage-sensitive strain of *S.* Rissen (R^W, 1×10^6 CFU/mL) was incubated at 37°C for 3 hours alone, with purified antibodies derived from mice immunized with R^R- or R^W-LPS, with complement or with both purified antibodies and complement. Data are represented as Log_{10} of CFU/mL (OD_{600} = 1 = 5×10^8 CFU/mL) and represent means ± SD of three independent experiments, each performed in triplicate. One-way ANOVA followed by Turkey *post-hoc* correction was used to compare Log_{10} CFU/mL among different experimental conditions. $^{**}p < 0.01$; $^{***}p < 0.001$; $^{****}p < 0.0001$.

the host humoral immune response and provides protection against pathogens (72, 73). However, LPS also plays an essential role in bacterial virulence through its endotoxic component (Lipid A), which raises concerns about its safety as "subunit" vaccine in its native form.

Several efforts have been made to attenuate the Lipid A toxicity while preserving the LPS immunostimulatory properties. Mutations in the *msbB* and *PagP* genes, both involved in the Lipid A acylation pattern, have been shown to reduce the capacity of bacteria to induce a pro-inflammatory response in the host (22, 74). As a result, *msbB* and *PagP* mutant strains are considered promising candidates for vaccine development, particularly in the context of outer membrane vesicle (OMV)-based vaccines (75). However, despite this, *Salmonella msbB* mutants display growth defects and increased sensitivity to environmental stressors such as physiological CO_2 levels and low pH (76, 77), limiting their survival and complicating large-scale vaccine production.

In this study, we propose - for the first time - phage resistance as a promising biological tool for producing under-acylated variants of LPS, overcoming the limitations mentioned above.

Phage-resistance, as a naturally occurring selection mechanism, bypasses the need for microbial genetic manipulation, thus avoiding challenging related to the stability of mutations and the maintenance of the desired phenotypic traits. Moreover, by enhancing bacterial fitness, phage-resistance promotes bacterial survival under stress conditions, offering a cost-effective and sustainable alternative to conventional genetic, chemical and enzymatic methods.

To explore the role of prophages in remodeling Lipid A molecules and modulating *S.* Rissen virulence, we first examined the presence of phage genetic elements in the R^R and R^W genomes. Both strains contained phage genome elements. However, R^R acquired the superinfection exclusion gene (*SieB*), which confers a competitive advantage increasing bacterial fitness by inhibiting further phage infections (78) (Supplementary Figure S1; Figure 1). This superinfection resistance likely arises from alterations in cell membrane elements, such as the LPS and its endotoxic portion (30). Modifications to the LPS structure may occur at each step of its biosynthetic process, as well as from additional enzymes (79). We recently showed that R^R expresses higher levels of the *LpxR* gene than R^W (26). *LpxR* encodes a deacylase responsible for removing acyl chains from Lipid A. Therefore, we hypothesized the capability of R^R of producing deacylated Lipid A species.

In the present study, we validated the above hypothesis. Mass spectrometry analysis revealed that, unlike the R^W strain, R^R produces a higher abundance of two alternative variants of Lipid A as the penta-acylated and the tetra-acylated form (Figure 2). Both these two structures are less stimulatory for TLR4 and elicit a mitigated innate immune response. These results demonstrate that the acquisition of the *SieB* gene, which is associated with the distinctive phage-resistant phenotype of R^R, improves bacterial fitness and provides virulence factors (LpxR) which attenuate the innate immune response in the eukaryotic host.

Metabolic changes in bacteria often influence the production of virulence factors and contribute to bacterial pathogenicity (80). Short chain fatty acids (SCFAs; propionate, acetate and butyrate) regulate the expression of genes in *Salmonella* pathogenicity island 1 (*SPI1*, 81). Specifically, acetate promotes *SPI1* genes expression, while butyrate suppresses genes like *hilD*, which plays transcriptional regulatory roles (81). Notably, *hilD* also activates *LpxR* (82). In line with these findings, R^R uptook from the growth medium more acetate than R^W (Supplementary Figure S5), suggesting that phage-resistance enhances the expression of virulence factors like LpxR, which regulate LPS structure and modulate the host innate immune response. This result is confirmed by our previously published data which demonstrate up-regulation of the *LpxR* gene in AGS cells infected by the R^R strain (26). Additionally, R^R implemented the extracellular concentration of γ-aminoisobutyric acid (GABA), glucose and pyruvate compared to R^W (Supplementary Figure S5). GABA improves bacterial survival in acidic environments and supports colonization of gastro-intestinal tract (83). Similarly, accumulation of glucose in the growth medium, together with pyruvate production from acetate, confer advantages to bacteria, preserving them from acidic environments (84). These findings suggest that phage Φ1 provides R^R with an adaptive advantage by enhancing bacterial fitness.

As living organisms, bacteria ordinarily require energy to support their physiological functions. However, under particular conditions - such as the acquisition of phage-resistance - bacteria demand higher levels of energy. In agreement with this requirement, R^R uptook more hypoxanthine from the growth medium than R^W (Supplementary Figure S5). As an intermediate of the purine biosynthetic pathway, hypoxanthine consumption increases the ATP production to provide energy for the more metabolically active R^R cells. R^R also uptook more amino acids, including arginine, lysine, isoleucine, leucine, proline and phenylalanine which serve as effective source of carbon and nitrogen (Supplementary Figure S5, 85). Amino acids contribute to ammonium production, which is vital for synthetizing macromolecules through glutamate biosynthesis (86). Consistent with this evidence, R^R released glutamate into the growth medium (Supplementary Figure S5), which also participates in glutathione biosynthesis – a key antioxidant molecule that counteracts reactive oxygen species (ROS) produced by the host immune system (87). Higher levels of methionine - the major precursor of glutathione (88) - were detected in the growth medium of R^R (Supplementary Figure S5), aligning with our previous results showing increased expression of the *SodC1* and *gogB* genes in cells infected by the R^R strain (26). *SodC1* is a superoxide dismutase which protects bacteria from the oxidative burst induced by the host immune cells, while *gogB* attenuates both the inflammatory response and ROS production (28). Taken together, these results suggest that phage-resistance, at least in this case, enhances bacterial fitness and reduces bacterial effectiveness in inducing cell host damage.

These results were confirmed *in vivo*. R^R, in fact, curbs the mortality of mice. The highest tested concentration of R^R (10^9 CFU/animal) resulted in 33% mortality in mice, compared to 100% mortality in those exposed to the same concentration of R^W (Figure 5). This reduced mortality may reflect under-acylation of Lipid A and consequently reduced activation of the innate immune response.

Under-acylated Lipid A molecules, in fact, compete with native species of Lipid A (hexa-acylated forms) and inhibit the hexa-acylated Lipid A-MD2 complex functions, thus inducing a deficient TLR4 signaling and a reduced secretion of pro-inflammatory cytokines (58).

As expected, mice stimulated with R^R-LPS produced lower levels of pro-inflammatory cytokines, compared to those stimulated with the R^W-LPS (Figure 7). They showed lower concentrations of the MyD88-dependent cytokines TNF-α, IL-6 and G-CSF (Figures 7A–C) – all involved in the early stages of infection – thus suggesting the inability of R^R in mounting an immediate inflammatory response. Importantly, R^R-LPS suppressed the IFN-γ production (Figure 7D), which plays a key role in the pathogenesis of septic shock (89), while increased the production of TRIF-dependent cytokines RANTES and IFN-β (Figures 7F–G), which limit inflammation and promote adaptive immunity (65, 66). Alteration in the stability of TLR4-MD-2, due to under-acylated ligands, in fact, impairs the canonical LPS-induced receptor dimerization and, as a consequence, the traditional signal transduction pathway involving both MyD88 and TRIF-pathways. These results, together with the secretion of the anti-inflammatory cytokine IL-10 (Figure 7E), explain reduced signs of endotoxemia in mice stimulated with the R^R-LPS (Figure 6).

To determine the protective effect of the R^R-LPS against *S.* Rissen *in vivo*, we immunized mice and evaluated the bacterial count in the splenic tissue. A significant reduction in bacterial burden ($< 10^3$) was observed in mice immunized with the R^R-LPS compared to those immunized with the R^W-LPS (Table 1). This protection was attributed to LPS-specific antibodies targeting the O-antigen (Supplementary Table S5; Figure 9). Both R^R-LPS and R^W-LPS induced an early production of IgA, with a significant higher expression in mice immunized with R^R-LPS (Figure 8C).

IgA is the most important class of antibodies released in the intestinal secretion and plays an essential role in protecting the gastro-intestinal tract from *Salmonella* pathogens (90). Moreover, early IgA production – as in our case – represents a valuable immunological memory to polysaccharidic antigens (91, 92),. In addition, mice immunized with the R^R-LPS also showed an immune response profile characterized by higher production of IgG than those immunized with the R^W-LPS (Figures 8A, B). As a selective activator of the TRIF-dependent pathway, R^R-LPS induces the recruitment of the adaptive immune response through the expression of *type I-IFN*-encoding genes and IL-10 production (Figure 7), which stimulate both maturation and differentiation of $CD80^+$ and $CD86^+$ dendritic cells through selection and expansion of pathogen-specific T and B cells (93). These events culminate in the T-dependent antibody production – enhanced by the peptide carrier, which enables the antigen presentation to T cell through the MHCII – thus eliciting a protective immunological memory through the antibody switching (93, 94), and explaining the higher expression of IgG in R^R-LPS immunized mice. Altogether, these results give reason for attributing the host immune protection to the antibody production (Figure 9) and, hypothesizing that R^R-LPS immunization could confer cross-protection against different *Salmonella* serovars by targeting shared O-antigens (Supplementary Table 4). However, further in-depth investigation is needed to elucidate the exact mechanism of protection and ascertain whether antibodies are the unique contributors to the R^R-LPS induced immune protection.

In conclusion, this study demonstrates that under-acylated LPS molecules - derived from the bacteriophage-resistant strain of *S.* Rissen - induce an attenuated innate immune response, while promoting an effective adaptive immune protection. These properties make R^R-LPS a potentially promising candidate for vaccine development. Moreover, this study also highlights the potential use of phages as an alternative to conventional chemical or genetic methods for producing vaccines. Nevertheless, further studies are required to provide further insight into mechanism, length and contribution of additional factors in improving vaccine potency and efficacy, and finally, the possibility to extend this approach to other bacterial infections.

Data availability statement

The datasets presented in this study can be found in online repositories. The names of the repository/repositories and accession number(s) can be found in the article/Supplementary Material.

Ethics statement

The studies involving humans were approved by the Committee of Villa Betania Hospital, in accordance with the principles of good clinical practices (Declaration of Helsinki). The studies were conducted in accordance with the local legislation and institutional requirements. The participants provided their written informed consent to participate in this study. The animal study was approved by the Italian Ministry of Health. The study was conducted in accordance with the local legislation and institutional requirements.

Author contributions

PC: Data curation, Formal analysis, Validation, Writing – original draft. CM: Writing – original draft, Data curation, Formal analysis, Validation. AC: Methodology, Writing – review & editing. AG: Validation, Writing – review & editing. CF: Validation, Writing – review & editing. MMC: Methodology, Supervision, Validation, Writing – review & editing. RC: Conceptualization, Supervision, Writing – review & editing.

Funding

The author(s) declare that no financial support was received for the research, authorship, and/or publication of this article.

Conflict of interest

The authors declare that the research was conducted in the absence of any commercial or financial relationships that could be construed as a potential conflict of interest.

Publisher's note

All claims expressed in this article are solely those of the authors and do not necessarily represent those of their affiliated organizations, or those of the publisher, the editors and the reviewers. Any product that may be evaluated in this article, or claim that may be made by its manufacturer, is not guaranteed or endorsed by the publisher.

Supplementary material

The Supplementary Material for this article can be found online at: https://www.frontiersin.org/articles/10.3389/fimmu.2024.1450600/full#supplementary-material

References

1. Majowicz SE, Musto J, Scallan E, Angulo FJ, Kirk M, O'Brien SJ, et al. International Collaboration on Enteric Disease "Burden of Illness" Studies. The global burden of nontyphoidal Salmonella gastroenteritis. *Clin Infect Dis*. (2010) 50:882–9. doi: 10.1086/650733

2. Radhakrishnan A, Als D, Mintz ED, Crump JA, Stanaway J, Breiman RF, et al. Introductory article on global burden and epidemiology of typhoid fever. *Am J Trop Med Hyg*. (2018) 99:4–9. doi: 10.4269/ajtmh.18-0032

3. Murugaiyan J, Anand Kumar P, Rao GS, Iskandar K, Hawser S, Hays JP, et al. Progress in alternative strategies to combat antimicrobial resistance: focus on antibiotics. *Antibiotics*. (2022) 11:200. doi: 10.3390/antibiotics11020200

4. Zhou A, Li J, Xu Z, Ni J, Guo J, Yao YF, et al. Whole-genome comparative and pathogenicity analysis of salmonella enterica subsp. *enterica serovar rissen*. *G3 Genes Genomes Genet*. (2020) 10:2159–70. doi: 10.1534/g3.120.401201

5. Sears KT, Galen JE, Tennant SM. Advances in the development of Salmonella-based vaccine strategies for protection against Salmonellosis in humans. *J Appl Microbiol*. (2021) 131:2640–58. doi: 10.1111/jam.15055

6. Birkhold M, Mwisongo A, Pollard AJ, Neuzil KM. Typhoid conjugate vaccines: advancing the research and public health agendas. *J Infect Dis*. (2021) 224:S781–7. doi: 10.1093/infdis/jiab449

7. MacLennan CA, Martin LB, Micoli F. Vaccines against invasive Salmonella disease: Current status and future directions. *Hum Vaccines Immunother*. (2014) 10:1478–93. doi: 10.4161/hv.29054

8. Kantele A, Pakkanen SH, Karttunen R, Kantele JM. Head-to-head comparison of humoral immune responses to vi capsular polysaccharide and salmonella typhi ty21a typhoid vaccines-A randomized trial. *PloS One*. (2013) 8:e60583. doi: 10.1371/journal.pone.0060583

9. Jossi SE, Arcuri M, Alshayea A, Persaud RR, Marcial-Juárez E, Palmieri E, et al. Vi polysaccharide and conjugated vaccines afford similar early, IgM or IgG-independent control of infection but boosting with conjugated Vi vaccines sustains the efficacy of immune responses. *Front Immunol*. (2023) 14:1139329. doi: 10.3389/fimmu.2023.1139329

10. De Benedetto G, Alfini R, Cescutti P, Caboni M, Lanzilao L, Necchi F, et al. Characterization of O-antigen delivered by Generalized Modules for Membrane Antigens (GMMA) vaccine candidates against nontyphoidal Salmonella. *Vaccine*. (2017) 35:419–26. doi: 10.1016/j.vaccine.2016.11.089

11. Mancini F, Micoli F, Necchi F, Pizza M, Berlanda Scorza F, Rossi O. GMMA-based vaccines: the known and the unknown. *Front Immunol*. (2021) 12:715393. doi: 10.3389/fimmu.2021.715393

12. Wang X, Quinn PJ. Endotoxins: Lipopolysaccharides of gram-negative bacteria. *Subcell Biochem*. (2010) 53:3–25. doi: 10.1007/978-90-481-9078-2_1

13. Raetz CRH, Whitfield C. Lipopolysaccharide endotoxins. *Annu Rev Biochem*. (2002) 71:615–49. doi: 10.1146/annurev.biochem.71.110601.135414

14. Cavaillon JM. André Boivin: A pioneer in endotoxin research and an amazing visionary during the birth of molecular biology. *Innate Immun*. (2020) 26:165–71. doi: 10.1177/1753425919842307

15. Cross AS. Hit 'em where it hurts: gram-negative bacterial lipopolysaccharide as a vaccine target. *Microbiol Mol Biol Rev*. (2023) 87:e0004522. doi: 10.1128/mmbr.00045-22

16. Gorman A, Golovanov AP. Lipopolysaccharide structure and the phenomenon of low endotoxin recovery. *Eur J Pharm Biopharm*. (2022) 180:289–307. doi: 10.1016/j.ejpb.2022.10.006

17. Ahmad TA, El-Sayed LH, Haroun M, Hussein AA, El Ashry ESH. Development of immunization trials against Klebsiella pneumoniae. *Vaccine*. (2012) 30:2411–20. doi: 10.1016/j.vaccine.2011.11.027

18. Ledov VA, Golovina ME, Alkhazova BI, Lvov VL, Kovalchuk AL, Aparin PG. A pentavalent shigella flexneri LPS-based vaccine candidate is safe and immunogenic in animal models. *Vaccines*. (2023) 11:345. doi: 10.3390/vaccines11020345

19. Nagy G, Pál T. Lipopolysaccharide: A tool and target in enterobacterial vaccine development. *Biol Chem*. (2008) 389:513–20. doi: 10.1515/BC.2008.056/MACHINEREADABLECITATION/RIS

20. Ahmed A, Akhade AS, Qadri A. Accessibility of O antigens shared between salmonella serovars determines antibody-mediated cross-protection. *J Immunol*. (2020) 205:438–46. doi: 10.4049/jimmunol.1900624

21. Rossi O, Caboni M, Negrea A, Necchi F, Alfini R, Micoli F, et al. Toll-like receptor activation by generalized modules for membrane antigens from lipid A mutants of salmonella enterica serovars typhimurium and enteritidis. *Clin Vaccine Immunol*. (2016) 23:304–14. doi: 10.1128/CVI.00023-16

22. Watson PR, Benmore A, Khan SA, Jones PW, Maskell DJ, Wallis TS. Mutation of waaN reduces Salmonella enterica serovar typhimurium-induced enteritis and net secretion of type III secretion system 1-dependent proteins. *Infect Immun*. (2000) 68:3768–71. doi: 10.1128/IAI.68.6.3768-3771.2000

23. Wang X, Quinn PJ. Lipopolysaccharide: Biosynthetic pathway and structure modification. *Prog Lipid Res*. (2010) 49:97–107. doi: 10.1016/j.plipres.2009.06.002

24. Gerke C, Colucci AM, Giannelli C, Sanzone S, Vitali CG, Sollai L, et al. Production of a Shigella sonnei vaccine based on generalized modules for membrane antigens (GMMA), 1790GAHB. *PloS One*. (2015) 10. doi: 10.1371/journal.pone.0134478

25. Papaianni M, Contaldi F, Fulgione A, Woo SL, Casillo A, Corsaro MM, et al. Role of phage ϕ1 in two strains of Salmonella Rissen, sensitive and resistant to phage ϕ1. *BMC Microbiol 2018 181*. (2018) 18:1–10. doi: 10.1186/S12866-018-1360-Z

26. Capparelli R, Cuomo P, Papaianni M, Pagano C, Montone AMI, Ricciardelli A, et al. Bacteriophage-resistant salmonella rissen: an *in vitro* mitigated inflammatory response. *Viruses*. (2021) 13:2468. doi: 10.3390/V13122468

27. Castledine M, Buckling A. Critically evaluating the relative importance of phage in shaping microbial community composition. *Trends Microbiol*. (2024) 32:957–69. doi: 10.1016/j.tim.2024.02.014

28. Taylor VL, Fitzpatrick AD, Islam Z, Maxwell KL. The diverse impacts of phage morons on bacterial fitness and virulence. *Adv Virus Res*. (2019) 103:1–31. doi: 10.1016/bs.aivir.2018.08.001

29. Folimonova SY. Superinfection exclusion is an active virus-controlled function that requires a specific viral protein. *J Virol*. (2012) 5554:61. doi: 10.1128/jvi.00310-12

30. Wahl A, Battesti A, Ansaldi M. Prophages in Salmonella enterica: a driving force in reshaping the genome and physiology of their bacterial host? *Mol Microbiol*. (2019) 111:303–16. doi: 10.1111/MMI.14167

31. Lennette EH, Spaulding EH, Truant JP. Manual of clinical microbiology. *Amsocmicrobiol,Washington,Dc*. (1974) 970p. doi: 10.4269/ajtmh.1971.20.3.tm0200030508a

32. Glonti T PJ. *In vitro* techniques and measurements of phage characteristics that are important for phage therapy success. *Viruses*. (2022) 14:1490. doi: 10.3390/v14071490

33. Bonilla N, Rojas MI, Cruz GNF, Hung SH, Rohwer F, Barr JJ. Phage on tap-a quick and efficient protocol for the preparation of bacteriophage laboratory stocks. *PeerJ*. (2016) 4:e2261. doi: 10.7717/peerj.2261

34. Alikhan NF, Petty NK, Ben Zakour NL, Beatson SA. BLAST Ring Image Generator (BRIG): Simple prokaryote genome comparisons. *BMC Genomics*. (2011) 12:402. doi: 10.1186/1471-2164-12-402

35. Galanos C, Lüderitz O, Westphal O. A new method for the extraction of R lipopolysaccharides. *Eur J Biochem*. (1969) 9:245–9. doi: 10.1111/j.1432-1033.1969.tb00601.x

36. Laemmli UK FM. Maturation of the head of bacteriophage T4. *I. DNA packaging events.e. J Mol Biol*. (1973) 80:575–99. doi: 10.1016/0022-2836(73)90198-8

37. Tsai CM FC. A sensitive silver stain for detecting lipopolysaccharides in polyacrylamide gels. *Anal Biochem*. (1982) 119:115–9. doi: 10.1016/0003-2697(82)90673-X

38. Casillo A, Parrilli E, Filomena S, Lindner B, Lanzetta R, Parrilli M, et al. Structural investigation of the oligosaccharide portion isolated from the lipooligosaccharide of the permafrost psychrophile Psychrobacter arcticus 273-4. *Mar Drugs*. (2015) 13:4539–55. doi: 10.3390/md13074539

39. Ionel Ciucanu FK. A simple and rapid method for the permethylation of carbohydrates. *Carbohydr Res*. (1984) 131:209–17. doi: 10.1016/0008-6215(84)85242-8

40. Abid Y, Casillo A, Gharsallah H, Joulak I, Lanzetta R, Corsaro MM, et al. Production and structural characterization of exopolysaccharides from newly isolated probiotic lactic acid bacteria. *Int J Biol Macromol*. (2018) 108:719–28. doi: 10.1016/j.ijbiomac.2017.10.155

41. Carillo S, Pieretti G, Parrilli E, Tutino ML, Gemma S, Molteni M, et al. Structural investigation and biological activity of the lipooligosaccharide from the psychrophilic bacterium pseudoalteromonas haloplanktis TAB 23. *Chem - A Eur J*. (2011) 17:7053–60. doi: 10.1002/chem.201100579

42. Stephens M, Liao S, von der Weid PY. Ultra-purification of Lipopolysaccharides reveals species-specific signalling bias of TLR4: importance in macrophage function. *Sci Rep*. (2021) 11:1335. doi: 10.1038/s41598-020-79145-w

43. Masoud H. LPS-based conjugate vaccines composed of saccharide antigens of smooth-type Salmonella enteritidis and rough-type S. *gallinarum 9R bound to bovine serum albumin. Scand J Infect Dis*. (2007) 39:315–22. doi: 10.1080/00365540601034782

44. Papaianni M, Cuomo P, Fulgione A, Albanese D, Gallo M, Paris D, et al. Bacteriophages promote metabolic changes in bacteria biofilm. *Microorganisms*. (2020) 8:480. doi: 10.3390/microorganisms8040480

45. Hwang TL, Shaka AJ. Water suppression that works. Excitation sculpting using arbitrary wave-forms and pulsed-field gradients. *J Magn Reson - Ser A*. (1995) 112. doi: 10.1006/jmra.1995.1047

46. Bax A, Davis DG. MLEV-17-based two-dimensional homonuclear magnetization transfer spectroscopy. *J Magn Reson*. (1985) 65. doi: 10.1016/0022-2364(85)90018-6

47. Kay LE, Keifer P, Saarinen T. Pure absorption gradient enhanced heteronuclear single quantum correlation spectroscopy with improved sensitivity. *J Am Chem Soc*. (1992) 114. doi: 10.1021/ja00052a088

48. Schleucher J, Schwendinger M, Sattler M, Schmidt P, Schedletzky O, Glaser SJ, et al. A general enhancement scheme in heteronuclear multidimensional NMR employing pulsed field gradients. *J Biomol NMR*. (1994) 4:301–6. doi: 10.1007/BF00175254

49. Fan TWM. Metabolite profiling by one- and two-dimensional NMR analysis of complex mixtures. *Prog Nucl Magn Reson Spectrosc*. (1996) 28:161–219. doi: 10.1016/0079-6565(95)01017-3

50. Greco I, Molchanova N, Holmedal E, Jenssen H, Hummel BD, Watts JL, et al. Correlation between hemolytic activity, cytotoxicity and systemic *in vivo* toxicity of synthetic antimicrobial peptides. *Sci Rep*. (2020) 10:13206. doi: 10.1038/s41598-020-69995-9

51. Ramakrishnan MA. Determination of 50% endpoint titer using a simple formula. *World J Virol*. (2016) 5:85–6. doi: 10.5501/wjv.v5.i2.85

52. Soromou LW, Jiang L, Wei M, Chen N, Huo M, Chu X, et al. Protection of mice against lipopolysaccharide-induced endotoxic shock by pinocembrin is correlated with regulation of cytokine secretion. *J Immunotoxicol*. (2014) 11:56–61. doi: 10.3109/1547691X.2013.792886

53. Verrillo M, Cuomo P, Montone AMI, Savy D, Spaccini R, Capparelli R PA. Humic substances from composted fennel residues control the inflammation induced by Helicobacter pylori infection in AGS cells. *PloS One*. (2023) 18:e0281631. doi: 10.1371/journal.pone.0281631

54. Lin AV. Indirect ELISA. *Methods Mol Biol*. (2015) 1318:51–9. doi: 10.1007/978-1-4939-2742-5_5

55. Capparelli R, Ventimiglia I, Longobardo L, Iannelli D. Quantification of gliadin levels to the picogram level by flow cytometry. *Cytom Part A*. (2005) 63:108–13. doi: 10.1002/cyto.a.20109

56. Fishman JB, Berg EA. Protein A and protein G purification of antibodies. *Cold Spring Harb Protoc*. (2019) 2019. doi: 10.1101/pdb.prot099143

57. Ranade K, Poteete AR. Superinfection exclusion (sieB) genes of bacteriophages P22 and lambda. *J Bacteriol*. (1993) 175:4712. doi: 10.1128/JB.175.15.4712-4718.1993

58. Teghanemt A, Zhang D, Levis EN, Weiss JP, Gioannini TL. Molecular basis of reduced potency of underacylated endotoxins. *J Immunol*. (2005) 175:4669–76. doi: 10.4049/jimmunol.175.7.4669

59. Park BS, Lee JO. Recognition of lipopolysaccharide pattern by TLR4 complexes. *Exp Mol Med*. (2013) 45:e66. doi: 10.1038/emm.2013.97

60. Kim HM, Park BS, Kim JI, Kim SE, Lee J, Oh SC, et al. Crystal structure of the TLR4-MD-2 complex with bound endotoxin antagonist eritoran. *Cell*. (2007) 130:906–17. doi: 10.1016/j.cell.2007.08.002

61. Schulz C, Hammerschmidt S. Exploitation of physiology and metabolomics to identify pneumococcal vaccine candidates. *Expert Rev Vaccines*. (2013) 12:1061–75. doi: 10.1586/14760584.2013.824708

62. Caroff M, Karibian D, Cavaillon JM, Haeffner-Cavaillon N. Structural and functional analyses of bacterial lipopolysaccharides. *Microbes Infect*. (2002) 4:915–26. doi: 10.1016/S1286-4579(02)01612-X

63. Ogawa R, Yen H, Kawasaki K, Tobe T. Activation of lpxR gene through enterohaemorrhagic Escherichia coli virulence regulators mediates lipid A modification to attenuate innate immune response. *Cell Microbiol*. (2018) 20. doi: 10.1111/cmi.12806

64. Watanabe S, Kumazawa Y, Inoue J. Liposomal lipopolysaccharide initiates TRIF-dependent signaling pathway independent of CD14. *PloS One*. (2013) 8:2–8. doi: 10.1371/journal.pone.0060078

65. Ciesielska A, Matyjek M, Kwiatkowska K. TLR4 and CD14 trafficking and its influence on LPS-induced pro-inflammatory signaling. *Cell Mol Life Sci*. (2021) 78:1233–61. doi: 10.1007/s00018-020-03656-y

66. Chang EY, Guo B, Doyle SE, Cheng G. Cutting edge: involvement of the type I IFN production and signaling pathway in lipopolysaccharide-induced IL-10 production. *J Immunol*. (2007) 178:6705–9. doi: 10.4049/jimmunol.178.11.6705

67. Lin TL, Shu CC, Chen YM, Lu JJ, Wu TS, Lai WF, et al. Like cures like: pharmacological activity of anti-inflammatory lipopolysaccharides from gut microbiome. *Front Pharmacol*. (2020) 11:554. doi: 10.3389/fphar.2020.00554

68. Zarri A, van der L. Biosynthetically engineered lipopolysaccharide as vaccine adjuvant. *Expert Rev Vaccines*. (2015) 14:861–76. doi: 10.1586/14760584.2015.1026808

69. Arenas J, Pupo E, Phielix C, David D, Zariri A, Zamyatina A, et al. Shortening the lipid A acyl chains of Bordetella pertussis enables depletion of lipopolysaccharide endotoxic activity. *Vaccines*. (2020) 8:594. doi: 10.3390/vaccines8040594

70. Yanagibashi T, Nagai Y, Watanabe Y, Ikutani M, Hirai Y, Takatsu K. Differential requirements of MyD88 and TRIF pathways in TLR4-mediated immune responses in murine B cells. *Immunol Lett*. (2015) 163:22–31. doi: 10.1016/j.imlet.2014.11.012

71. Lin R, Chen H, Shu W, Sun M, Fang L, Shi Y, et al. Clinical significance of soluble immunoglobulins A and G and their coated bacteria in feces of patients with inflammatory bowel disease. *J Transl Med*. (2018) 16:359. doi: 10.1186/s12967-018-1723-0

72. Singh SP, Williams YU, Klebba PE, Macchia P, Miller S. Immune recognition of porin and lipopolysaccharide epitopes of Salmonella typhimurium in mice. *Microb Pathog*. (2000) 28:157–67. doi: 10.1006/mpat.1999.0332

73. Zhao Y, Arce-Gorvel V, Conde-Álvarez R, Moriyon I, Gorvel JP. Vaccine development targeting lipopolysaccharide structure modification. *Microbes Infect*. (2018) 20:455–60. doi: 10.1016/j.micinf.2017.11.006

74. d'Hauteville H, Khan S, Maskell DJ, Kussak A, Weintraub A, Mathison J, et al. Two msbB Genes Encoding Maximal Acylation of Lipid A Are Required for Invasive Shigella flexneri to Mediate Inflammatory Rupture and Destruction of the Intestinal Epithelium. *J Immunol*. (2002) 168:5240–51. doi: 10.4049/jimmunol.168.10.5240

75. Micoli F, Rondini S, Alfini R, Lanzilao L, Necchi F, Negrea A, et al. Comparative immunogenicity and efficacy of equivalent outer membrane vesicle and glycoconjugate vaccines against nontyphoidal Salmonella. *Proc Natl Acad Sci U.S.A*. (2018) 115:10428–33. doi: 10.1073/pnas.1807655115

76. Murray SR, Bermudes D, De Felipe KS, Low KB. Extragenic suppressors of growth defects in msbB Salmonella. *J Bacteriol*. (2001) 183:5554–61. doi: 10.1128/JB.183.19.5554-5561.2001

77. Karsten V, Murray SR, Pike J, Troy K, Ittensohn M, Kondradzhyan M, et al. MsbB deletion confers acute sensitivity to CO2in Salmonella enterica serovar Typhimurium that can be suppressed by a loss-of-function mutation in zwf. *BMC Microbiol*. (2009) 9:170. doi: 10.1186/1471-2180-9-170

78. Bondy-Denomy J, Qian J, Westra ER, Buckling A, Guttman DS, Davidson AR, et al. Prophages mediate defense against phage infection through diverse mechanisms. *ISME J*. (2016) 10:2854–66. doi: 10.1038/ismej.2016.79

79. Simpson BW, Trent MS. Pushing the envelope: LPS modifications and their consequences. *Nat Rev Microbiol*. (2019) 17:403–16. doi: 10.1038/s41579-019-0201-x

80. Rudra P, Boyd JM. Metabolic control of virulence factor production in Staphylococcus aureus. *Curr Opin Microbiol*. (2020) 55:81–7. doi: 10.1016/j.mib.2020.03.004

81. Gantois I, Ducatelle R, Pasmans F, Haesebrouck F, Hautefort I, Thompson A, et al. Butyrate specifically down-regulates Salmonella pathogenicity island 1 gene expression. *Appl Environ Microbiol*. (2006) 72:946–9. doi: 10.1128/AEM.72.1.946-949.2006

82. Martínez-Flores I, Pérez-Morales D, Sánchez-Pérez M, Paredes CC, Collado-Vides J, Salgado H, et al. In silico clustering of Salmonella global gene expression data reveals novel genes co-regulated with the SPI-1 virulence genes through HilD. *Sci Rep*. (2016) 6:37858. doi: 10.1038/srep37858

83. De Biase D, Pennacchietti E. Glutamate decarboxylase-dependent acid resistance in orally acquired bacteria: Function, distribution and biomedical implications of the gadBC operon. *Mol Microbiol*. (2012) 86:779–86. doi: 10.1111/mmi.12020

84. Wu J, Li Y, Cai Z, Jin Y. Pyruvate-associated acid resistance in bacteria. *Appl Environ Microbiol*. (2014) 80:4108–13. doi: 10.1128/AEM.01001-14

85. Liu YK, Kuo HC, Lai CH, Chou CC. Single amino acid utilization for bacterial categorization. *Sci Rep*. (2020) 10:12686. doi: 10.1038/s41598-020-69686-5

86. Krysenko S WW. Polyamine and ethanolamine metabolism in bacteria as an important component of nitrogen assimilation for survival and pathogenicity. *Med Sci*. (2022) 10:40. doi: 10.3390/medsci10030040

87. Fu RY, Chen J, Li Y. The function of the glutathione/glutathione peroxidase system in the oxidative stress resistance systems of microbial cells. *Chin J Biotechnol*. (2007) 23:770–5. doi: 10.1016/S1872-2075(07)60048-X

88. Mohany NAM, Totti A, Naylor KR, Janovjak H. Microbial methionine transporters and biotechnological applications. *Appl Microbiol Biotechnol*. (2021) 105:3919–29. doi: 10.1007/s00253-021-11307-w

89. Varma TK, Lin CY, Toliver-Kinsky TE, Sherwood ER. Endotoxin-induced gamma interferon production: Contributing cell types and key regulatory factors. *Clin Diagn Lab Immunol*. (2002) 9:530–43. doi: 10.1128/CDLI.9.3.530-543.2002

90. Costello CM, Willsey GG, Richards AF, Kim J, Pizzuto MS, Jaconi S, et al. Transcytosis of igA attenuates salmonella invasion in human enteroids and intestinal organoids. *Infect Immun*. (2022) 90:e0004122. doi: 10.1128/iai.00041-22

91. Ledov VA, Golovina ME, Markina AA, Knirel YA, L'vov VL, Kovalchuk AL, et al. Highly homogenous tri-acylated S-LPS acts as a novel clinically applicable vaccine against Shigella flexneri 2a infection. *Vaccine*. (2019) 37:1062–72. doi: 10.1016/j.vaccine.2018.12.067

92. Pauli NT, Henry Dunand CJ, Wilson PC. Exploiting human memory B cell heterogeneity for improved vaccine efficacy. *Front Immunol*. (2011) 2:77. doi: 10.3389/fimmu.2011.00077

93. Gandhapudi SK, Chilton PM, Mitchell TC. TRIF is required for TLR4 mediated adjuvant effects on T cell clonal expansion. *PloS One*. (2013) 8:e56855. doi: 10.1371/journal.pone.0056855

94. Obukhanych TV, Nussenzweig MC. T-independent type II immune responses generate memory B cells. *J Exp Med*. (2006) 203:305–10. doi: 10.1084/jem.20052036

frontiers | Frontiers in Immunology

TYPE Original Research
PUBLISHED 06 January 2025
DOI 10.3389/fimmu.2024.1432989

OPEN ACCESS

EDITED BY
Jiae Kim,
Henry M. Jackson Foundation for the Advancement of Military Medicine (HJF), United States

REVIEWED BY
Victor C. Huber,
University of South Dakota, United States
Zachary Beau Reneer,
University of North Carolina at Chapel Hill, United States

*CORRESPONDENCE
Shuying Liu
liushuying1968@imau.edu.cn

RECEIVED 15 May 2024
ACCEPTED 11 December 2024
PUBLISHED 06 January 2025

CITATION
Zhang Y, Zhang P, Du X, Shi X, Wang J and Liu S (2025) A gram-positive enhancer matrix particles vaccine displaying swine influenza virus hemagglutinin protects mice against lethal H1N1 viral challenge.
Front. Immunol. 15:1432989.
doi: 10.3389/fimmu.2024.1432989

A gram-positive enhancer matrix particles vaccine displaying swine influenza virus hemagglutinin protects mice against lethal H1N1 viral challenge

Yufei Zhang[1,2,3], Pei Zhang[1,2,3], Xiaoyue Du[1,2,3], Xiaona Shi[1,2,3], Jinling Wang[1,2,3] and Shuying Liu[1,2,3]*

[1]College of Veterinary Medicine, Inner Mongolia Agricultural University, Hohhot, China, [2]Inner Mongolia Key Laboratory of Basic Veterinary Science, Inner Mongolia Agricultural University, Hohhot, China, [3]Key Laboratory of Clinical Diagnosis and Treatment Technology in Animal Disease, Ministry of Agriculture, Hohhot, China

Introduction: Animal influenza viruses pose a danger to the general public. Eurasian avian-like H1N1 (EA H1N1) viruses have recently infected humans in several different countries and are often found in pigs in China, indicating that they have the potential to cause a pandemic. Therefore, there is an urgent need to develop a potent vaccine against EA H1N1.

Methods: In this study, we report the effective intramuscular (i.m.) and/or intranasal (i.n.) vaccination of mice with a subunit influenza vaccine utilizing safe adjuvant gram-positive enhancer matrix (GEM) particles derived from the food-grade bacterium *Lactococcus lactis*. The hemagglutinin (HA)-protein anchor (PA) subunit vaccine can be simply mixed with GEM particles to produce vaccines.

Results: After two booster injections, the i.m.+i.n. administered GEM subunit vaccine achieved hemagglutination inhibition titers in the serum that were equivalent to those observed using the conventional i.m. method. The mucosal and Th1-biased immune responses generated by the i.m. administered subunit vaccine alone were inferior to those induced by the i.n. and i.m.+i.n. administered subunit vaccines. Vaccinated mice were challenged with live viruses (G4 EA H1N1 and A/PR/8/34) to determine whether the adjuvant combination protected against the virus after vaccination with the influenza subunit vaccine. Compared to mice inoculated with HA alone, mice immunized with i.m.+i.n. or i.n. HA-PA-GEM displayed undetectable viral titers in the lungs, at 5 d after challenge.

Discussion: Overall, this study not only offers other potential platforms for the generation of swine influenza vaccines, but also a theoretical foundation for vaccine vector platforms that can be utilized for future research on other infections.

KEYWORDS

influenza, swine influenza, vaccine, intranasal vaccine, gram-positive enhancer matrix (GEM) particles

1 Introduction

Due to their vulnerability to avian, swine, and human influenza A viruses (IAVs), pigs are regarded as "mixing vessels" for the creation of influenza viruses with the potential to cause a pandemic (1–4). Moreover, these reassortants may evolve mutations to adapt to humans, resulting in a human influenza pandemic (5). With the emergence of pdm/09H1N1, the global health threat posed by novel swine influenza viruses (SIVs) has been clearly illustrated (5, 6). There are several genotypes of Eurasian avian-like H1N1 (EA H1N1) swine IAVs in pigs in China, and recent findings suggest that the potentially pandemic genotype 4 (G4) reassortment has been predominant among swine populations in China since 2016 (4, 7, 8).

Despite its low mortality in swine herds, swine influenza is an economically significant respiratory infectious disease that causes high morbidity in pigs worldwide (7). Prevention of H1N1 SIVs will contribute to improving public health by reducing the risk of transmission from pigs to humans. Effective immunization is currently the most affordable public health measure for controlling SIV infections. Recently, various influenza vaccines have been developed for pigs, including inactivated whole-virus, live attenuated, subunit, and vectored vaccines (9, 10). Inactivated whole-virus vaccines are currently the most used and commercially accessible option for preventing SIV infections (11). Since influenza virus outbreaks are caused by the antigenic structure of the virus, hemagglutinin (HA) is a crucial component in the design of a vaccine against them (12). HA antigenic matching between the vaccine strain and prevalent strain is essential for the inactivated influenza vaccine to effectively protect against epidemic strains.

Vaccines using inactivated viruses and/or subunit vaccines frequently contain adjuvants to boost the strength and caliber of immune responses, while also accelerating the onset and lengthening the duration of protection. Numerous adjuvants can boost immune responses and encourage defense against infections with influenza virus strains that are similar to one another, in both humans and animals (9). The food-grade bacterium *Lactococcus lactis* (*L. lactis*) is heated and acidified to remove its DNA and most of its proteins, resulting in the formation of peptidoglycan spheres known as gram-positive enhancer matrix (GEM) nanoparticles (13, 14). This novel adjuvant technology of GEM particles can significantly increase the immunogenicity of vaccines (15–20). Toll-like receptor 2 recognizes GEM particles, which activate innate immunity and improve the capacity of the natural immune system to kill harmful microorganisms (13, 20). It has been found that the GEM-protein anchor (PA) surface display system, which uses a PA made from the *L. lactis* peptidoglycan hydrolase, AcmA, may efficiently elicit systemic immune responses, in addition to offering other advantages, such as quick and simple antigen purification (15–20). Recent studies of GEM particles have demonstrated their safety in the treatment of a number of pathogens, including shigellosis, human papillomavirus, porcine circovirus type 2, hepatitis E virus and foot-and-mouth disease virus (15–20). GEM particles are safe and effective adjuvants for intranasal (i.n.) and intramuscular (i.m.) injections during influenza subunit vaccination (20).

In this study, we examined how well BALB/c mice responded to i.m. and i.n. administration of an influenza subunit vaccine used in combination with GEM particles as an adjuvant. For this, we tested whether (a) the GEM particles had adjuvant/immunostimulatory activity for intranasal immunization; (b) the adjuvants enhanced mucosal and systemic immune responses to influenza; and (c) the mice were protected against a fatal EA H1N1 swine IAV challenge through the passive administration of influenza formulations that were or were not adjuvanted.

Abbreviations: EA H1N1, Eurasian avian-like H1N1; ELISA, Enzyme-linked immunosorbent assay; ELISpot, Enzyme-linked immunosorbent spot; GEM, Gram-positive enhancer matrix; HA, Hemagglutinin; HAI, Hemagglutination inhibition; HRP, Horseradish peroxidase; IAVs, Influenza A viruses; IFN-γ, Interferon gamma; IL, Interleukin; i.m., Intramuscular; i.n., Intranasal; LPS, lipopolysaccharide; MDCK, Madin-Darby canine kidney; NO, Nitric oxide; PA, Protein anchor; PBS, Phosphate-buffered saline; SIgA, Secretory IgA; SIVs, Swine influenza viruses; TNF-α, Tumor necrosis factor alpha; WIV, Whole-inactivated virus.

2 Materials and methods

2.1 Viruses, cells, and bacterial strains

The G4 EA H1N1 swine isolate [A/swine/Jiangsu/65/2015 (H1N1)] and influenza virus A/PR/8/34 (HIN1) were kindly provided by Meilin Jin (21). Allantoic inoculation of the seed virus was performed to cultivate the virus in embryonated chicken eggs. The virus was purified and inactivated as previously described, to obtain whole-inactivated virus (WIV) vaccines (22, 23). In brief, the G4 EA H1N1 swine isolate culture supernatant was treated with 0.1 M β-propiolactone (BPL) (P5648, MilliporeSigma, USA) for overnight viral inactivation at 4°C. BPL was then hydrolyzed at 37°C for 90 minutes. Inactivated viruses were concentrated by ultracentrifugation at 50,000 g for 2 h and purified using a 20-60% sucrose density gradient. Total protein of the purified viruses was quantified with a bicinchoninic acid (BCA) protein assay kit (Sangon Biotech, Shanghai, China). Madin-Darby canine kidney (MDCK) and RAW 264.7 (mouse macrophage) cells were obtained from the American Type Culture Collection (ATCC). The cells were cultured in Dulbecco's Modified Eagle's Medium (Gibco, Shanghai, China), at 37°C, in an incubator containing 5% CO_2. Adherent Spodoptera frugiperda (Sf9) cells (Life Technologies, USA) were cultured at 27°C and maintained in SFM 900 II medium (Life Technologies, Beijing, China) supplemented with 10% heat-inactivated fetal bovine serum and 1% penicillin-streptomycin. *L. lactis* MG1363 was purchased from the China Committee for Culture Collection of Microorganisms (Beijing, China). Standing cultures of the cells were maintained at 30°C in M17 medium containing 1% glucose.

2.2 GEM preparation

The *L. lactis* strain MG1363 was cultured overnight and harvested. The cells were then washed with sterile distilled water, following which hydrochloric acid (HCl; 0.1 M) was added to them,

and they were placed in a hot water bath for 30 min, at 99°C. The bacteria were killed by treatment with acid and heat, to generate the GEM particles. After three washes with PBS, the GEM particles were diluted to one unit (1 U=2.5×10^9 particles/mL) and stored at −70°C.

2.3 Transmission and scanning electron microscopy

For transmission electron microscopy, the *L. lactis* strain MG1363 and GEM particles were centrifuged to obtain precipitates, which were reconstituted in sterile filtered water following fixation with 2% glutaraldehyde (no suspension), overnight at 4°C. A simple carbon grid was used to hold the *L. lactis* MG1363 and GEM formulations. After placing on the grid, the samples were washed with water and stained twice with 5 µL of 2 wt% uranyl acetate. Images of the samples were captured with an UltraScan 4000SP CCD camera (Gatan).

Particles of *L. lactis* strains MG1363 and GEM were deposited on a metal disc using double-sided adhesive carbon tape and coated with approximately 10 nm of gold using a Balzer's 120B sputtering apparatus (Balzer UNION, Liechtenstein). Following that, the *L. lactis* strain MG1363 and GEM preparations were imaged using a JEOL JSM 6301-F microscope (JEOL Ltd., Tokyo, Japan), at magnifications of 500× and 5000×.

2.4 Particle size analysis

A Litesizer™ 500 system (Anto Paar, Austria) was used to analyze the particle size of the *L. lactis* strain MG1363 and GEM particles (at a dilution factor of 1:100), with distilled water used as the diluent.

2.5 Nitrite assay

The nitrite assay has been described in detail elsewhere (24). RAW 264.7 cells were stimulated with 0.1, 0.5, or 1 U doses of GEM particles, and the culture supernatants were collected 48 h after incubation, to measure the nitric oxide (NO) levels. While the cells in the negative control group received only cell culture medium, those in the positive control groups were stimulated with Pam3CK4 or lipopolysaccharide (LPS), at concentrations of 0.1, 1, or 10 µg/mL. Griess assay was used to measure NO production, according to the manufacturer's protocol (Promega, Madison, WI, USA).

2.6 Quantitative real-time PCR

Total RNA extraction from the samples was carried out using TRIzol® (Invitrogen, Beijing, China), as per the manufacturer's instructions. Conventional and quantitative real-time PCR (qRT-PCR) assays were conducted on the extracted RNA following cDNA synthesis. SYBR® Premix Ex Taq™ (Tli RNase H Plus; Takara, Dalian, China) was used for qRT-PCR, to examine the expression of nitric oxide synthase (iNOSl), interleukin (IL)-1, interferon gamma (IFN-γ), tumor necrosis factor alpha (TNF-α), and IL-6 on an ABI 7500 system (Applied Biosystems, USA). Relative gene expression was analyzed based on the threshold cycle ($2^{-\Delta\Delta CT}$) method, with GAPDH used as an internal control. Three independent experiments were conducted. The qRT-PCR primers used are listed in Supplementary Figure 1 (21, 25).

2.7 Immunohistology

All mouse heads were fixed in 10% neutral-buffered formalin for 48 h, after being skinned. Six pieces were cut from the tip of the nose to the foramen occipitale magnum using a diamond saw. The sections were gently decalcified for 7 d, at room temperature, in an RDF Mild Decalcifier (CellPath Ltd., The United Kingdom). The tissues (lungs and thymus) were fixed in 10% neutral-buffered formalin for 72 h, before being transferred to 70% ethanol for paraffin embedding. The implanted tissues were routinely divided into sections that were 3~4 µm thick, stained with Masson's trichrome as well as hematoxylin and eosin, and then examined by a veterinary pathologist. As previously described (4, 25, 26), immunohistochemistry was carried out using the horseradish peroxidase (HRP) method. Sections of 5 µm were cut, deparaffinized in xylene, rehydrated in graded alcohol, and microwaved in sodium citrate buffer (pH 6.0) for antigen retrieval. Endogenous peroxidase activity was blocked with 3% H_2O_2 for 15 min, and the lung tissue sections were then blocked with 5% BSA for 30 min, both at room temperature. The samples were incubated with Rat anti-mouse cluster of differentiation (CD) 45R (clone B220; BD Biosciences; B cells), rabbit anti-CD3 [ab16669; Abcam (Shanghai, China); T cells], and rabbit anti-Iba-1 (ab178847; Abcam; macrophages and dendritic cells) for 14 h at 4°C. The slides were incubated with a secondary antibody using the ImmPRESS™ HRP Universal Antibody Polymer Detection Kit (Vector Laboratories, MP-7500) for 1 hour at room temperature. After 25 seconds of DAB staining and 30 seconds of counterstaining with hematoxylin in 1% ammonia solution, the slides were mounted with VectaMount medium, examined, and photographed using an Olympus BX41 microscope. Images were acquired using cellSens software (Olympus). 5 random sections were chosen for the intensity quantification. The marker staining intensities were evaluated by relative quantification using digital image analysis platform DefiniensTissueStudio (Definiens AG).

2.8 Construction and expression of recombinant baculoviruses

The HA sequence (GenBank: OL468248.1) of the G4 EA H1N1 swine isolate and PA sequence from the *L. lactis* MG1363 strain were retrieved and synthesized by Sangon Biotech (Shanghai, China). A 6×His-tag and flexible linker sequence were added to the N- and C-termini of the HA gene, respectively, and then cloned into the pFastBac1 vector, immediately downstream of a cassette

encoding an envelope glycoprotein signal peptide (gp64) from the nucleopolyhedrovirus *Autographa californica* (Figure 1A). A full-length HA protein without the signal peptide, transmembrane, or internal motif was expressed in this study, corresponding to amino acids 20–530 (GenBank: OL468248.1).

PFastBac1-HA-PA was transformed into *Escherichia coli* DH10Bac competent cells to generate recombinant bacmids. The recombinant baculovirus was created by transiently transfecting the recombinant bacmid into Sf9 insect cells with Cellfectin® II (Life Technologies), as directed by the manufacturer. First-generation (P1) recombinant baculovirus-containing supernatants were collected 72 h after transfection and passed through three generations of Sf9 cells to produce the fourth-generation (P4) recombinant baculoviruses. In the culture supernatant, HA-PA was expressed as a soluble secreted protein. To express recombinant proteins, 2×10^6 cells/mL of Sf9 cells were infected with amplified high-titer recombinant HA-PA baculoviral stocks at 5% (a multiplicity of index of ~3). Expression was carried out at 27°C for 72 h, on an orbital shaker rotating at 120 rpm. Similarly, HA expression was done in Sf9 cells using the pFastBac baculovirus system. The procedure was identical to the above. The only difference between HA and HA-PA is the missing PA tag. The protein was purified from the supernatant while the cell pellet was discarded.

2.9 Purification of recombinant proteins

To optimize the expression of recombinant HA-PA or HA protein in scaled-up 1L cultures, Sf9 cells were cultured in shaking flasks with orbital rotation at 125 rpm at 27°C and subsequently infected with P3 baculoviral stock. After 72 hours, the recombinant HA-PA or HA protein was purified from the supernatant, with the cell pellet being discarded. The purification process was conducted using Ni-NTA-affinity chromatography (BIOFOUNT, Beijing,

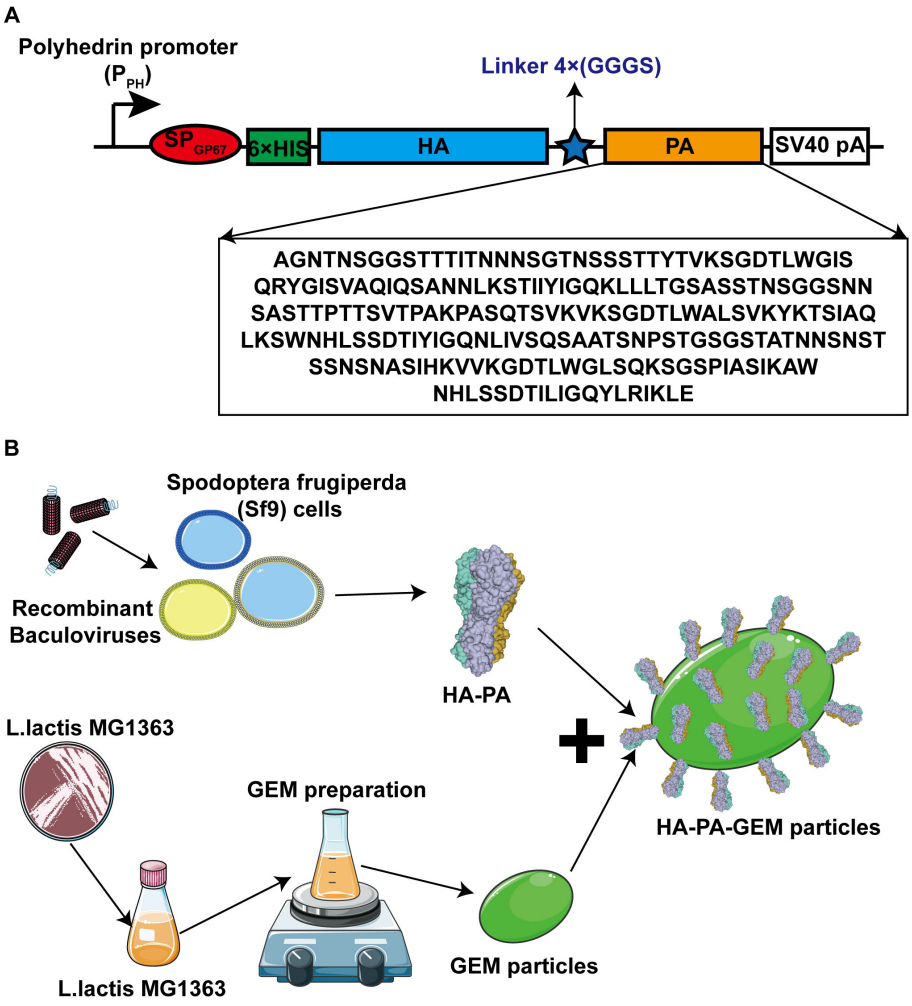

FIGURE 1
Schematic diagrams of antigen design and HA-PA protein binding to GEM particles. **(A)** The secreted signal peptide gp67 was added to the N-terminal of HA in both the constructs. The PA sequence was added after the HA sequence, and a 6×His tag was added to the C-terminal of gp67. **(B)** Combination diagram of HA-PA protein binding to GEM particles. HA, hemagglutinin; GEM, gram-positive enhancer matrix; PA, protein anchor.

China) in accordance with the manufacturer's instructions. The supernatant was subjected to purification using a Ni-NTA column (10 mL, 1.6 × 5 cm) at a flow rate of 1 mL/min. The column was sequentially washed with washing buffer 1 (PBS, pH 7.4), washing buffer 2 (25 mmol/L imidazole in PBS, pH 7.4), and washing buffer 3 (70 mmol/L imidazole in PBS, pH 7.4). Subsequently, the recombinant HA-PA or HA was eluted using a stepwise imidazole gradient ranging from 200 to 400 mM in PBS (pH 7.4). The concentration of the purified HA-PA or HA was quantified using the bicinchoninic acid (BCA) assay.

2.10 Binding of the fusion protein to GEM particles

The HA-PA-GEM particles were assembled in a single step at room temperature, as shown in Figure 1B. Three days after injecting the recombinant baculovirus into Sf9 cells at a multiplicity of index of 3, the cells were harvested by means of centrifugation (1600 × *g* for 30 min), and the supernatant was collected. The purification process was conducted using Ni-NTA-affinity chromatography (BIOFOUNT, Beijing, China) in accordance with the manufacturer's instructions. Subsequently, 5 μg/μL HA-PA fusion protein was mixed with 1 U GEM particles (2.5×10^9) at room temperature, for 1 h, in a rotational shaker. To acquire the fusion-GEM complexes, the precipitate was centrifuged at 6000 × *g* for 10 min, washed five times with PBS, and then resuspended in PBS. Samples were then analyzed by Western blot.

2.11 Western blot and immunofluorescence assay

To study antibody binding, the proteins were resolved on a 10% w/v polyacrylamide gel and then transferred to a polyvinylidene difluoride membrane. The blots were blocked with 5% skim milk powder in PBS before being incubated with 0.5 μg/mL of an anti-6×His-tag monoclonal antibody diluted in 1% skim milk powder in PBS, overnight at 4°C. The blots were then incubated with HRP-conjugated rabbit anti-mouse immunoglobulin G (IgG) from Abcam (diluted 1:10000 with 1% skimmed milk powder in PBS) for 1 h, at room temperature. Chemiluminescence was detected using the Clarity Western ECL Substrate Kit (Bio-Rad, UK). To further evaluate the antigenicity of HA-PA, positive sera from A/swine/Jiangsu/65/2015 (H1N1) were employed as the primary antibody. The sera were obtained 20 days following infection of pigs with A/swine/Jiangsu/65/2015 (H1N1). The secondary antibody employed was goat anti-pig IgG H&L (Abcam, ab6910, Shanghai, China).

For the immunofluorescence assay (IFA), the centrifuged HA-PA-GEM complex precipitate was suspended and blocked with 5% non-fat milk in Eppendorf tubes. Next, the cells were stained with an anti-6×His-tag monoclonal antibody (1:200) as the primary antibody and FITC-conjugated anti-mouse IgG (1:400) as the secondary antibody. A fluorescence microscope was used to view the dyed complexes on slides (Olympus Corp., Tokyo, Japan).

2.12 Hemagglutination assay

Hemagglutination assays were performed as described previously (16). The HA-PA-GEM complex were reconstituted in PBS to a concentration of 25 μg/mL, and 50 μL of this preparation was added to 96-well V bottom plates already containing 50 μL of PBS. Following a two-fold serial dilution of the entire mixture, 50 μL of a 1.5% adult chicken erythrocyte suspension were added to each well, and the plates were then stored at room temperature for 2 h. The maximum dilution at which red blood cell agglutination was observed was used to express the hemagglutination titers, which were read after 2 h.

2.13 Animal study design

2.13.1 Vaccine immunizing evaluation

The Committee for Animal Experiments of the Inner Mongolia Agricultural University in China examined and authorized the animal research, in compliance with the provisions of the Chinese Animal Protection Act. BALB/c mice (6–8-weeks old) were purchased from Beijing Vital River Laboratory Animal Technology Co. Ltd. The female mice were divided into nine groups (i.n. PBS group, i.m. PBS group, i.n. GEM group, i.m. GEM group, i.m. HA subunit vaccine group, i.m. WIV, i.m. HA-PA-GEM group, i.n. HA-PA-GEM group, i.m.+i.n. HA-PA-GEM group) of eight each. These experimental animals are mainly used to study the immune response to vaccines. In order to immunize mice with an i.m. vaccine, a dose of the vaccine contained 1.5 μg of whole-inactivated virus antigen in 25 μL of phosphate-buffered saline (PBS) containing 25 μL of adjuvant AddaVax (vac-adx-10, InvivoGen) (per mouse in 50 μL). HA subunit vaccine group mice were injected with HA protein (0.2 μg/μL) was mixed with an equal volume of incomplete Freund's adjuvant (Sigma-Aldrich, Shanghai, Chain) (per mouse in 50 μL). Immediately before vaccination, the GEM particles and HA-PA were mixed. Under inhalation anesthesia (isoflurane/O_2), the test group received 25 μL of GEM-adjuvanted vaccination, through the i.n. or/and i.m. routes [12 uL of the 1U per mL of GEMs combined with 5 μg HA-PA]. The animals were administered the vaccine on three occasions, at days 0, 14, and 28, via the intramuscular route and subsequently humanely euthanized on day 40 of the trial.

On day 40, the mice were euthanized, after which their orbital plexus was punctured to collect blood for antibody measurements. Bronchoalveolar lavage fluid was collected to assess the secretory IgA (SIgA) antibodies. Briefly, the lungs from sacrificed mice were flushed three times with 1 mL PBS, then centrifuged at 3,500 g for 10 minutes. Roche's "complete" protease inhibitor was used in 1 mL of PBS, as per the manufacturer's instructions, for the bronchoalveolar lavage fluid. All lavage samples were stored at −20°C.

2.13.2 Viral challenge

In the present study, two animal studies were performed to investigate protection against heterologous challenge by H1N1 viruses with different antigens (Supplementary Figure 1). In study 1, 80 BALB/c mice aged 6-8 weeks were divided into 10 groups (Supplementary Figure 2). The intramuscular vaccination groups included mock vaccine control group (PBS), HA subunit vaccine group (HA), WIV group, GEM group and HA-PA-GEM group. These mice were nasally inoculated with the G4 EA H1N1 swine isolate (1×10^5 $TCID_{50}$/0.1 mL) via 2.5% avertin (0.02 mL/g body weight) 1 week after the third immunization, and negative controls were treated with 0.9% saline. The intranasal vaccination groups included blank control (PBS), HA subunit vaccine (HA) group, GEM group, HA-PA-GEM group, i.m.+i.n. HA-PA-GEM group. Similarly, these mice were nasally inoculated with the G4 EA H1N1 swine isolate (1×10^5 $TCID_{50}$/0.1 mL) via 2.5% avertin (0.02 mL/g body weight) 1 week after the third immunization, and the negative control group was treated with 0.9% saline.

In study 2, 48 BALB/c mice aged 6-8 weeks were divided into 6 groups (Supplementary Table 2). The intramuscular vaccination groups included blank control (PBS), WIV group and HA-PA-GEM group. These mice were nasally inoculated with influenza virus A/PR/8/34 (HIN1) (1×10^5 $TCID_{50}$/0.1 mL) via 2.5% avertin (0.02 mL/g body weight) 1 week after the third immunization, and the negative control group was treated with 0.9% saline. The intranasal vaccination groups included blank control (PBS), HA-PA-GEM group, i.m.+i.n. HA-PA-GEM group. Similarly, these mice were nasally inoculated with influenza virus A/PR/8/34 (HIN1) (1×10^5 $TCID_{50}$/0.1 mL) via 2.5% avertin (0.02 mL/g body weight) 1 week after the third immunization and the negative control group was treated with 0.9% saline.

2.14 Enzyme-linked immunosorbent assay for detection of HA-specific antibodies

Serum, and bronchoalveolar lavage fluid samples were collected on 12 day after 3rd immunization, and ELISA was performed to detect HA-specific antibodies in them, as described previously (21). Antigen-specific serum IgG and SIgA antibodies were also detected using ELISA. Whole-inactivated H1N1 virus (100 µL/well) was diluted to a concentration of 10 µg/mL in carbonate-bicarbonate buffer (pH 9.6), and then used to coat 96-well plates, overnight at 4°C. Following that, the wells were blocked with 250 µL of 2% bovine serum albumin in PBS, at 37°C, for 3 h. We diluted the serum samples 100-fold and lavage samples 20-fold. The diluted samples were added to the wells, maintained to 37°C for 2 h, and then rinsed three times with PBS containing Tween-20. The plates were blotted with 100 µL each of HRP-conjugated goat anti-mouse IgG and IgA alpha chain antibodies from Abcam, for 1 h, at room temperature. After this incubation, the wells were washed three times with a 100 µL wash solution. After 15 min of dark incubation at 37°C with a 3,3,5,5′-tetramethylbenzidine substrate solution in sterile water, the bound antibodies were detected. After addition of 100 µL of stop solution to halt the enzyme process, the absorbance of each microwell at the wavelength of 450 nm was measured using a spectrophotometer. Two independent tests were performed.

2.15 Hemagglutination inhibition and microneutralization assays

We carried out an HAI test to assess the titers of HA antigen-specific antibodies in the sera or bronchoalveolar lavage fluid of unvaccinated and immunized mice. To inactivate nonspecific inhibitors, the serum samples were pre-treated with a receptor-destroying enzyme (RDE) obtained from Denka Seiken Company, Chuo, Tokyo, before testing. Specifically, three volumes of RDE were combined with one volume of serum and incubated overnight at 37°C. Subsequently, the RDE was inactivated by incubating the serum-RDE mixture at 56°C for approximately 45 minutes. Before being incubated in 96-well microtiter plates with 4 HA units for 30 min at 37°C, the serum or bronchoalveolar lavage fluid samples were serially diluted twice with PBS. Thereafter, an equal volume of fresh, 1% (v/v), chicken red blood cells were added, and the mixture was incubated at 37°C for 30 min. For descriptive and analytic statistics, the assay limit of detection was set at 1:10 for HAI titers. The HAI titer was measured from the highest dilution showing non-agglutinated RBCs. Each plate included positive and negative serum controls. Initially, mice had no antibodies (HAI titer <1:10) against the four vaccine viruses. Positive control pig sera (G4 EA H1N1 swine isolate) and negative controls (antigen-alone wells and PBS with RBCs) were used in the assay.

The viral neutralization experiment was performed as mentioned previously (21). Serum neutralizing antibody titers were measured by seeding 1.5×10^4 MDCK cells per well into 96-well culture plates, and growing them at 37°C in a 5% CO_2-containing incubator, to form a monolayer. Serial two-fold dilutions of blood samples were prepared in 96-well cell culture plates containing Dulbecco's Modified Eagle's Medium with 0.3% bovine serum albumin, 100 U/mL penicillin, and 100 µg/mL streptomycin (starting dilution of 1:10). Thereafter, an identical volume (50 µL) of diluted virus with 100 $TCID_{50}$ was fixed to the diluted serums, and the mixture was incubated for 1 h, at 37°C. We added 100 µL of serum and virus mixture to 96-well plates containing 90% confluent monolayers of MDCK cells, and then incubated the plates at 37°C for 48 hours. After 48 h, the cell supernatant was collected and an hemagglutination test was carried out.

2.16 Splenocyte proliferation and cytokine assay

Splenocytes were harvested from the spleens of three mice (The samples were collected on 12 day after 3rd immunization) and their proliferation was measured (21). For this, splenocytes (1.0×10^6) were seeded into each well of a 96-well microwell plate, with recombinant H1N1 HA antigen (the G4 EA H1N1 swine isolate, GenBank: OL468248.1) (10 ng/mL) as the specific antigen for the

vaccine groups and concanavalin A (10 ng/mL) as the positive control, or without stimulation. They were then stimulated for 48 h at 37°C in a humidified environment containing 5% CO_2. Each mouse sample was examined in triplicate. The MTT assay was used to measure cell viability (21).

Splenocyte stimulation and cytokine analysis were performed as previously described (21). We evaluated the concentrations of Th1 (IFN-γ and IL-12) and Th2 (IL-4) cytokines in the supernatants of splenocytes from control and test animals, in accordance with the manufacturer's instructions, using commercially available cytokine-specific ELISA kits (R&D Systems, Shanghai, China).

2.17 IFN-γ and IL-4 enzyme-linked immunosorbent spot assays

Splenocytes were isolated from the vaccinated mice after the third vaccination. In a 96-well ELISpot plate, 1×10^6 splenocytes were grown with pure H1N1-HA antigen (the G4 EA H1N1 swine isolate, GenBank: OL468248.1) (20 μg/mL). The cells were grown for 24 h in preparation for the ELISpot assay and then detected using a commercial kit (MABTECH, Nacka, Sweden), in accordance with the manufacturer's instructions. The spot-forming cells were counted using an automated ELISpot reader (ELISPOT reader iSpot, AID, Germany).

2.18 Viral challenge, clinical observation, and histopathological examination

We anaesthetized mice with 2.5% avertin (0.02 mL/g body weight) and then i.n. inoculated them with G4 EA H1N1 swine isolate or A/PR/8/34 (HIN1) (1×10^5 $TCID_{50}$/0.1 mL). All mice were monitored for general physical activity and pathophysiological measures, to determine the protective effects of the HA-PA-GEM particles (body weight, fur ruffling, and conjunctivitis). Clinical scoring was conducted by an individual who was blinded to both the study design and the identity of the animals. The scoring was based on the following scale: 0 = no visible signs of disease; 1 = slight ruffling of fur; 2 = ruffled fur with reduced mobility (2 points for 10-15% weightloss); 3 = ruffled fur, reduced mobility, and rapid breathing (3 points for 15-20% weightloss); 4 = ruffled fur, minimal mobility, huddled appearance, and rapid and/or labored breathing (4 points for 20-30% weightloss); 5 = euthanasia (A weight loss of greater than 30% was deemed to be a reason for euthanasia.).

The mice were observed daily for signs of distress by monitoring their general appearance, respiratory distress, weight loss and animal survival. Mice that lost more than 30% of their initial body weight were humanely euthanized by carbon dioxide inhalation and cervical dislocation. The sole criterion employed to ascertain whether mice should be euthanized was their body weight. One half of the lung was fixed for histopathological analysis. One half of the lung of virus were titered using median tissue culture infectious dose 50 (TCID 50) assay. For histopathological analysis, lungs were collected on the seventh day post-infection (n = 2), then inflated and fixed with 10% neutral buffered formalin (NBF). For TCID 50 analysis, the lungs were weighed before homogenization in Hanks balanced salt solution (HBSS) and centrifugation at 500 g for 5 minutes. With MDCK cells, TCID 50 tests were conducted to determine virus titers.

Mice from each group had their lungs preserved in 10% neutral-buffered formalin, embedded in paraffin according to accepted practices, sectioned to a thickness of 4 mm, and stained with hematoxylin and eosin. The slides were examined under a light microscope (EX200, Nikon) to detect histological lung lesions. The participants in the evaluation were all postgraduate students in veterinary pathology, and none of them had any prior knowledge of the experiment. The histological assessment criteria for lung damage are categorized into three distinct groups, yielding a cumulative score of up to 10 points per specimen. The evaluation of pulmonary edema involves an examination of both the location and severity of edema within the lung tissue, with a scoring range from 0 (indicating no edema) to 3 (indicating diffuse alveolar space edema affecting multiple lung lobes). Specifically, the scoring is delineated as follows: a score of 1 denotes alveolar wall edema confined to a single lobe, a score of 1.5 indicates alveolar wall edema present in more than one lobe, a score of 2 represents diffuse edema within a single lobe, and a score of 3 corresponds to diffuse edema across multiple lobes. Alveolar infiltration is assessed to determine the extent of infiltration within the alveolar septa and spaces. The evaluation utilizes a scoring system ranging from 0 to 3, where 0 indicates no infiltration and 3 denotes diffuse alveolar space infiltration affecting more than one lobe. The specific scores are defined as follows: a score of 1 corresponds to peribronchiolar and/or perivascular infiltration; a score of 1.5 indicates similar infiltration with localized involvement of the alveolar walls; a score of 2 represents significant tissue consolidation within a single lobe; and a score of 3 signifies extensive infiltration across multiple lobes. Pulmonary vasculitis quantifies the extent of inflammation within vascular structures, utilizing a scoring system that ranges from 0 (indicating no inflammation) to 4 (denoting extensive infiltration across multiple lobes). The criteria for these scores are as follows: a score of 1 corresponds to the presence of perivascular edema and/or infiltration; a score of 2 indicates mild infiltration of the vessel wall without endothelial involvement; a score of 3 signifies intensive infiltration of the vessel wall and/or endothelium confined to a single lobe; and a score of 4 reflects similar intensive infiltration affecting multiple lobes.

2.19 Statistical analysis

The data were collected from at least three different experiments and displayed as mean ± standard error of mean. The assays were conducted in triplicate, with at least three independent biological replicates. The reactions were performed in triplicate on each of two biological replicates. Differences were examined using Prism (GraphPad version 5.0). One-way analysis of variance with Bonferroni's *post-hoc* multiple comparison test was used to determine the statistical significance of differences in cytokine, IgG and SIgA levels between the experimental groups at different

time-points. The survival percentages were examined using the Kaplan-Meier technique. A *p*-value of ≤0.05 was considered statistically significant.

3 Results

3.1 Induction of NO production and gene expression in macrophages by GEM particles

Hot TCA treatment of *L. lactis* MG1363 resulted in the generation of non-living particles (GEM particles), most likely by influencing the protein and DNA content of the GEM particles. The GEM particles had the same size and shape as live *L. lactis* MG1363 (Supplementary Figures 2A–D). Hot TCA treatment causes unraveling of the peptidoglycan, which is widely found on the cell wall of *L. lactis* MG1363 and preserves its structural integrity (13–20).

The objective of this study was to investigate the impact of GEM particles on macrophages. To this end, RAW 264.7 cells were stimulated with doses of GEM particles at 0.1, 0.5, or 1 U, and the culture supernatants were collected 48 hours after incubation to measure the nitric oxide (NO) levels. RAW 264.7 cells were treated with three different concentrations of LPS or Pam3CK4 (as positive controls) for 48 h. NO production was measured as a marker of macrophage activation. GEM-stimulated macrophages produced considerably higher nitrite concentrations than unstimulated controls ($p<0.001$) (Figure 2A).

We also examined the iNOSl, IL-1β, IL-6, IFN-γ, and TNF-α mRNA levels in the GEMs(1U)-, LPS(10 μg/mL)-, and Pam3CK4 (10 μg/mL)-stimulated RAW 264.7 macrophage cells. At 12 h post-treatment, iNOSl expression in cells treated with GEMs, LPS, and Pam3CK4 was upregulated by 20.8- ($p<0.001$), 54.2- ($p<0.001$), and 17.6-fold ($p<0.001$), respectively (Figure 2B); IL-1β expression was upregulated by 13- ($p<0.001$), 9.5- ($p<0.001$), and 12.6-fold ($p<0.001$), respectively (Figure 2C); IL-6 expression was

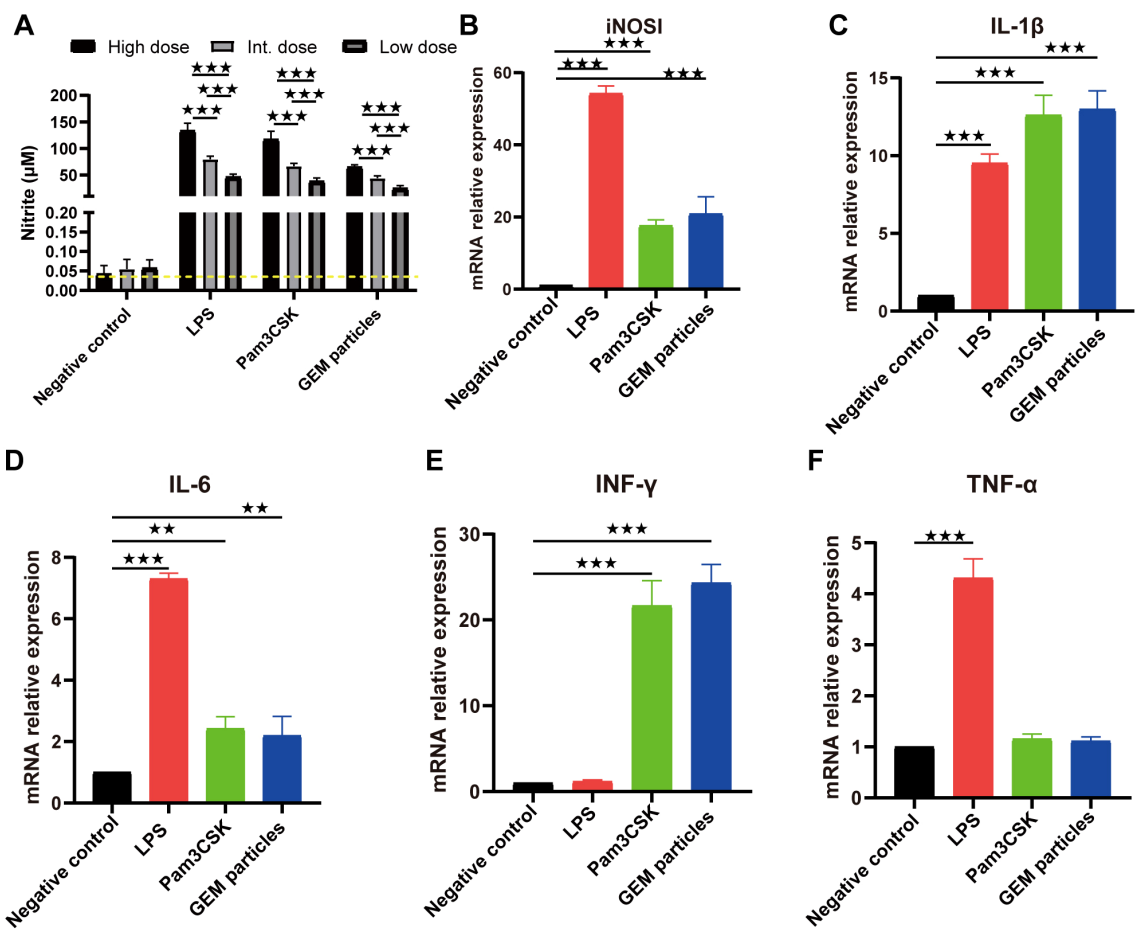

FIGURE 2
Nitrite production and mRNA expression in RAW 264.7 cells stimulated with GEM particles. **(A)** Nitrite levels in the supernatants were measured using the Griess assay, after 48 h of stimulation. RT-qPCR was performed for iNOSl **(B)** and the cytokines IL-1β **(C)**, IL-6 **(D)**, IFN-γ **(E)**, and TNF-α **(F)**. The gene expression was quantitated relative to that of the housekeeping gene GAPDH. The analysis was performed with a one-way ANOVA. Differences were considered significant at **p<0.01, ***p<0.001, as compared to the respective control cells. The experiment was performed in triplicate. iNOSl, nitric oxide synthase; IL, interleukin; IFN-γ, interferon gamma; TNF-α, tumor necrosis factor alpha; GEM, gram-positive enhancer matrix.

upregulated by 2.2- ($p<0.01$), 7.3- ($p<0.001$), and 2.4-fold ($p<0.01$), respectively (Figure 2D); IFN-γ expression was upregulated by 24.3- ($p<0.001$), 1.2- ($p>0.05$) and 21.7-fold ($p<0.001$), respectively (Figure 2E); and TNF-α expression was upregulated by 1.1- ($p>0.05$), 4.3- ($p<0.001$) and 1.2-fold ($p>0.05$), respectively (Figure 2F). These results indicated that GEM particles activated macrophages to induce inflammatory cytokines.

3.2 GEM particles have inherent adjuvanticity

Adjuvants are frequently added to inactivated, split virus vaccines, and nanoparticulate subunit vaccines, to improve their immunogenicity and reduce the number of doses and amount of antigen (or pathogen component) required to elicit a protective immune response, particularly in immunocompromised individuals (27–29). i.n. administration of GEM in PBS was used to test the adjuvant effects of the GEMs in this study. Under inhalation anesthesia (isoflurane/O_2), the test group received of GEM, through the i.n. routes [2.5×10^9 GEM particles (1 U)]. The control group was substituted with PBS. The head and thoracic organs were removed *en bloc* after 5 d and histologically and immunohistologically investigated (Figure 3; Supplementary Figure 3) for the presence of organized lymphoid structures and follicles that signify an active immune response. Both the nasal cavity (nasal-associated lymphoid tissue) in Figures 3A–D and lungs (bronchus-associated lymphoid tissue, BALT) in Figures 3E–H feature large structured lymphoid follicles, including dendritic cells, T cells, and a considerable number of B cells. It was demonstrated that the administration of GEM via the intranasal route in mice resulted in an increase in the number of B cells within the nasal passages and lungs, as well as T cells and dendritic cells in lungs. The number of nasal T cells and dendritic cells remained unaltered. These immunological changes were not observed in mice treated with PBS alone (Figure 3). We also evaluated the cytotoxic effects of various doses of GEM administered i.n. (Supplementary Figure 4). The findings suggest that the quantity of GEM particles employed should not exceed 5 U (equivalent to 2.5×10^9 GEM particles, or 1 U) per mouse (20 g) to guarantee the well-being of the mice. In conclusion, GEM particles have inherent adjuvanticity and native GEM particles can be i.n. administered with no negative health consequences and no tissue pathology visible in the treated animals postmortem, from a bio-safety perspective.

3.3 Expression of H1N1 HA-PA fusion protein and identification of HA-PA-GEM particles

Transfection of Sf9 cells with the recombinant bacmid pFBac-H1N1-HA-PA led to effective recovery of the recombinant baculovirus, Bac-H1N1-HA-PA. Compared to the control cells, Sf9 cells expressing the HA-PA fusion protein showed strong red fluorescence (Figure 4A). Moreover, a 100 kDa band matching the HA-PA fusion protein was detected upon western blot analysis of the cell lysate from Sf9 cells infected with the recombinant baculovirus, thus demonstrating its expression (Figure 4B). This result suggested that the HA-PA protein reacted well with seropositive swine H1N1 samples, with good antigenicity.

HA-PA-GEMs were subjected to both immunofluorescence (Figures 4C, D) and western blot (Figure 4E) analyses, to confirm whether the HA-PA fusion protein was capable of binding to GEM particles via PA. Immunofluorescence analysis results showed that, compared to GEM particles alone (Supplementary Figure 5A), the combination of GEM particles and HA-PA fusion protein emitted strong green fluorescence (Figure 4C) upon staining with anti-6×His-tag monoclonal antibody. Likewise, compared to GEM particles alone (Supplementary Figure 5B), the combination of GEM particles and HA-PA fusion protein emitted strong red fluorescence (Figure 4D) in samples seropositive for swine H1N1. In addition, western blot analysis confirmed that the GEM particles alone contained no detectable HA-PA fusion protein, as expected. HA-PA-GEMs confirmed the presence of the H1N1-HA-PA fusion protein (Figure 4E). The HA-PA fusion protein was linked to GEM particles according to the aforementioned data. Furthermore, an HA assay was performed to determine whether the receptor-binding activity of HA was still present. The inclusion of GEM particles resulted in an increase in the hemagglutination titers, thereby demonstrating that GEM particles had a positive impact on the biological activity of HA (Figure 4F).

3.4 Serum influenza-specific IgG levels after immunization with HA-PA-GEM particles

i.m. or i.n. immunization with HA-PA-GEM particles was performed on eight groups of mice, with control animals receiving PBS alone. The animals in each group received a primary vaccination, two follow-up immunizations at 2 and 4 weeks later, and weekly serum collection until one week after the third repeat immunization (Figure 5A). After immunization, the mice exhibited no abnormalities or negative effects. BALB/c mice immunized with HA-PA-GEM particles were found to have HA protein-specific IgG specific to the G4 EA H1N1 swine isolate (Figure 5B), while those immunized with PBS did not.

The response was further characterized by determining IgG isotypes. At week 6, we measured the quality of the humoral response using IgG2a, IgG2b, and IgG1 subtype-specific H1N1 ELISAs (Figures 5C–E). According to earlier research (4–6), a strong IgG1 response was induced by subunit vaccine i.m. immunization, but low IgG2a and IgG2b responses occurred, indicating a skewed Th2-type response. After i.n.+i.m. immunization with HA-PA-GEM, IgG2a and IgG2b responses were significantly higher ($p<0.001$) compared to i.m. immunization with HA-PA-GEM, while IgG1 responses were significantly lower ($p<0.001$) compared to i.m. immunization with HA-PA-GEM. HA-PA-GEM induced a different nature of

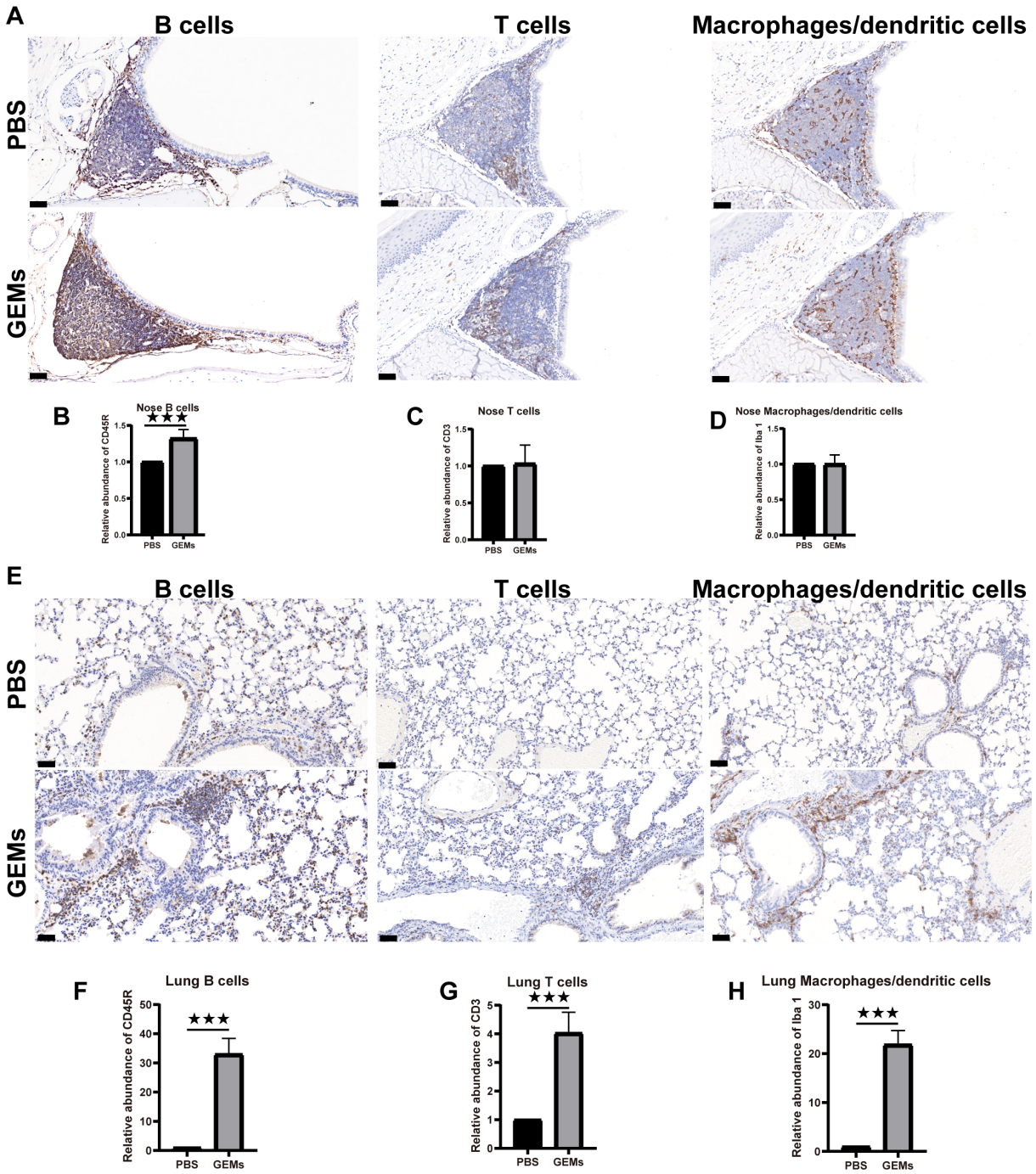

FIGURE 3
Intrinsic adjuvanticity of the GEMs. **(A)** The mice were intranasally administered PBS alone or GEMs in PBS. Five days later, the mice heads were processed for immunohistology, to visualize immune cell activation and formation of organized lymphoid tissue containing CD45R+ B cells (B220) **(B)**, CD3+ T cells (CD3), (C) and macrophages/dendritic cells (Iba-1) (D) in the nasal-associated lymphoid tissue. **(E)** The lungs were processed for immunohistology, to visualize immune cell activation and formation of organized lymphoid tissue containing CD45R+ B cells (B220) **(F)**, CD3+ T cells (CD3) **(G)**, and macrophages/dendritic cells (Iba-1) **(H)** in the bronchus-associated lymphoid tissue. Statistical analyses were performed using t tests. Differences were considered significant at ***p<0.001, as compared to the respective control groups. PBS, phosphate-buffered saline; CD, cluster of differentiation; GEM, gram-positive enhancer matrix.

immunity biased to Th1- and Th2-type, respectively, as judged by the ratio of H1N1-specific IgG isotypes (IgG2a/IgG1 and IgG2b/IgG1) (Supplementary Figure 6). Based on these results, we concluded that HA-PA-GEM vaccination induced antibody responses with a Th1 phenotype, which were markedly different from those induced by traditional i.m. vaccination.

Serum HI titers were measured to further evaluate systemic immune responses. After the third booster shot, the HI titers for

10.3389/fimmu.2024.1432989

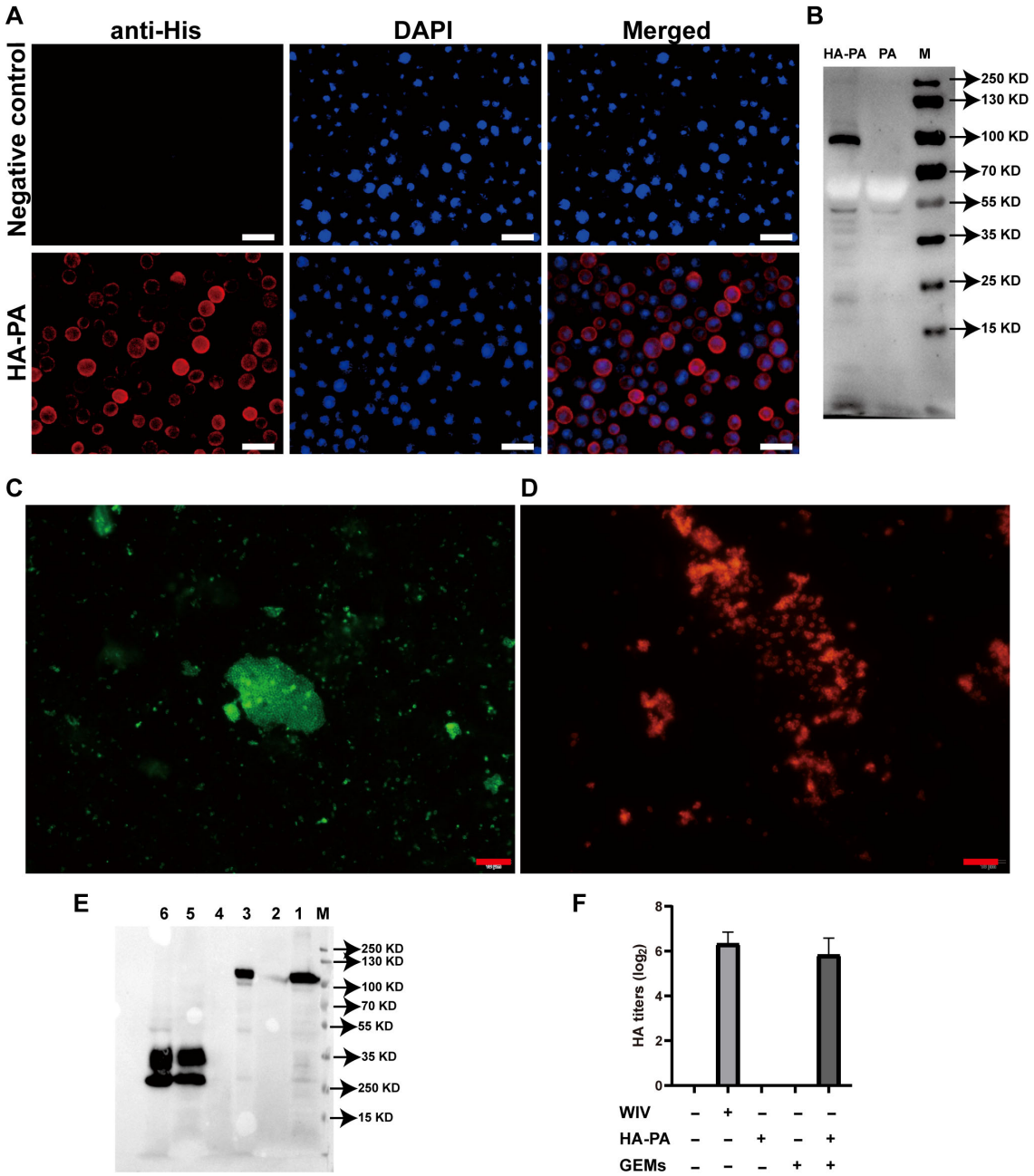

FIGURE 4
Investigation of fusion-GEM-complex binding. **(A)** IFA of HA-PA expression in baculovirus-infected Sf9 insect cells. **(B)** Western blot analysis of antibody specificity. Lane M: molecular weight marker; Lane PA: recombinant baculovirus (PA)-infected Sf9 cell lysate; Lane HA-PA: recombinant baculovirus (HA-PA)-infected Sf9 cell lysate. **(C)** Fusion proteins on the surface of GEM particles were detected using IFA. Immunofluorescence was detected as green fluorescence using anti-6xHis-tag monoclonal antibody and FITC-conjugated goat anti-mouse antibody, while **(D)** red fluorescence was detected in samples seropositive from swine H1N1, upon staining with DyLight 594-conjugated goat anti-swine IgG. **(E)** The maximum binding capacity of the fusion protein displayed on GEM particles was determined using western blot. Lane M: protein marker. Lane 1: recombinant baculovirus (HA-PA)-infected Sf9 cell lysate. Lane 2: 1 U GEM particles. Lane 3: 1 U HA-PA-GEM particles. Lane 4: Sf9 cell lysate. Lane 5: recombinant baculovirus (PA)-infected Sf9 cell lysate. Lane 6: 1 U PA-GEM particles. **(F)** The HA activity of WIV, HA-PA, GEM particles or HA-PA-GEM particles. IFA, immunofluorescence analysis; HA, hemagglutinin; PA, protein anchor; GEM, gram-positive enhancer matrix.

each mouse were measured. I.n. HA-PA-GEM formulations showed a trend toward lesser HI titers than similar the WIV vaccine after the third immunization (Figure 5F). Even after the third booster shot, vaccination with the WIV vaccine alone produced same HI titers. Microneutralization titers were consistent with those of HI (Figure 5G).

3.5 Mucosal influenza-specific SIgA antibody levels after immunization with HA-PA-GEM particles

IAV infection occurs mainly through mucosal tissues, whereas SIgA from the mucosa can block IAV infection. Therefore, we

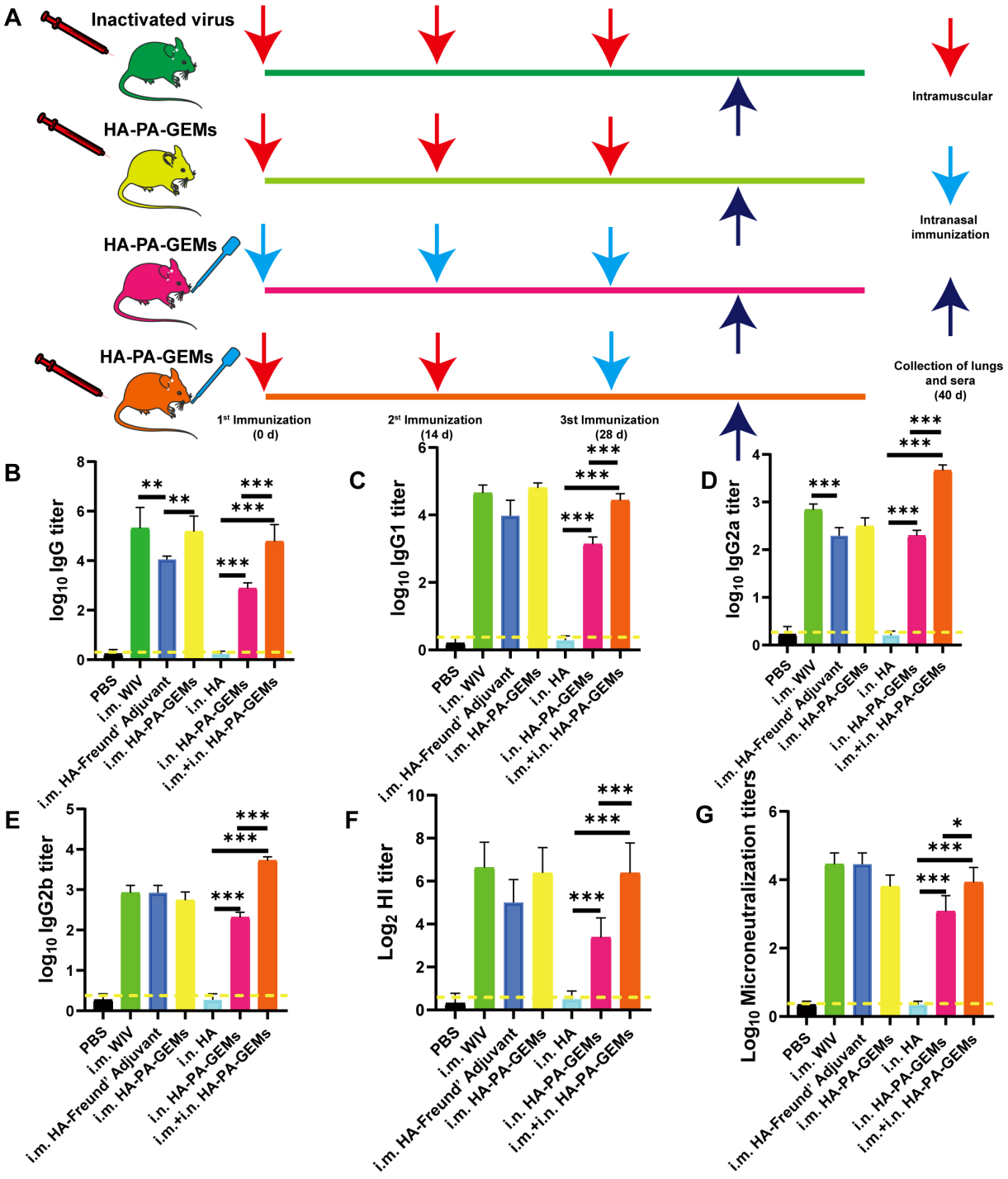

FIGURE 5
Serum antibody levels induced by the GEM-adjuvanted H1N1 vaccine. **(A)** Experimental protocol for i.m. and i.n. immunization of mice with HA-PA-GEMs and inactivated virus. HA-specific **(B)** IgG, **(C)** IgG1, **(D)** IgG2a, **(E)** IgG2b levels in the serum were assessed using indirect ELISA. **(F)** HI and **(G)** micro-neutralization titers in the serum. The dotted yellow line shows the limit of detection. Dotted line indicate a 1:1.5 HAI titer. The analysis was performed with a one-way ANOVA. Differences were considered significant at $*p<0.05$, $**p<0.01$, $***p<0.001$. GEM, gram-positive enhancer matrix; i.m., intramuscular; i.n., intranasal; HA, hemagglutinin; PA, protein anchor; ELISA, enzyme-linked immunosorbent assay; HI, hemagglutination inhibition.

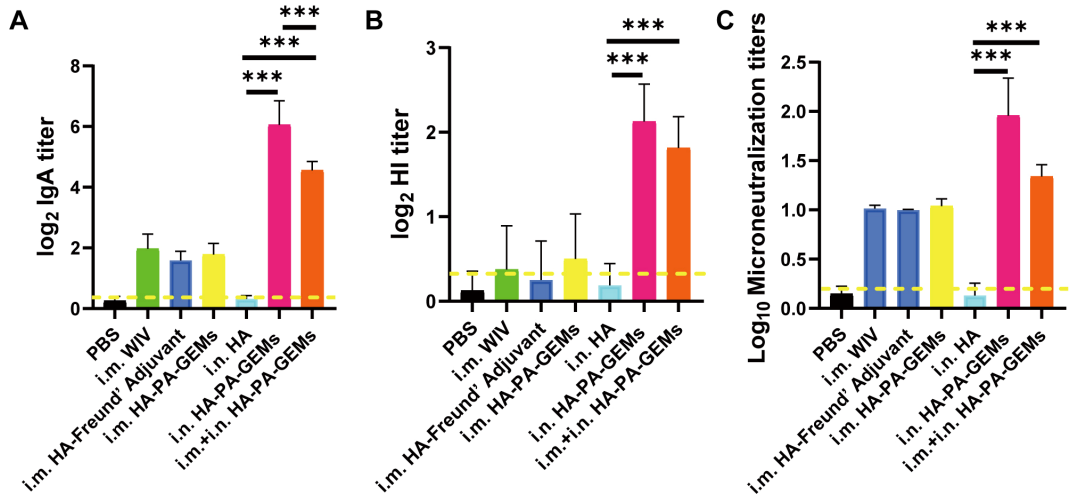

FIGURE 6
IgA, HAI and microneutralization titers induced by GEM-adjuvanted H1N1 vaccines. Bronchoalveolar lavage fluid was collected 12 day after the third immunization, for detection of HI and virus neutralization antibody titers. **(A)** HA-specific IgA and **(B)** HI antibody titers were determined upon challenge with swIAV H1N1 virus, and the results were calculated as log2. **(C)** Virus neutralization antibody titers were determined against 100 TCID50 swIAV H1N1 virus, and the results were calculated as log10. The dotted yellow line shows the limit of detection. Dotted line indicate a 1:1.5 HAI titer. The analysis was performed with a one-way ANOVA with Bonferroni's post-hoc multiple comparison test. Differences were considered significant at ***$p<0.001$. GEM, gram-positive enhancer matrix; HA, hemagglutinin; HI, hemagglutination inhibition; IgA, immunoglobulin A; PA, protein anchor; WIV, whole-inactivated virus; $TCID_{50}$, median tissue culture infectious dose.

tested the ability of the vaccine to induce mucosal immunity (Figure 6A). In most mice, i.m. immunization resulted in SIgA levels below the limit of detection in the lung lavage. Furthermore, the lung lavage produced low SIgA titers following immunization with the subunit vaccine alone. In contrast, i.n. vaccination with HA-PA-GEM induced high SIgA levels in the lungs of all the mice ($p<0.001$). Furthermore, we measured HI (Figure 6B) and microneutralization titers (Figure 6C) for these samples, which maintained a tendency consistent with the aforementioned relationship. Finally, we concluded that i.n. HA-PA-GEM immunization induced a strong mucosal airway immune response.

3.6 Splenocyte proliferation after *ex vivo* stimulation and antigen-specific T-cell immune responses

The effect of the immunostimulatory agents on the proliferative response of splenocytes was assessed 12 d after the last vaccination. Splenocytes from the inoculated animals multiplied more quickly after H1N1-HA protein stimulation *ex vivo* than those from control mice ($p<0.01$) (Figure 7A). Additionally, the i.m. HA-PA-GEM group and i.m.+i.n. HA-PA-GEM group exhibited the highest increase in cell proliferation ($p<0.001$). Figures 7B, C shows the identification of the splenocytes from the infected mice that generated IFN-γ and IL-4 specific to the antigen, in order to further evaluate the kind of immune response. ELISpot assays were used to measure IFN-γ and IL-4 secretion by mouse splenocytes (Figures 7B, C). These results showed that spot-forming cells, which are indicators of the production of IFN-γ by splenocytes, were significantly higher in mice immunized with i.m.+i.n. HA-PA-GEM than those immunized with i.m. or i.n. HA-PA-GEM ($p<0.001$), thus demonstrating that both the Th1 and Th2 arms of adaptive immunity were activated. Next, we examined the capacity of immune cells extracted from the spleens of immunized mice to release cytokines in response to *ex vivo* stimulation with the H1N1-HA protein, to evaluate the cellular immunological response induced by the HA-PA-GEM experimental vaccines. The levels of IFN-γ, TNF-α, IL-4, IL-6, IL-10, and IL-12 secreted by splenocytes were assayed using commercial ELISA kits. Compared to the animals in the other groups, the mice immunized with i.m.+i.n. HA-PA-GEM released significantly higher quantities of the cytokines IFN-γ, TNF-α, IL-4, IL-6, IL-10, and IL-12 from their splenocytes ($p<0.001$) (Figures 7D–I). IFN-γ, TNF-α, IL-6, and IL-12 production was linked to a Th1 profile, whereas IL-4 and IL-10 secretion was linked to a Th2 immune response. These findings showed that HA-PA-GEM vaccination increased the splenocyte production of both type 1 and type 2 cytokines.

3.7 Protective efficacy against G4 EA H1N1 challenge

To determine whether the HA-PA-GEM vaccine was protective, the mice (Supplementary Table 2) were i.n. infected with G4 EA H1N1 1 week after the third repeated immunization. Following that, the body weights (Figures 8A, B) and survival rates (Figures 8C, D) of the animals (8 mice per group) were recorded daily for two weeks. These findings demonstrated that immunization of mice with i.m. WIV, i.m. HA, i.m. HA-PA-GEM, i.n. HA-PA-GEM, and i.m.+i.n. HA-PA-GEM prevented weight loss and mortality. A challenge with i.m. GEM and i.n. HA resulted in all mice hitting clinical endpoint within 10 d of immunization. The mock-vaccinated (PBS) group as well as those immunized with i.m. GEM and i.n. HA exhibited lung viral titers of

10.3389/fimmu.2024.1432989

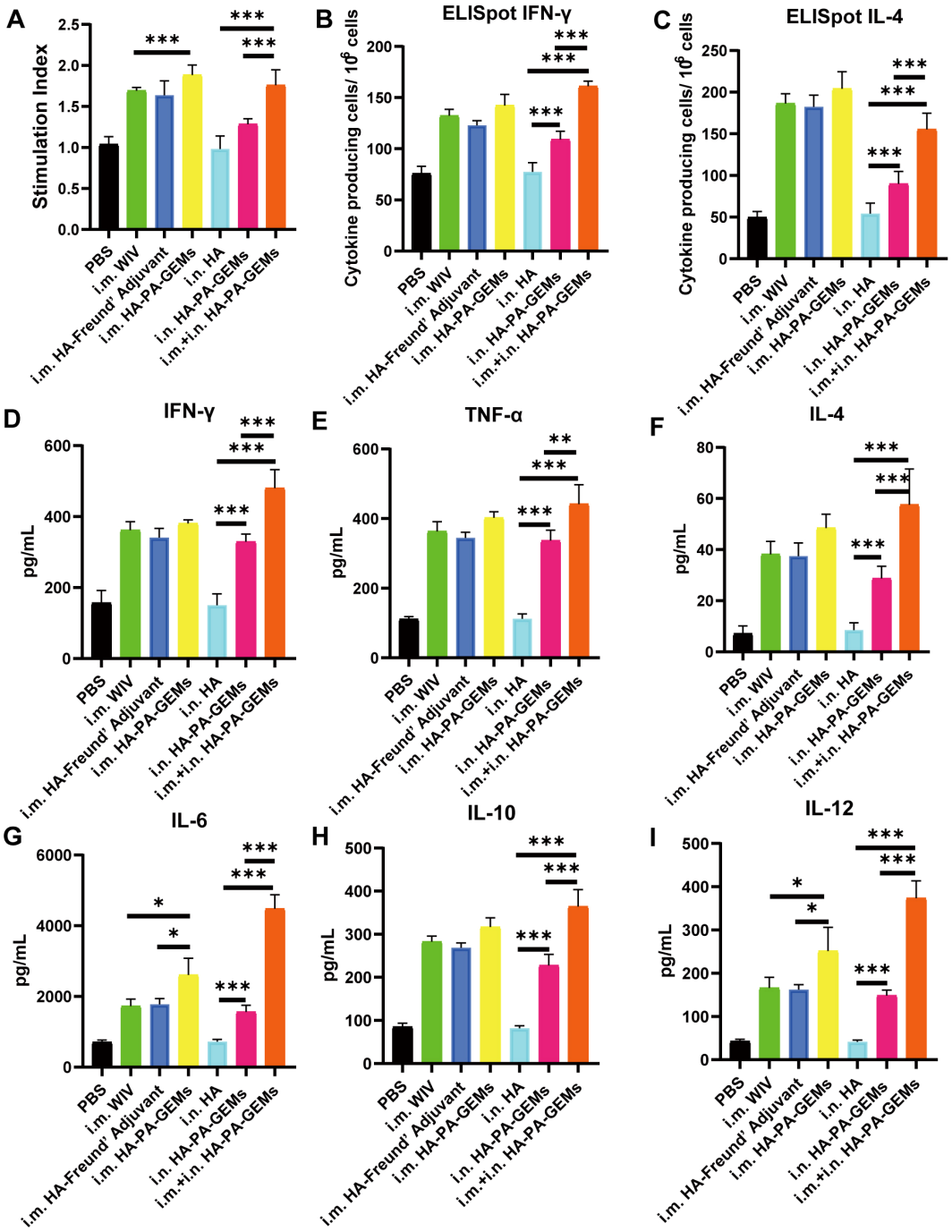

FIGURE 7
Detection of cellular responses in mice immunized with HA-PA-GEMs. **(A)** Splenocyte proliferation analysis. The stimulation index of the splenocytes was detected using a Cell Counting Kit-8 assay, upon stimulation with purified H1N1 HA protein. The levels of **(B)** INF-γ and **(C)** IL-4 secreted by the splenocytes were quantified using an ELISpot assay. The levels (pg/mL) of the cytokines **(D)** INF-γ, **(E)** TNF-α, **(F)** IL-4, **(G)** IL-6, **(H)** IL-10, and **(I)** IL-12 in the cell-free supernatants harvested from the splenocytes at 48 h after incubation were measured using commercial ELISA. The analysis was performed with a one-way ANOVA with Bonferroni's *post-hoc* multiple comparison test. Differences were considered significant at $*p<0.05$, $**p<0.01$, $***p<0.001$. ELISpot assay, enzyme-linked immunosorbent spot assay; HA, hemagglutinin; PA, protein anchor; GEM, gram-positive enhancer matrix; IL, interleukin; ELISA, enzyme-linked immunosorbent assay; INF-γ, interferon gamma; TNF-α, tumor necrosis factor alpha.

approximately 7×10^3 $TCID_{50}$/mL on day 7 post-challenge, whereas mice immunization with i.m. WIV, i.m. HA, i.m. HA-PA-GEM, i.n. HA-PA-GEM, and i.m.+i.n. HA-PA-GEM showed no detectable virus in the lungs (Figures 8E, F). In addition, on day 7 post-exposure, the challenge virus titer in the lungs of the mice i.n. inoculated with GEM particles was lower than that in the lungs of the mock-vaccinated mice, indicating that the i.n. GEM particles vaccinated mice shed or replicated less in their lungs.

10.3389/fimmu.2024.1432989

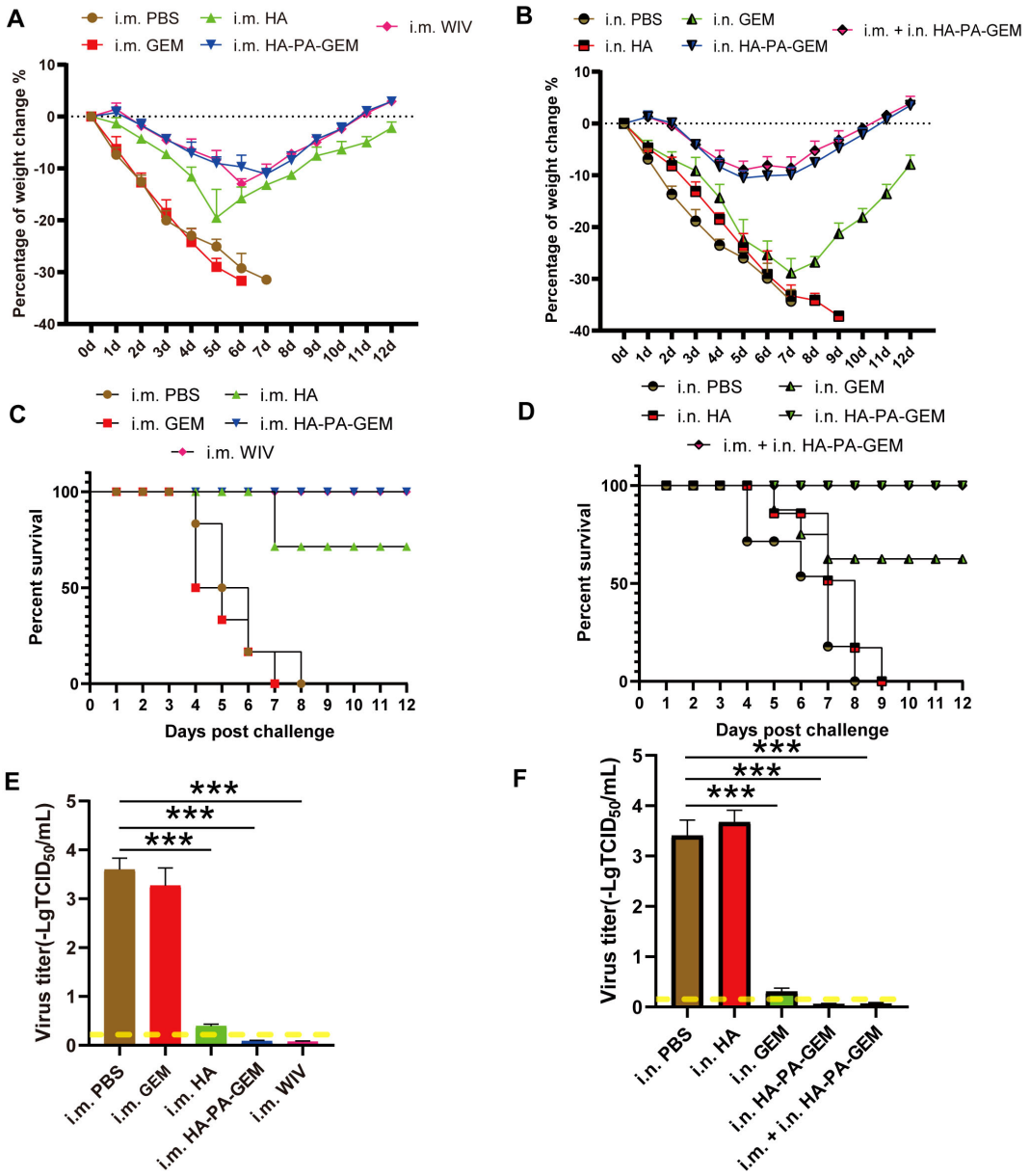

FIGURE 8
Immunization and challenge studies.Seven days after the last immunization, all the mice in the study group were i.n. challenged with the H1N1 virus. **(A)** Body weight and **(C)** survival of mice i.m. administered PBS, HA, GEM, or HA-PA-GEM were monitored daily for 12 d following the virus challenge; **(B)** Body weight and **(D)** survival of mice administered i.n. PBS, HA, GEM, HA-PA-GEM, or i.m. HA-PA-GEM were monitored daily for 12 d following virus challenge. Virus titers in the lungs of mice **(E)** i.m. injected with PBS, HA, GEM, or HA-PA-GEM and **(F)** i.n. injected with PBS, HA, GEM, HA-PA-GEM, or HA-PA-GEM, at DPC 7. The dotted yellow line shows the limit of detection. The analysis was performed with a one-way ANOVA. Differences were considered significant at ***p<0.001. DPC, days post-challenge; i.n., intranasal; i.m., intramuscular; PBS, phosphate-buffered saline; PA, protein anchor; GEM, gram-positive enhancer matrix; HA, hemagglutinin.

3.8 Histopathological analysis of the lungs of mice challenged with G4 EA H1N1

We exposed the mice to the G4 EA H1N1 virus after vaccination and conducted a histological investigation on day 7 after the challenge, to determine whether the HA-PA-GEM-elicited antigen-specific mucosal, humoral, and cell-mediated immunity in mice led to pulmonary tissue damage (Figure 9). Lung pathology images (Figure 9A) revealed that the vaccination groups (i.m. WIV, i.m. HA, and i.m. HA-PA-GEM) had significantly fewer infiltrating cells in the mouse lung tissues, and the alveoli were clearly visible. However, in the control groups, the number of infiltrating cells of the alveolar cavity increased, the alveolar wall thickened, and the majority of the alveolar contours vanished (i.m. PBS and i.m. GEM). I.m. WIV- and HA-PA-GEM-immunized groups exhibited similar histopathological scores (Figure 9B). On day 7 post-challenge, the

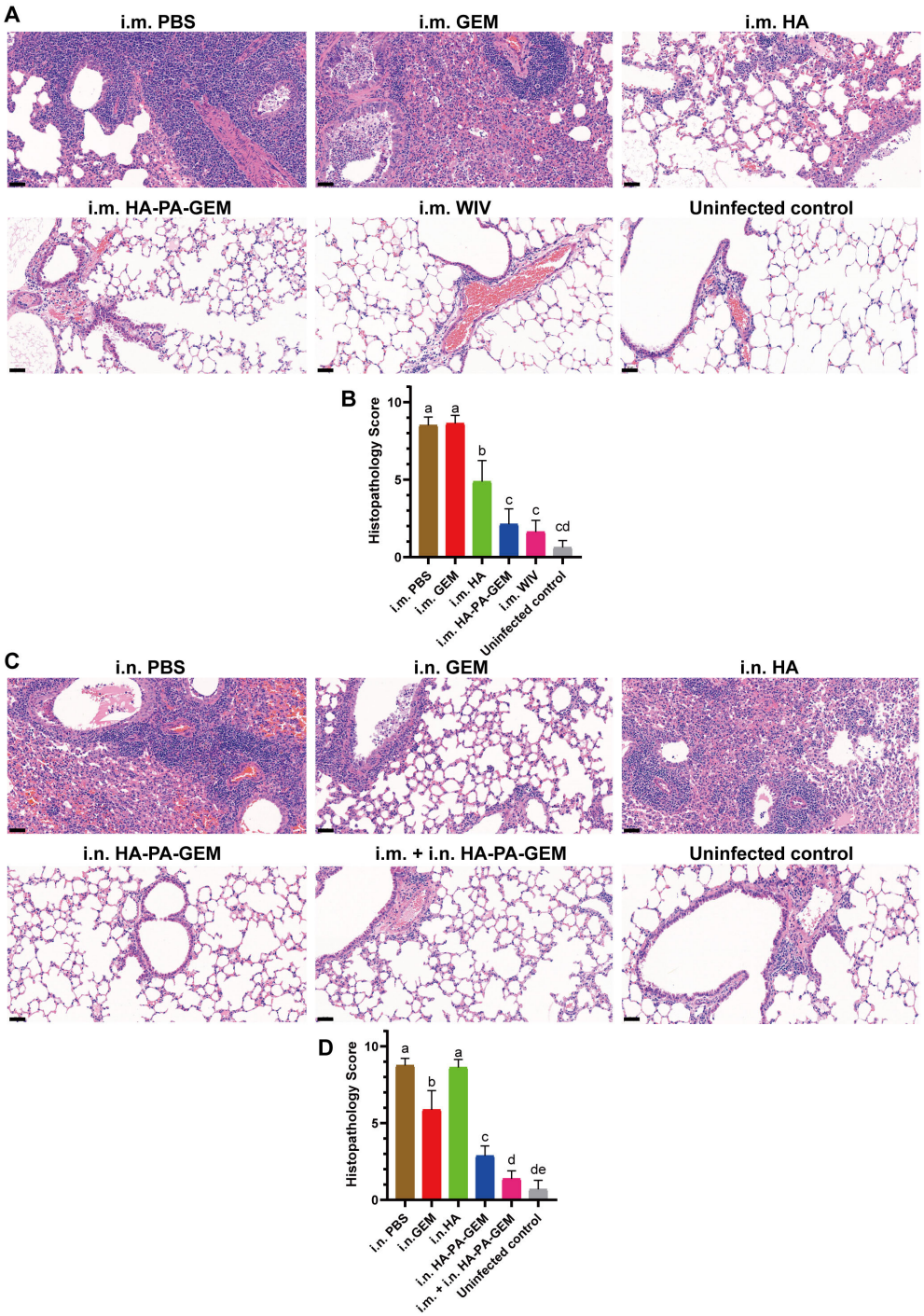

FIGURE 9
H&E-stained histopathological lesions in the lungs of H1N1-challenged mice. H&E staining for the **(A, B)** i.m. and **(C, D)** i.n administered groups; Scale bar (black): 200 μm. Differences were considered statistically significant at $p<0.05$. Different letters represent significant differences, and same letters represent no significant differences. H&E, hematoxylin and eosin; i.m., intramuscular; i.n., intranasal; PBS, phosphate-buffered saline; GEM, gram-positive enhancer matrix; HA, hemagglutinin; PA, protein anchor.

lungs stained with hematoxylin and eosin revealed noticeably more inflammation in the PBS-inoculated group and in those that received i.n. HA vaccination than in those that received i.n. HA-PA-GEM vaccination. Moreover, i.n. HA-PA-GEM and i.m.+i.n. HA-PA-GEM immunizations caused the least amount of inflammation at seven days post-challenge, as compared to that observed in the PBS- and HA-treated groups (Figure 9C). The i.m.+i.n. HA-PA-GEM group showed significantly ($p<0.01$) lower

histopathological scores at 7 d post-challenge than the other groups (Figure 9D). Thus, the HA-PA-GEM vaccination may successfully prevent the H1N1 influenza virus from harming mouse lung tissues.

3.9 Protection against lethal PR8 virus challenge

In PR8 H1N1 challenge studies, the i.m. WIV- and i.m. HA-PA-GEM-immunized animals exhibited weight loss of >15%, while the i.n. and i.m.+i.n. HA-PA-GEM-immunized animals exhibited a reduced weight loss of <10%, as shown in Supplementary Figures 7A–B. The results demonstrate that the animals immunized via the intramuscular (i.m.) routes with the HA-PA-GEM vaccine exhibited moderate cross-protective efficacy against the PR8 H1N1 strain. However, the animals immunized via the intranasal (i.n.) routes with the HA-PA-GEM vaccine demonstrated superior cross-protective efficacy against the PR8 H1N1 strain. This may be attributed to the role of mucosal immunity. This also provides a promising indication that GEM, when used as an adjuvant through intranasal immunization, can achieve a favorable immunoprotection rate. When challenged with the PR8 virus, the mice i.m. immunized with WIV and HA-PA-GEM displayed survival rates of 46%–52% (Supplementary Figure 7C). We found fewer viruses in the lung samples from the i.m. WIV- and HA-PA-GEM-immunized animals than those from the mock-vaccinated mice (Supplementary Figure 7E). As supported by the 100% survival rate, the i.n. HA-PA-GEM- and i.m.+i.n. HA-PA-GEM-immunized groups exhibited significantly better protection against deadly PR8 viral infections (Supplementary Figure 7D). In addition, the mice in the i.n. HA-PA-GEM- and i.m.+i.n. HA-PA-GEM-immunized groups showed significantly lower mean viral lung titers than those observed in the mock-vaccinated animals (Supplementary Figure 7F). Therefore, these results showed that both the i.n. and i.m.+i.n. HA-PA-GEM-immunized groups conferred cross-protection against PR8 IAVs.

4 Discussion

Pigs are crucial hosts for studying and managing mammalian influenza viruses. It is common for humans and pigs to come in contact with each other, leading to interspecies transmission and reassortment, which can in turn result in the development of new influenza strain (30–32). There is a need to regularly update the vaccine formulation for swine IAV immunization to act as an effective control measure to lower the disease burden and pandemic influenza risk (30–32). Utilizing adjuvants is a crucial tactic for improving immunogenicity and antigen sparing (18, 33). In this study show that GEM particles can be used as adjuvants for i.n. and i.m. delivery of influenza subunit vaccines. The inclusion of GEM particles in influenza subunit vaccination markedly improved the systemic and mucosal immune responses. Additionally, GEM particles improve immune response quality by ensuring a balanced Th1/Th2-type response, instead of a Th2-dominated response (18). These results are in keeping with previous observational studies, which the intravenously delivered subunit vaccines were more immunogenic when delivered with GEM particles (13, 34–40). This study is the first to demonstrate that GEM particles in swine influenza subunit vaccines significantly enhance both systemic and mucosal immune responses. These results will be widely beneficial to both the biomedical and veterinary fields.

Previous studies have reported that the following benefits for GEM surface display systems: (1) Easy purification of foreign proteins (38); (2) Generally, *L. lactis* is regarded as a safe probiotic. After treatment, GEM particles pose no safety risks as a carrier, because they do not contain proteins or nucleic acids (38, 41, 42); (3) GEM particles can effectively boost the immune system's reaction (19, 38). Consequently, this method has been used in numerous vaccine studies (38, 43, 44). Macrophages are crucial components of the innate immune system that help the host defend itself against infections and launch immunological responses (24, 45). Macrophages are the antigen-presenting cells that are responsible for triggering adaptive immunity by releasing inflammatory cytokines (IL-1, IL-6, *etc.*) and chemokines (TNF-α, IFN-γ, *etc.*) (24, 46, 47). This study found that GEM particles led to a significant increase in nitrite production in RAW 264.7 cells, indicating their activation. In addition, after stimulation with GEM, the gene expression data showed higher levels of iNOSl and cytokines, similar to those observed upon treatment with the Pam3CK4 control. Overall, this study strengthens the idea that GEM particles are potent stimulators of innate immunity. These findings align with numerous prior studies on Feline herpesvirus 1 (35), C. perfringens (CPMEA) (48), and Canine distemper virus (CDV) (34). Peptidoglycan, a key component of BLPs, binds to TLR2, which forms a heterodimer with TLR1 or TLR6 to activate innate immune cells (49). Ramirez et al. demonstrated that GEMs interact solely with HEK293 cells expressing human TLR2, triggering NF-κB activation (50). Research is being conducted on GEMs-activated TLR receptors *in vivo*, including a study with GEMs mixed with a split influenza vaccine. Nasally immunized TLR2KO mice exhibited reduced serum IgG, lower sIgA in nasal and lung lavages, and fewer IFN-γ producing T-cells and B-cells in local dLN and spleen compared to wild-type controls (20, 49). In this study we assess the adjuvant properties of GEM particles, mice were i.n. administered a single dose of native GEM particles in PBS. The findings showing that these mice had large, organized lymphoid follicles in both lungs and nasal cavities. These tissues, also called bronchus- and nasal-associated lymphoid tissues, contain dendritic cells, T cells, and a significant number of B cells.

Commercially available inactivated SIV vaccines offer only a modest level of protection against heterologous viruses, although they provide sterile immunity against homologous viruses (32, 51). Therefore, there is an urgent need to develop alternative inactivated vaccine platforms. The adjuvant properties of GEM (gram-positive enhancer matrix) particles have garnered significant attention in recent years due to their potential to enhance immune responses in various vaccination strategies. GEM particles serve not only as carriers for antigens but also as immunostimulants that can modulate the immune system effectively. For instance, GEM particles have been utilized to display antigens, such as the E2 glycoprotein of the classical swine fever virus, enhancing the immunogenicity of the vaccine formulations. The E2-Spy-PA-GEM

complex has shown to induce high levels of antibodies in immunized mice, indicating that GEM particles can significantly improve the immune response to specific antigens (52). Further, Numerous studies have shown that the use of GEMs for i.n. vaccination has many benefits over the use of inactivated vaccines. This platform is a strong alternative to the traditional inactivated vaccines used in swine, because of its quick turnaround time, stimulation of an immune response similar to that caused by a natural route of infection, lack of need for an additional adjuvant, and effectiveness with a single dose (18, 38). In this study, we found that the presence of GEM particles increased HI titers, improved the Th1/Th2-type immune response, decreased lung viral titers, and completely cleared the virus by day 7 post challenge. Moreover, we demonstrated that i.n. immunization of mice with influenza HA subunit vaccine+GEM complexes enhanced mucosal and humoral immune responses, as compared to that observed upon immunization of mice with subunit vaccine alone. The increased viral clearance in mice given adjuvanted vaccination may be due to the generation of higher IgG2a titers and a comparatively high IFN-γ/IL-4 ratio. In contrast, the i.m.+i.n. HA-PA-GEM influenza vaccine induced a skewed response toward the Th1 type. Leenhouts et al. extensively studied GEM's impact on boosting influenza vaccine immunity. They found that adding GEMs to an intranasally administered H1N1 vaccine significantly increased serum IgG, HI levels, and sIgA titers in mice, providing complete protection against both homologous and heterologous influenza infections and reducing lung viral titers (17). Oral immunization with a monovalent subunit vaccine of strain A/Hiroshima (H3N2) mixed with GEMs induced stronger systemic and local antibody responses and a more balanced Th1/Th2 response than inactivated influenza vaccines with alum. Similarly, combining GEMs with seasonal HA (A/Wisconsin/67/2005 [H3N2]) significantly enhanced systemic immune responses and achieved a more balanced Th1/Th2 response compared to HA alone administered intramuscularly (19). Our results corroborate the findings of a great deal of the previous work in nasal immunization with a subunit vaccine combined with GEMs reduced IL-4-producing cells and significantly increased IFN-γ-producing cells, shifting the immune response to a Th1-type. Moreover, GEMs-based vaccines showed promising safety and immunogenicity in the FluGEM phase I trial (42).

Mucosal immunization, by emulating the natural invasion pathways of pathogens, stimulates mucosal immunity through the production of secretory immunoglobulin A (sIgA) and elicits a systemic immune response characterized by immunoglobulin G (IgG) production (53). Furthermore, this needle-free approach to immunization minimizes immune-related side effects and is well-suited for large-scale vaccination initiatives and repeated immunization protocols (54). As most viruses enter and begin their reproduction at mucosal surfaces, mucosal vaccination is highly desired to increase protection against infectious illnesses. The size of GEMs is similar to that of live *L. lactis*, around 1 μm, making them suitable for uptake by M cells in the nasal-associated lymphoid tissue (NALT) (55). Researchers have confirmed that after i.m. vaccination, most mice have SIgA levels in lung lavage that are below the limit of detection (56–58). Using different immunization route, we explored whether HA-PA-GEM vaccination induces a mucosal SIgA response in this study. In the present study, it was found that mice immunized with i.n. or i.m.+i.n. HA-PA-GEM showed high SIgA titers in lung lavages after i.n. administration. In accordance with the present results, previous studies have demonstrated that that i.n. vaccination with GEM vaccines enhances SIgA levels in BALB/c mice, as compared to parenteral vaccination (19, 20, 52). This intriguing result might be explained by the fact that HA-PA-GEM vaccination could drive the entire mucosal immune system. An *in vitro* assay showed that GEMs activate human nasal epithelial cells, increasing IL-6 and IL-8 levels (59–61). To explore M cell interaction with GEMs, mice were intranasally given fluorescent GEMs. After 15 minutes, staining revealed that M cells efficiently absorbed GEMs (59–61). Additionally, some lamina propria DCs extend dendrites through the epithelium to directly capture antigens (61). These findings will help others to better understand the GEMs vaccination of the local mucosa activates the whole mucosal system.

In this study, cellular and humoral immunological responses to influenza virus infection were induced by the HA-PA-GEM vaccines, thus showing that they effectively stimulate the immune system. In every instance, the vaccinated mice produced hemagglutinating antibodies against the relevant vaccination antigen. The EA H1N1 SIV HA is generated from influenza viruses of avian origin that have little cross-reactivity with seasonal or classic swine H1N1 viruses (62, 63). Antigenic alterations in HA may result from mutations, particularly in the HA1 region. Consequently, in the current study, G4 EA H1N1 and PR8 viruses were used as challenge viruses to assess the efficacy of HA-PA-GEM immunization against homologous and heterologous viral infections in mice. In addition to providing total protection against homologous viral infections, inoculation with i.n. or i.m.+i.n. HA-PA-GEM resulted in strong cross-protection against heterologous H1N1 viral infections. It should be noted that the experimental animals used in this experiment were mice, rather than pigs. Consequently, further validation of these data is required on a porcine model, which is a key objective of our future research program. GEMs are an efficient, cost-effective, and safe tool, particularly useful in subunit vaccine development due to their simple preparation and antigen display system. However, enhancing GEMs vaccine efficacy is still challenging. Future advancements in GEMs display systems will likely rely on improving vaccine performance.

5 Conclusion

HA-PA-GEMs triggered specific immune responses in BALB/c mice. Intramuscular administration led to strong serum IgG responses and a higher IgG2a/IgG1 ratio but did not enhance systemic or mucosal SIgA responses. In contrast, intranasal immunization with HA-PA-GEMs, unlike HA alone, effectively induced systemic and mucosal SIgA responses and significantly boosted IFN-γ responses, promoting Th1-type immunity. As a result, HA-PA-GEMs stand out as an innovative and promising vaccine

candidate for protecting veterinary animals from influenza viruses. This vaccine offers several advantages over alternative methods, including safety, appropriateness of mucosal administration (which makes it practical for widespread use), robust immunogenicity, and broad protective capacity. The findings of this study call for further investigation of this hypothesis in swine.

Data availability statement

The original contributions presented in the study are included in the article/Supplementary Material. Further inquiries can be directed to the corresponding author.

Ethics statement

Approval and licensure for the entire experimental protocol were granted by the Specialized Committee on Scientific Research and Academic Ethics of Inner Mongolia Agricultural University. The study was conducted in accordance with the local legislation and institutional requirements.

Author contributions

YZ: Conceptualization, Data curation, Formal analysis, Funding acquisition, Investigation, Methodology, Project administration, Resources, Software, Supervision, Validation, Visualization, Writing – original draft, Writing – review & editing. PZ: Data curation, Formal analysis, Investigation, Software, Writing – review & editing. XD: Conceptualization, Formal analysis, Methodology, Project administration, Writing – review & editing. XS: Investigation, Methodology, Validation, Writing – review & editing. JW: Data curation, Formal analysis, Validation, Visualization, Writing – review & editing. SL: Conceptualization, Data curation, Formal analysis, Funding acquisition, Investigation, Methodology, Project administration, Resources, Software, Supervision, Validation, Visualization, Writing – review & editing.

Funding

The author(s) declare financial support was received for the research, authorship, and/or publication of this article. This research was supported by the National Natural Science Foundation of China (Grant numbers 32460873), The Special Program for Scientific Research on First-Class Disciplines of the Education Department of the Inner Mongolia Autonomous Region (YLXKZX-NND-025, YLXKZX-NND-012), the Natural Science Foundation of Inner Mongolia (Grant numbers 2024LHMS03041), Grassland Excellence Research Project Funding - Newly Introduced Talents since 2022 (Grant numbers RS2400000096), Research Support Funds for Introducing High-level Talents to Institutions at the Inner Mongolia Autonomous Region Level for the Year 2022 (Grant numbers DC2300001267), the National Natural Science Foundation of China (Grant numbers 32072819, and 32360863), Science and Technology Major Special Project of Inner Mongolia (Grant numbers 2021ZD0010), Grassland Talents Innovative Team Project of Inner Mongolia (Grant numbers 20151031), the Innovation team project of Education Department of Inner Mongolia (Grant numbers NMGIRT2412), the Scientific Research Innovation Team Project of Inner Mongolia Colleges and Universities (Grant numbers 2200001130) and High-level Talents Introduction to Scientific Research Start-up Project of Inner Mongolia Agricultural University (NDYB2022-6).

Acknowledgments

We would like to express our gratitude to everyone who took part in this study.

Conflict of interest

The authors declare that the research was conducted in the absence of any commercial or financial relationships that could be construed as a potential conflict of interest.

Publisher's note

Supplementary material

The Supplementary Material for this article can be found online at: https://www.frontiersin.org/articles/10.3389/fimmu.2024.1432989/full#supplementary-material

SUPPLEMENTARY FIGURE 1
Experimental immunization and challenge diagram.

SUPPLEMENTARY FIGURE 2
Physical and biological characterization of GEM particles. **(A)** MG1363 and GEM staining gram-positive (magnification: 1000×). **(B)** Transmission electron microscopy analysis. Untreated MG1363 cells and the GEM particles obtained from MG1363 cells. **(C)** Scanning electron microscopy analysis. Particle size of **(D)** MG1363 cells and the GEM particles obtained from MG1363 cells.

SUPPLEMENTARY FIGURE 3
H&E staining of cross-sections revealed the histological characteristics of the murine nasal, lung parenchyma, and mediastinal adipose tissues. Mice were intranasally administered with PBS alone or native GEMs in PBS. Five days later, the heads and thoracic tissues obtained from the animals were processed for H&E staining. **(A, A1, D, D1)** murine nasal tissues; **(B, B1, E,**

E1) lung parenchyma tissues; and **(C, C1, F, and F1)** mediastinal tissues. Scale bar: red=1 mm, green=200 µm. H&E, hematoxylin and eosin.

SUPPLEMENTARY FIGURE 4
The cytotoxic effects of various doses of gram-positive enhancer matrix particles administered through the intranasal route. **(A)** 2000 U (1:0); **(B)** 200 U (1:10); **(C)** 20 U (1:100); **(D)** 2 U (1:1000); **(E)** 1 U (1:2000); **(F)** Quantitative analysis of the hematoxylin and eosin staining. Scale bar: 1 mm. U, unit.

SUPPLEMENTARY FIGURE 5
Fusion proteins on the surface of GEM particles were detected using IFA. **(A)** Immunofluorescence was detected as green fluorescence using anti-6×His-tag monoclonal antibody and FITC-conjugated goat anti-mouse antibody, while **(B)** red fluorescence was detected in samples seropositive from swine H1N1, upon staining with DyLight 594-conjugated goat anti-swine IgG.

SUPPLEMENTARY FIGURE 6
HA-specific IgG subclass binding antibody responses. **(A)** IgG2a/IgG1 ratio; **(B)** IgG2b/IgG1 ratio.

SUPPLEMENTARY FIGURE 7
Weight changes and percent survival in mice after challenge with live virus (A/PR/8/34). Groups of immunized and unimmunized mice intranasally challenged with live virus (A/PR/8/34), at 1 week after the third immunization. Average body weight changes **(A, B)** and survival rates **(C, D)** were monitored for 12 d. The lungs of each mouse group were collected for **(E, F)** viral titer detection, at 7 days post-challenge in MDCK cells, and the results were calculated as log10. The dotted yellow line shows the limit of detection. The analysis was performed with a one-way ANOVA. Differences were considered significant at *p<0.05, **p<0.01, ***p<0.001. PBS, phosphate-buffered saline; WIV, whole-inactivated virus; HA, hemagglutinin; GEM, gram-positive enhancer matrix.

SUPPLEMENTARY TABLE 1
Primers sequences and real-time PCR amplification parameters.

SUPPLEMENTARY TABLE 2
Animal study design.

References

1. Ma W, Kahn RE, Richt JA. The pig as a mixing vessel for influenza viruses: Human and veterinary implications. *J Mol Genet Med*. (2008) 3:158–66.

2. Ito T, Couceiro JN, Kelm S, Baum LG, Krauss S, Castrucci MR, et al. Molecular basis for the generation in pigs of influenza A viruses with pandemic potential. *J Virol*. (1998) 72:7367–73. doi: 10.1128/JVI.72.9.7367-7373.1998

3. Shi Y, Wu Y, Zhang W, Qi J, Gao GF. Enabling the 'host jump': structural determinants of receptor-binding specificity in influenza A viruses. *Nat Rev Microbiol*. (2014) 12:822–31. doi: 10.1038/nrmicro3362

4. Sun H, Xiao Y, Liu J, Wang D, Li F, Wang C, et al. Prevalent Eurasian avian-like H1N1 swine influenza virus with 2009 pandemic viral genes facilitating human infection. *Proc Natl Acad Sci U S A*. (2020) 117:17204–10. doi: 10.1073/pnas.1921186117

5. Sun H, Liu J, Xiao Y, Duan Y, Yang J, Chen Y, et al. Pathogenicity of novel reassortant Eurasian avian-like H1N1 influenza virus in pigs. *Virology*. (2021) 561:28–35. doi: 10.1016/j.virol.2021.06.001

6. Garten RJ, Davis CT, Russell CA, Shu B, Lindstrom S, Balish A, et al. Antigenic and genetic characteristics of swine-origin 2009 A(H1N1) influenza viruses circulating in humans. *Science*. (2009) 325:197–201. doi: 10.1126/science.1176225

7. Ruan BY, Yao Y, Wang SY, Gong XQ, Liu XM, Wang Q, et al. Protective efficacy of a bivalent inactivated reassortant H1N1 influenza virus vaccine against European avian-like and classical swine influenza H1N1 viruses in mice. *Vet Microbiol*. (2020) 246:108724. doi: 10.1016/j.vetmic.2020.108724

8. Liang H, Lam TT, Fan X, Chen X, Zeng Y, Zhou J, et al. Expansion of genotypic diversity and establishment of 2009 H1N1 pandemic-origin internal genes in pigs in China. *J Virol*. (2014) 88:10864–74. doi: 10.1128/JVI.01327-14

9. Magiri RB, Lai KJ, Mutwiri GK, Wilson HL. Experimental pcep-adjuvanted swine influenza H1N1 vaccine induced strong immune responses but did not protect piglets against heterologous H3N2 virus challenge. *Vaccines (Basel)*. (2020) 8:235. doi: 10.3390/vaccines8020235

10. Chen Q, Madson D, Miller CL, Harris DL. Vaccine development for protecting swine against influenza virus. *Anim Health Res Rev*. (2012) 13:181–95. doi: 10.1017/S1466252312000175

11. Ma W, Richt JA. Swine influenza vaccines: current status and future perspectives. *Anim Health Res Rev*. (2010) 11:81–96. doi: 10.1017/S146625231000006X

12. Rockman S, Laurie KL, Parkes S, Wheatley A, Barr IG. New technologies for influenza vaccines. *Microorganisms*. (2020) 8:1745. doi: 10.3390/microorganisms8111745

13. Hu M, Wang F, Li N, Xing G, Sun X, Zhang Y, et al. An antigen display system of GEM nanoparticles based on affinity peptide ligands. *Int J Biol Macromol*. (2021) 193:574–84. doi: 10.1016/j.ijbiomac.2021.10.135

14. van Roosmalen ML, Kanninga R, El Khattabi M, Neef J, Audouy S, Bosma T, et al. Mucosal vaccine delivery of antigens tightly bound to an adjuvant particle made from food-grade bacteria. *Methods*. (2006) 38:144–9. doi: 10.1016/j.ymeth.2005.09.015

15. Zhang Y, Yu X, Hou L, Chen J, Li P, Qiao X, et al. CTA1: Purified and display onto gram-positive enhancer matrix (GEM) particles as mucosal adjuvant. *Protein Expr Purif*. (2018) 141:19–24. doi: 10.1016/j.pep.2017.08.010

16. Tomar J, Biel C, de Haan CAM, Rottier PJM, Petrovsky N, Frijlink HW, et al. Passive inhalation of dry powder influenza vaccine formulations completely protects chickens against H5N1 lethal viral challenge. *Eur J Pharm Biopharm*. (2018) 133:85–95. doi: 10.1016/j.ejpb.2018.10.008

17. Saluja V, Visser MR, van Roosmalen ML, Leenhouts K, Huckriede A, Hinrichs WL, et al. Gastro-intestinal delivery of influenza subunit vaccine formulation adjuvanted with Gram-positive enhancer matrix (GEM) particles. *Eur J Pharm Biopharm*. (2010) 76:470–4. doi: 10.1016/j.ejpb.2010.08.003

18. Saluja V, Visser MR, Ter Veer W, van Roosmalen ML, Leenhouts K, Hinrichs WL, et al. Influenza antigen-sparing by immune stimulation with Gram-positive enhancer matrix (GEM) particles. *Vaccine*. (2010) 28:7963–9. doi: 10.1016/j.vaccine.2010.09.066

19. Saluja V, Amorij JP, van Roosmalen ML, Leenhouts K, Huckriede A, Hinrichs WL, et al. Intranasal delivery of influenza subunit vaccine formulated with GEM particles as an adjuvant. *AAPS J*. (2010) 12:109–16. doi: 10.1208/s12248-009-9168-2

20. Keijzer C, Haijema BJ, Meijerhof T, Voorn P, de Haan A, Leenhouts K, et al. Inactivated influenza vaccine adjuvanted with bacterium-like particles induce systemic and mucosal influenza A virus specific T-cell and B-cell responses after nasal administration in a TLR2 dependent fashion. *Vaccine*. (2014) 32:2904–10. doi: 10.1016/j.vaccine.2014.02.019

21. Zhang Y, Yang L, Zhang J, Huang K, Sun X, Yang Y, et al. Oral or intranasal immunization with recombinant Lactobacillus plantarum displaying head domain of Swine Influenza A virus hemagglutinin protects mice from H1N1 virus. *Microb Cell Fact*. (2022) 21:185. doi: 10.1186/s12934-022-01911-4

22. Abente EJ, Rajao DS, Santos J, Kaplan BS, Nicholson TL, Brockmeier SL, et al. Comparison of adjuvanted-whole inactivated virus and live-attenuated virus vaccines against challenge with contemporary, antigenically distinct H3N2 influenza A viruses. *J Virol*. (2018) 92:e01323–18. doi: 10.1128/JVI.01323-18

23. Souza CK, Rajao DS, Sandbulte MR, Lopes S, Lewis NS, Loving CL, et al. The type of adjuvant in whole inactivated influenza a virus vaccines impacts vaccine-associated enhanced respiratory disease. *Vaccine*. (2018) 36:6103–10. doi: 10.1016/j.vaccine.2018.08.072

24. Yang R, Zhang S, Yu Y, Hong X, Wang D, Jiang Y, et al. Adjuvant effects of bacterium-like particles in the intranasal vaccination of chickens against Newcastle disease. *Vet Microbiol*. (2021) 259:109144. doi: 10.1016/j.vetmic.2021.109144

25. Zhang Y, Huang K, Wang T, Deng F, Gong W, Hui X, et al. SARS-CoV-2 rapidly adapts in aged BALB/c mice and induces typical pneumonia. *J Virol*. (2021) 95:e02477–20. doi: 10.1128/JVI.02477-20

26. Zhang Y, Gao J, Huang K, Zhao Y, Hui X, Wang T, et al. SARS-coV-2 infection causes hyperglycemia in cats. *J Infect Dis*. (2022) 226:1568–76. doi: 10.1093/infdis/jiac143

27. Carvalho AL, Fonseca S, Miquel-Clopes A, Cross K, Kok KS, Wegmann U, et al. Bioengineering commensal bacteria-derived outer membrane vesicles for delivery of biologics to the gastrointestinal and respiratory tract. *J Extracell Vesicles*. (2019) 8:1632100. doi: 10.1080/20013078.2019.1632100

28. Del Giudice G, Rappuoli R, Didierlaurent AM. Correlates of adjuvanticity: A review on adjuvants in licensed vaccines. *Semin Immunol*. (2018) 39:14–21. doi: 10.1016/j.smim.2018.05.001

29. Saroja C, Lakshmi P, Bhaskaran S. Recent trends in vaccine delivery systems: A review. *Int J Pharm Investig*. (2011) 1:64–74. doi: 10.4103/2230-973X.82384

30. Skarlupka AL, Owino SO, Suzuki-Williams LP, Crevar CJ, Carter DM, Ross TM. Computationally optimized broadly reactive vaccine based upon swine H1N1 influenza hemagglutinin sequences protects against both swine and human isolated viruses. *Hum Vaccin Immunother*. (2019) 15:2013–29. doi: 10.1080/21645515.2019.1653743

31. Everett HE, Aramouni M, Coward V, Ramsay A, Kelly M, Morgan S, et al. Vaccine-mediated protection of pigs against infection with pandemic H1N1 2009 swine influenza A virus requires a close antigenic match between the vaccine antigen and challenge virus. *Vaccine*. (2019) 37:2288–93. doi: 10.1016/j.vaccine.2019.02.078

32. Wu Y, Yang D, Xu B, Liang W, Sui J, Chen Y, et al. Immune efficacy of an adenoviral vector-based swine influenza vaccine against antigenically distinct H1N1 strains in mice. *Antiviral Res*. (2017) 147:29–36. doi: 10.1016/j.antiviral.2017.09.009

33. Atmar RL, Keitel WA. Adjuvants for pandemic influenza vaccines. *Curr Top Microbiol Immunol*. (2009) 333:323–44. doi: 10.1007/978-3-540-92165-3_16

34. Liu L, Wang J, Li R, Wu J, Zhao Y, Yan F, et al. A bacterium-like particle vaccine displaying envelope proteins of canine distemper virus can induce immune responses in mice and dogs. *Viruses*. (2024) 16:549. doi: 10.3390/v16040549

35. Jiao C, Jin H, Zhang M, Liu D, Huang P, Bai Y, et al. A bacterium-like particle vaccine displaying protective feline herpesvirus 1 antigens can induce an immune response in mice and cats. *Vet Microbiol*. (2023) 287:109898. doi: 10.1016/j.vetmic.2023.109898

36. Su K, Wang Y, Yuan C, Zhang Y, Li Y, Li T, et al. Intranasally inoculated bacterium-like particles displaying porcine epidemic diarrhea virus S1 protein induced intestinal mucosal immune response in mice. *Front Immunol*. (2023) 14:1269409. doi: 10.3389/fimmu.2023.1269409

37. Wang F, Hu M, Li N, Sun X, Xing G, Zheng G, et al. Precise assembly of multiple antigens on nanoparticles with specially designed affinity peptides. *ACS Appl Mater Interfaces*. (2022) 14:39843–57. doi: 10.1021/acsami.2c10684

38. Jin H, Bai Y, Wang J, Jiao C, Liu D, Zhang M, et al. A bacterium-like particle vaccine displaying Zika virus prM-E induces systemic immune responses in mice. *Transbound Emerg Dis*. (2022) 69:e2516–29. doi: 10.1111/tbed.14594

39. Matsuzaki C, Shiraishi T, Chiou TY, Nakashima Y, Higashimura Y, Yokota SI, et al. Role of lipoteichoic acid from the genus apilactobacillus in inducing a strong igA response. *Appl Environ Microbiol*. (2022) 88:e0019022. doi: 10.1128/aem.00190-22

40. Zhang S, Yan F, Liu D, Li E, Feng N, Xu S, et al. Bacterium-like particles displaying the rift valley fever virus gn head protein induces efficacious immune responses in immunized mice. *Front Microbiol*. (2022) 13:799942. doi: 10.3389/fmicb.2022.799942

41. Jing H, Yong L, Haiyan L, Yanjun M, Yun X, Yu Z, et al. Oral administration of Lactococcus lactis delivered heat shock protein 65 attenuates atherosclerosis in low-density lipoprotein receptor-deficient mice. *Vaccine*. (2011) 29:4102–9. doi: 10.1016/j.vaccine.2011.03.105

42. Van Braeckel-Budimir N, Haijema BJ, Leenhouts K. Bacterium-like particles for efficient immune stimulation of existing vaccines and new subunit vaccines in mucosal applications. *Front Immunol*. (2013) 4:282. doi: 10.3389/fimmu.2013.00282

43. Fujihashi K, Sato S, Kiyono H. Mucosal adjuvants for vaccines to control upper respiratory infections in the elderly. *Exp Gerontol*. (2014) 54:21–6. doi: 10.1016/j.exger.2014.01.006

44. Xu S, Jiao C, Jin H, Li W, Li E, Cao Z, et al. A novel bacterium-like particle-based vaccine displaying the SUDV glycoprotein induces potent humoral and cellular immune responses in mice. *Viruses*. (2019) 11:1149. doi: 10.3390/v11121149

45. Wynn TA, Chawla A, Pollard JW. Macrophage biology in development, homeostasis and disease. *Nature*. (2013) 496:445–55. doi: 10.1038/nature12034

46. Li P, Xia P, Wen J, Zheng M, Chen J, Zhao J, et al. Up-regulation of the MyD88-dependent pathway of TLR signaling in spleen and caecum of young chickens infected with Salmonella serovar Pullorum. *Vet Microbiol*. (2010) 143:346–51. doi: 10.1016/j.vetmic.2009.12.008

47. Nawab A, An L, Wu J, Li G, Liu W, Zhao Y, et al. Chicken toll-like receptors and their significance in immune response and disease resistance. *Int Rev Immunol*. (2019) 38:284–306. doi: 10.1080/08830185.2019.1659258

48. Guo Z, Ren H, Chang Q, Liu R, Zhou X, Xue K, et al. Lactobacilli-derived adjuvants combined with immunoinformatics-driven multi-epitope antigens based approach protects against Clostridium perfringens in a mouse model. *Int J Biol Macromol*. (2024) 267:131475. doi: 10.1016/j.ijbiomac.2024.131475

49. Zhou X, Gao M, De X, Sun T, Bai Z, Luo J, et al. Bacterium-like particles derived from probiotics: progress, challenges and prospects. *Front Immunol*. (2023) 14:1263586. doi: 10.3389/fimmu.2023.1263586

50. Ramirez K, Ditamo Y, Rodriguez L, Picking WL, van Roosmalen ML, Leenhouts K, et al. Neonatal mucosal immunization with a non-living, non-genetically modified Lactococcus lactis vaccine carrier induces systemic and local Th1-type immunity and protects against lethal bacterial infection. *Mucosal Immunol*. (2010) 3:159–71. doi: 10.1038/mi.2009.131

51. Vincent AL, Lager KM, Janke BH, Gramer MR, Richt JA. Failure of protection and enhanced pneumonia with a US H1N2 swine influenza virus in pigs vaccinated with an inactivated classical swine H1N1 vaccine. *Vet Microbiol*. (2008) 126:310–23. doi: 10.1016/j.vetmic.2007.07.011

52. de Haan A, Haijema BJ, Voorn P, Meijerhof T, van Roosmalen ML, Leenhouts K. Bacterium-like particles supplemented with inactivated influenza antigen induce cross-protective influenza-specific antibody responses through intranasal administration. *Vaccine*. (2012) 30:4884–91. doi: 10.1016/j.vaccine.2012.04.032

53. Bi J, Li F, Zhang M, Wang H, Lu J, Zhang Y, et al. An HIV-1 vaccine based on bacterium-like particles elicits Env-specific mucosal immune responses. *Immunol Lett*. (2020) 222:29–39. doi: 10.1016/j.imlet.2020.03.002

54. Jia Z, Liu R, Chang Q, Zhou X, De X, Yang Z, et al. Proof of concept in utilizing the peptidoglycan skeleton of pathogenic bacteria as antigen delivery platform for enhanced immune response. *Int J Biol Macromol*. (2024) 264:130591. doi: 10.1016/j.ijbiomac.2024.130591

55. Bosma T, Kanninga R, Neef J, Audouy SA, van Roosmalen ML, Steen A, et al. Novel surface display system for proteins on non-genetically modified gram-positive bacteria. *Appl Environ Microbiol*. (2006) 72:880–9. doi: 10.1128/AEM.72.1.880-889.2006

56. Pliasas VC, Neasham PJ, Naskou MC, Neto R, Strate PG, North JF, et al. Heterologous prime-boost H1N1 vaccination exacerbates disease following challenge with a mismatched H1N2 influenza virus in the swine model. *Front Immunol*. (2023) 14:1253626. doi: 10.3389/fimmu.2023.1253626

57. Zuckermann FA, Grinkova YV, Husmann RJ, Pires-Alves M, Storms S, Chen WY, et al. An effective vaccine against influenza A virus based on the matrix protein 2 (M2). *Vet Microbiol*. (2024) 298:110245. doi: 10.1016/j.vetmic.2024.110245

58. Wymore Brand M, Souza CK, Gauger P, Arruda B, Vincent Baker AL. Biomarkers associated with vaccine-associated enhanced respiratory disease following influenza A virus infection in swine. *Vet Immunol Immunopathol*. (2024) 273:110787. doi: 10.1016/j.vetimm.2024.110787

59. Neutra MR, Pringault E, Kraehenbuhl JP. Antigen sampling across epithelial barriers and induction of mucosal immune responses. *Annu Rev Immunol*. (1996) 14:275–300. doi: 10.1146/annurev.immunol.14.1.275

60. Teng Z, Meng LY, Yang JK, He Z, Chen XG, Liu Y. Bridging nanoplatform and vaccine delivery, a landscape of strategy to enhance nasal immunity. *J Control Release*. (2022) 351:456–75. doi: 10.1016/j.jconrel.2022.09.044

61. Iwasaki A. Mucosal dendritic cells. *Annu Rev Immunol*. (2007) 25:381–418. doi: 10.1146/annurev.immunol.25.022106.141634

62. Sui J, Yang D, Qiao C, Xu H, Xu B, Wu Y, et al. Protective efficacy of an inactivated Eurasian avian-like H1N1 swine influenza vaccine against homologous H1N1 and heterologous H1N1 and H1N2 viruses in mice. *Vaccine*. (2016) 34:3757–63. doi: 10.1016/j.vaccine.2016.06.009

63. Brownlee GG, Fodor E. The predicted antigenicity of the haemagglutinin of the 1918 Spanish influenza pandemic suggests an avian origin. *Philos Trans R Soc Lond B Biol Sci*. (2001) 356:1871–6. doi: 10.1098/rstb.2001.1001

frontiers | Frontiers in Immunology

TYPE Original Research
PUBLISHED 07 January 2025
DOI 10.3389/fimmu.2024.1446751

OPEN ACCESS

EDITED BY
Mara Jana Broadhurst,
University of Nebraska Medical Center,
United States

REVIEWED BY
Fabio Fiorino,
LUM University Giuseppe Degennaro, Italy
Bekir Kocazeybek,
Istanbul University-Cerrahpasa, Türkiye

*CORRESPONDENCE
Huiling Wang
58781502@qq.com
Yi Li
liyilebmed@henu.edu.cn
Xiaohuan Zhang
ZXH1215822@163.com

†These authors have contributed equally to this work

RECEIVED 10 June 2024
ACCEPTED 16 December 2024
PUBLISHED 07 January 2025

CITATION
Xu J, Yuan Y, Chen G, Ma B, Zou YL, Wang B, Yan W, Zhang Q, Ma Q, Mao X, Wang H, Li Y and Zhang X (2025) Characteristics of humoral responses to the first coronavirus disease booster vaccine and breakthrough infection in central China: a multicentre, prospective, longitudinal cohort study. *Front. Immunol.* 15:1446751. doi: 10.3389/fimmu.2024.1446751

Characteristics of humoral responses to the first coronavirus disease booster vaccine and breakthrough infection in central China: a multicentre, prospective, longitudinal cohort study

Junhong Xu[1†], Youhua Yuan[2†], Guohua Chen[3†], Bing Ma[1], Yin Long Zou[4], Baoya Wang[1], Wenjuan Yan[1], Qi Zhang[1], Qiong Ma[1], Xiaohuan Mao[2], Huiling Wang[5*], Yi Li[1*] and Xiaohuan Zhang[2*]

[1]Department of Clinical Microbiology, Henan Provincial People's Hospital, People's Hospital of Zhengzhou University, and People's Hospital of Henan University, Zhengzhou, China, [2]Department of Special Laboratory, Henan Provincial People's Hospital, People's Hospital of Zhengzhou University, and People's Hospital of Henan University, Zhengzhou, China, [3]Department of Laboratory, Zhengzhou Municipal Chinese Medicine Hospital, Zhengzhou, China, [4]Department of Laboratory, Dengzhou Municipal Central Hospital, Dengzhou, China, [5]Department of PCR, Henan Provincial People's Hospital, People's Hospital of Zhengzhou University, and People's Hospital of Henan University, Zhengzhou, China

Introduction: The long-term immunogenicity, adverse effects, influencing factors, and protection from booster vaccines remain unclear. Specifically, little is known regarding the humoral immunity and breakthrough infections associated with COVID-19 booster immunization. Therefore, we evaluated the immunogenicity, reactogenicity, influencing factors, and protective effects of the first coronavirus disease booster vaccine 23 months before and after implementation of dynamic zero epidemic control measures among healthcare staff.

Methods: We prospectively included 389 healthcare staff members in China with negative pre-enrolment severe acute respiratory syndrome coronavirus 2 test results. Neutralising serum antibodies were evaluated every two months till 23 months post-booster vaccination. Breakthrough infection was recorded or confirmed by SARS-CoV-2 specific PCR testing via throat swabs from participants before and after dynamic zero epidemic control measures.

Results: At 15–30 days after vaccination, the mean concentration of the booster vaccine was 6.4 times above initial concentrations. Poorer antibody responses by booster vaccine correlated with male sex, longer post-booster duration, same-manufacturer vaccines, post-routine epidemic control measures implementation and intervals >210 days between primary and booster vaccinations. Higher breakthrough rates were associated with longer post-booster durations and post-routine epidemic control measures

implementation but not associated with levels of neutralising antibodies after booster vaccination from participants. Adverse reactions were non-serious. These booster vaccine doses induced rapid, robust antibody responses, maintained for only 6–7 months.

Discussion: Neutralizing antibodies induced by breakthrough infection with SARS-CoV-2 were weaker than those induced by the first COVID-19 booster vaccine, predicting that antibodies induced by SARS-CoV-2 may be very different from those of other known infectious pathogens.

KEYWORDS

breakthrough infections, COVID-19, humoral immunity, kinetics, neutralising antibodies, booster immunization

1 Introduction

Coronavirus disease (COVID-19) is an emerging respiratory disease caused by severe acute respiratory syndrome coronavirus 2 (SARS-CoV-2) and has become a common infectious disease with worldwide spread (1, 2). Administration of a primary and booster vaccination is one of the most effective measures to control the spread of infectious diseases, including COVID-19 (3, 4). We previously showed that neutralising antibodies elicited by inactivated SARS-CoV-2 vaccines decline within 6–8 months of a primary two-dose inactivated vaccine program (5). Therefore, to control the epidemic, the Chinese Government provided the first booster vaccination dose freely to all citizens beginning in October 2021 (6), when strict dynamic zero-epidemic control measures were implemented against COVID-19 (7). This strict epidemic control measures referred when any residents tested positive for COVID-19 in a residential community, the positive residents were immediately sent to a centralised isolation hospital for free isolation, treatment, and observation. Other residents in the community were required to undergo throat swab nucleic acid testing and isolation at home for seven consecutive days so as to ensure none of positive resident live in this community. Coverage of the first dose of COVID-19 booster vaccine has reached 71.7% of the population requiring vaccination in July 2022 (8). Beginning on December 13,2022, routine epidemic control measures against COVID-19 were implemented (9). However, the neutralising antibody response after the first booster vaccination and its protective effect after the implementation of routine epidemic control measures remain unknown (10).

Currently, more than four types of COVID-19 vaccines have been approved for use globally (11, 12): mRNA, adenovirus, inactivated virus, and recombinant protein vaccines. In China, apart from not being able to produce mRNA vaccines, the other three vaccines have been approved and produced by eight different manufacturers, including Beijing Kexing Zhongwei, Beijing Biologics, Changchun Biologics, Beijing Kexing, Wuhan Biologics, Lanzhou Biologics, Tianjin CanSino, and Anhui Zhifei. So far, only a small number of Chinese have been vaccinated by booster adenovirus or recombinant protein vaccine, and most have been vaccinated by booster inactivated virus vaccine.

Booster vaccinations have been shown to be effective against other infectious diseases (3, 13); however, whether or not they are effective against emerging diseases such as COVID-19 is unclear. Additionally, previous studies have shown that the antibody level after primary vaccination of the COVID-19 vaccine is associated with age, sex, blood type, BMI (body mass index), occupation, interval of doses, the type of vaccination, and most importantly, the decreasing levels of antibody with time (5). Furthermore, studies from other countries have shown that different types of booster vaccines produce higher antibody titers among participants than the homologous type of booster vaccine (14) and last only five months; after this period from the booster vaccination, the number of breakthrough infections began to increase (15). However, in China, whether the antibody levels and maintained duration of the COVID-19 vaccine after the booster vaccine are related to these factors and the characteristics of SARS-CoV-2 breakthrough infections have not yet been reported since the first booster vaccine before and after the routine control measures.

This study aimed to assess the immunogenicity, reactogenicity, influencing factors, neutralizing antibody kinetics, and protective effects of the first booster vaccine dose during 23 months among medical staff.

2 Materials and methods

2.1 Ethics statement

This study was approved by the Ethics Committee of Henan Provincial People's Hospital (approval number 20210051, approval date: 24 May 2021) and complied with the principles of the Declaration of Helsinki and Good Clinical Practice.

2.2 Study design and participants

This multicentre, prospective, longitudinal cohort study was performed at Henan Provincial People's Hospital and Zhengzhou Municipal Chinese Medicine Hospital in Central China.

Healthy medical staff (18-80 years of age) members who received the first dose of the COVID-19 booster vaccine within 1 to 690 days between 20 October 2021 and 16 September 2023 were recruited. Participants with documented reverse transcription (RT)-PCR-confirmed COVID-19 or who had received any other vaccine, such as hepatitis B, were excluded. Symptoms or signs of clinically typical acute respiratory diseases such as a body temperature higher than 38°C, cough, signs consistent with COVID-19, or any contraindications to receiving the booster vaccine (such as allergies or pregnancy) within 24 hours before the target study vaccine dose were excluded (15).

All recruitment criteria were provided in crowded public places or announced on social networks such as Wechat groups. Interested candidates were invited to contact the researcher directly; at the same time, interviews by researchers were scheduled to explain these selection criteria. All participants provided written informed consent prior to enrolment.

When collecting the blood of a participant previously vaccinated with a booster dose, the study staff enquired and recorded whether the volunteer was or had been infected with SARS-CoV-2 after the booster vaccination. Simultaneously, a throat swab was collected for SARS-CoV-2 PCR testing; those with positive results were confirmed to have a breakthrough infection. Additionally, the related participant information was recorded in an investigation questionnaire and subsequently transferred to an electronic Excel form, including name, telephone contact, sex, age, body weight, and height. Detailed and accurate information on COVID-19 primary and booster vaccinations, including vaccine manufacturers, vaccination dates, and whether the vaccine was the adenovirus or recombinant protein vaccine type, could be obtained via the mini-program of the COVID-19 vaccination record on the Alipay platform. Currently, Chinese eight different manufacturers, including Beijing Kexing Zhongwei, Beijing Biologics, Changchun Biologics, Beijing Kexing, Wuhan Biologics, Lanzhou Biologics produced inactivated COVID-19 vaccine, Tianjin CanSino produced adenovirus recombinant live attenuated vaccine, and Anhui Zhifei produced recombinant protein vaccine. If a volunteer's booster vaccine and the primary vaccine are both of the homologous type of vaccine, such as an inactivated vaccine, they are classified into the homologous group, and conversely, they are classified into the heterologous group. The ABO blood types of the volunteers were determined using identification reagents.

Hospitalized patients or other study participants from November 2022 to April 2024 were considered as having positive SARS-CoV-2 tests based on positive SARS-CoV-2 PCR results and infectious disease reports from the PCR department of Henan Provincial People's Hospital; these results were eventually reported to the related administration section of the Chinese CDC.

2.3 Experimental procedures

For each booster, the vaccine was given as a single intramuscular injection with the same or different primary dose. All participants underwent clinical evaluation and blood samples were taken on the day of evaluation for neutralising antibodies. Significant signs and symptoms were measured for 1–30 days, and any solicited and unsolicited adverse events were reviewed, and medical records were updated. Two-millilitre blood samples were collected from each volunteer every 2 months, with the anticoagulant EDTA added into each tube to centrifuge with 3000g for 10 minutes, then,1 ml of plasma was drawn into 2 separate tubes, frozen in the -80°C refrigerator. The duration of neutralising antibodies for each participant was determined as the time interval between the booster vaccination date and the blood collection date. All participants (those with the heterologous type of vaccine and those with the booster dose of the homologous type of vaccine) remained at their local community health centre for at least 30 minutes following vaccination for the investigation and recording of any adverse events. When a serious adverse event occurred, participants contacted the researchers and rated the intensity of the adverse event on a severity scale as follows:1 = mild; 2 = moderate; 3 = severe; or 4 = life-threatening. Adverse event definitions and the list of solicited adverse events are categorized by previous description (16).

The neutralising antibody was detected by the commercial enzyme-linked immunosorbent assay (anti-SARS-CoV-2 S kit (Shanghai GeneoDx Biotechnology Co., LTD., Shanghai, China). The kit detects neutralising IgG antibodies only against the SARS-CoV-2 spike protein receptor binding domain not against nucleoprotein, which are available in a universal microplate reader (DNM-9602; Beijing Pulong Co., LTD., Beijing, China). A value greater than 6.5 IU/mL is regarded as positive. According to the manufacturer's protocols and instructions, values greater than 100 IU/mL were considered to be 100 IU/mL. ABO blood group was determined via the test tube method according to the reagent's instructions (Chengdu United Co., LTD., Chengdu, China).

Throat swab samples were collected for SARS-CoV-2 analysis using RT-PCR (Shanghai Zhijiang Biotechnology Ltd.). Cycle threshold values of ≤44 on RT-PCR were counted as positive.

2.4 Statistical analysis

A multivariable linear regression model was used to analyse factors influencing the concentration of neutralising antibodies, with one of the classification variances used as a reference to calculate the B-value (17). Due to missing data for some neutralising antibodies, we used a mixed linear model that could handle the unequal number of repeated observations of individuals with randomly missing data. To analyse the change of neutralising antibodies over time, we used a mixed linear model with the continuous log2 conversion concentration of neutralising antibodies from day 1 to 690 as the dependent variable. Age, sex,

BMI, vaccination method, duration since the booster dose, interval between primary and booster dose, with or without breakthrough of SARS-CoV-2 infection, epidemic control measures, and ABO blood group were independent variables in the model. Additionally, we used multivariate binary logistic regression analysis to get the risk factors associated with breakthrough infection with SARS-CoV-2. In this analysis, the outcome variable was SARS-CoV-2 infection with 1–690 days post-booster vaccination, while other factors, including blood type, BMI, sex, age, vaccination mode, log2-transformed concentration of neutralising antibodies, duration post-booster vaccination, the interval between primary and booster vaccination, and epidemic control measures were used as independent variables. To investigate any correlation between neutralising antibody concentration and breakthrough infection rate over time after booster vaccination, we used the trend chi-square test and linear correlation analysis. Additionally, survival curve analysis was used to compare whether there was a difference in breakout rates between the two modes of booster vaccination (heterologous and homologous types). Moreover, chi-square test was used to compare the difference of adverse effects between individuals vaccinated with booster vaccines from the homologous and heterologous types as the primary vaccine.

Based on methods described in a previous study (18), we divided participants into three BMI groups: <18.5, 18.5–23.9, and>23.9 kg/cm2. Additionally, based on the Chinese COVID-19 booster vaccination procedure (6–8 months), we divided the interval between primary and booster doses into two groups:180–210 days and >210 days. We divided the participants into three groups by age: 18–30, 31–50, and >50 years (5, 18). We divided the duration after booster vaccination into 10 groups: 1–14, 15–30, 30–90, 91–150, 151–210, 211–300,301–365,366–420, 421–480, and 481–690 days. Additionally, other variables, including sex, vaccination type, presence or absence of SARS-CoV-2 breakthrough infection, epidemic measures, and blood type, were divided into different categories based on their natural classifications. Mixed model distribution curves of log2-transformed neutralising antibodies responses with duration, adjusted for age, sex, BMI, ABO blood type, vaccination mode, the interval between primary doses and booster doses of vaccination, SARS-CoV-2 breakthrough infection, epidemic measures, and time elapsed since booster dose were plotted using Prism 8.0 (GraphPad Software Inc., La Jolla, CA). We only included variables that showed significant associations with neutralising antibodies in the mixed model, even if potential confounders were controlled by the statistical analysis.

The results of the adverse reaction analysis were expressed as a percentage of participants and included all participants who received their first dose of booster vaccine and experienced local or systemic adverse events for 30 consecutive days following vaccination.

Sample size calculation for a log2-transformed neutralizing concentration was done to assess the humoral immune response against SARS-CoV-2 spike protein during 1-690 days after the first booster dose of in participants that received a homologous booster type, as compared with heterologous type. A sample size of 360 participants (n=240 in the homologous group) was required to identify a 15% increase in antibody concentration between two different vaccination group during 1-690 days, assuming a coefficient of variation equal to 1·2 or 1·0 and similar between groups, at least 80% power and a two-sided 5% significance level. The sample size was increased by 15% due to possible loss of visit.

An independent data monitoring committee composed of independent scientists not involved in this study regularly reviewed the data for safety.

All analyses, including linear mixed models, logistic regression, and adverse effects analyses were conducted using SPSS (version 25.0; IBM Corporation, Armonk, NY), and figures were plotted using Prism 8.0 (GraphPad, Inc.).

3 Results

3.1 Basic characteristics of study participants

We collected 791 serum samples from 389 medical staff members (Figure 1). Owing to missing data, we excluded 45 candidates from the regression and mixed model analyses:13 withdrew consent, seven did not meet the inclusion criteria, three missed a follow-up visit, 10 did not answer the body mass index (BMI) question, and 12 were not willing to provide blood samples (Figure 1). The concentration kinetics of neutralising antibodies were detected for all study participants at least once during the 690-day timeframe and a maximum of six times for 132 participants (33.9%). Before 13 December 2022, when the dynamic zero COVID-19 epidemic policy was implemented, 447 serum samples were collected from 113 participants, while 344 serum samples from 276 participants were collected after this date when the COVID-19 epidemic prevention and control measures were replaced with routine measures. Among 791 serum samples from 389 medical staff, 306 samples were confirmed to be SARS-CoV-2-positive by polymerase chain reaction (PCR) on the throat or memory information. The average breakthrough infection rate was 38.7% (306/791) during the study period (20 October 2021 to 16 September 2023). The cumulative SARS-CoV-2 infection rate for 276 samples collected from 13 December 2022 to 16 September 2023 was 86.2% (238/276). In contrast, before December 13, 2022, the cumulative infection rate was <8.1% (36/447). Baseline characteristics, including vaccination groups, age, breakthrough SARS-CoV-2 infection, and epidemic control measures, are indicated in Table 1.

3.2 Factors influencing neutralising antibody production after booster vaccination

Linear mixed model regression analysis showed that sex, interval between primary and booster vaccinations, COVID-19 epidemic control measures, vaccination duration booster, and vaccination type were significantly associated with neutralising antibody level (Table 2, Appendix Tables 1–9, and Figures 2A–E).

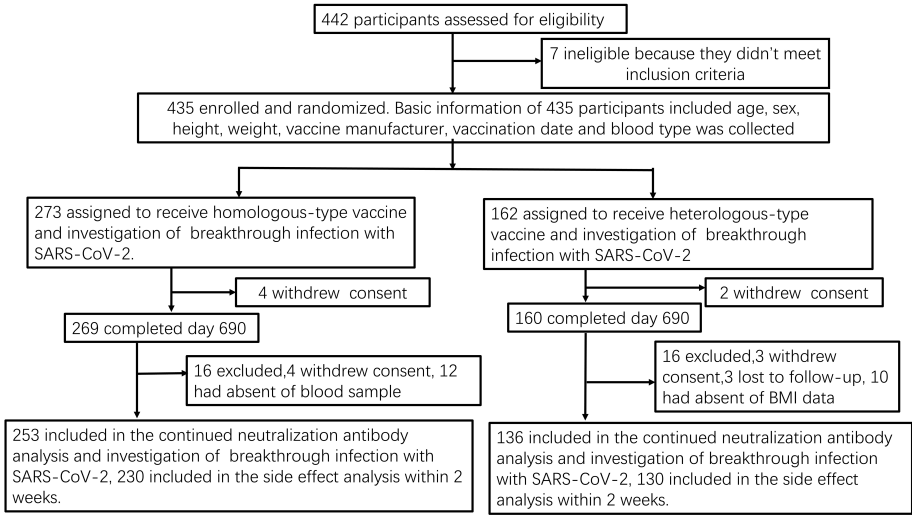

FIGURE 1
Study flow-chart Prospective cohort of Chinese individuals who received the booster vaccine against COVID-19 and underwent serological assays. Following vaccination, the participating medical staff members of Henan Provincial People's Hospital and Zhengzhou Municipal Traditional Medicine Hospital in Central China were followed up at two-month intervals for 23 months between October 19, 2021, and September 30, 2023. BMI, body mass index; COVID-19, coronavirus disease; SARS-CoV-2, severe acute respiratory syndrome coronavirus 2.

Neutralising antibody levels were 32.4 IU/mL higher in women than in men after adjusting for age, booster vaccine type, blood group, duration of primary and booster vaccination intervals, duration of vaccination, COVID-19 outbreak control measures, SARS-CoV-2 breakthrough infection, and BMI (B = 0.23; 95% confidence interval [CI], 0.11–0.43; P = 0.022; least square mean difference = 32.4; 95% CI, 22.3–45.1, P= 0.001) (Figure 2A, Table 2; Appendix Table 5). In addition, at days 31–90, the geometric mean concentration (GMC) of neutralising antibodies in the mixed vaccine group was 97.8 IU/mL, significantly higher than that in the same vaccine group (64.9 IU/mL) (P<0.001; Figure 2B, Table 2; Appendix Table 4). From days 211 to 300, the GMC of neutralising antibodies in both groups declined rapidly. After 210 days of booster vaccination, the GMC of neutralising antibody in the homologous vaccination group decreased to 29.9 IU/mL, which was significantly lower than that in the mixed vaccination group (43.9 IU/mL; P<0.001; Appendix Table 4; Figure 2B). In addition, we determined that the duration after booster vaccination was a major factor in the decline or rise of neutralising antibodies to booster vaccines; neutralising antibody GMC increased by 6.4 times; from 13.3 IU/mL before vaccination to 98.4 IU/mL 15 to 30 days after vaccination. GMC for all participants decreased from the highest level of 98.4 IU/mL at 15–30 days to the lowest level of 37.6 IU/mL at 210–300 days (mean decline:68% or 2.6-fold), indicating an average monthly decline of 8.7% (Figure 2B).

However, after the change in epidemic containment measures on 13 December 2022, the GMC of neutralising antibodies increased slightly again on days 301–366, from the lowest level to 86.9 IU/mL on days 481–690 (Figures 2A–E; Appendix Tables 1-10). This trend is consistent with research findings that the COVID-19 prevention and control measures was a major affect factor associated with neutralising antibodies. After strict control measures were removed, individuals produced fewer neutralising antibodies than before that date (B= -0.4; 95% CI, -0.7 to 0.2; P < 0.001; Table 2, Figure 2C). In addition, neutralising antibody levels were lower in patients with an interval of >210 days between primary vaccination and booster vaccination than in patients with an interval of 180–210 days (B=-021; 95% CI, -0.4 to -0.21; P= 0.021; Figure 2D, Table 2; Appendix Table 8). Neutralising antibody levels were not associated with SARS-CoV-2 breakthrough infection (B= -0.12; 95% CI, -0.28 to 0.10; P= 0.378; Table 2).

3.3 Characteristics of reactogenicity after the first booster vaccination

Adverse effect analysis was based on the solicited adverse events in 253 and 136 homologous- and heterologous-type vaccination groups, respectively, by 30 days after the first booster vaccination. In both groups, most adverse events were mild (n = 16, 76.2%) or moderate (n = 5, 23.8%), and self-limiting. The most common adverse effects were fatigue (n = 7), followed by fever (n = 4), pain at the injection site (n = 4), malaise (n = 4), rash (n = 2), and pruritus (n = 2). The incidence of fever and malaise in the heterologous-type vaccination group was slightly but significantly higher (2/136, 1.47%) (P<0.01) than that in the homorologous-type vaccination group (2/253, 0.79%; Figure 2E).

3.4 Factors influencing SARS-CoV-2 breakthrough infection after booster vaccination

The results of the univariate and multivariate analyses to identify influencing factors associated with SARS-CoV-2 breakthrough infection after the first booster vaccination are shown in Table 3 and Figure 3A. The following factors were found to be associated with

TABLE 1 Baseline characteristics of study participants (N = 389).

Factor	Heterologous type (n = 136)	Homologous type (n = 253)	*p*	Overall
Sex				
Men	30	36	0.05	66
Women	106	217		323
Age (years), M (P25, P75) *	25 (21, 44)	36 (26, 50)	0.001	33 (22, 49)
Age group (years)				
18–30	94	121	0.001	215
31–50	13	73		86
>50	29	59		88
Blood type				
A	33	64	0.833	97
B	38	62		100
O	51	104		155
AB	14	23		37
BMI (kg/m^2)				
<18.5	11	16	0.196	27
18.5–23.9	96	162		258
>23.9	29	75		104
SARS-CoV-2 breakthrough infection				
Yes	95	142	0.008	237
No	41	111		152
Epidemic control measures against COVID-19				
Dynamic zero measures before 13 December 2022	25	88	0.001	113
Routine control measures after 13 December 2022	111	165		276

*M (P25, P75): median (interquartile range). BMI, body mass index; COVID-19, coronavirus disease; SARS-CoV-2, severe acute respiratory syndrome coronavirus 2.

post-booster vaccination SARS-CoV-2 breakthrough infection after univariate analysis: age, blood type, booster vaccination type, BMI, duration after booster vaccination, the interval between primary and booster vaccinations, COVID-19 epidemic control measures, and neutralising antibody concentration. Independent risk factors for SARS-CoV-2 breakthrough infection post-booster vaccination included COVID-19 epidemic control measures and duration after booster vaccination after multivariate analysis.

The risk of post-booster vaccination breakthrough infection was at its highest at 7 months after booster vaccination (9.5 times higher than that at 15 days post-booster vaccination). Additionally, the SARS-CoV-2 breakthrough infection risk after implement of routine epidemic prevention and control measures was 10.6-fold higher than that of duration when dynamic zero policy was strictly implemented (Table 3, Figure 3). This tendency was consistent with the results of nucleic acid testing for hospitalized patients and other populations in Henan Provincial People's Hospital from November 2022 to April 2024 (Figure 3C; Appendix Table 10). No link was found between SARS-CoV-2 breakthrough infection and GMC neutralising antibodies (adjusted odds ratio,0.9; 95%CI, 0.7–1.1, P=0.387; Table 3). However, within 6 months post-booster vaccination, the SARS-CoV-2 breakthrough infection rate increased with the decrease in GMC (linear correlation x2 = 318.7, P<0.001; r=-0.81, P=0.034, respectively; Figures 2A–D, Figure 3C). No difference was found in the rate of breakthrough infection among participants between the two modes of booster vaccination (heterologous and homologous types) (Figure 3D).

As shown in Figure 3B and Appendix Table 10, before 13 December 2022, when dynamic zero measures were implemented, the proportion of the entire population infected with SARS-CoV-2 was below 0.27%. Conversely, after 13 December 2022, with the release of epidemic measures, the SARS-CoV-2 infection rate among the overall population increased rapidly to 43.57%. After 6 months and up to May 2023, the number of hospitalized patients with SARS-CoV-2 further increased to 47.5%. However, during the subsequent 6 months up to November 2023, no outbreak of SARS-

10.3389/fimmu.2024.1446751

TABLE 2 Factors associated with neutralising antibody concentration after Chinese COVID-19 booster vaccine administration.

Factors	*n* (%)	B (95% CI)	*p*
Sex			
Men	66 (24.5)	Reference	
Women	323 (75.5)	0.23 (0.1 to 0.43)	0.022
Age (years)			
18–30	215 (55.3)	Reference	
31–50	86 (22.1)	0.08 (-0.63 to 0.06)	0.978
>50	88 (22.6)	0.18(-0.03 to 0.37)	0.074
Blood type			
A	97 (24.9)	Reference	
B	100 (25.7)	0.06 (-0.2 to 0.3)	0.504
O	155 (39.8)	-0.05 (-0.3 to 0.2)	0.427
AB	37 (9.5)	0.04 (-0.2 to 0.3)	0.272
Booster vaccination type			
Homologous type	253 (73.1)	Reference	
Heterologous type	136 (26.9)	0.37(0.19 to 0.54)	<0.001
BMI (kg/m^2)			
<18.5	27 (6.9)	Reference	
18.5–23.9	258 (66.3)	-0.14 (-1.1 to 0.85)	0.053
>23.9	104 (26.7)	-0.05 (-1.1 to 0.9)	0.525
Duration since booster vaccination (Mean days)			
1–14	31 (7.9)	Reference	
15–30	33 (8.5)	0.2 (-0.04 to 0.4)	0.997
31–90	40 (10.3)	0.2 (-0.16 to 0.5)	0.287
91–150	28 (7.2)	0.1 (-0.1 to 0.4)	0.850
151-210	17 (4.4)	0.4 (-0.3 to 1.2)	0.257
211–300	25 (6.4)	-0.9(-1.3 to -0.4)	0.001
301–365	61 (15.7)	−0.5(-0.9 to -0.1)	0.006
366–420	63 (16.2)	-1.1(-1.4 to -0.7)	0.001
421–480	66 (16.9)	0.2(-0.2 to 0.4)	0.585
481–690	53 (13.6)	0.5 (0.1 to 0.9)	0.026
Interval between primary and booster vaccinations (Mean days)			
180–210	185 (47.6)	Reference	0.021
>210	204 (52.4)	-0.21 (-0.4 to -0.1)	
SARS-CoV-2 breakthrough infection			
Yes	237 (60.9)	Reference	0.378
No	152 (39.1)	-0.12 (-0.28 to 0.1)	
Epidemic control measures against COVID-19			
Dynamic zero policy before 13 December 2022	113 (29.0)	Reference	<0.001
Routine control measures after 13 December 2022	276 (71.0)	-0.4 (-0.7 to -0.2)	

BMI, body mass index; CI, confidence interval; COVID-19, coronavirus disease; SARS-CoV-2, severe acute respiratory syndrome coronavirus 2.

CoV-2 infections occurred, and the infection rate was maintained at about 20% among hospitalized patients as of April 2024. This implies that the neutralising antibody levels in the entire population may have been elevated to a level that protects against COVID-19 outbreaks, which is consistent with our finding that the neutralising antibody levels in medical staff or the general populations only maintained for 6–7 months after booster vaccination (Figures 2A–D).

4 Discussion

To the best of our knowledge, no previous study has reported on the induction of humoral responses in medical staff after the first dose of the Chinese COVID-19 booster vaccine before and after the implementation of dynamic zero measures. The findings of this study indicate an association between booster vaccination and an acceptable adverse effect spectrum during the 690 days following vaccination of heterologous type and homologous type. Additionally, this study identified that change of COVID-19 epidemic control measures and duration after booster vaccination were two influence factors associated with SARS-CoV-2 breakthrough infection within 690 days after booster vaccination in medical staff. To date, the lifting of dynamic zero control measures and a longer interval between primary and booster vaccination that reduced humoral immunogenicity, which led to a higher breakthrough infection rate, has not previously been reported by studies on COVID-19 booster vaccines.

We also found that after the lifting of COVID-19 epidemic control measures, neutralising antibody production in medical staff that had received the booster vaccine was lower than that before this time point, which is contrary to the traditional understanding of infectious diseases. The traditional theory posits that neutralising antibody production increases with a rising incidence of infectious diseases. (19) As we know, smallpox, measles, chickenpox, these infectious diseases are life-long antibody immunity, and the vaccine against these infectious diseases can only provide a maximum of 7 years of antibody protection, requiring regular booster vaccination (20–22). This finding may be explained by the fact that the immune effect of natural SARS-CoV-2 infections after the lifting of dynamic zero measures was not as strong as that of the neutralising antibodies produced after booster vaccination. This phenomenon may be due to the special character of COVID-19 and needs to be verified using larger sample sizes and more rigorous trials.

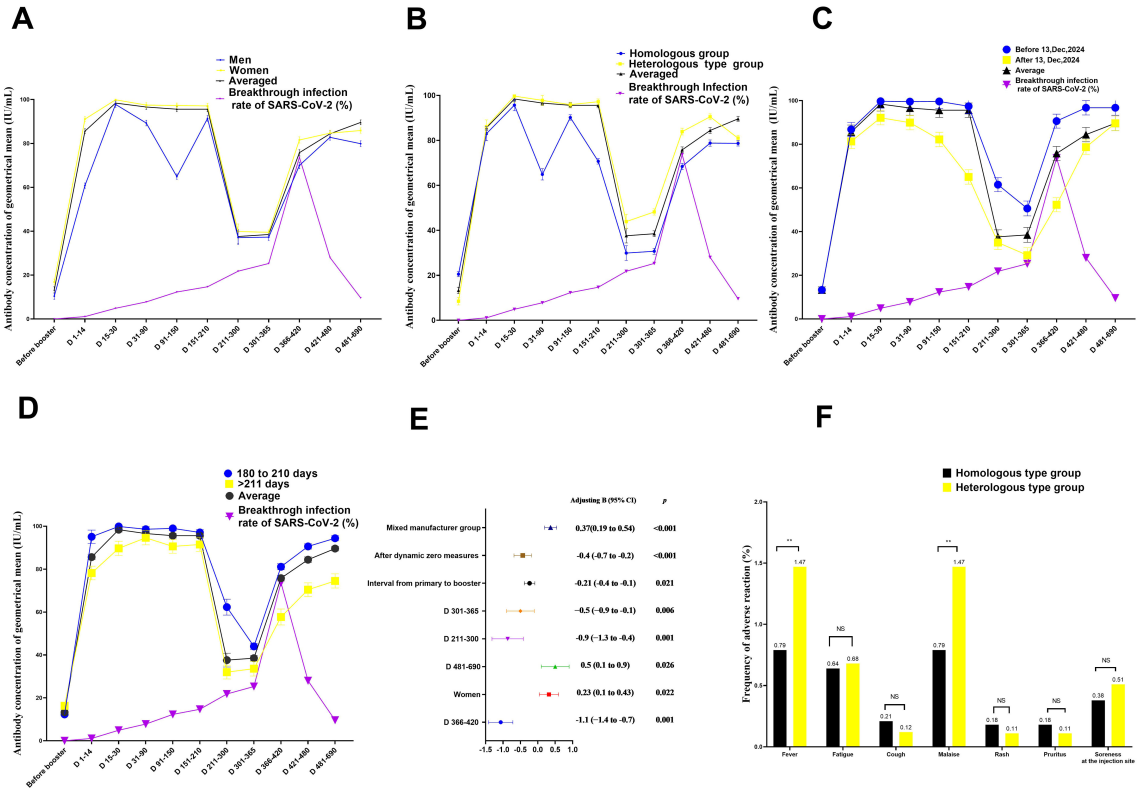

FIGURE 2
Quantitation of antibodies on days 1–690 following administration of the Chinese booster vaccine **(A–D)** Kinetics of neutralising antibodies according to **(A)** sex, **(B)** vaccination type, **(C)** control measures against COVID-19, and **(D)** interval between primary and booster vaccinations, **(E)** Factors influencing neutralising antibody production after booster vaccination in medical staff **(F)** comparison of adverse effects between individuals vaccinated with booster vaccines from the same and different types as the primary vaccine. Data are presented as mean (95% confidence interval [CI]) from the linear mixed-effects model adjusted for vaccine type, sex, blood type, age, interval between primary and booster vaccinations, COVID-19 control measures, and BMI. The $\log_2$-transformed levels of neutralising antibodies were used as independent variables. Chi-square test was used to compare the difference of adverse effects between individuals vaccinated with booster vaccines from the same and different types as the primary vaccine. BMI, body mass index; LSMD, least-squares mean difference; COVID-19, coronavirus disease; SARS-CoV-2, severe acute respiratory syndrome coronavirus 2.

The humoral response observed within 690 days of the first booster vaccine dose supports the effectiveness of the heterologous manufacturer (type) approach (4). Although vaccine receipts in the heterologous-type vaccination group reported a higher incidence of adverse events, the side effects associated with the heterologous vaccination were within the range of those reported for homologous vaccination. The observed result of the solicited adverse events of the booster vaccine in this study was similar to that of a previous study (17). Neutralising antibody levels typically increase more after booster administration using a heterologous booster vaccine than

TABLE 3 Factors associated with breakthrough infection of SARS-CoV-2 after administration of the Chinese COVID-19 booster vaccine.

Factors	Infected person times (n =306) %	Uninfected person times (n = 485) %	Univariate analysis		Multivariate analysis	
			OR (95% CI)	p	OR (95% CI)	P
Sex						
Men	82 (26.8)	138 (28.5)	Reference	0.613	*	
Women	224 (73.2)	347 (71.5)	1.1 (0.8–1.3)		*	–
Age (years)						
18–30	124 (40.5)	132 (27.2)	Reference	<0.001	Reference	
31–50	92 (30.1)	86 (17.7)	0.88 (0.6-1.3)		1.1(0.5–2.1)	0.847
>50	90 (29.4)	267 (55.1)	2.8 (2.0-3.9)		0.9(0.5–1.8)	0.865

(Continued)

TABLE 3 Continued

Factors	Infected person times (n =306) %	Uninfected person times (n = 485) %	Univariate analysis		Multivariate analysis	
			OR (95% CI)	p	OR (95% CI)	P
Blood type						
A	79 (20.83)	168 (29.17)	Reference	<0.001	Reference	
B	61 (31.94)	75 (36.11)	1.7 (1.1–2.7)		0.625(0.3–1.3)	0.191
O	115 (37.50)	100 (40.28)	2.4 (1.7–3.6)		0.959(0.5–1.8)	0.898
AB	51 (11.11)	142 (10.42)	0.7 (0.5–1.2)		0.674(0.3–1.4)	0.275
Booster vaccination type						
Homologous type	203 (66.3)	407 (83.9)	Reference	0.001	Reference	
Heterologous type	103 (33.7)	78 (16.1)	0.6 (0.5-0.8)		1.3(0.7–2.3)	0.351
BMI (kg/m^2)						
<18.5	21 (6.9)	6 (1.3)	Reference	0.001	Reference	
18.5–23.9	173 (56.5)	328 (67.6)	6.6 (2.6–16.7)		0.9(0.3–2.8)	0.896
>23.9	112 (36.6)	151 (31.1)	4.7 (1.8-2.1)		1.5(0.5–4.9)	0.522
Duration since booster vaccination (Mean days)						
1–14	15 (4.9)	84 (17.3)	Reference		Reference	
15–30	4 (1.3)	77 (15.9)	0.29 (0.1–0.9)	<0.001	0.3(0.1–1.3)	0.107
31–90	10 (3.3)	119 (24.5)	0.5 (0.2–1.1)		0.5(0.2–1.2)	0.114
91–150	19 (6.2)	136 (28.0)	0.8 (0.4–1.6)		0.8(0.4–1.8)	0.604
151–210	3 (0.98)	4 (0.82)	4.2 (0.9–20.7)		1.5(0.2–10.3)	0.708
211–300	22 (7.2)	3 (0.62)	41.1 (10.9–54.6)		9.5(2.0–13.9)	0.004
301–365	58 (18.9)	10 (2.1)	32.5 (13.6–77.3)		5.1(1.8–14.8)	0.002
366–420	56 (18.3)	19 (3.9)	16.5 (7.7–35.2)		2.5 (0.97–5.3)	0.059
421-480	72 (23.5)	28 (5.8)	14.4 (7.1–29.0)		4.6(2.0–10.4)	<0.001
481-690	47 (15.4)	5 (1.0)	52.6 (18.0–54.0)		8.8(2.7–19.1)	<0.001
Interval between primary and booster vaccinations (Mean days)						
180-210	170 (55.6)	371 (76.5)	Reference	<0.001	Reference	
>210	136 (44.4)	114 (23.5)	1.4(1.2–1.5)		1.1(0.6–1.8)	0.844
Epidemic control measures for COVID-19						
Dynamic zero policy before 13 December 2022	36 (11.8)	411 (84.7)	Reference	<0.001	Reference	<0.001
Routine control measures after 13 December 2022	270 (88.2)	74 (15.3)	7.2(5.3–9.8)		10.6(6.1–18.3)	
Neutralising antibody concentration (IU/mL) Mean± SD	58.1 ± 2.8	87.1 ± 1.6	–	<0.001	0.9(0.7–1.1)	0.387

"*": Multivariate analysis was not included, "-": not available.
BMI, body mass index; COVID-19, coronavirus disease; CI, confidence interval; OR, odds ratio; SARS-CoV-2, severe acute respiratory syndrome coronavirus 2; SD, standard deviation.

that of homologous booster group in our study, which was similar with other mRNA booster heterologous vaccination (23–26). However, the mechanism of neutralizing antibody difference between two types of booster vaccination was unclear to need further explore.

A recent report from the United States Center for Disease Control and Prevention (CDC) revealed that the vaccine efficiency in people who had received the first booster dose of mRNA vaccines declined from 87% to 31% after 5 months in the omicron variant epidemic period (15). This result is similar to that of our study,

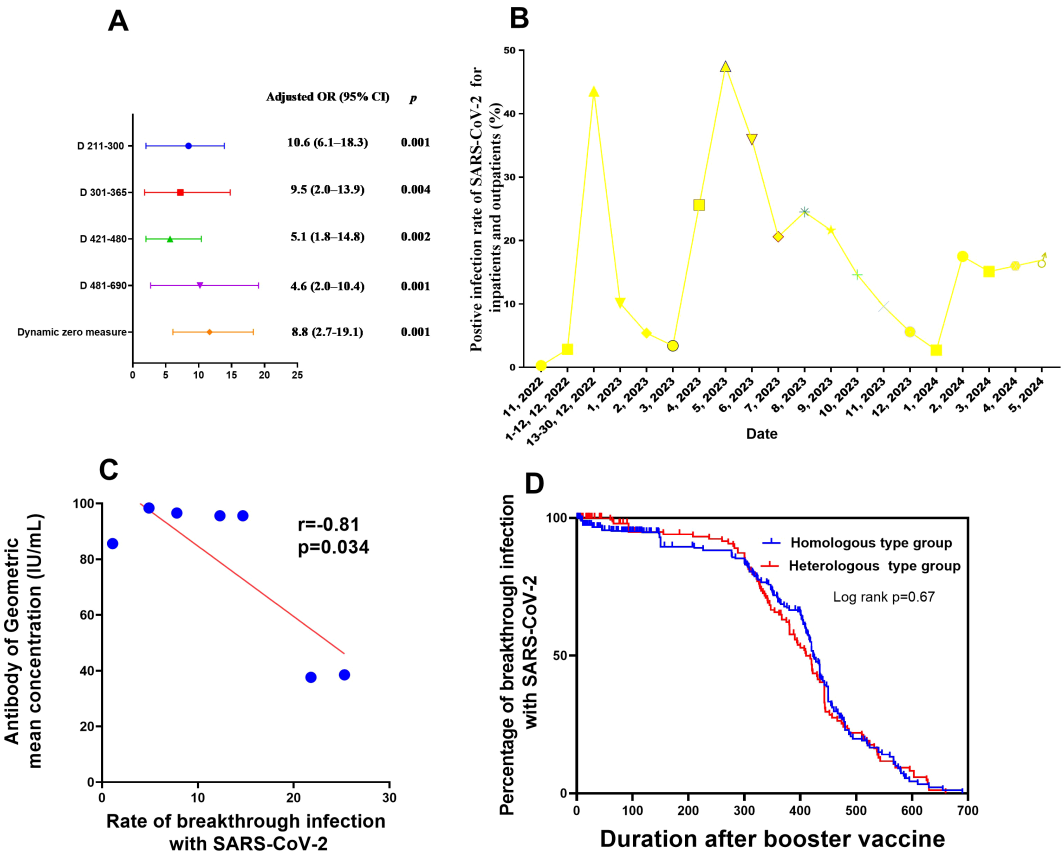

FIGURE 3
Factors influencing neutralising antibody production after booster vaccination, as well as SARS-CoV-2 breakthrough infection **(A)** Factors associated with breakthrough SARS-CoV-2 infection after booster vaccination in medical staff. **(B)** Rate of PCR-positivity for SARS-CoV-2 for inpatients and outpatients from Nov 2022 to Apr 2024. **(C)** Correlation between neutralising antibody production and breakthrough SARS-CoV-2 infection after booster vaccination in medical staff. **(D)** Survival curves of breakthrough infection between two modes of booster vaccination (mix and homologous types). CI, confidence interval; PCR, polymerase chain reaction; OR, odds ratio; SARS-CoV-2, severe acute respiratory syndrome coronavirus 2.

indicating that recipients are increasingly susceptible to infection with SARS-CoV-2 with a decrease in neutralising antibody levels by 6–7 months post-booster vaccination.

Associations between blood type and neutralising antibody production or breakthrough infection rate among medical staff were not investigated in this study. However, previous studies have reported that patients with blood group A have an increased risk of SARS-CoV-2 infection, whereas those with blood group O have a decreased risk (27, 28). In the hospital inpatients in this study, the SARS-CoV-2-infection rate showed that since April 2024, the natural SARS-CoV-2-infection rate among the general population is no longer accurately following the previous cycle of one outbreak every 6 months, perhaps indicating that booster vaccinations break the link between blood types and infection susceptibility or involve COVID-19 outbreak cycles.

In the present study, we found that participants with an appropriate interval between vaccination doses (180–210 days) had elevated neutralising antibody levels than those with longer intervals (>210 days). This result supports the current 6–7-month booster interval for the COVID-19 vaccine, as vaccines produce fewer neutralising antibodies when the interval exceeds 7 months.

This study has some limitations. First, the number of participants was relatively small, and some participants had recall bias about whether they had experienced SARS-CoV-2 breakthrough infection, given that COVID-19 symptoms and signs can be confused with flu or the common cold in the absence of specific tests (29, 30). Additionally, in the population included in our study, fewer individuals received the heterologous type vaccine than those who received the homologous type vaccine, because when beginning the first booster vaccine, according to the booster vaccination guidelines released by the health administration, it was recommended that boosters receive the vaccine of the same manufacturer or homologous type as the primary immunization, in order to reduce the side effects of vaccination. Given our resource limitations, we could not conduct pseudo-virus neutralization tests for neutralising antibodies against the latest SARS-CoV-2 variant (31). Therefore, we could not determine the levels of neutralising antibodies against viruses causing breakthrough infections. We only found a trend for correlation between decreasing neutralising antibodies and an increasing rate of SARS-CoV-2 infection after vaccination over time. Some studies have shown that due to the emergence of the novel coronavirus variant KP.2,XEC, and XDV.1, the antibodies

produced by the booster vaccine cannot neutralize the current variant strain (9–11). We speculate that the main reason is that the vaccine strain used in the booster vaccine is the prototype strain rather than the variant strain, which can also explain the high infection rate in the population despite the vaccination booster. In addition, the antibody and infection rate with SARS-CoV-2 for populations without vaccination for COVID-19 were not investigated; therefore, the comparison between the two population groups could not be calculated to obtain the protection rate of the booster vaccine. Moreover, we only investigated the antibody and breakthrough among medical staff in this study. Future studies should expand to more occupations, including workers or students, to compare the difference between antibody and breakthrough infection among different occupations. Furthermore, our results can be reported the neutralizing antibody response against to spike protein of SARS-CoV-2 to the currently Chinese COVID-19 booster vaccine used for this study, and not as a general message, perhaps a different antibody response against to nucleoprotein of SARS-CoV-2 (12, 13) was observed using a different vaccinate type, as mRNA vaccine (2, 14). We aim to include more participants and conduct pseudo-virus neutralization tests to address these limitations in the future.

In conclusion, this study evaluated the humoral immune responses and SARS-CoV-2 breakthrough infection within 690 days after the first booster vaccination dose in 389 medical staff members. Most participants rapidly developed increasing neutralising antibody levels after receiving a single second dose of the Chinese booster COVID-19 vaccine 1–2 weeks after the first. However, the neutralising antibody levels only last for 6–7 months following booster vaccination, after which the SARS-CoV-2-infection breakthrough rate increased significantly. We demonstrated relationships between blood type, age, sex, BMI, and duration after booster vaccination, reactivity, and breakthrough infection rate. Individuals with a longer antibody-level duration following booster vaccination and longer intervals between primary and booster vaccination after implementation of routine epidemic control measures had lower levels of antibodies and were more susceptible to infection with SARS-CoV-2 variants after the first booster dose than their counterparts. Our findings suggest that cooperation among researchers for the exploration of a broad spectrum and long duration neutralizing antibody of COVID-19 vaccines to booster population is a good idea to combat the immune escape of the increasing number of SARS-CoV-2 variants (32, 33).

Data availability statement

The original contributions presented in the study are included in the article/Supplementary Material, further inquiries can be directed to the corresponding authors.

Ethics statement

The studies involving humans were approved by the Ethics Committee of Henan Provincial People's Hospital (approval number 20210051, approval date: 24 May 2021) and complied with the principles of the Declaration of Helsinki and Good Clinical Practice. The studies were conducted in accordance with the local legislation and institutional requirements. The participants provided their written informed consent to participate in this study.

Author contributions

JX: Data curation, Writing – review & editing, Project administration, Resources. YY: Data curation, Project administration, Conceptualization, Formal analysis, Methodology, Software, Supervision, Writing – original draft. GC: Data curation, Project administration, Supervision, Resources, Writing – review & editing. BM: Data curation, Resources, Writing – review & editing, Investigation. YZ: Data curation, Investigation, Writing – review & editing. BW: Writing – review & editing, Funding acquisition. WY: Writing – review & editing, Validation, Visualization. QZ: Writing – review & editing, Data curation, Formal analysis, Supervision. QM: Writing – review & editing, Investigation, Methodology. XM: Methodology, Writing – review & editing, Data curation, Project administration. HW: Data curation, Writing – review & editing, Funding acquisition. YL: Funding acquisition, Writing – review & editing, Project administration. XZ: Funding acquisition, Writing – review & editing, Data curation.

Funding

The author(s) declare that financial support was received for the research, authorship, and/or publication of this article. This work was funded by the Henan Provincial Key Programs in Science and Technology (received by BW, grant number:242102310116) and the Joint Program of Medical Science and Technology Research of Henan Province (received by YL, grant number: LHGJ 20230021), the Henan Natural Science Foundation (grant number: 222300420355 and 242300421502) from the Henan Provincial Department of Education, and the Henan Province Science and Technology Research Program Project (grant number: SBGJ202103016) from the Henan Provincial Health Commission (received by HW and XZ). The funder played no role in study design, data collection, analysis and interpretation of data, or the writing of this manuscript.

Acknowledgments

We thank all study participants, including volunteers and study partners, the Henan Provincial People's Hospital data safety monitoring board, and the study steering committee. In addition, we are grateful to our colleagues—Wenning Yang, Yafei Chu, Nan Jing, Jiangfeng Zhang, Shanmei Wang, and Wenbo Xu—who assisted with sample collection and part of the experiments.

Conflict of interest

The authors declare that the research was conducted in the absence of any commercial or financial relationships that could be construed as a potential conflict of interest.

Publisher's note

All claims expressed in this article are solely those of the authors and do not necessarily represent those of their affiliated organizations, or those of the publisher, the editors and the reviewers. Any product that may be evaluated in this article, or claim that may be made by its manufacturer, is not guaranteed or endorsed by the publisher.

Supplementary material

The Supplementary Material for this article can be found online at: https://www.frontiersin.org/articles/10.3389/fimmu.2024.1446751/full#supplementary-material

References

1. Martens JP, Rutjens BT. Spirituality and religiosity contribute to ongoing COVID-19 vaccination rates: comparing 195 regions around the world. *Vaccin X*. (2022) 12:100241. doi: 10.1016/j.jvacx.2022.100241

2. Yie KY, Chien TW, Yeh YT, Chou W, Su SB. Using social network analysis to identify spatiotemporal spread patterns of COVID-19 around the world: online dashboard development. *Int J Environ Res Public Health*. (2021) 18:2461. doi: 10.3390/ijerph18052461

3. Oda Y, Kumagai Y, Kanai M, Iwama Y, Okura I, Minamida T, et al. Immunogenicity and safety of a booster dose of a self-amplifying RNA COVID-19 vaccine (ARCT-154) versus BNT162b2 mRNA COVID-19 vaccine: a double-blind, multicentre, randomised, controlled, phase 3, non-inferiority trial. *Lancet Infect Dis*. (2024) 24:351–60. doi: 10.1016/S1473-3099(23)00650-3

4. Terada-Hirashima J, Takamatsu Y, Shimizu Y, Uemura Y, Takeuchi JS, Tomita N, et al. Immunogenicity and safety of single booster dose of KD-414 inactivated COVID-19 vaccine in adults: an open-label, single-center, non-randomized, controlled study in Japan. *Hum Vaccin Immunother*. (2023) 19:2193074. doi: 10.1080/21645515.2023.2193074

5. Yuan Y, Xu J, Ma B, Chen G, Wang Z, Wang S, et al. Characteristics of humoral and cellular responses to coronavirus disease 2019 (COVID-19) inactivated vaccine in central China: a prospective, multicenter, longitudinal study. *Front Immunol*. (2023) 14:1107866. doi: 10.3389/fimmu.2023.1107866

6. Fidler S, Fox J, Tipoe T, Longet S, Tipton T, Abeywickrema M, et al. Booster vaccination against SARS-CoV-2 induces potent immune responses in people with human immunodeficiency virus. *Clin Infect Dis*. (2023) 76:201–9. doi: 10.1093/cid/ciac796

7. Ma Y, Xu S, An Q, Qin M, Li S, Lu K, et al. Coronavirus disease 2019 epidemic prediction in Shanghai under the" dynamic zero-COVID policy" using time-dependent SEAIQR model. *J Biosaf Biosecur*. (2022) 4:105–13. doi: 10.1016/j.jobb.2022.06.002

8. Wu F, Yuan Y, Deng Z, Yin D, Shen Q, Zeng J, et al. Acceptance of COVID-19 booster vaccination based on the protection motivation theory: a cross-sectional study in China. *J Med Virol*. (2022) 94:4115–24. doi: 10.1002/jmv.27825

9. Li H, Zheng S, Liu F, Liu W, Zhao R. Fighting against COVID-19: innovative strategies for clinical pharmacists. *Res Soc Adm Pharm*. (2021) 17:1813–8. doi: 10.1016/j.sapharm.2020.04.003

10. Zhou M, Liu L, Gu SY, Peng XQ, Zhang C, Wu QF, et al. Behavioral intention and its predictors toward COVID-19 booster vaccination among Chinese parents: applying two behavioral theories. *Int J Environ Res Public Health*. (2022) 19:7520. doi: 10.3390/ijerph19127520

11. Kutasi K, Koltai J, Szabó-Morvai Á, Röst G, Karsai M, Biró P, et al. Understanding hesitancy with revealed preferences across COVID-19 vaccine types. *Sci Rep*. (2022) 12:13293. doi: 10.1038/s41598-022-15633-5

12. Alhinai Z, Park S, Choe YJ, Michelow IC. A global epidemiological analysis of COVID-19 vaccine types and clinical outcomes. *Int J Infect Dis*. (2022) 124:206–11. doi: 10.1016/j.ijid.2022.09.014

13. Wang C, Hou B. The booster immunization using commercial vaccines effectively protect chickens against novel variants of infectious bursal disease virus (genotype A2dB1). *Poult Sci*. (2024) 103:103552. doi: 10.1016/j.psj.2024.103552

14. Cheng SM, Mok CK, Li JK, Chan KK, Luk KS, Lee BH, et al. Cross-neutralizing antibody against emerging Omicron subvariants of SARS-CoV-2 in infection-naïve individuals with homologous BNT162b2 or BNT162b2(WT + BA.4/5) bivalent booster vaccination. *Virol J*. (2024) 21:70. doi: 10.1186/s12985-024-02335-9

15. Ferdinands JM, Rao S, Dixon BE, Mitchell PK, DeSilva MB, Irving SA, et al. Waning 2-dose and 3-dose effectiveness of mRNA vaccines against COVID-19-associated emergency department and urgent care encounters and hospitalizations among adults during periods of delta and omicron variant predominance - VISION network, 10 states, august 2021-january 2022. *MMWR Morb Mortal Wkly Rep*. (2022) 71:255–63. doi: 10.15585/mmwr.mm7107e2

16. Salaets T, Lacaze-Masmonteil T, Hokuto I, Gauldin C, Taha A, Smits A, et al. Prospective assessment of inter-rater reliability of a neonatal adverse event severity scale. *Front Pharmacol*. (2023) 14:1237982. doi: 10.3389/fphar.2023.1237982

17. Gackowska M, Cofta P, Śrutek M, Marciniak B. Multivariate linear regression model based on cross-entropy for estimating disorganisation in drone formations. *Sci Rep*. (2023) 13:12750. doi: 10.1038/s41598-023-39926-5

18. Lustig Y, Sapir E, Regev-Yochay G, Cohen C, Fluss R, Olmer L, et al. BNT162b2 COVID-19 vaccine and correlates of humoral immune responses and dynamics: a prospective, single-centre, longitudinal cohort study in health-care workers. *Lancet Respir Med*. (2021) 9:999–1009. doi: 10.1016/S2213-2600(21)00220-4

19. Meidert AS, Hermann S, Brandes F, Kirchner B, Buschmann D, Billaud JN, et al. Extracellular vesicle-associated miRNAs regulate signaling pathways involved in COVID-19 pneumonia and progression to severe acute respiratory corona virus-2 syndrome. *Front Immunol*. (2021) 12:784028. doi: 10.3389/fimmu.2021.784028

20. Marchi S, Piccini G, Cantaloni P, Guerrini N, Zanella R, Coluccio R, et al. Evaluation of monkeypox- and vaccinia-virus neutralizing antibodies before and after smallpox vaccination: a sero-epidemiological study. *J Med Virol* (2024) 96:e29728. doi: 10.1002/jmv.29728

21. Shin H, Lee S, Choi MM, Yi H, Chung YS. Development of Smallpox antibody testing and surveillance following Smallpox vaccination in the Republic of Korea. *Vaccines (Basel)*. (2024) 12:1105. doi: 10.3390/vaccines12101105

22. Zyla DS, Della MR, Niemeyer G, Zipursky G, Stearns K, Leedale C, et al. A neutralizing antibody prevents postfusion transition of measles virus fusion protein. *Science* (2024) 384:eadm8693. doi: 10.1126/science.adm8693

23. Ailsworth SM, Keshavarz B, Richards NE, Workman LJ, Murphy DD, Nelson MR, et al. Enhanced SARS-CoV-2 IgG durability following COVID-19 mRNA booster vaccination and comparison of BNT162b2 with mRNA-1273. *Ann Allergy Asthma Immunol* (2023) 130:67–73. doi: 10.1016/j.anai.2022.10.003"10.1016/j.anai.2022.10.003

24. Pastore G, Polvere J, Fiorino F, Lucchesi S, Montesi G, Rancan I, et al. Homologous or heterologous administration of mRNA or adenovirus-vectored vaccines show comparable immunogenicity and effectiveness against the SARS-CoV-2 Omicron variant. *Expert Rev Vaccines* (2024) 23:432–44. doi: 10.1080/14760584.2024.2333952

25. Lee WS, Audsley J, Trieu MC, Reynaldi A, Aurelia LC, Mehta PH, et al. Randomized controlled trial reveals no benefit to a 3-month delay in COVID-19 mRNA booster vaccine. *J Clin Invest*. (2024) 134:e181244. doi: 10.1172/JCI181244

26. Itamochi M, Yazawa S, Saga Y, Shimada T, Tamura K, Maenishi E, et al. COVID-19 mRNA booster vaccination induces robust antibody responses but few adverse events among SARS-CoV-2 naive nursing home residents. *Sci Rep* (2024) 14:23295. doi: 10.1038/s41598-024-73004-8

27. Leung VK, Fox A, Carolan LA, Aban M, Laurie KL, Druce J, et al. Impact of prior vaccination on antibody response and influenza-like illness among Australian healthcare workers after influenza vaccination in 2016. *Vaccine*. (2021) 39:3270–8. doi: 10.1016/j.vaccine.2021.04.036

28. Arthur CM, Cummings RD, Stowell SR. Unraveling the mystery of blood groups and COVID-19. *Clin Chem Lab Med*. (2024) 62:371–2. doi: 10.1515/cclm-2023-1195

29. Luo J, Craver A, Zakin P, Stepniak L, Moore K, King J, et al. Race may modify the association between blood type and COVID-19 infection. *EJHaem*. (2022) 3:903–7. doi: 10.1002/jha2.539

30. Bouzid D, Mullaert J, Hingrat QL, Laurent O, Duval X, Lescure X, et al. Characteristics associated with COVID-19 or other respiratory viral infections in a

single-center emergency department. *PloS One*. (2020) 15:e243261. doi: 10.1371/journal.pone.0243261

31. Zhang H, Xu N, Xu Y, Qin P, Dai R, Xu B, et al. Safety and immunogenicity of Ad5-nCoV immunization after three-dose priming with inactivated SARS-CoV-2 vaccine in Chinese adults. *Nat Commun*. (2023) 14:4757. doi: 10.1038/s41467-023-40489-2

32. Lee CY, Suzuki JB. COVID-19: variants, immunity, and therapeutics for non-hospitalized patients. *Biomedicines*. (2023) 11:2055. doi: 10.3390/biomedicines11072055

33. Li X, Xu M, Yang J, Zhou L, Liu L, Li M, et al. Nasal vaccination of triple-RBD scaffold protein with flagellin elicits long-term protection against SARS-CoV-2 variants including JN.1. *Signal Transduct Target Ther*. (2024) 9:114. doi: 10.1038/s41392-024-01822-3

frontiers | Frontiers in Immunology

TYPE Original Research
PUBLISHED 28 January 2025
DOI 10.3389/fimmu.2024.1503853

OPEN ACCESS

EDITED BY
Ousman Jobe,
Henry M. Jackson Foundation for the Advancement of Military Medicine (HJF), United States

REVIEWED BY
Sandeep Kumar Dhanda,
St. Jude Children's Research Hospital, United States
Pankaj Kumar,
University of Texas Southwestern Medical Center, United States

*CORRESPONDENCE
Jeong Ho Hwang
jeongho.hwang@kitox.re.kr

RECEIVED 29 September 2024
ACCEPTED 26 December 2024
PUBLISHED 28 January 2025

CITATION
Sethi G, Kim YK, Han S-C and Hwang JH (2025) Designing a broad-spectrum multi-epitope subunit vaccine against leptospirosis using immunoinformatics and structural approaches.
Front. Immunol. 15:1503853.
doi: 10.3389/fimmu.2024.1503853

Designing a broad-spectrum multi-epitope subunit vaccine against leptospirosis using immunoinformatics and structural approaches

Guneswar Sethi[1,2], Young Kyu Kim[1], Su-Cheol Han[2] and Jeong Ho Hwang[1,2]*

[1]Animal Model Research Group, Korea Institute of Toxicology, Jeonguep, Jeollabuk-do, Republic of Korea, [2]Center for Companion Animal New Drug Development, Korea Institute of Toxicology, Jeonguep, Jeollabuk-do, Republic of Korea

Introduction: Leptospirosis, caused by *Leptospira interrogans*, is a neglected zoonotic disease that poses a significant global health risk to both humans and animals. The rise of antimicrobial resistance and the inefficacy of existing vaccines highlight the urgent need for new preventive strategies.

Methods: An immunoinformatics approach was employed to design a multi-epitope subunit vaccine (MESV) against leptospirosis. B-cell, cytotoxic T lymphocyte (CTL), and helper T lymphocyte (HTL) epitopes were selected from five key *Leptospira* proteins. These epitopes were fused with a heparin-binding hemagglutinin (HBHA) adjuvant and appropriate linkers to construct the broad-spectrum vaccine. The physicochemical properties of the vaccine were assessed, including antigenicity, immunogenicity, allergenicity, and conservation. The vaccine's 3D structure was modeled, optimized, and validated. Molecular docking, molecular dynamics simulations, and MM-GBSA analysis were performed to assess the vaccine's binding interactions with Toll-like receptors (TLR2 and TLR4). Immune simulations and *in silico* cloning were also conducted to evaluate the vaccine's immune response and expression potential.

Results: The MESV demonstrated high antigenicity, immunogenicity, non-allergenicity, and conservation across different *Leptospira* strains. Population coverage analysis revealed that T-cell epitopes significantly interacted with HLA molecules, covering 95.7% of the global population. Molecular docking showed strong and stable binding with TLR2 and TLR4, with binding energies of -1,357.1 kJ/mol and -1,163.7 kJ/mol, respectively. Molecular dynamics simulations and MM-GBSA analysis confirmed the stability of these interactions and accurately calculated the intermolecular binding free energies. Immune simulations indicated robust B and T cell responses, and *in silico* cloning demonstrated that the vaccine could be successfully expressed in *E. coli*.

Discussion: These findings suggest that MESV is a promising candidate for leptospirosis prevention, providing robust immune responses and broad population coverage. However, further *in vivo* studies are necessary to validate its efficacy and safety.

KEYWORDS

leptospirosis, multi-epitope subunit vaccine, immunoinformatics, population coverage, molecular docking, molecular dynamics simulation, *in silico* cloning

1 Introduction

Leptospirosis is a widespread and reemerging zoonotic disease caused by spirochetes of the genus *Leptospira* (1). It affects an estimated 1 million individuals annually, resulting in approximately 60,000 fatalities worldwide (2, 3). The disease is particularly prevalent in tropical and subtropical regions, where environmental and socioeconomic factors such as poor sanitation, frequent flooding, and close human-animal interactions create ideal conditions for transmission (3). The disease manifests as flu-like symptoms or severe complications like Weil's disease, leading to multi-organ failure (4, 5). Similarly, the disease has a significant economic impact on agriculture and companion animals, particularly in underdeveloped countries, where it can cause abortions, infertility, decreased milk production, and cattle death (6). Despite identifying 66 *Leptospira* species and over 300 pathogenic serovars (7, 8) grouped into 26 serogroups, effective treatment and prevention options remain limited (9). Currently, inactivated bacterial vaccines are the only approved prophylactic measure, but they offer limited cross-protection against diverse serovars and provide only short-term immunity (10, 11). Moreover, antibiotics such as azithromycin, doxycycline, penicillin, and cephalosporins are used to treat *Leptospira* infections. Still, challenges like antibiotic resistance and delayed diagnosis due to non-specific symptoms complicate disease management (12). This underscores the urgent need for a universal vaccination strategy.

Vaccination efforts have shown promise in countries like Cuba (13), Russia (14), and China (15). In Cuba, the Vax-Spiral® vaccine, registered in 1998, became part of the National Leptospirosis Prevention and Control Program (16). A phase III clinical trial demonstrated 78.1% efficacy with no serious adverse effects (16, 17). However, these vaccines often fail to address the extensive diversity of *Leptospira* strains, and single-antigen formulations require frequent boosters, which can lead to side effects and leave gaps in widespread protection. Challenges also include local serovar variations, potential autoimmune reactions (e.g., uveitis) (18), and an incomplete understanding of protective immunity mechanisms. Moreover, *Leptospira*'s genetic diversity and immune evasion strategies, such as antigenic variation, complement evasion, and rapid tissue infiltration, make developing a broadly effective vaccine particularly complex. A key limitation of current approaches is the lack of a standardized animal model to evaluate human vaccine candidates, coupled with variability in immune responses across different populations and regions. Despite ongoing efforts, including clinical trials of multi-serovar and subunit vaccines, no universally protective vaccine has been established. These gaps underscore the need for innovative strategies to elicit sustained, cross-protective immunity against leptospirosis, particularly through the development of vaccines that can overcome antigenic diversity and immune evasion mechanisms.

Our study aims to address these gaps by designing a multi-epitope subunit vaccine (MESV) incorporating immunogenic proteins to provide broad-spectrum protection. Multi-epitope vaccine designs are gaining recognition for their potential to induce comprehensive immune responses while minimizing side effects against Leptospirosis (19–22). Previous studies, such as Majid et al. (19), demonstrated computationally designed MESVs' potential to enhance immune responses through IFN-gamma induction. Additionally, Pankaj et al. explored proteins like LigA and LigB, which are promising candidates due to their roles in *Leptospira* virulence (20, 22).

Outer membrane proteins (OMPs) are promising vaccine candidates due to their surface exposure and involvement in virulence (23, 24). Notable OMPs, such as LipL32, LigA, and LigB, have demonstrated substantial protective efficacy in mouse models (17, 25). In this study, we selected five immunogenic proteins: LipL71, TonB-dependent receptor (TBDR), putative lipoprotein (irpA), sphingomyelinase C2 (Sph2), and general secretory pathway protein D (GspD) (26) as vaccine targets based on their roles in leptospiral pathogenesis and immunogenicity. LipL71 plays a role in pathogenesis by binding peptidoglycan and inducing antibody responses (27–29). TBDR and irpA are essential for iron uptake, survival, and virulence (30, 31). Sph2, a key virulence factor, causes host cell apoptosis and inflammatory tissue damage and serves as a diagnostic marker due to its early presence in infections (32, 33). GspD, a type 2 secretion system secretin, elicits bactericidal antibody responses, targeting multiple *Leptospira* species (34).

Advances in immunoinformatics enable rapid and cost-effective vaccine design, predicting immunogenic epitopes for robust immune responses (35). This approach has been successfully applied to pathogens like *Mycobacterium tuberculosis* (36, 37),

Plasmodium falciparum (38), and *Pseudomonas aeruginosa* (39). By integrating epitope prediction, TLR docking, and immune simulations, our study aims to overcome traditional vaccine development limitations and provide sustained, cross-protective immunity against leptospirosis.

2 Material and methods

2.1 Protein selection and retrieval

The prioritized target proteins, including LipL71 (UniProt ID: Q8F1N5), TBDR (UniProt ID: Q8F0M4), irpA (UniProt ID: Q8F0M3), Sph2 (UniProt ID: P59116), and GspD (UniProt ID: Q72S17), were retrieved from the UniProt database in FASTA format (40). For the vaccine design, we used a pathogenic strain of *L. interrogans* serogroup Icterohaemorrhagiae serovar Lai (strain 56601; Proteome ID: UP000001408). Subsequently, VaxiJen v2.0, an online prediction server, was used to identify the most potent antigenic protein through alignment-independent prediction with a threshold of 0.4 (41). Determining the subcellular localization and allergenicity of the selected proteins is essential for designing potential vaccine candidates. CELLO v.2.5 and PSORTb v3.0.3 were selected for their high accuracy for bacterial subcellular localization predictions, and allergenicity was evaluated using AllergenFP v.1.0 (42–44). To reduce the risk of autoimmunity, antigenic proteins were analyzed against the human proteome using the BLASTp tool with default parameters (45). Signal peptides were removed from the candidate proteins before the epitopes were predicted. We used the SignalP 5.0 server to identify and exclude these signal peptides. The workflow used in this study is presented in Figure 1. A detailed list of the databases, software, and web services utilized in this study is provided in Supplementary Table S1.

2.2 Prediction and screening of epitopes

To predict B-cell epitopes, we utilized the ABCpred server v.2.0, a bioinformatics tool well-regarded for predicting antigenic epitopes or antibody-binding sites within protein sequences (46). This tool was specifically chosen for its demonstrated reliability and high predictive accuracy across various pathogens, including bacteria, viruses, and parasites, making it suitable for vaccine candidate development. Using artificial neural networks (ANN), ABCPred predicts linear and continuous B-cell epitopes with high sensitivity and specificity. In our analysis, we applied a threshold of 0.85, generating 16-mer epitopes and focusing on top-scoring immunogenic epitopes for further investigation.

To predict HTL epitopes, which are crucial for immune system activation, we used the IEDB MHC II binding prediction server with the NetMHCIIpan 4.1 EL method (47, 48). This server is considered one of the most accurate tools for predicting peptide-MHC class II interactions based on a comprehensive set of experimentally validated epitopes. All parameters were kept at their default settings except for allele selection. We selected a reference set of HLA alleles covering 99% of the global allele distribution to ensure that the prediction results are applicable across diverse populations. Peptides with the lowest percentile ranks, indicating the highest predicted affinities, were then selected for further investigation. The IFNepitope and IL4Pred servers were used to predict Interferon-gamma (IFN-γ) and Interleukin-4 (IL-4) induction (49, 50), both of which are critical for assessing immune activation. These servers employ a combination of support vector machine (SVM) and motif-based approaches to differentiate between IFN-γ-producing and non-producing peptides. This step helped prioritize HTL epitopes most likely to trigger a strong immune response, which is crucial for vaccine efficacy.

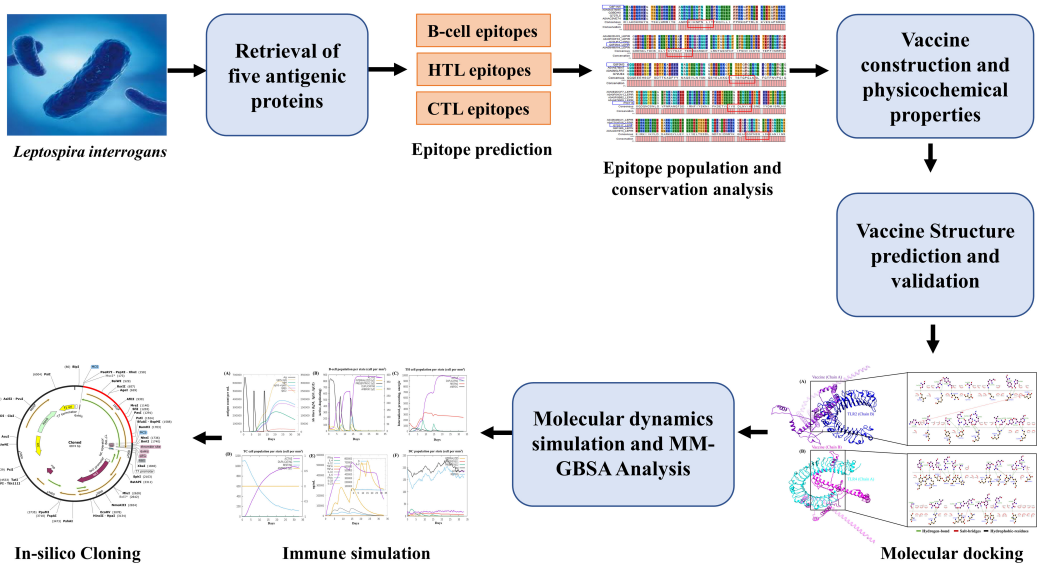

FIGURE 1
Methodology adopted for developing a multi-epitope subunit vaccine against *Leptospira interrogans*.

NetCTL v1.2, with parameters for epitope identification (0.75), C-terminal cleavage (0.15), and TAP transport efficiency (0.05), was selected due to its integration of multiple prediction metrics for MHC class I binding (51). A3 and B44 supertypes were used for screening, ensuring high predictive coverage for CTL epitopes. Subsequently, we used the online tools VaxiJen 2.0, AllergenFP v.1.0, and ToxinPred (52) to evaluate the antigenicity, allergenicity, and toxicity of the selected B-cell, HTL, and CTL epitopes. Furthermore, the predicted epitopes were also cross-checked with the IEDB to identify known experimentally validated epitopes for *L. interrogans* (ID-173) (53, 54).

2.3 Epitope population and conservation analysis

The vaccine demographic reach of the CTL and HTL epitopes was evaluated using the IEDB population coverage analysis tool with default parameters (55). This tool can assess epitopes against their respective HLA genotype frequencies to ensure adequate coverage across the global human population. In designing the MESV, we evaluated the conservation of B-cell, HTL, and CTL epitopes across multiple *L. interrogans* strains. Using CLC Sequence Viewer v.8.0, we aligned the sequences of five selected proteins from various pathogenic strains with default parameters. WebLogo v.3 generated sequence logos highlighting conserved residues within the epitopes to visualize amino acid conservation and sequence preferences (56). The tool was used with default settings and a sequence weight of 1. Peptides were considered conserved if their amino acids consistently appeared across all analyzed strains. These conserved peptides were incorporated into the MESV to ensure broad applicability and effectiveness.

2.4 MESV construction and physicochemical property determination

Epitopes demonstrating high antigenicity, conservation, and non-toxicity were carefully selected for inclusion in the final MESV. Optimal B-cell, CTL, and HTL epitopes were selected based on superior scores and linked using appropriate linkers. To improve vaccine effectiveness, the heparin-binding hemagglutinin (HBHA; P9WIP9) sequence was obtained from the UniProt database and incorporated into the N-terminus as an adjuvant, using the EAAAK linker for facilitation. The KK and GPGPG linkers connected the B-cell and HTL epitopes, while CTL epitopes were linked using AAY linkers.

The physicochemical properties of the MESV, including isoelectric point (pI), molecular weight, and aliphatic index, were analyzed using the ProtParam tool (57). The ANTIGENpro server (58) was used for antigenicity prediction due to its pathogen-independent, sequence-agnostic approach, and the VaxiJen v2.0 server (41) provided an additional antigenicity assessment. AllerTOP v2.0, based on auto cross-covariance (ACC) transformation, was utilized to predict the allergenicity of the MESV sequence (59). Solubility predictions were made using SOLpro, an SVM-based tool, and Protein-Sol, which compares solubility profiles of input sequences against a solubility database (58, 60).

2.5 Structure modeling and validation

For vaccine development, understanding the 2D and 3D structures of the proposed MESV is essential, as these structures reveal functional characteristics and aid in docking studies. The 2D structure was modeled using PSIPRED v.4.0 and GORIV (61, 62). PSIPRED employs position-specific scoring matrices for precise sequence homology identification, while GORIV utilizes information theory and Bayesian statistics to provide complementary insights. For 3D structure prediction, trRosetta, integrating deep learning with the Rosetta platform, was selected due to its high precision in complex protein modeling (63). The modeled structure was further refined using the GalaxyRefine webserver. The server employs the ab initio method to model the missing loops and terminal ends (64). Model validation was conducted using ProSA-web for Z-score validation (65) and Ramachandran plot analysis with PROCHECK to assess stereochemical properties (66). The final 3D model was visualized with Chimera 1.17.1 to examine structural details (67).

2.6 Linear and conformational antibody epitope prediction

After creating the 3D model of the vaccine construct, continuous and discontinuous epitopes were predicted using the IEDB ElliPro online tool with default settings and an epitope threshold score of 0.5 (68).

2.7 Molecular docking

Toll-like receptors (TLRs), particularly TLR2 and TLR4, play a crucial role in recognizing *Leptospira* components and initiating immune responses (69). TLR4 specifically recognizes pathogen-associated molecular patterns (PAMPs), such as lipopolysaccharides, to trigger high-sensitivity immune responses (70). To investigate potential interactions between the MESV and TLRs, the crystal structures of TLR2 (PDB ID: 5D3I) and TLR4 (PDB ID: 4G8A) were retrieved from the Protein Data Bank. Pre-docking preparations were performed to remove non-essential molecules like water, minimizing interference during the binding assessment. The Dock Prep tool in UCSF Chimera v.1.17.1 refined the structures by adding hydrogen atoms and assigning proper atomic charges. For TLR4, the monomeric form was chosen to simplify the docking process with the vaccine construct. Docking was carried out using ClusPro 2.0 (71), from which the most favorable configuration based on binding energy was selected for further analysis. Visualization of receptor-vaccine interactions was carried out with UCSF Chimera 1.17.1 (64) and LigPlot+ v.2.2.5 (69), which was used to create 2D interaction maps displaying hydrophobic and hydrogen bonds between the vaccine and TLRs.

2.8 Molecular dynamics simulation

MDS was conducted using the GROMACS v2022 software package to examine the structural and binding stabilities of the MESV-TLR2 and MESV-TLR4 complexes. To perform the 100 ns simulation, we solvated the system with the GROMAS96 43a1 force field within a cubic box with 10.0 Å dimensions (72). The system's charge was neutralized by adding Na^+ and Cl^- ions. Energy minimization was performed using the steepest descent method and equilibrated through a 200 ps simulation at 300 K and 1 bar pressure in the NVT and NPT ensembles to remove unfavorable steric clashes. Van der Waals and electrostatic interactions were handled using the particle-mesh Ewald (PME) method with a 1 nm cutoff radius (73). LINCS and SETTLE algorithms were used to constrain the bond lengths and water geometry (74, 75). Temperature was controlled with the Berendsen thermostat using a V-rescale, and pressure was regulated using the Parrinello-Rahman method (76). The stability of the designed MESV was assessed using GROMACS tools by analyzing the root mean square deviation (RMSD), radius of gyration (Rg), root mean square fluctuation (RMSF), and solvent-accessible surface area (SASA). The binding energy of the MESV-TLR2 and MESV-TLR4 complexes was evaluated through the MM-GBSA method using the HawkDock server (77).

2.9 Immune simulation

In silico immune simulations were conducted using the C-ImmSim online server to assess the immune response characteristics of the vaccine design (78). These simulations generated specific immune responses to antigens using agent-based approaches, including positional score matrix and machine learning methods. Apart from time steps 1, 84, and 170, the simulation adhered to default parameters. Following the customary dosing intervals prevalent in conventional vaccine administration, three injections were administered at four-week intervals. This scheduling aligns with the optimal immune response induction guidelines and vaccine effectiveness. Plot analysis was conducted to determine the Simpson index (D), which served as a metric for diversity.

2.10 *In silico* cloning

Codon adaptation tools were used to address the differences in codon usage between humans and *E. coli* to enhance expression rates in the host system. Adjusting codon usage to align with that of prokaryotic organisms is essential for efficient expression (79). The sequence was optimized using the VectorBuilder Codon optimization tool to align the codon usage with *E. coli* strain K12 as the host. An ideal codon adaptation index (CAI) score and a GC content ranging from 30-70% were considered for this assessment. *XhoI* and *BamHI* restriction sites were added to the 5′ and 3′ ends of the vaccine sequence. The vaccine constructs were then cloned into the pET-28a (+) expression vector using SnapGene software, followed by a simulation of agarose gel electrophoresis.

3 Results

3.1 Protein selection

Five proteins from *L. interrogans* were selected based on a comprehensive literature review, and their corresponding FASTA sequences were retrieved. The selected proteins were subjected to antigenicity evaluation and subcellular localization prediction to gain insights into their immunogenic properties. Each prioritized protein displayed an antigenic score >0.4 and was predicted to localize to the outer membrane. The non-homology analysis confirmed that none of the selected proteins shared similarities with the host proteome. Additionally, the AllergenFP v.1.0 server analysis indicated that none of the selected proteins exhibited allergenic properties (Supplementary Table S2).

3.2 Prediction of immunogenic epitopes

Before epitope prediction, signal peptides were identified and removed from the candidate proteins (Supplementary Figure S1). B-cell epitope prediction is crucial in vaccine design, as these surface-exposed epitopes are essential for initiating antibody production and immune responses. The ABCpred server was used to identify 77 B-cell epitopes from five candidate proteins (Supplementary File 1). The top five epitopes were selected based on their high score, antigenicity, non-allergenicity, and non-toxicity predictions (Table 1).

Recognizing HTL epitopes is essential for creating an immunotherapeutic vaccine, given their pivotal role in triggering humoral and cell-mediated immune responses. HTL epitope screening was conducted by selecting epitopes with the lowest

TABLE 1 B-cell epitopes prediction for the input *Leptospira interrogans* protein sequences *via* ABCpred server.

Si. No	Protein name	Sequence	Start position	Score	Antigenicity	Allergenicity	Toxicity
1	LipL71	KIAGRDTKTEGNKNTK	367	0.90	2.316	Non-allergen	Non-toxic
2	TBDR	YSLAKSGNVRDHEVNN	440	0.94	1.223	Non-allergen	Non-toxic
3	irpA	FQATAARDTFCINLSE	360	0.93	1.095	Non-allergen	Non-toxic
4	Sph2	PRYVGVPFTWDAKTNE	363	0.96	0.809	Non-allergen	Non-toxic
5	GspD	NPVIQSEDLGSERKPP	252	0.95	0.660	Non-allergen	Non-toxic

TABLE 2 Selected HTL epitopes from *L. interrogans* proteins, with predictions for toxicity, antigenicity, allergenicity, and stimulation of IFN-γ and IL-4 production.

Si. No	Allele	Epitope	Percentile rank	Antigenicity	Allergenicity	Toxicity	IFN-γ inducer	IL-4 inducer
1	HLA-DRB1*09:01	AEENLKAAEESRVAA	0.01	1.0740	Non-allergen	Non-toxic	Positive	Positive
2	HLA-DRB5*01:01	RSYRFVGAESRYQQD	0.03	0.5564	Non-allergen	Non-toxic	Positive	Positive
3	HLA-DRB3*02:02	AVTAFAANNNPTAAD	0.01	0.4767	Non-allergen	Non-toxic	Positive	Positive
4	HLA-DRB1*04:01	GKKFHVIGTHAQSQD	0.03	1.2025	Non-allergen	Non-toxic	Positive	Positive
5	HLA-DQA1*01:02/ DQB1*06:02	LTVDNQEAEISVGQD	0.01	1.1496	Non-allergen	Non-toxic	Positive	Positive

percentile rank and IC50 values using the reference set of MHC-II HLA alleles provided in Supplementary Table S3. This study identified the top five epitopes from the selected proteins, revealing percentile rank and IC_{50} values ranging from 0.01 to 0.36 and 5 to 49, respectively. Furthermore, the HTL epitopes exhibiting a positive score for IFN-γ and IL-4 prediction were selected (Table 2).

Subsequently, we predicted CTL epitopes from the selected protein sequences using the NetCTL 1.2 server to assess the role of CTLs in immune activation. To enhance accuracy, residues in the signal peptide regions were excluded for the TBDR epitope sequence 'SEETNKPIL' and Sph2 sequence 'YLLLFSLIR.' This analysis identified the top 10 epitopes (Table 3). We focused on the HLA supertypes -B44 and -A3, as they can enhance immune responses and provide broad population coverage through effective HLA targeting [68,69]. To assess the number of experimentally validated epitopes for *L. interrogans*, we consulted the IEDB, which lists 46 known epitopes for this pathogen. Among these, two B-cell epitopes for Sphingomyelinase C2 (Sph2) were previously reported. However, upon cross-checking our computationally predicted B-cell epitopes for Sph2, we found none matched the reported ones, indicating that our identified B-cell epitope is novel. Furthermore, the B-cell, HTL, and CTL epitopes predicted for all five candidate proteins were not reported as known epitopes in the IEDB for *L. interrogans*, further highlighting their novelty. The detailed findings from the epitope screening are provided in Supplementary File 1.

3.3 Population and conservation analysis

The IEDB population coverage analysis tool was used to estimate the population coverage of the selected CTL and HTL epitopes. Globally, the combined epitopes had a population coverage of 95.7%. The highest coverage was found in Europe at 98.64%, and the lowest was in Central Africa, with a coverage of 70.78% (Figure 2 and Supplementary Table S4).

We conducted a conservation analysis of the selected peptides to develop a universal multi-epitope antibacterial vaccine. Using the CLC Main Workbench, we analyzed the amino acid sequences of five selected proteins. B-cell, HTL, and CTL epitopes from the proteins Lipl71, TBDR, and Sph2 were 100% conserved across various strains. The B-cell and HTL epitopes of irpA were 100% conserved. Among the two CTL epitopes in irpA, CTL epitope 1 (VTSTGPGLK) was 100% conserved, whereas CTL epitope 2

TABLE 3 Prediction of CTL epitopes from input *L. interrogans* protein sequences using NetCTL-1.2, alongside antigenicity, allergenicity, and toxicity assessments.

Protein name	Epitope	HLA class I supertypes	Antigenicity	Allergenicity	Toxicity
LipL71	KIKNPNLIY	A3	1.03	Non-allergen	Non-toxic
	GEEENPENL	B44	0.88	Non-allergen	Non-toxic
TBDR	KVYSAYTER	A3	0.57	Non-allergen	Non-toxic
	HEVNNTKSL	B44	0.45	Non-allergen	Non-toxic
irpA	VTSTGPGLK	A3	1.62	Non-allergen	Non-toxic
	AQMTYANVL	B44	0.60	Non-allergen	Non-toxic
Sph2	IVGDLNVIK	A3	0.81	Non-allergen	Non-toxic
	IEEKIQYIF	B44	0.47	Non-allergen	Non-toxic
GspD	GQFNSGLSK	A3	0.64	Non-allergen	Non-toxic
	REIKTSISI	B44	0.77	Non-allergen	Non-toxic

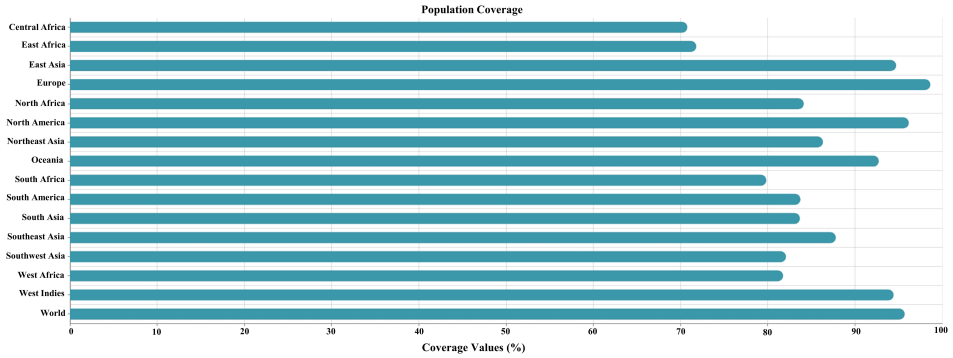

FIGURE 2
Global population coverage of the selected cytotoxic T lymphocyte (CTL) and helper T lymphocyte (HTL) epitopes. The x-axis represents the combined population coverage (HLA I and II), and the y-axis represents the countries.

(AQMTYANVL) was only 63.89% conserved. Similarly, for GspD, the HTL and CTL epitopes were 100% conserved. In contrast, the B-cell epitope was 97.5% conserved (Figure 3A). Additionally, we performed sequence logo analysis using WebLogo, which visually represents the frequency of each amino acid at specific positions across all sequences. This analysis revealed mutations in the CTL epitope 'AQMTYANVL' and B-cell epitope 'NPVIQSEDLGSERKPP'. However, other epitopes showed high conservation (Figure 3B). These results highlight the potential of this vaccine for broad population coverage and its conserved efficacy across various pathogenic strains, indicating its global applicability and effectiveness.

3.4 Final vaccine construct and physiochemical properties

The MESV construct comprised one adjuvant (HBHA) with a length of 199 amino acids, five B-cell epitopes, five HTL epitopes, ten CTL epitopes, one EAAAK, four KK linkers, five AAY linkers, five GPGPG linkers. The resulting MESV had a total length of 589 amino acids (Figure 4A).

Physicochemical characterization of the MESV was evaluated using the ExPASy ProtParam tool. The instability index (34.04) and GRAVY score (-0.632) indicated that MESV was stable and hydrophilic, which are advantageous traits for a subunit vaccine.

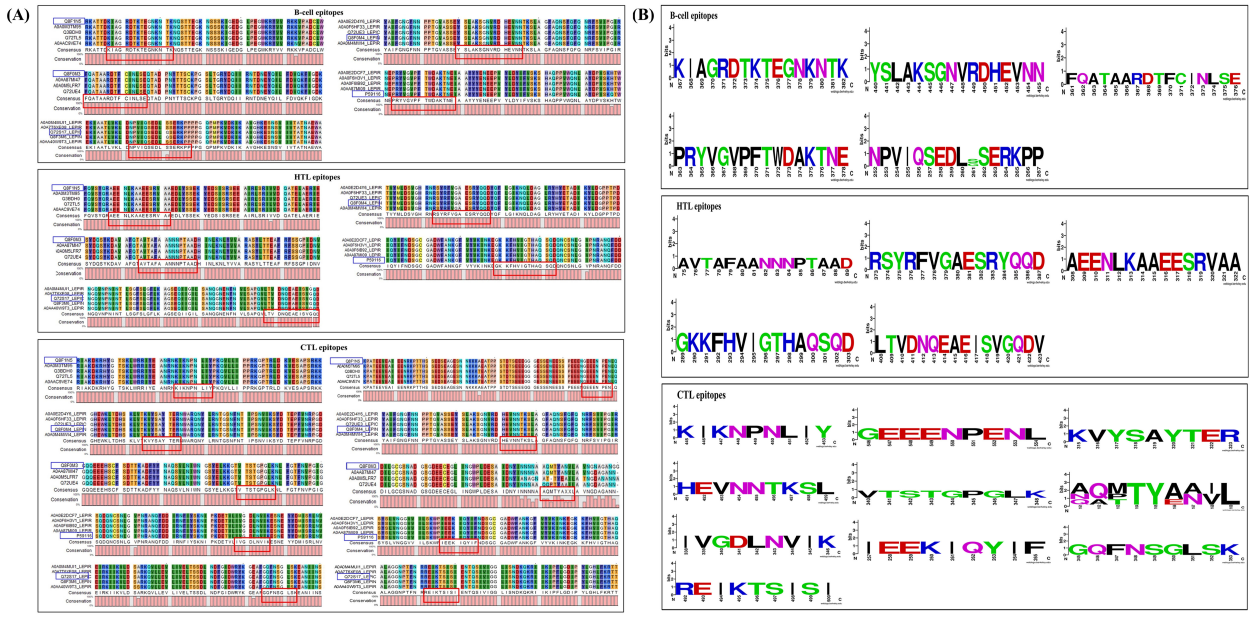

FIGURE 3
Epitope conservation analysis, featuring **(A)** alignments and consensus sequences for B-cell, HTL, and CTL epitopes associated with LipL71 (UniProt ID: Q8F1N5), TBDR (UniProt ID: Q8F0M4), irpA (UniProt ID: Q8F0M3), Sph2 (UniProt ID: P59116), and GspD, highlighted in red. The blue box indicates these epitopes, their corresponding proteins from other *L. interrogans strains*, and their UniProt IDs. **(B)** Sequence logo analysis of these epitopes for LipL71, TBDR, irpA, Sph2, and GspD. The x-axis represents the amino acid positions within the peptide sequences, while the y-axis indicates the frequency of each residue at a given position. The total height of the letters reflects the level of sequence conservation at each position.

10.3389/fimmu.2024.1503853

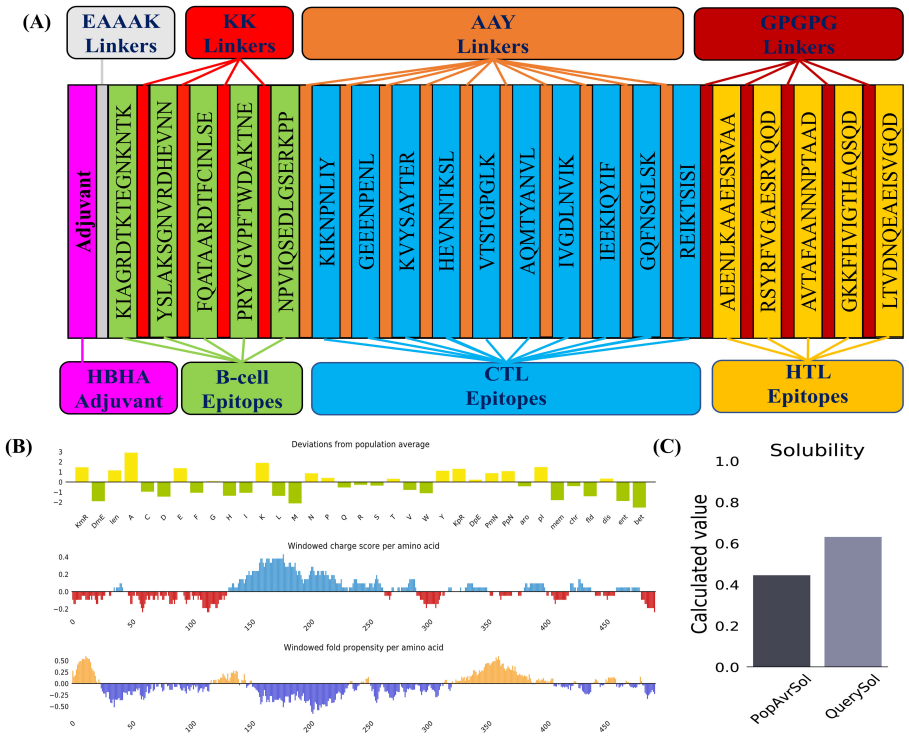

FIGURE 4
Vaccine construction and solubility prediction. **(A)** Diagrammatic representation of the critical components of the final vaccine construct. **(B)** Plot illustrating deviations from population averages across 35 features, including windowed charge scores and the folding propensity of amino acids. **(C)** Solubility prediction of the designed vaccine construct using the Protein-Sol server, compared to the population average across the analyzed datasets.

TABLE 4 Physicochemical properties of the vaccine construct are predicted by the ExPASy Protparam tool.

Physiochemical Properties of Vaccine	Values	Comment
Number of amino acids	512	Appropriate
Molecular weight	55.69 kDa	Appropriate
Theoretical pI	9.08	Basic
Total number of negatively charged residues (Asp + Glu)	66	–
Total number of positively charged residues (Arg + Lys)	75	–
Total number of atoms	7755	–
Instability index	34.04	Stable
Aliphatic Index	72.09	Thermostable
Grand Average of Hydropathicity (GRAVY)	-0.632	Hydrophilic
Antigenicity (VaxiJen)	0.8409	Antigenic
Antigenicity (ANTIGENpro)	0.929	Antigenic
Allergenicity (AllerTOP)	Non-allergen	Non-allergenic
Solubility (Protein_Sol)	0.632	Soluble
Solubility (SOLPro)	0.796	Soluble

The proposed vaccine demonstrated notable antigenicity, with scores of 0.8409 (VaxiJen) and 0.929 (ANTIGENPro), confirming its potential as an antigen. The AllerTop server revealed that the designed construct was non-allergenic. Moreover, the vaccine attained solubility scores of 0.632 and 0.796, calculated using the Protein-Sol and SOLpro servers, respectively (Table 4 and Figures 4B, C). Physicochemical evaluations suggested that the proposed vaccine exhibited favorable characteristics, making it a promising candidate for subsequent development.

3.5 Vaccine structure analysis

The 2D structure of the designed vaccine construct was analyzed using the GOR IV and PSIPRED webservers. The findings indicate that MESV comprises 66.04% α-helix, 26.99% coil, and 6.96% β-strand (Figure 5A). The 3D structural coordinates of the MESV were generated using trRosetta and are shown in Figure 5B. Subsequently, the 3D structure quality was enhanced, as evidenced by the Ramachandran plots. Figures 5C, D show the validation results before and after refinement. The Ramachandran plot of the refined MESV models showed that 96.4% of the residues were located in the most favored regions. The ProSA server initially revealed a Z-score of -4.93 for the model, which improved to -5.03 following refinement (Figures 5E, F).

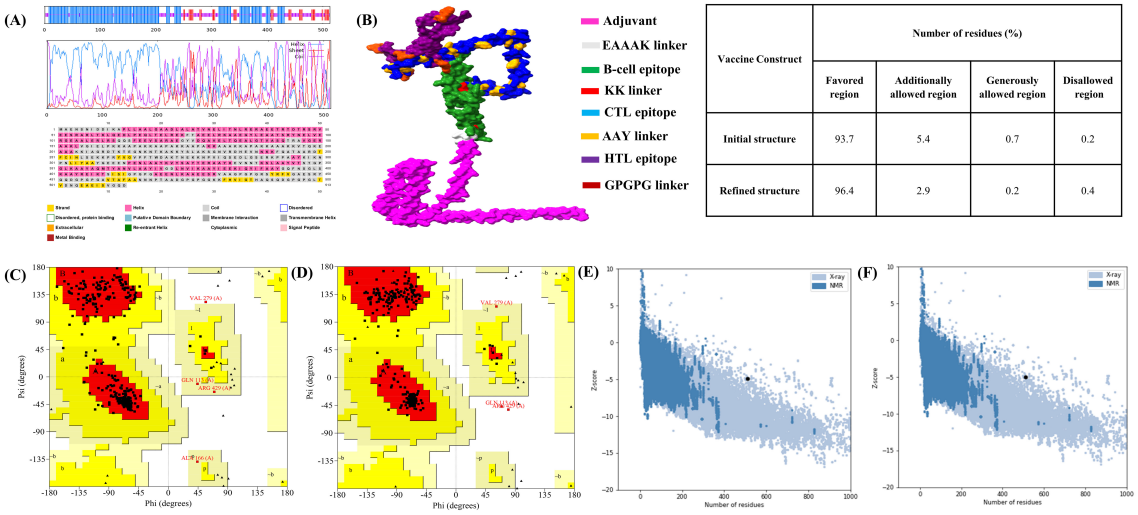

Vaccine Construct	Number of residues (%)			
	Favored region	Additionally allowed region	Generously allowed region	Disallowed region
Initial structure	93.7	5.4	0.7	0.2
Refined structure	96.4	2.9	0.2	0.4

FIGURE 5
Predicted 2D and 3D structure of the vaccine construct. **(A)** Graphical representation of the secondary structure predicted using the PSIPRED server. GOR IV server results indicate that the vaccine consists of α-helix (57.50%), coil (30.99%), and β-strand (11.50%). **(B)** Predicted 3D structure of the designed multi-epitope subunit vaccine. **(C, D)** Ramachandran plots showing the distribution of amino acids in the favored, allowed, and disallowed regions before and after refinement. **(E, F)** Z-scores of the vaccine model before and after refinement.

3.6 Determination of linear and conformational antibody epitopes

Determining linear and conformational (discontinuous) antibody epitopes is vital for understanding antigen-antibody interactions after developing a 3D vaccine model. The ElliPro server was used to predict epitopes in the 3D structure of the vaccine construct. Six continuous epitopes of various lengths were identified (Supplementary Table S5 and Figure S2A) alongside seven discontinuous epitopes (Supplementary Table S6 and Figure S2B-H).

3.7 Molecular docking and simulation study

The interaction between MESV and immune receptors is crucial because vaccine components should bind to immunoreceptors to

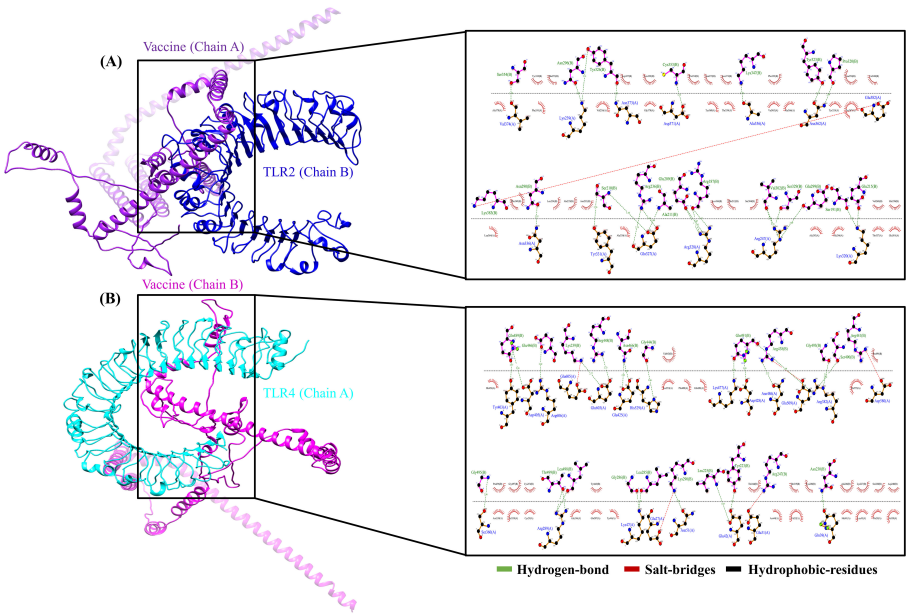

FIGURE 6
Molecular docking of the vaccine construct with immune receptors (Toll-like receptors (TLR) 2 and 4). **(A)** Cartoon representation of the vaccine-TLR2 complex, showing the interaction analysis between the vaccine (chain A) and TLR2 (chain B) using LigPlot. **(B)** The vaccine-TLR4 complex was illustrated using Chimera software, depicting the bond interactions between TLR4 (chain A) and the vaccine (chain B).

10.3389/fimmu.2024.1503853

TABLE 5 Molecular docking results and predicted hydrogen bond interactions and salt bridges between the vaccine and immune receptors.

Docked complex	Type of interaction	Interacting residue (Vaccine)	Interacting residue (TLR)
Vaccine-TLR2	Hydrogen bond	Lys239, Arg247, Lys320, Arg328, Glu327, Tyr331, Asn336, Ala356, Asn362, Asp371, Asn373, Val374, Glu382	Arg187, Ser191, Glu209, Ser210, Ala211, Glu215, Arg236, Asn290, Asn296, Glu299, Val302, Pro320, Tyr323, Tyr326, Ser329, Lys347, Cys353, Ser354
	Salt bridge	Glu382	Lys383
Vaccine-TLR4	Hydrogen bond	Tyr223, Leu225, Asn230, Lys239, Leu 285, Gly286, Lys290, Glu446, Arg448, Asn466, Gln489, Gly495, Leu498, Thr499,	Gln39, Glu42, Lys47, Asn51, Arg289, Ser360, Arg382, Tyr403, Asp405, Glu425, Asp428, Lys477, Asn486, His529, Arg606,
	Salt bridge	Lys239, Arg247, Lys290, Arg438, Arg441,	Glu27, Glu31, Glu509, Asp580, Glu605,

initiate protective immune responses by activating various immunomodulatory pathways. This interaction was accessed by molecular docking using ClusPro 2.0, with the lowest energy cluster considered optimal. TLR2 and TLR4 showed minimum energy values of -1,357.1 kJ/mol and -1,163.7 kJ/mol, respectively. LigPlot v.2.2.5 analysis further revealed specific interactions between MESV amino acids and TLR2 and TLR4 (Figures 6A, B). For the MESV-TLR2 complex, 23 hydrogen bonds and one salt bridge were identified. In contrast, the MESV-TLR4 complex formed 24 hydrogen bonds and five salt bridges (Table 5). These findings highlighted the potential effectiveness of the MESV vaccine in generating a targeted and strong adaptive immune response against leptospirosis.

The structural stability of the MESV-TLR complexes was validated using MD simulations, which demonstrated the ability of the vaccine to bind to immune receptors and its potential to induce immunity over a 100 ns period. For the MESV-TLR2 complex, the backbone RMSD plot indicated minor deviations between 38 and 60 ns; however, the system stabilized after, maintaining an RMSD between 2.5 and 3.0 Å (Figure 7A). In contrast, the MESV-TLR4 complex demonstrated consistent stability throughout the simulation, with the backbone RMSD remaining steady at an average value of 2.50 Å (Figure 7B). RMSF analysis revealed that the TLR4 and vaccine backbone exhibited fewer fluctuations (Figure 7D). In contrast, the TLR2 backbone, particularly chain B, showed greater dynamics and fluctuations (Figure 7C). Additionally, the vaccine backbone exhibits increased dynamics when bound to TLR2. In contrast, it remained more stable during the interaction with TLR4. The average Rg for the MESV-TLR2 and MESV-TLR4 complexes was calculated as 4.4 and 4.2 nm, respectively. Rg analysis revealed that the TLR2 complex displayed slightly different behavior over the 100 ns simulation, whereas the TLR4 complex remained consistently folded throughout the process

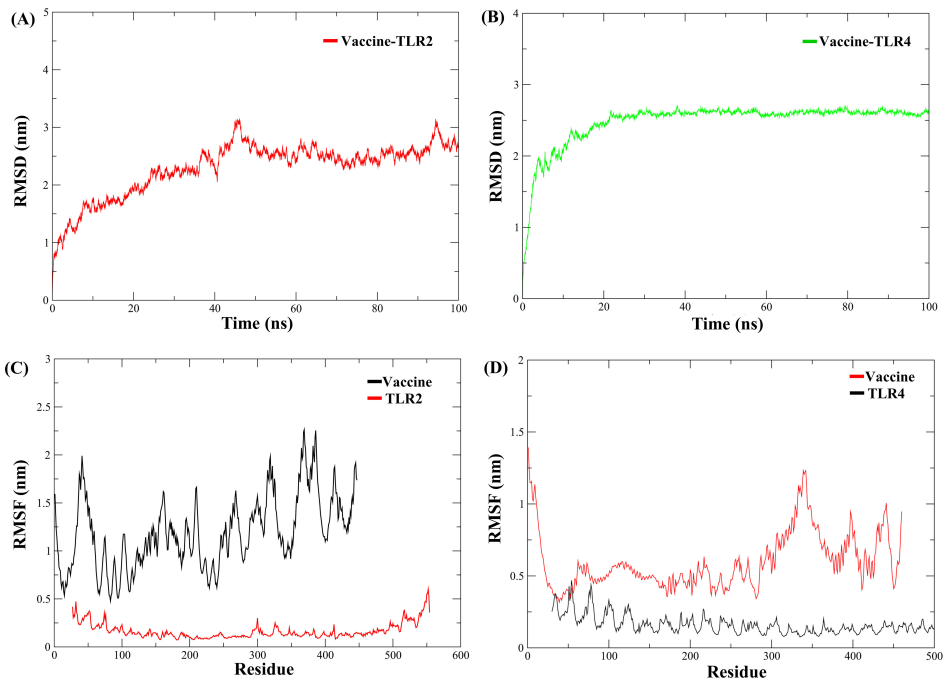

FIGURE 7
Molecular dynamics simulation of the vaccine complexed with immune receptors. **(A)** Root mean square deviation (RMSD) plot of the vaccine-TLR2 docked complex. **(B)** RMSD plot of the vaccine-TLR4 docked complex. **(C)** Root mean square fluctuation (RMSF) plot showing side-chain fluctuations within the vaccine-TLR2 complex. **(D)** RMSF plot illustrating side-chain fluctuations within the vaccine-TLR4 complex.

10.3389/fimmu.2024.1503853

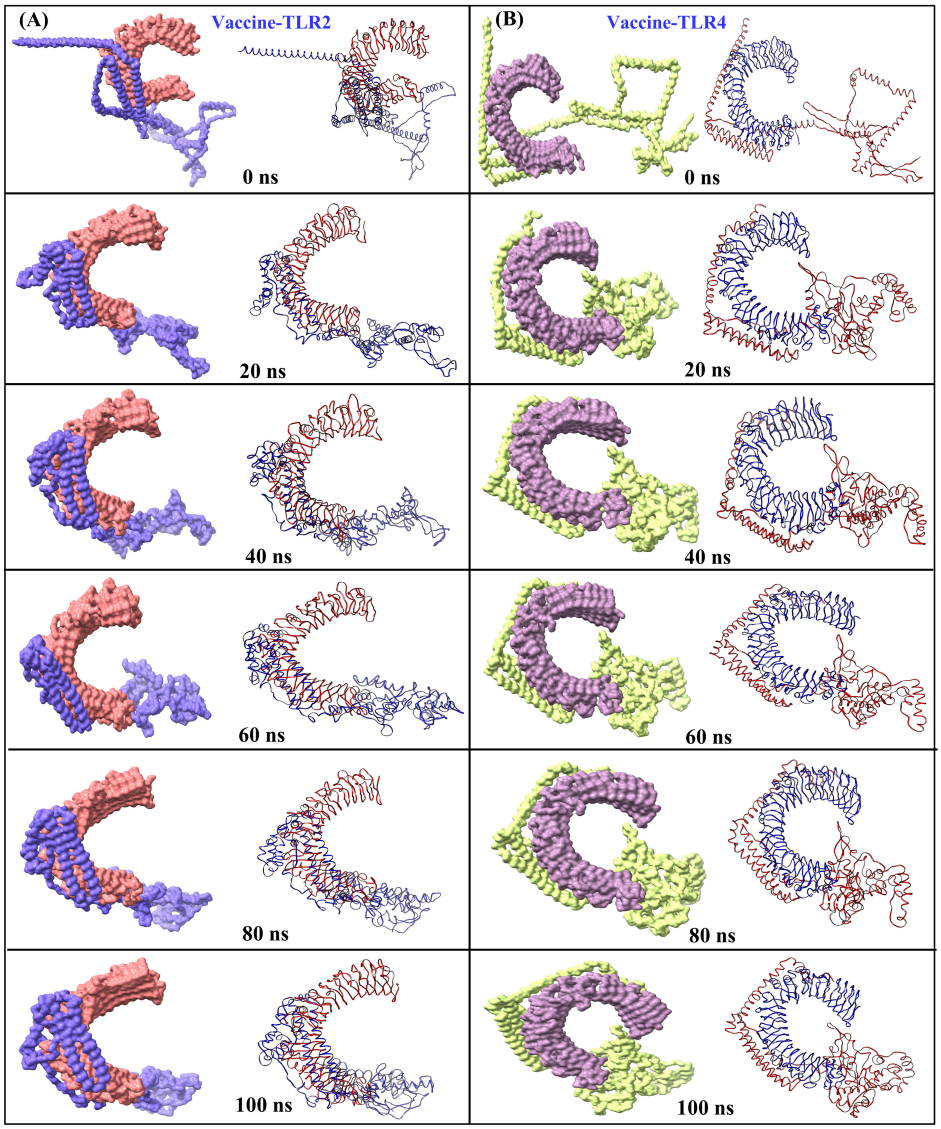

FIGURE 8
Snapshots of equilibrated (initial) systems and last trajectories: vaccine-bound complexes of **(A)** TLR2 and **(B)** TLR4 (surface and cartoons are shown for each snapshot).

(Supplementary Figure S3A, B). The average SASA values for the MESV bound to TLR2 and TLR4 were determined to be 4.75 nm^2 and 5.10 nm^2, respectively (Supplementary Figure S3C, D). Furthermore, we analyzed the interaction between the vaccine and TLRs at intervals of 0, 20, 40, 60, and 100 ns. The results demonstrated that the immune receptors, TLR2 and TLR4, effectively bound to the vaccine (Figure 8).

In addition, the binding energy was calculated by incorporating the specific interactions between each residue. This assessment revealed substantial energy contributions from the interactions with MESV and TLR protein residues. The significantly more negative total binding energy indicated a higher affinity of the vaccine for the TLR4 interface (-152.63 kcal/mol) than with TLR2 (-122.92 kcal/mol) (Table 6). These findings suggest stable and favorable interactions within the vaccine-receptor complexes throughout the simulation.

TABLE 6 Binding free energies of the docked complexes were calculated *via* MM-GBSA analysis, and all energy values are provided in kcal/mol.

MM/GBSA calculations (Kcal/mol)		
Energy parameters	Vaccine-TLR2	Vaccine-TLR4
VDW	-194.42	-280.52
ELE	-2488.49	-3847.97
GB	2584	4012.7
SA	-24.84	-36.83
Total binding energy	-122.92	-152.63

*VDW, Van der Waals potential; *ELE, Electrostatic potential; *GB, Polar Solvation free energy predicted using Generalized Born model; *SA, The empirical model calculated the nonpolar contribution to the solvation free energy; *TOTAL, Final estimated binding free energy (kcal/mol).

3.8 Immune simulation

The C-ImmSim server was used to generate the immune response profile for MESV. Following the three vaccine doses, the antibody response significantly increased, with elevated IgM and IgG antibodies, indicating a strong humoral immune response. Higher IgG1, IgG2, and IgM expressions were associated with increased B-cell density, reduced antigen concentration, and a notable increase in memory B-cells (Figures 9A, B). Similarly, the data showed the development of secondary and tertiary immune responses, with an increase in the density of helper and cytotoxic T-cells (Figures 9C, D). These findings suggested a robust secondary immune response, enhanced antigen clearance, and effective immune memory formation following each dose. Moreover, during the dosing period, IFN-γ and IL-2 levels were elevated post-immunization (Figure 9E). After vaccination, the number of resting dendritic cells increased, and the antigen-presenting dendritic cells (types 1 and 2) decreased (Figure 9F). These results demonstrated that the vaccine design effectively elicited robust immune responses against leptospirosis.

3.9 Vaccine optimization and cloning

The MESV sequence was subjected to codon optimization to enhance its expression efficiency in the chosen expression system (*E. coli* K12). This optimization yielded a GC content of 51.83%, and the vaccine CAI was calculated as 0.954, implying a favorable expression outcome in the host organism. To facilitate cloning, *XhoI and BamHI* restriction sites were introduced at the beginning and end of the codon-optimized sequence, respectively. The cloning study involved the use of pET28a (+) plasmid. Our study used the pET-28a (+) vector due to its strong T7 promoter, facilitating high-level gene expression in *E. coli*. The vector's His-6 tag simplifies protein purification, and the ampicillin resistance gene enhances selection efficiency. The MESV sequence, with a length of 6,874 bp, was constructed by integrating a 1,551 bp gene sequence. This process ensured efficient vaccine expression in the selected host system (Figure 10). Additionally, the size of the cloning product was verified using the simulated agarose gel feature of SnapGene software (Supplementary Figure S4).

4 Discussion

Leptospirosis, a globally significant zoonotic disease, poses a severe public health concern due to its diverse clinical presentations. The high fatality rate in severe cases, coupled with the lack of early diagnosis and effective treatment options, emphasizes the urgent need for novel preventive strategies. Current vaccines, primarily based on whole-cell inactivated leptospires, offer limited cross-protection among serovars and are associated with adverse effects.

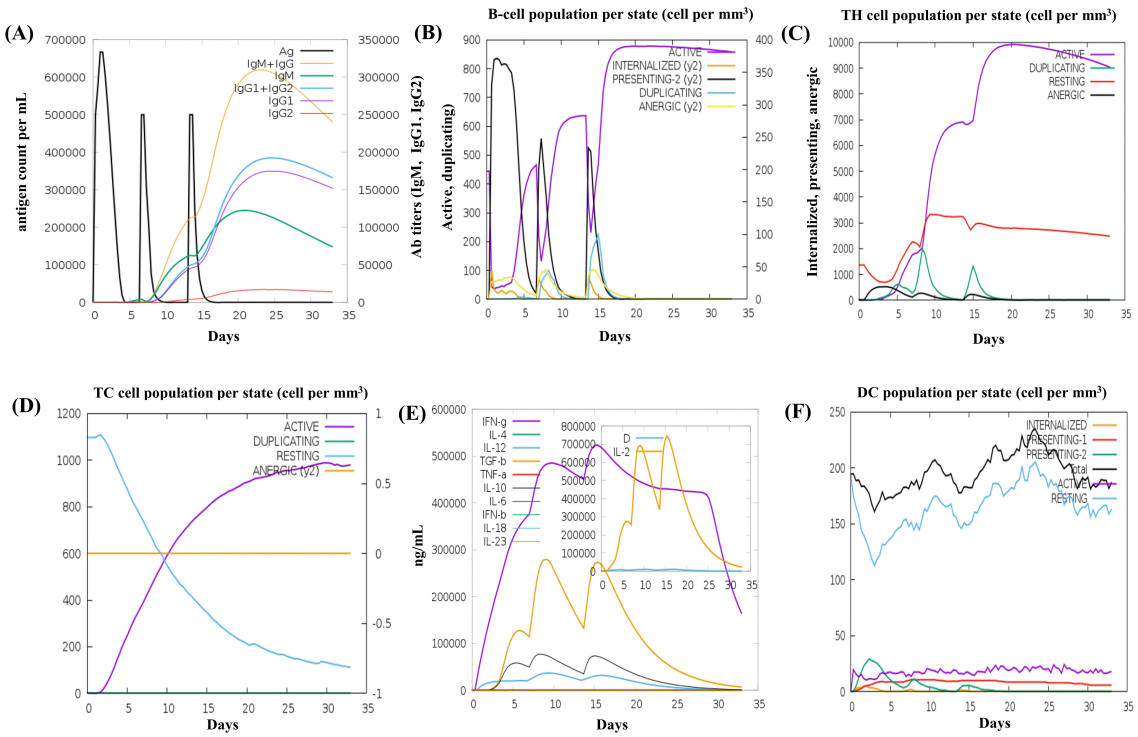

FIGURE 9
In silico immune simulation results of the vaccine construct using the C-ImmSim tool **(A)** The immunoglobulin response to antigen administration, depicted with colored peaks representing different immunoglobulin subclasses. **(B)** Active B-cell population observed after vaccination. **(C)** Generation of cytotoxic T cells in response to vaccination. **(D)** The emergence of helper T cells. **(E)** Graph showing the cytokine levels triggered by the vaccine, with an inset depicting the Simpson Index [D] for interleukin (IL)-2, used to measure diversity. **(F)** The dendritic cell population per state.

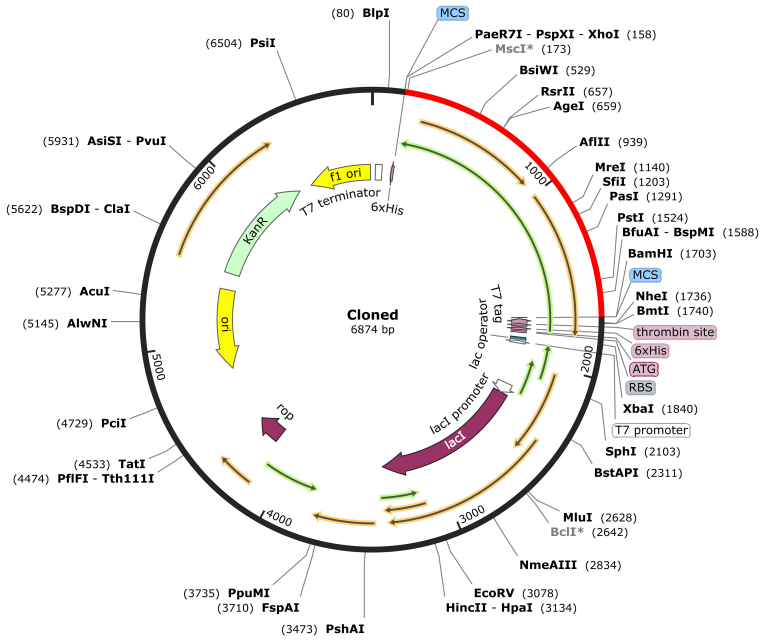

FIGURE 10
In silico cloning of the vaccine sequence into the pET-28a (+) expression vector. The vaccine sequence (red) was cloned between *XhoI* and *BamHI* restriction sites in the pET-28a (+) expression vector (black).

Advances in immunoinformatics and molecular biology have paved the way for multi-epitope subunit vaccines (MESV) that target conserved proteins across different strains. These innovative vaccines have the potential to overcome the shortcomings of traditional bacterin-based vaccines by providing broader protection, eliciting stronger, longer-lasting immune responses, and reducing adverse effects.

The development of effective vaccines for *Leptospira* is complicated by the pathogen's genetic diversity and the limited number of experimentally validated epitopes. We consulted the Immune Epitope Database (IEDB) to address these challenges, which lists 46 known epitopes for *L. interrogans*. The IEDB has previously characterized two linear B-cell epitopes, Sph2 (176–191) and Sph2 (446–459), which have been shown to elicit immune responses in human leptospirosis (80). When we explored the IEDB, we found that all of our predicted B-cell, HTL, and CTL epitopes spanning multiple proteins, including Sph2, LipL71 (Q8F1N5), TBDR (Q8F0M4), irpA (Q8F0M3), and GspD (Q72S17) have not been reported before. This confirms that these epitopes are novel and distinct. Importantly, these newly identified epitopes show strong potential for inducing immune responses against *L. interrogans*, further supporting their suitability as vaccine targets. We also cross-checked our predicted epitopes for Sph2 with those previously reported and found no overlap with the known Sph2 (176–191) and Sph2 (446–459) epitopes. This comprehensive validation process ensures that our multi-epitope vaccine design is based on novel targets, which could enhance immunogenicity and broaden protection across different *Leptospira* serovars. Several studies have made notable contributions to *in-silico* vaccine design for leptospirosis. Lata et al. (21) explored the *Leptospira* proteome and identified lipoprotein Q75FL0 as a promising vaccine candidate. Similarly, Lin et al. developed a multi-epitope chimeric vaccine (r4R) using B and T-cell epitopes from LipL32, OmpL1, and LipL21, demonstrating its potential as a cross-reactive, protective antigen against leptospirosis (81). Abdullah et al. used an integrated vaccinomics approach to design a multi-epitope vaccine with B and T-cell epitopes, selecting six proteins (NP_712625, NP_714239, WP_011669637, WP_011670051, WP_011670465, WP_011671327), thus contributing additional vaccine candidates (82). Fernandes et al. (83) developed a chimeric multi-epitope protein (rChi) using five *Leptospira* proteins (LigA, Mce, Lsa45, OmpL1, and LipL41), demonstrating its potential to protect against lethal leptospirosis infection in a hamster model. Ibrahim et al. designed an Lsa46-based multi-epitope peptide vaccine against leptospirosis using an immunoinformatic approach (84). Our study extends these efforts by introducing novel epitopes from LipL71, TBDR, irpA, and GspD, proteins not previously explored in vaccine design. While studies by Majid et al. (19) and Pankaj et al. (22) focused on more widely studied proteins such as Hap1, LigA, LAg42, SphH, HSP58, and the LipL, LigA, and LigB family lipoproteins, our work broadens the pool of candidate antigens by identifying novel targets that have not been addressed previously. These newly identified proteins are involved in key *Leptospira* virulence mechanisms, including immune evasion and nutrient acquisition, making them strong candidates for vaccine development (26). In addition, our research incorporates population coverage analysis, providing a more comprehensive evaluation of the potential global applicability of the vaccine, which was not present in earlier studies.

In response to the urgent need for an effective leptospirosis vaccine, we designed an MESV incorporating five immunogenic antigens, predicting the B-cell, HTL, and CTL epitopes. Previous studies have demonstrated that γδ T cells from humans and bovines

can proliferate and produce IFN-γ in response to *Leptospira* (85). Consistent with these findings, the identified epitopes in this study showed the potential to induce both IFN-γ and IL-4, as indicated by their positive scores. This highlights their capacity to trigger an IFN-γ-mediated immune response, reinforcing the vaccine's ability to activate essential immune pathways against *Leptospira*. Each epitope was meticulously screened for allergenicity, toxicity, and antigenicity to ensure they could effectively elicit the desired immune response without causing adverse effects. Conservation analysis revealed that most B-cell, HTL, and CTL epitopes in the selected proteins were highly conserved across *Leptospira* strains, ensuring broad coverage. Minor mutations were observed in specific CTL and B-cell epitopes. The CTL and HTL epitopes were also selected according to the predicted HLA alleles specific to various ethnic groups. The results indicated that the selected epitopes provided a global population coverage of 99.77%, encompassing diverse geographic regions. Linkers such as AAY, GPGPG, and KK have been used to connect CTL, HTL, and B-cell binding epitopes in constructing the MESV. The adjuvant and vaccine sequences were joined using the EAAAK linker, which provided structural stiffness and maintained consistent spacing between them. Its α-helical structure reduces domain interference, encouraging proper folding and enhancing the fusion protein's stability and functionality (86). Several studies have shown that adding GPGPG and AAY linkers between anticipated HTL and CTL epitope sequences induces junctional immunogenicity, allowing for the logical design and production of a potent MESV (36, 87). Previous studies have indicated that the KK linker prevents the development of antibodies against the amino acid sequence created by integrating two peptides. This enabled the antibody to recognize each peptide individually (88). Adjuvants, also known as innate immune stimulants, are selected based on their ability to elicit specific immunological responses. In our study, we chose HBHA due to its affinity for TLR4, which activates dendritic cells and skews the immune response towards a Th1-type profile (89). This is particularly advantageous for combating intracellular pathogens like *Leptospira interrogans*, which rely on strong cellular immunity for effective control (17). Moreover, HBHA has been shown to enhance the immunogenicity of peptide-based vaccines, making it an ideal candidate to amplify innate and adaptive immune responses (22). By incorporating HBHA, our multi-epitope vaccine strategy aims to elicit a more potent and targeted immune response against *Leptospira*.

MESV physicochemical analysis revealed promising characteristics with strong antigenic properties sufficient to trigger an effective immune response. Various server evaluations confirmed the vaccines' high solubility and hydrophilicity. Additionally, the instability index of the vaccines was found to be within the acceptable range (below 40), indicating that they would remain stable within the host organism. Helices are essential for biomolecular recognition and play a key role in protein synthesis (90). In a previous MESV design against *L. interrogans* by Pankaj et al. (22), the presence of α-helix was reported to be 16.96%. In contrast, our designed vaccine model demonstrated a significantly higher α-helix content of 66.04%. This increased helix presence may enhance the stability and efficacy of the vaccine. The MESV's 3D structure was predicted and refined using the GalaxyRefine server, resulting in significant quality improvements, with most residues positioned in the favored and allowed regions of the Ramachandran plot.

TLR2 and TLR4 receptors in vaccines boost protection against various pathogens by improving antigen presentation to T cells, causing the activation of $CD4^+$ and $CD8^+$ T cells, which are vital for a robust adaptive immune response. Additionally, existing literature emphasizes the crucial involvement of immune receptors, particularly TLR2 and TLR4, in coordinating host immunity against *Leptospira* infection. TLR2 mainly plays a predominant role in recognizing lipoproteins, highlighting its specific involvement in the immune response mechanisms against *Leptospira* (91, 92). Recent studies also show that TLR2 and TLR4 recognize *Leptospira* strains used in canine vaccine production, contributing to understanding innate immune responses in dogs, humans, and mice (69). Our observations showed that MESV interacts strongly with TLR2 and TLR4, with protein-protein docking revealing multiple hydrogen bonds and salt bridges. Notably, the vaccine exhibited higher binding energy with TLR4 than TLR2, indicating stronger interactions with TLR4. These findings highlight the potential effectiveness of the MESV in generating a targeted and strong adaptive immune response against leptospirosis.

The structural stability of the MESV-TLR complexes was validated using MD simulations, which demonstrated the vaccine's ability to bind with immune receptors and its potential to induce immunity. The simulations showed that the MESV-TLR2 complex had a lower RMSD than the MESV-TLR4 complex, indicating high stability. The RMSF plot revealed that the regions involved in MESV-TLR interactions were less flexible. Moreover, the negative binding energies of MESV and receptors in the MMGBSA study reinforced the stability of the complexes. Immune simulation results indicated significant increases in B and Th-cell populations, with elevated levels of TGF-β, IL-10, and IFN-γ, essential for managing inflammation and controlling leptospirosis. Pankaj et al. (22) previously reported strong cellular and humoral responses, including elevated B-cell populations and IFN-γ levels. Our study expands on these findings by examining the role of T cytotoxic and dendritic cells, which demonstrated enhanced activation. This broader immune response highlights the vaccine's potential for leptospirosis immunization. Induction of cytokines like IL-10 is vital for maintaining immune balance, while TGF-β helps regulate inflammation. The vaccine's ability to increase B and Th-cell populations, alongside substantial production of TGF-β, IL-10, and IFN-γ, supports its efficacy in controlling disease progression. Furthermore, *in silico* cloning analysis indicated that MESV could be efficiently expressed in *E. coli* as a host system. However, further *in vivo* studies are needed to validate the efficacy and safety of this vaccine.

4 Conclusion

This study emphasizes the effectiveness of computational immunology in optimizing vaccine design. Our MESV against Leptospirosis demonstrated strong antigenicity, conservation, and

safety, successfully eliciting robust immune responses, and showed broad population coverage with strong interactions with TLR4 and TLR2. Additionally, successful *in silico* cloning in *E. coli* supports its feasibility for expression. However, while the *in silico* approach yielded promising results, several limitations must be acknowledged. The antigenic variability among leptospirosis serovars and the reliance on computational predictions, which may not fully reflect complex biological interactions, emphasize the need for *in vivo* validation. Further research is required to address potential differences in vaccine effectiveness across diverse populations and challenges in expressing the vaccine in *E. coli*. These results underscore the importance of further experimental validation while demonstrating the valuable role of immunoinformatics in advancing vaccine development.

Data availability statement

The datasets presented in this study can be found in online repositories. The names of the repository/repositories and accession number(s) can be found in the article/Supplementary Material.

Author contributions

GS: Conceptualization, Data curation, Investigation, Methodology, Software, Writing – original draft, Writing – review & editing. YK: Formal analysis, Investigation, Visualization, Writing – review & editing. S-CH: Funding acquisition, Investigation, Resources, Validation, Writing – review & editing. JH: Conceptualization, Funding acquisition, Investigation, Supervision, Validation, Writing – review & editing.

Funding

The author(s) declare financial support was received for the research, authorship, and/or publication of this article. This research was supported by the National Research Council of Science & Technology (NST) (Grant Number: CRC21022). Additionally, it was funded by the Regional Innovation Mega Project Program through the Korea Innovation Foundation, supported by the Ministry of Science and ICT (Project Number: 17112028880).

Acknowledgments

The authors thank the Korea Institute of Toxicology (KIT) for providing research resources.

Conflict of interest

The authors declare that the research was conducted in the absence of any commercial or financial relationships that could be construed as a potential conflict of interest.

Generative AI statement

The author(s) declare that no Generative AI was used in the creation of this manuscript.

Publisher's note

Supplementary material

The Supplementary Material for this article can be found online at: https://www.frontiersin.org/articles/10.3389/fimmu.2024.1503853/full#supplementary-material

References

1. Fraga TR, Barbosa AS, Isaac L. Leptospirosis: aspects of innate immunity, immunopathogenesis and immune evasion from the complement system. *Scand J Immunol.* (2011) 73:408–19. doi: 10.1111/j.1365-3083.2010.02505.x

2. Costa F, Hagan JE, Calcagno J, Kane M, Torgerson P, Martinez-Silveira MS, et al. Global morbidity and mortality of leptospirosis: A systematic review. *PloS Negl Trop Dis.* (2015) 9:e0003898. doi: 10.1371/journal.pntd.0003898

3. Bradley EA, Lockaby G. Leptospirosis and the environment: A review and future directions. *Pathogens.* (2023) 12:1167. doi: 10.3390/pathogens12091167

4. Haake DA, Levett PN. Leptospirosis in humans. *Curr Top Microbiol Immunol.* (2015) 387:65–97. doi: 10.1007/978-3-662-45059-8_5

5. Liu Y-H, Chen Y-H, Chen C-M. Fulminant leptospirosis presenting with rapidly developing acute renal failure and multiorgan failure. *Biomedicines.* (2024) 12:435. doi: 10.3390/biomedicines12020435

6. Carvalho HGAC, Silva DM, Rodrigues GRD, Gameiro AH, Dos Santos RF, Raineri C, et al. Estimation of economic losses due to leptospirosis in dairy cattle. *Prev Vet Med.* (2024) 229:106255. doi: 10.1016/j.prevetmed.2024.106255

7. Caimi K, Ruybal P. *Leptospira* spp., a genus in the stage of diversity and genomic data expansion. *Infect Genet Evol.* (2020) 81:104241. doi: 10.1016/j.meegid.2020.104241

8. Vincent AT, Schiettekatte O, Goarant C, Neela VK, Bernet E, Thibeaux R, et al. Revisiting the taxonomy and evolution of pathogenicity of the genus Leptospira through the prism of genomics. *PloS Negl Trop Dis.* (2019) 13:e0007270. doi: 10.1371/journal.pntd.0007270

9. Abd Rahman AN, Hasnul Hadi NH, Sun Z, Thilakavathy K, Joseph N. Regional prevalence of intermediate leptospira spp. *Humans: A Meta-Analysis. Pathog.* (2021) 10:943. doi: 10.3390/pathogens10080943

10. Xu Y, Ye Q. Human leptospirosis vaccines in China. *Hum Vaccines Immunother*. (2018) 14:984–93. doi: 10.1080/21645515.2017.1405884

11. Silveira MM, Oliveira TL, Schuch RA, McBride AJA, Dellagostin OA, Hartwig DD. DNA vaccines against leptospirosis: A literature review. *Vaccine*. (2017) 35:5559–67. doi: 10.1016/j.vaccine.2017.08.067

12. Mukadi P, Tabei K, Edwards T, Brett-Major DM, Smith C, Kitashoji E, et al. Antibiotics for treatment of leptospirosis. *Cochrane Database Syst Rev*. (2022) 2022). doi: 10.1002/14651858.CD014960

13. Martínez Sánchez R, Obregón Fuentes AM, Pérez Sierra A, Baly Gil A, Díaz González M, Baró Suárez M, et al. The reactogenicity and immunogenicity of the first Cuban vaccine against human leptospirosis. *Rev Cubana Med Trop*. (1998) 50:159–66.

14. Ikoev VN, Gorbunov MA, Vachaev BF, Iagovkin EA, Kondratenko VF, Anan'ina IV, et al. The evaluation of the reactogenicity and immunogenic activity of a new concentrated inactivated leptospirosis vaccine. *Zh Mikrobiol Epidemiol Immunobiol*. (1999) 7-8:39–43.

15. Chen T. Development and present status of a leptospiral vaccine and the technology of vaccine production in China. *Nihon Saikingaku Zasshi Jpn J Bacteriol*. (1985) 40:755–62. doi: 10.3412/jsb.40.755

16. Martínez R, Pérez A, Quiñones M del C, Cruz R, Alvarez A, Armesto M, et al. Efficacy and safety of a vaccine against human leptospirosis in Cuba. *Rev Panam Salud Publica Pan Am J Public Health*. (2004) 15:249–55. doi: 10.1590/s1020-49892004000400005

17. Barazzone GC, Teixeira AF, Azevedo BOP, Damiano DK, Oliveira MP, Nascimento ALTO, et al. Revisiting the development of vaccines against pathogenic leptospira: innovative approaches, present challenges, and future perspectives. *Front Immunol*. (2022) 12:760291. doi: 10.3389/fimmu.2021.760291

18. Arrieta-Bechara CE, Carrascal-Maldonado AY. Ocular leptospirosis: a review of current state of art of a neglected disease. *Romanian J Ophthalmol*. (2022) 66:282. doi: 10.22336/rjo.2022.53

19. Validi M, Karkhah A, Prajapati VK, Nouri HR. Immuno-informatics based approaches to design a novel multi epitope-based vaccine for immune response reinforcement against Leptospirosis. *Mol Immunol*. (2018) 104:128–38. doi: 10.1016/j.molimm.2018.11.005

20. Kumar P, Shiraz M, Akif M. Multiepitope-based vaccine design by exploring antigenic potential among leptospiral lipoproteins using comprehensive immunoinformatics and structure-based approaches. *Biotechnol Appl Biochem*. (2023) 70:670–87. doi: 10.1002/bab.2389

21. Lata KS, Kumar S, Vaghasia V, Sharma P, Bhairappanvar SB, Soni S, et al. Exploring Leptospiral proteomes to identify potential candidates for vaccine design against Leptospirosis using an immunoinformatics approach. *Sci Rep*. (2018) 8:6935. doi: 10.1038/s41598-018-25281-3

22. Kumar P, Lata S, Shankar UN, Mohd A. Immunoinformatics-based designing of a multi-epitope chimeric vaccine from multi-domain outer surface antigens of leptospira. *Front Immunol*. (2021) 12:735373. doi: 10.3389/fimmu.2021.735373

23. Yan W, Faisal SM, McDonough SP, Chang C-F, Pan M-J, Akey B, et al. Identification and characterization of OmpA-like proteins as novel vaccine candidates for Leptospirosis. *Vaccine*. (2010) 28:2277–83. doi: 10.1016/j.vaccine.2009.12.071

24. Petakh P, Behzadi P, Oksenych V, Kamyshnyi O. Current treatment options for leptospirosis: a mini-review. *Front Microbiol*. (2024) 15:1403765. doi: 10.3389/fmicb.2024.1403765

25. Haake DA, Matsunaga J. Leptospiral immunoglobulin-like domain proteins: roles in virulence and immunity. *Front Immunol*. (2021) 11:579907. doi: 10.3389/fimmu.2020.579907

26. Zeng L, Wang D, Hu N, Zhu Q, Chen K, Dong K, et al. A Novel Pan-Genome Reverse Vaccinology Approach Employing a Negative-Selection Strategy for Screening Surface-Exposed Antigens against leptospirosis. *Front Microbiol*. (2017) 8:396. doi: 10.3389/fmicb.2017.00396

27. Verma A, Artiushin S, Matsunaga J, Haake DA, Timoney JF. LruA and lruB, novel lipoproteins of pathogenic leptospira interrogans associated with equine recurrent uveitis. *Infect Immun*. (2005) 73:7259–66. doi: 10.1128/IAI.73.11.7259-7266.2005

28. Verma A, Kumar P, Babb K, Timoney JF, Stevenson B. Cross-reactivity of antibodies against leptospiral recurrent uveitis-associated proteins A and B (LruA and lruB) with eye proteins. *PloS Negl Trop Dis*. (2010) 4:e778. doi: 10.1371/journal.pntd.0000778

29. Zhang K, Murray GL, Seemann T, Srikram A, Bartpho T, Sermswan RW, et al. Leptospiral lruA is required for virulence and modulates an interaction with mammalian apolipoprotein AI. *Infect Immun*. (2013) 81:3872–9. doi: 10.1128/iai.01195-12

30. Murray GL, Ellis KM, Lo M, Adler B. Leptospira interrogans requires a functional heme oxygenase to scavenge iron from hemoglobin. *Microbes Infect*. (2008) 10:791–7. doi: 10.1016/j.micinf.2008.04.010

31. Lo M, Murray GL, Khoo CA, Haake DA, Zuerner RL, Adler B. Transcriptional response of leptospira interrogans to iron limitation and characterization of a perR homolog. *Infect Immun*. (2010) 78:4850–9. doi: 10.1128/IAI.00435-10

32. Che R, Ding S, Zhang Q, Yang W, Yan J, Lin X. Haemolysin Sph2 of induces cell apoptosis via intracellular reactive oxygen species elevation and mitochondrial membrane injury. *Cell Microbiol*. (2019) 21:e12959. doi: 10.1111/cmi.12959

33. Ashaiba A, Arun AB, Prasad KS, Tellis RC. Leptospiral sphingomyelinase Sph2 as a potential biomarker for diagnosis of leptospirosis. *J Microbiol Methods*. (2022) 203:106621. doi: 10.1016/j.mimet.2022.106621

34. Schuler EJA, Marconi RT. The Leptospiral General Secretory Protein D (GspD), a secretin, elicits complement-independent bactericidal antibody against diverse Leptospira species and serovars. *Vaccine X*. (2021) 7:100089. doi: 10.1016/j.jvacx.2021.100089

35. Olawade DB, Teke J, Fapohunda O, Weerasinghe K, Usman SO, Ige AO, et al. Leveraging artificial intelligence in vaccine development: A narrative review. *J Microbiol Methods*. (2024) 224:106998. doi: 10.1016/j.mimet.2024.106998

36. Sethi G, Varghese RP, Lakra AK, Nayak SS, Krishna R, Hwang JH. Immunoinformatics and structural aided approach to develop multi-epitope based subunit vaccine against Mycobacterium tuberculosis. *Sci Rep*. (2024) 14:15923. doi: 10.1038/s41598-024-66858-5

37. Kumari RS, Sethi G, Krishna R. Development of multi-epitope based subunit vaccine against Mycobacterium Tuberculosis using immunoinformatics approach. *J Biomol Struct Dyn*. (2023) 42:12365–84. doi: 10.1080/07391102.2023.2270065

38. Bhalerao P, Singh S, Prajapati VK, Bhatt TK. Exploring malaria parasite surface proteins to devise highly immunogenic multi-epitope subunit vaccine for. *Plasmodium falciparum*. *J Genet Eng Biotechnol*. (2024) 22:100377. doi: 10.1016/j.jgeb.2024.100377

39. Roy SK, Biswas MS, Foyzur Raman M, Hasan R, Rahmann Z, Uddin PK MM. A computational approach to developing a multi-epitope vaccine for combating Pseudomonas aeruginosa–induced pneumonia and sepsis. *Brief Bioinform*. (2024) 25:bbae401. doi: 10.1093/bib/bbae401

40. Apweiler R, Bairoch A, Wu CH, Barker WC, Boeckmann B, Ferro S, et al. UniProt: The universal protein knowledgebase. *Nucleic Acids Res*. (2004) 32:D115–9. doi: 10.1093/nar/gkh131

41. Doytchinova IA, Flower DR. VaxiJen: a server for prediction of protective antigens, tumour antigens and subunit vaccines. *BMC Bioinf*. (2007) 8:4. doi: 10.1186/1471-2105-8-4

42. Yu C-S, Lin C-J, Hwang J-K. Predicting subcellular localization of proteins for Gram-negative bacteria by support vector machines based on n-peptide compositions. *Protein Sci Publ Protein Soc*. (2004) 13:1402–6. doi: 10.1110/ps.03479604

43. Yu NY, Wagner JR, Laird MR, Melli G, Rey S, Lo R, et al. PSORTb 3.0: improved protein subcellular localization prediction with refined localization subcategories and predictive capabilities for all prokaryotes. *Bioinforma Oxf Engl*. (2010) 26:1608–15. doi: 10.1093/bioinformatics/btq249

44. Dimitrov I, Naneva L, Doytchinova I, Bangov I. AllergenFP: allergenicity prediction by descriptor fingerprints. *Bioinformatics*. (2014) 30:846–51. doi: 10.1093/bioinformatics/btt619

45. Altschul SF, Gish W, Miller W, Myers EW, Lipman DJ. Basic local alignment search tool. *J Mol Biol*. (1990) 215:403–10. doi: 10.1016/S0022-2836(05)80360-2

46. Saha S, Raghava GPS. Prediction of continuous B-cell epitopes in an antigen using recurrent neural network. *Proteins Struct Funct Bioinforma*. (2006) 65:40–8. doi: 10.1002/prot.21078

47. Wang P, Sidney J, Dow C, Mothé B, Sette A, Peters B. A systematic assessment of MHC class II peptide binding predictions and evaluation of a consensus approach. *PloS Comput Biol*. (2008) 4:e1000048. doi: 10.1371/journal.pcbi.1000048

48. Wang P, Sidney J, Kim Y, Sette A, Lund O, Nielsen M, et al. Peptide binding predictions for HLA DR, DP and DQ molecules. *BMC Bioinf*. (2010) 11:568. doi: 10.1186/1471-2105-11-568

49. Dhanda SK, Vir P, Raghava GPS. Designing of interferon-gamma inducing MHC class-II binders. *Biol Direct*. (2013) 8:30. doi: 10.1186/1745-6150-8-30

50. Dhanda SK, Gupta S, Vir P, Raghava GPS. Prediction of IL4 inducing peptides. *Clin Dev Immunol*. (2013) 2013:263952. doi: 10.1155/2013/263952

51. Larsen MV, Lundegaard C, Lamberth K, Buus S, Lund O, Nielsen M. Large-scale validation of methods for cytotoxic T-lymphocyte epitope prediction. *BMC Bioinf*. (2007) 8:424. doi: 10.1186/1471-2105-8-424

52. Gupta S, Kapoor P, Chaudhary K, Gautam A, Kumar R, Raghava GPS. In silico approach for predicting toxicity of peptides and proteins. *PloS One*. (2013) 8:e73957. doi: 10.1371/journal.pone.0073957

53. Vita R, Mahajan S, Overton JA, Dhanda SK, Martini S, Cantrell JR, et al. The immune epitope database (IEDB): 2018 update. *Nucleic Acids Res*. (2019) 47:D339–43. doi: 10.1093/nar/gky1006

54. Fleri W, Paul S, Dhanda SK, Mahajan S, Xu X, Peters B, et al. The immune epitope database and analysis resource in epitope discovery and synthetic vaccine design. *Front Immunol*. (2017) 8:278. doi: 10.3389/fimmu.2017.00278

55. Bui H-H, Sidney J, Dinh K, Southwood S, Newman MJ, Sette A. Predicting population coverage of T-cell epitope-based diagnostics and vaccines. *BMC Bioinf*. (2006) 7:153. doi: 10.1186/1471-2105-7-153

56. Crooks GE, Hon G, Chandonia J-M, Brenner SE. WebLogo: a sequence logo generator. *Genome Res*. (2004) 14:1188–90. doi: 10.1101/gr.849004

57. Gasteiger E, Gattiker A, Hoogland C, Ivanyi I, Appel RD, Bairoch A. ExPASy: the proteomics server for in-depth protein knowledge and analysis. *Nucleic Acids Res.* (2003) 31:3784–8. https://www.ncbi.nlm.nih.gov/pmc/articles/PMC168970/.

58. Magnan CN, Randall A, Baldi P. SOLpro: accurate sequence-based prediction of protein solubility. *Bioinformatics*. (2009) 25:2200–7. doi: 10.1093/bioinformatics/btp386

59. Dimitrov I, Bangov I, Flower DR, Doytchinova I. AllerTOP v.2—a server for in silico prediction of allergens. *J Mol Model.* (2014) 20:2278. doi: 10.1007/s00894-014-2278-5

60. Hebditch M, Carballo-Amador MA, Charonis S, Curtis R, Warwicker J. Protein–Sol: a web tool for predicting protein solubility from sequence. *Bioinformatics*. (2017) 33:3098–100. doi: 10.1093/bioinformatics/btx345

61. McGuffin LJ, Bryson K, Jones DT. The PSIPRED protein structure prediction server. *Bioinformatics*. (2000) 16:404–5. doi: 10.1093/bioinformatics/16.4.404

62. Kouza M, Faraggi E, Kolinski A, Kloczkowski A. The GOR method of protein secondary structure prediction and its application as a protein aggregation prediction tool. In: Zhou Y, Kloczkowski A, Faraggi E, Yang Y, editors. *Prediction of protein secondary structure. Methods in molecular biology*. Springer, New York, NY (2017). p. 7–24. doi: 10.1007/978-1-4939-6406-2_2

63. Du Z, Su H, Wang W, Ye L, Wei H, Peng Z, et al. The trRosetta server for fast and accurate protein structure prediction. *Nat Protoc.* (2021) 16:5634–51. doi: 10.1038/s41596-021-00628-9

64. Heo L, Park H, Seok C. GalaxyRefine: protein structure refinement driven by side-chain repacking. *Nucleic Acids Res.* (2013) 41:W384–8. doi: 10.1093/nar/gkt458

65. Wiederstein M, Sippl MJ. ProSA-web: interactive web service for the recognition of errors in three-dimensional structures of proteins. *Nucleic Acids Res.* (2007) 35: W407–10. doi: 10.1093/nar/gkm290

66. Lovell SC, Davis IW, Arendall WB III, de Bakker PIW, Word JM, Prisant MG, et al. Structure validation by Cα geometry: ϕ,ψ and Cβ deviation. *Proteins Struct Funct Bioinforma.* (2003) 50:437–50. doi: 10.1002/prot.10286

67. Pettersen EF, Goddard TD, Huang CC, Couch GS, Greenblatt DM, Meng EC, et al. UCSF Chimera—A visualization system for exploratory research and analysis. *J Comput Chem.* (2004) 25:1605–12. doi: 10.1002/jcc.20084

68. Ponomarenko J, Bui H-H, Li W, Fusseder N, Bourne PE, Sette A, et al. ElliPro: a new structure-based tool for the prediction of antibody epitopes. *BMC Bioinf.* (2008) 9:514. doi: 10.1186/1471-2105-9-514

69. Novak A, Pupo E, van't Veld E, Rutten VPMG, Broere F, Sloots A. Activation of canine, mouse and human TLR2 and TLR4 by inactivated leptospira vaccine strains. *Front Immunol.* (2022) 13:823058. doi: 10.3389/fimmu.2022.823058

70. Akira S, Uematsu S, Takeuchi O. Pathogen recognition and innate immunity. *Cell.* (2006) 124:783–801. doi: 10.1016/j.cell.2006.02.015

71. Kozakov D, Hall DR, Xia B, Porter KA, Padhorny D, Yueh C, et al. The ClusPro web server for protein–protein docking. *Nat Protoc.* (2017) 12:255–78. doi: 10.1038/nprot.2016.169

72. Abraham MJ, Murtola T, Schulz R, Páll S, Smith JC, Hess B, et al. GROMACS: High performance molecular simulations through multi-level parallelism from laptops to supercomputers. *SoftwareX*. (2015) 1–2:19–25. doi: 10.1016/j.softx.2015.06.001

73. Berendsen HJC, Postma JPM, van Gunsteren WF, DiNola A, Haak JR. Molecular dynamics with coupling to an external bath. *J Chem Phys*. (1984) 81:3684–90. doi: 10.1063/1.448118

74. Hess B, Bekker H, Berendsen HJC, Fraaije JGEM. LINCS: A linear constraint solver for molecular simulations. *J Comput Chem.* (1997) 18:1463–72. doi: 10.1002/(SICI)1096-987X(199709)18:12<1463::AID-JCC4>3.0.CO;2-H

75. Miyamoto S, Kollman PA. Settle: An analytical version of the SHAKE and RATTLE algorithm for rigid water models. *J Comput Chem.* (1992) 13:952–62. doi: 10.1002/jcc.540130805

76. Parrinello M, Rahman A. Polymorphic transitions in single crystals: A new molecular dynamics method. *J Appl Phys.* (1981) 52:7182–90. doi: 10.1063/1.328693

77. Weng G, Wang E, Wang Z, Liu H, Zhu F, Li D, et al. HawkDock: a web server to predict and analyze the protein-protein complex based on computational docking and MM/GBSA. *Nucleic Acids Res.* (2019) 47:W322–30. doi: 10.1093/nar/gkz397

78. Rapin N, Lund O, Bernaschi M, Castiglione F. Computational immunology meets bioinformatics: the use of prediction tools for molecular binding in the simulation of the immune system. *PloS One*. (2010) 5:e9862. doi: 10.1371/journal.pone.0009862

79. Carbone A, Zinovyev A, Képès F. Codon adaptation index as a measure of dominating codon bias. *Bioinformatics*. (2003) 19:2005–15. doi: 10.1093/bioinformatics/btg272

80. Ataides LS, de Moraes Maia F, Conte FP, Isaac L, Barbosa AS, da Costa Lima-Junior J, et al. Sph2(176–191) and sph2(446–459): identification of B-cell linear epitopes in sphingomyelinase 2 (Sph2), naturally recognized by patients infected by pathogenic leptospires. *Vaccines*. (2023) 11:359. doi: 10.3390/vaccines11020359

81. Lin X, Xiao G, Luo D, Kong L, Chen X, Sun D, et al. Chimeric epitope vaccine against Leptospira interrogans infection and induced specific immunity in Guinea pigs. *BMC Microbiol.* (2016) 16:241. doi: 10.1186/s12866-016-0852-y

82. Abdullah M, Kadivella M, Sharma R, Faisal SM, Azam S. *Designing of multiepitope-based vaccine against Leptospirosis using Immuno-Informatics approaches*. New York, USA: Cold Spring Harbor Laboratory (2021) 2021.02.22.431920. doi: 10.1101/2021.02.22.431920.

83. Fernandes LGV, Teixeira AF, Filho AFS, Souza GO, Vasconcellos SA, Heinemann MB, et al. Immune response and protective profile elicited by a multi-epitope chimeric protein derived from Leptospira interrogans. *Int J Infect Dis IJID Off Publ Int Soc Infect Dis.* (2017) 57:61–9. doi: 10.1016/j.ijid.2017.01.032

84. Ibrahim JM, Satheeshkumar PK, Nair AS, Oommen OV, Sudhakaran PR. Designing lsa46-based multi-epitope peptide vaccine against leptospirosis: immunoinformatic approach. *Medinformatics*. (2024). doi: 10.47852/bonviewMEDIN42022655

85. Teixeira AF, Gillespie A, Yirsaw A, Britton E, Telfer JC, Nascimento ALTO, et al. Identification of leptospiral protein antigens recognized by WC1+ γδ T cell subsets as target for development of recombinant vaccines. *Infect Immun.* (2022) 90:e00492–21. doi: 10.1128/IAI.00492-21

86. Chen X, Zaro JL, Shen W-C. Fusion protein linkers: Property, design and functionality. *Adv Drug Delivery Rev.* (2013) 65:1357–69. doi: 10.1016/j.addr.2012.09.039

87. Ahmad S, Demneh FM, Rehman B, Almanaa TN, Akhtar N, Pazoki-Toroudi H, et al. In silico design of a novel multi-epitope vaccine against HCV infection through immunoinformatics approaches. *Int J Biol Macromol.* (2024) 267:131517. doi: 10.1016/j.ijbiomac.2024.131517

88. Tarrahimofrad H, Rahimnahal S, Zamani J, Jahangirian E, Aminzadeh S. Designing a multi-epitope vaccine to provoke the robust immune response against influenza A H7N9. *Sci Rep.* (2021) 11:24485. doi: 10.1038/s41598-021-03932-2

89. Jung ID, Jeong SK, Lee C-M, Noh KT, Heo DR, Shin YK, et al. Enhanced efficacy of therapeutic cancer vaccines produced by co-treatment with mycobacterium tuberculosis heparin-binding hemagglutinin, a novel TLR4 agonist. *Cancer Res.* (2011) 71:2858–70. doi: 10.1158/0008-5472.CAN-10-3487

90. Mahon AB, Arora PS. End-capped α-helices as modulators of protein function. *Drug Discovery Today Technol.* (2012) 9:e57–62. doi: 10.1016/j.ddtec.2011.07.008

91. Werts C, Tapping RI, Mathison JC, Chuang T-H, Kravchenko V, Saint Girons I, et al. Leptospiral lipopolysaccharide activates cells through a TLR2-dependent mechanism. *Nat Immunol.* (2001) 2:346–52. doi: 10.1038/86354

92. Werts C. Interaction of leptospira with the innate immune system. *Curr Top Microbiol Immunol.* (2018) 415:163–87. doi: 10.1007/82_2017_46

frontiers | Frontiers in Immunology

TYPE Original Research
PUBLISHED 07 February 2025
DOI 10.3389/fimmu.2025.1514845

OPEN ACCESS

EDITED BY
Jiae Kim,
Henry M. Jackson Foundation for the Advancement of Military Medicine (HJF), United States

REVIEWED BY
Ebony Gary,
Wistar Institute, United States
Kerri Guth Lal,
Henry M. Jackson Foundation for the Advancement of Military Medicine (HJF), United States

*CORRESPONDENCE
Yongjun Sui
suiy@mail.nih.gov

RECEIVED 21 October 2024
ACCEPTED 22 January 2025
PUBLISHED 07 February 2025

CITATION
Sui Y, Kar S, Chawla B, Hoang T, Yu Y, Wallace SM, Andersen H and Berzofsky JA (2025) Adjuvanted subunit intranasal vaccine reduces SARS-CoV-2 onward transmission in hamsters.
Front. Immunol. 16:1514845.
doi: 10.3389/fimmu.2025.1514845

Adjuvanted subunit intranasal vaccine reduces SARS-CoV-2 onward transmission in hamsters

Yongjun Sui[1]*, Swagata Kar[2], Bhavna Chawla[2], Tanya Hoang[1], YuanKai Yu[3], Shannon M. Wallace[4], Hanne Andersen[2] and Jay A. Berzofsky[1]

[1]Vaccine Branch, National Cancer Institute, National Institutes of Health, Bethesda, MD, United States, [2]Bioqual Inc., Rockville, MD, United States, [3]Cancer Genetics Branch, National Cancer Institute, National Institutes of Health, Bethesda, MD, United States, [4]Experimental Pathology Laboratories, Inc., Sterling, VA, United States

Introduction: Most COVID-19 vaccine trials have focused on recipient protection, not protection of their contacts, a critical need. As a subunit intranasal COVID-19 vaccine reduced nasopharyngeal virus more than did an intramuscular (IM) vaccine, we hypothesized that this vaccine might reduce onward transmission to others.

Methods: We vaccinated hamsters with either the IM-administrated licensed mRNA vaccine twice or one dose of mRNA IM followed by adjuvanted subunit intranasal vaccine. 24 hours after SARS-CoV-2 challenge, these animals were housed with naïve recipients in a contactless chamber that allows airborne transmission.

Results: Onward airborne transmission was profoundly blocked: the donor and recipients of the intranasal vaccine-boosted group had lower oral and lung viral loads (VL), which correlated with mucosal ACE2 inhibition activity. Notably, in this head-to-head comparison of COVID-19 booster vaccines on SARS-CoV-2 onward transmission, we found that statistically significant viral reduction in the lung tissues and oral swabs was observed only in the intranasal S1 nanoparticle vaccine-boosted group, but not in the systemic mRNA vaccine-boosted group, suggesting the superior protection of this intranasal vaccine, which could act as an attractive vaccine booster candidate to complement the current licensed systemic vaccines.

Discussion: Overall, our study strongly supports the use of the intranasal vaccine as a boost to protect not only the vaccinated person, but also people exposed to the vaccinated person, a key public health goal.

KEYWORDS

SARS-CoV-2 vaccine, mucosal vaccine, adjuvant subunit vaccine, onward transmission, mRNA vaccine

Introduction

Blocking viral transmission is an important function of efficient vaccines. From a public health point of view, preventing SARS-CoV-2 transmission to other susceptible individuals is extremely critical. However, most COVID-19 vaccine clinical trials studied only safety and protection of the vaccine recipient, but not prevention of transmission to others. Indeed, the currently licensed SARS-CoV-2 vaccines are successful to alleviate COVID-19-related hospitalization and deaths, but less effective against acquisition of infection and onward transmission (1–3). Though studies on SARS-CoV-2 breakthrough infections suggested that vaccine breakthrough infections are less contagious than primary infections in unvaccinated individuals (4, 5), the effects of these vaccines on reducing transmissibility have not been well evaluated.

As SARS-CoV-2 transmission is mostly through the nasopharynx, mucosal immunity could potentially reduce or abort the SARS-CoV-2 replication at the portal of entry (nasopharynx) to prevent virus from being transmitted to others. Intranasal administration of current vaccines, however, led to inconsistent results against SARS-CoV-2 infections (6, 7). The adjuvant subunit mucosal vaccine, which induces vigorous mucosal immunity in the upper and lower respiratory tracts (8–10), and is more effective at clearing upper airway virus than a similar subunit vaccine given intramuscularly (IM), may have the potential to better reduce SARS-CoV-2 onward transmission. Here, we assessed whether the adjuvanted subunit vaccine (SARS-CoV-2 spike S1+S2 trimer of variants D614G and B.1.1.529 in DOTAP nanoparticles together with adjuvants Poly I:C, CpG and recombinant murine IL-15) delivered intranasally could protect from onward transmission of SARS-CoV-2 in a hamster model better than the systemic mRNA vaccine. As SARS-CoV-2 virus can be effectively transmitted among the hamsters, this represents a more natural dose and route of infection/transmission (11).

Results and discussion

To vaccinate the donor hamsters, we first primed IM two groups of male animals (n=5/group) with Moderna bivalent mRNA COVID-19 vaccine (Moderna Therapeutics, MA) to mimic the fact that many individuals have already been vaccinated with at least one or more doses of systemic vaccines. Male animals were chosen as they are more likely to have higher viral load (VL) and more severe disease (10) (Figure 1A). Three weeks later, Group 1 was boosted with the same mRNA vaccine (IM), while Group 2 was boosted intranasally (IN) with CP-15 adjuvanted (CpG+polyI:C+IL15) spike protein in DOTAP. Four weeks later, all groups, including a naïve control group (Group 3), were intranasally challenged with SARS-CoV-2 virus.

Before studying forward transmission, we wanted to assess the immunity induced by the intranasal vs IM vaccine boosters in the immunized animals to be used as donors in the transmission study. In the serum, total IgG and IgA against WT SARS-CoV-2 (the original Wuhan or WA strain) and against Omicron were comparable, whereas the control animals had negligible binding IgG or IgA (Figure 1A) (ELISA titrations are shown in Supplementary Figure S1). In the previous studies using macaques and mice (refs 8, 9, and 15), we have extensively characterized the immunogenicity of the CP-15 adjuvanted mucosal vaccine, and found that it induced both systemic and mucosal antigen-specific humoral and cellular immune responses (Supplementary Figure S2). Here, we assessed the ACE2 inhibition activity (a surrogate neutralizing antibody assay (12), that is antibody blocking binding to the cell's receptor for SARS-CoV-2, the Angiotensin converting enzyme 2) against the original Wild type (WT, WA or Wuhan) and 9 Omicron sub-strains in the serum and oral swabs of the vaccinated animals. In the serum, Group 1 had similar or higher levels of ACE2 inhibition activity compared to Group 2 (Figures 1B, C). Only the titers against XBB.1.5 were significantly higher in Group 1 vs Group 2 (p=0.0079), and the titers against BF.7(P=0.095), BQ.1 (p=0.095), BQ.1.1(P=0.095), XBB.1 (p=0.056) showed trends of higher titers in Group 1 than in Group 2 (Figure 1C). However, in contrast, in the oral swabs (Figure 2A), it is important to note that the opposite was true, i.e., the mucosal ACE2 inhibition titers were consistently higher for group 2 than for group 1 against most of the variants. This difference was significant for BA.5 (p = 0.032), BN.1 (p = 0.0079), BQ.1 (p = 0.032), BQ1.1 (p = 0.016), XBB.1(P=0.032), and a strong trend for WT (p = 0.056), BA.1 (p = 0.056), and BF.7 (p=0.056). These multiple corroborative results support that conclusion that the mucosal vaccine was more effective at inducing neutralizing activity in the mucosal secretions than in the serum. These results corroborate for these donor animals what we have seen with live virus neutralization assays in our previous studies in hamsters and rhesus macaques (8–10, 13). Likewise, these earlier studies confirm that neutralizing activity is detectable by live virus neutralization assays in both non-human primates and hamsters, supporting the findings by ACE2 binding inhibition here (See Supplementary Figure S2). Moreover, ACE2 inhibition activity in oral swabs was inversely correlated with oral VLs two weeks after viral oropharyngeal challenge, suggesting the mucosal immunity might play a more important role in reducing viral infections (Figure 2B). We also observed that some of the animals in naïve control group had higher ACE2 binding inhibition activities. We speculate that a high variability of background activity for fluids collected from mucosal tissues such as oral cavity might account for this. Nevertheless, these data might also explain the observation that asymptomatic or mildly symptomatic breakthrough infections occurred in subjects who maintained their systemic antibody and T-cell responses (14). We also note that the findings in Figures 1, 2 that the mucosal boost increases only mucosal antibody, not serum antibody, above the levels induced by the IM boost provides indirect evidence suggesting that the mucosal nanoparticles do not leak out to the systemic immune system.

After this characterization of vaccine-induced immune response and protection of the intended "donor" animals, we could set up the main study, to examine forward transmission from infected vaccinated animals to naïve recipients exposed only by the airborne route. Three groups of naïve hamsters (n=5/group) were used as recipients to assess the transmission rate 24 hours after the SARS-CoV-2 viral challenge. In each contact-free cage, under BSL3 containment, one donor animal was housed with one naive recipient animal for 8 hours with unidirectional air flow, through a permeable membrane that prevented physical touching or transfer of

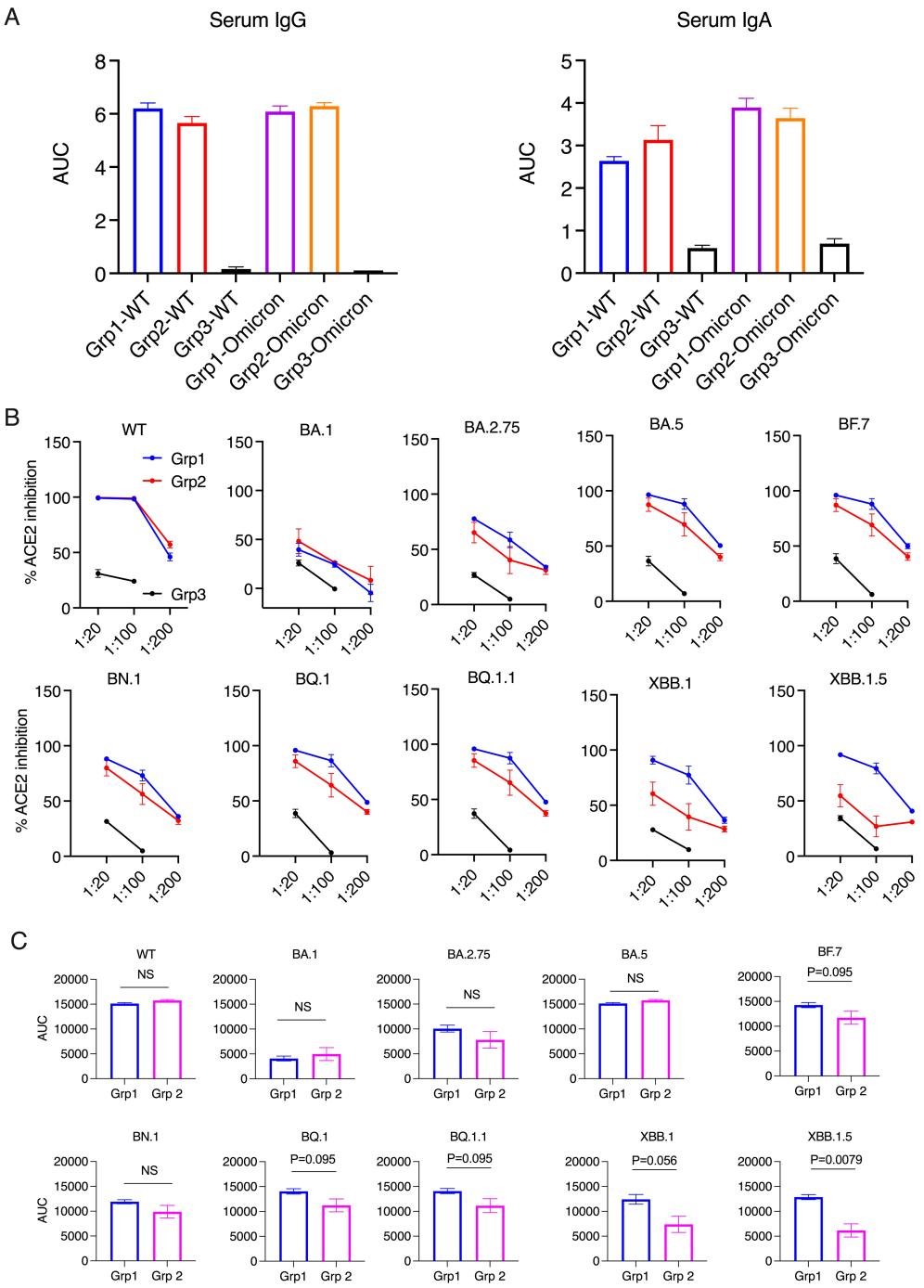

FIGURE 1
Serum antibody responses and ACE2 inhibition activity in the donor animals 2 weeks after the boost. **(A)**. Anti-spike IgG and IgA in serum samples were measured using ELISA. The serum samples were diluted from 1:100, 4-fold dilution, and 6 dilutions. Area under curve (AUC) of serum IgG and IgA are shown. **(B, C)**. The ACE2 inhibition activity against wild type (WT) and Omicron sub-strains in the serum samples of the donor animals (2 weeks after the boost). Area under curve (AUC) of serum ACE2 inhibition activities were calculated and compared between the two vaccinated groups **(C)**. Mann-Whitney tests were used for group comparisons.

secretions, but allowed airborne transmission of virus, from the donor to the recipient. The donor animals were monitored for weight loss, oral VL for an additional 8 days after housing, while the recipient groups were necropsied at day 3 post viral exposure to examine the VL in the lung tissues (Figure 3A). Neither donor vaccine group showed significant weight loss, suggesting both vaccines as a booster could provide sufficient protection against disease (Figure 3B). Despite the small number of animals, both vaccine donor groups demonstrated significantly reduced gRNA (genomic RNA interpreted as input virus) in the lung tissues (at day 10) compared to the naïve group (P=0.016 and P=0.0079 for Group 1 and 2 respectively). However, statistically significant reduction of sgRNA (subgenomic RNA, which is present only in replicating virus and taken as a measure of replicating virus) was

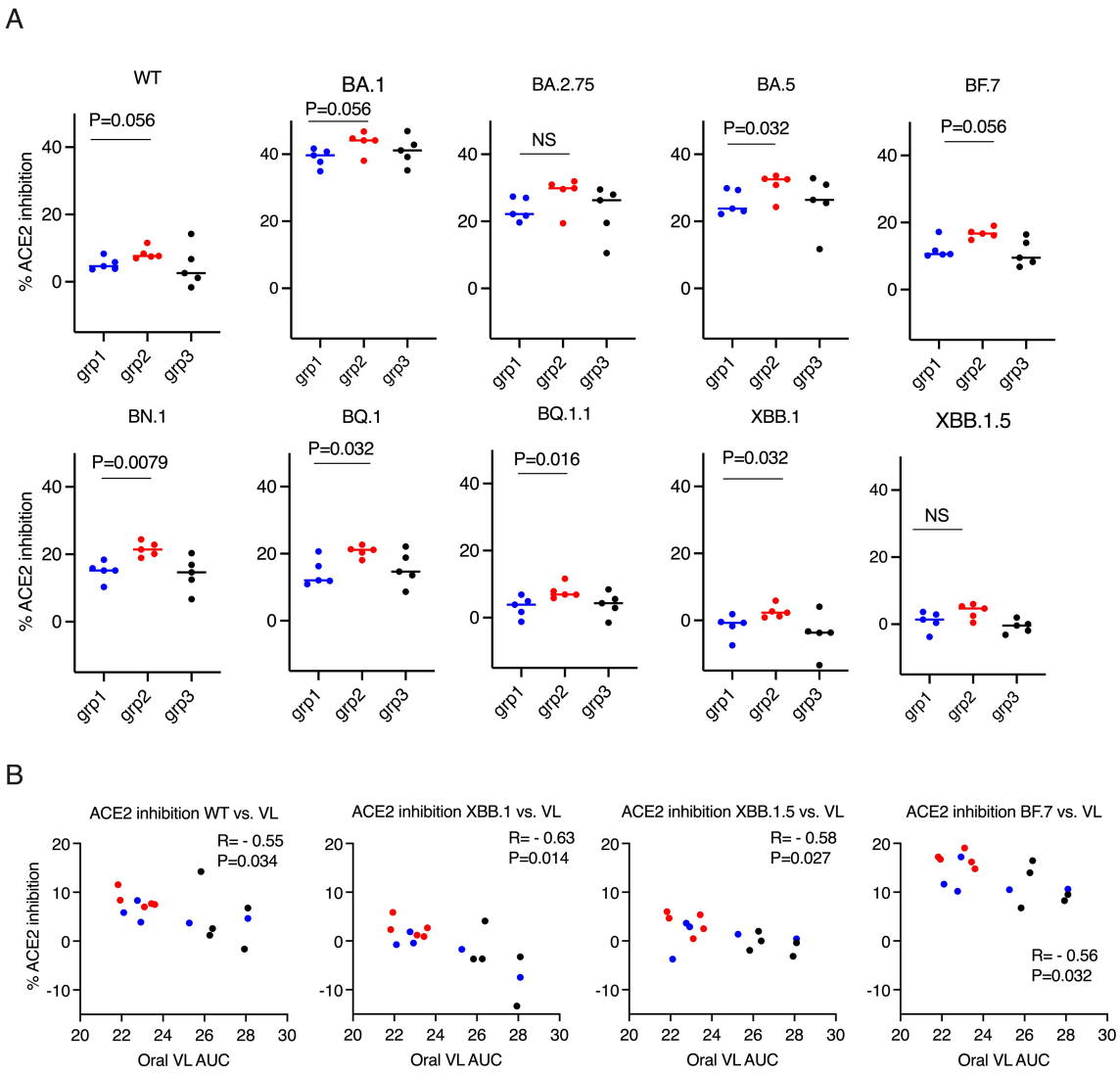

FIGURE 2
ACE2 inhibition activity was inversely correlated with viral load (VL) in the oral swabs. **(A)**. the ACE2 inhibition activity against wild type (WT) and Omicron sub-strains in the oral swabs of the donor animals (2 weeks after the boost). Mann-Whitney tests were used for group comparisons. **(B)**. Spearman's correlations between ACE2 inhibition activity against WT/Omicron sub-strains XBB. 1/XBB. 1.5/BF.7 and the viral load (VL) in oral swabs. The groups are color coded, with Blue, red, and black denoting group 1-3 donor animals respectively. R and P values of Spearman's correlations are shown.

observed in Group 2 (P=0.032) with the mucosal boost, but not in Group 1 (P=0.056). Moreover, both the median gRNA, which were 3.04X10^5/g in Group 1, 8.36X10^4/g in Group 2, and 2.32X10^7/g in the naïve group, and the median sgRNA, which were 6900/g in Group 1, 50/g in Group 2, and 2.93X10^5 in the naïve group, follow a similar trend. In the oral swabs, we observed again that Group 2 (P=0.0079), but not Group 1 (P=0.10), showed significant viral reduction (Figure 3C) (AUC in Figure 3 is based on time course data in Supplementary Figure S3 upper row).

For recipient groups after airborne exposure, none of the 5 animals housing with Group 2 had detectable oral VLs, indicating complete protection, while 3 out of 5 animals housing with Group 3 and 2 out of 5 housing with Group 1 showed oral VLs (Figure 3D) (Oral virus AUC based on time course data presented in Supplementary Figure S3, lower row). In the lung, the replicating virus titer (measured by tissue-culture infectious dose-50 or TCID50, therefore virus particles capable of infecting cells in culture) and sgRNA were significantly reduced only in the animals housed with Group 2 (mucosal boost) compared to those cohoused with control Group 3 (P=0.0079 for replicating virus titer, and P=0.016 for sgRNA), while no significant protection was observed in the animals housed with Group 1 (P=0.056 and P=0.095, respectively; Figure 3D). The median replicating virus titer was 4.97X10^5 in recipients housed with IM Group 1, but only 1.68X10^3 in recipients housed with mucosal Group 2 (2.5 logs lower), compared to 4.12X10^9 in recipients housed with the naïve group, and the sgRNA was 8.48X10^5 in recipients housed with group 1, but only 9.44X10^3 (2 logs lower) in those housed with mucosal Group 2, compared to 5.37X10^9 in naïve control. Nevertheless, both systemic and mucosal vaccines demonstrated significant reduction of SARS-CoV-2 gRNA in recipients (P=0.032 for group 1, and P=0.0079 for Group 2), with median gRNA in Group 1 and 2 recipients of 1.19X10^7, but only 6.87

10.3389/fimmu.2025.1514845

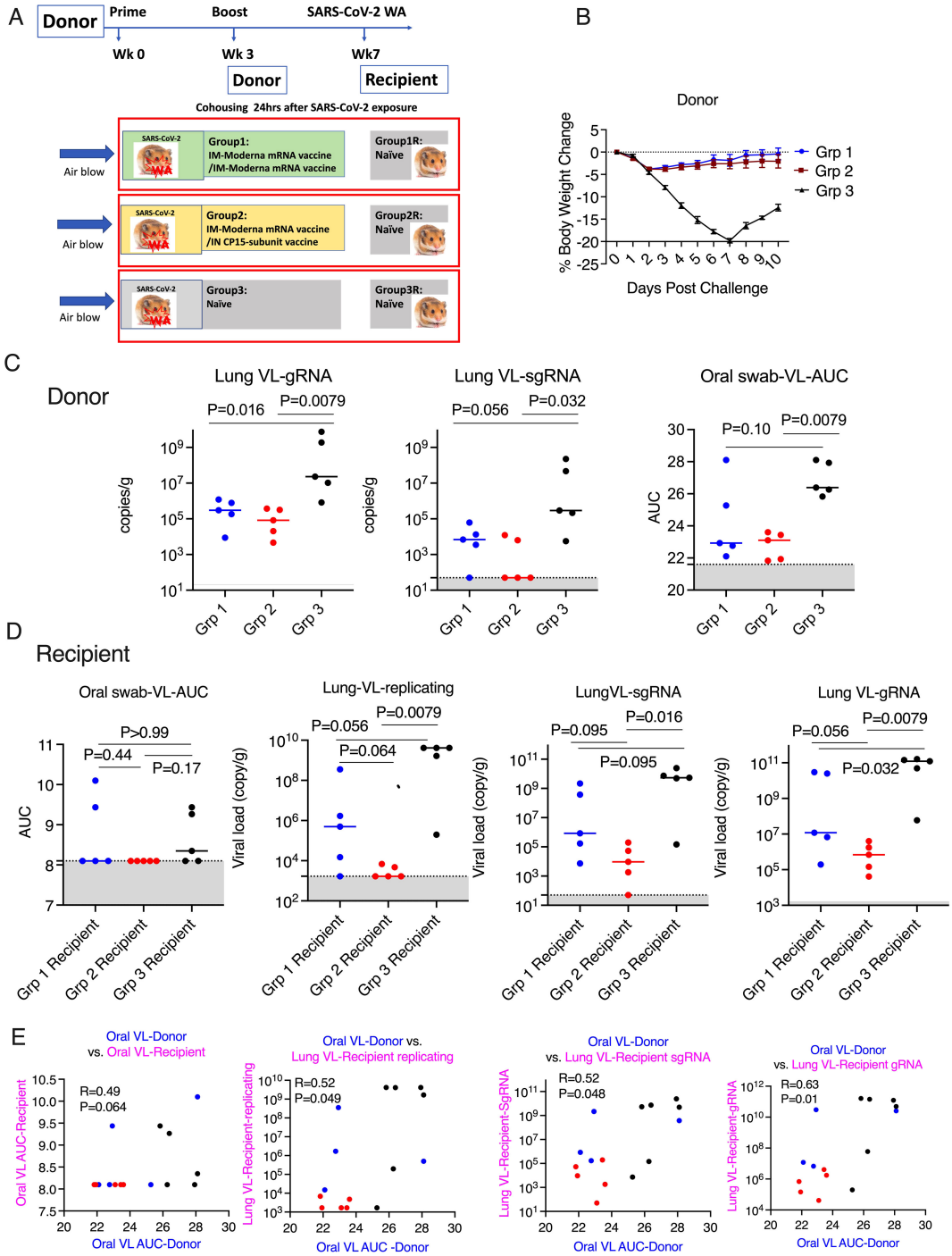

FIGURE 3
Mucosal vaccine prevented SARS-CoV-2 onward transmission in hamsters. **(A)**. Schematic of SARS-CoV-2 transmission study. **(B)**. Body weight change in the donor hamsters after the challenge of SARS-CoV-2 Washington strain. **(C)**. Area under curve (AUC) of viral load (VL) in oral swabs at Days 1, 2, 5, and 7, and sgRNA/gRNA VL in the lung at Day 10 after viral challenge in the donor hamsters. **(D)**. AUC of VL in oral swabs at Day 1, 2, and 3, replicating, sgRNA/gRNA VL in the lung at Day 3 after housing in the recipient hamsters. **(E)**. the Spearman's correlations between the VL in the donor animals and the VL in the recipient animals. Mann-Whitney and Spearman analyses were used for group comparisons and correlations. The groups are color coded, with Blue, red, and black denoting group 1-3 donor and recipient animals respectively. Dotted lines and grey shading indicate the lower limit of detection.

X10^5 respectively, compared to 1.23X10^11 in naïve group. Thus, even though the conventional IM route vaccination does not prevent viral transmission, the viral loads in the recipients were lower, compared to these not vaccinated but not nearly as low as in recipients housed with mucosally boosted animals. Though a statistical trend due to the small number of animals (P=0.056 for gRNA and replicating virus titers, and P=0.095 for sgRNA), the hamsters in the recipient group housing with group 2 consistently

had a log or two lower median gRNA, sgRNA, and replicating viral load levels in the lungs and oral swabs than those housed with group 1 (Figure 3D). Indeed, only the mucosal vaccine group 2 recipients (that received the intranasal S1 protein+ adjuvant nanoparticles) had a consistently significantly lower transmission than the control group in all 3 measures of lung VL, Lung replicating VL ($p = 0.0079$), Lung sgRNA ($p= 0.016$) and lung gRNA ($p = 0.0079$), whereas group 1 IM vaccine was significant only in the last of these ($p = 0.056$, 0.095 and 0.032, respectively). Also, in the oral swabs, only the recipients of group 2 were all completely negative (Figure 3D left). By these criteria, the mucosal vaccine (with the intranasal S1 protein+adjuvant nanoparticles) was more consistently effective and quantitatively more effective against air-borne transmission to naïve hamsters than the IM vaccine. These finding supports the greater efficacy of the intranasal vaccine for preventing onward transmission to naïve hamsters. Histopathological exams revealed that both vaccines were effective in reducing SARS-CoV-2-related microscopic findings in the lung when compared to Group 3 animals; Group 2 was most effective with the lowest incidence of findings (Table 1 and Supplementary Figure S4). Note that Groups 1-3 (donor animals) were necropsied on day 10 after viral challenge, whereas the recipients Groups 4-6 were necropsied on day 3 after co-housing to detect transmission, before much pathological change in the lungs developed. Additionally, both vaccines were effective in eliminating the transmission of SARS-CoV-2 related microscopic findings in the lung of untreated co-housed animals (Table 1 and Supplementary Figure S4), although the day 3 necropsy of the recipients was too early to see much inflammation. We also found that oral VL in the donors was weakly correlated with lung and oral VLs in the recipients ($P=0.064$ for oral VL, $P=0.049$ and 0.048 and 0.01 for lung replicating VL and sgRNA and gRNA; Figure 3E), which was consistent with the previous finding that onward viral transmission is multifactorial, and the level of infectious virus in the donor oropharynx was one of the key parameters (15). Overall, the data indicated that as a booster, the mucosal intranasal vaccine with the S1 protein+adjuvant nanoparticles provided substantially better blockage against onward transmission than the systemic mRNA vaccine did.

One limitation of this study is that we could not evaluate IgG subtypes or the cell-mediated immunity (CMI) (T cell response), which is important for the durability of the vaccine, as the reagents for measuring IgG subtypes and T cell responses in hamsters are limited or largely non-existing. However, in our recent study, we found that the same CP-15 adjuvanted mucosal vaccine as a booster induced robust CMI responses in mouse models (16). As most current vaccines prevent COVID-19 disease but do not prevent initial infection and spread to others, it is important to focus on developing vaccines that block SARS-CoV-2 onward transmission. Previous studies using adenovirus type 5 SARS-CoV-2 mucosal vaccines showed reducing viral transmission compared to naïve donors (17). However, the data to compare the protection capacity against onward transmission with currently licensed systemic vaccines are lacking. Here we did a head-to-head comparison of a subunit mucosal vaccine versus a licensed mRNA vaccine boost for their ability to induce mucosal immunity and subsequently prevent airborne SARS-CoV-2 onward transmission from vaccinated donors to naïve recipients. Our results demonstrated that CP-15 adjuvanted subunit mucosal intranasal vaccine, as a booster, mediated at least as good, and by most parameters, better protection against onward airborne transmission, compared to the licensed systemic mRNA SARS-CoV-2 vaccine (more consistent and quantitatively stronger protection compared to the control group than the systemic vaccine). The induction of mucosal naso-oropharyngeal immunity was a correlate of protection (Figure 2B) and showed consistently higher titers of ACE2-inhibiting antibody in the mucosal secretions after mucosal boost than the systemic vaccine against multiple viral variants of concern. Thus, this mucosal vaccine, along with other mucosal vaccines, could act as attractive vaccine booster candidates to complement the current licensed systemic vaccines to limit SARS-CoV-2 onward transmission and fulfill a critical public health need that has not been addressed.

Materials and methods

Animals

All animal studies were approved by the BIOQUAL Animal Care and Use Committee (Rockville, MD). Thirty male Syrian golden hamsters (Envigo), 8–10 weeks old, were housed and conducted in compliance with all relevant regulations.

Vaccination

The hamsters were grouped randomly into 6 groups (N=5/group). Group 1-3 were the donor groups, and Group 4-6 were the recipient groups. 10 μg/dose Moderna COVID-19 bivalent vaccine (containing mRNA for both original and Omicron BA.4/BA.5 variants) (in 100μl) was given to Group 1 -2 intramuscularly at Day 0. On Day21, Group1 got the same dose/route of Moderna COVID-19 vaccine. Group 2 received intranasally CP-15 adjuvanted mucosal vaccine, which was composed of 20 μg of SARS-CoV-2 Spike S1+S2 trimer protein (10 μg D614G + 10 μg B.1.1.529) (40589-V08H8, 40589-V08H26, Sino Biological. Inc.), mixed with 20 μg of D-type CpG oligodeoxynucleotide (vac-1826-1, *In vivo*Gen), 40 μg of Poly I:C (vac-pic, *In vivo*Gen), and 20 μg of recombinant murine IL-15 (210-15, PeproTech) in 20 μl of DOTAP (11 811 177 001, Roche Inc.)((1,2-dioleoyl-3-trimethylammonium propane) is a cationic lipid used for DNA transfection of cells. We use it as an adjuvant by mixing the antigen and TLR ligand adjuvants and cytokines with DOTAP to form micellular nanoparticles that protect the components from degradation and deliver them to cells.). The variants used were the most recent available for animal use at the time of the study. Moreover, the purpose of the study was to test proof of principle that the mucosal vaccine would be more effective at reducing the risk of onward transmission, so the specific strain of SARS-CoV-2 was not critical to this goal. For the intranasal procedures, the hamsters were sedated with Ketamine (80μg/kg)/Xylazine(5μg/kg), and 50 uL/nare, total 100uL vaccine was administrated per hamster. The dosing material was more likely to penetrate further into the

TABLE 1 SARS-CoV-2-related microscopic findings in the lung of the donor (necropsied at Day 10 post challenge) and the recipient animals (necropsied at Day 3 post housing) *.

Groups	1	2	3	Groups	1 Recipient	2 Recipient	3 Recipient
Animals/Group	5	5	5[a]	Animals/Group	5	5	5
Inflammation, mixed or mononuclear cell, alveolar or bronchoalveolar	3	–	5	**Inflammation, mononuclear cell, alveolar**	–	–	1
minimal	3	–	–	minimal	–	–	1
mild	–	–	4				
moderate	–	–	–				
marked	–	–	1				
Inflammation, mononuclear cell, vascular/perivascular	–	–	5	**Inflammation, mononuclear cell, vascular/perivascular**	–	–	3
minimal	–	–	3	minimal	–	–	2
mild	–	–	2	mild	–	–	1
Fibrosis or fibroplasia, pleural	–	–	2				
minimal	–	–	1				
mild	–	–	1				
Syncytial cell	–	–	5				
minimal	–	–	5				
Hyperplasia, bronchiolo-alveolar or alveolar	5	1	5				
minimal	3	–	–				
mild	2	1	–				
moderate	–	–	3				
marked	–	–	2				
Hyperplasia, endothelial	–	–	2				
minimal	–	–	2				
Hemorrhage	–	–	2				
minimal	–	–	–				
mild	–	–	2				
Hypertrophy, mesothelial cell	–	–	1				
minimal	–	–	–				
mild	–	–	1				

*Findings were graded 1-5, depending upon severity. Microscopic findings, if applicable, are correlated with macroscopic observations. For severity grades, equivalent numbered grades are 1 = minimal, 2 = mild, 3 = moderate, 4 = marked, 5 = severe.

respiratory tract, getting to the lungs by using this procedure (sedation and size of the inoculum).

Viral challenge and viral transmission

Four weeks after the last vaccination, Group 1-3 (Group 3 was the naïve control group) were challenged with $6x10^3$ PFU SARS-CoV-2 WAS-CALU-3 (LOT: 12152020-1235, BEI Resources). The animals were sedated, and virus challenge was given intranasally with 50 µl/nare as described before (10). Body weights were monitored before and after the viral challenge. 24hrs after the viral challenge, each animal from Group1-3 was housed with one naïve hamster from Group 4-6 respectively. The housing was in a single contract-free transmission chamber as described before (17). The chamber was designed so that the airflow was unidirectional: from the infected donor animal to the naïve recipient one. Animals were housed 1:1 with a transmission divider for 8 hours, then single housed. The donor animals were monitored for an additional 8 days for body weights, oral VLs. At Day10, the donor animals were necropsied, and lung viral loads were measured. For recipient groups, body weights and oral VLs was monitored and at Day3, the animals were necropsied, and lung VLs were measured.

ELISA and ACE2 inhibition assay

ELISA and ACE2 inhibition assay were performed as described (10, 12). The V-PLEX-SARS-CoV-2 Panel 32 (ACE2) Kit was used according to the manufacturer's instructions using a Sector Imager 2400 (Meso Scale discovery). Serum samples (diluted 20-, 100-, and 200-fold), or oral samples (2-fold dilution) were added into the pre-coated V-plex plates. ACE2 binding and detection reagents were sequentially added.

Viral load measurements

TCID50 assays were used to measure live virus as described before (10). Briefly, 20 µL of sample was 10-fold serially diluted and added to Vero TMPRSS2 cells, cultured in DMEM + 2% FBS + Gentamicin at 37°C, 5.0% CO2 for 4 days. Virus stock of known infectious titer was included in the assay as a positive control, while medium only served as a negative control. Cytopathic effect (CPE) was inspected, and the TCID50 value was calculated using the Read-Muench formula. SARS-CoV-2 RNA levels were assessed by reverse transcription PCR at BIOQUAL, Inc. as previously described (8). RNA was extracted from oral swab and homogenized lung tissue samples. Subgenomic/viral RNA using different primer/probe sets, targeting the viral E gene mRNA or the viral nucleocapsid respectively, was measured. VLs are shown as copies per swab for oral samples, and copies per gram for lung tissues, with a cutoff value of 50 copies.

Histopathological exams

Groups 1-3 were euthanized on Day 10 post viral challenge. Recipient groups were euthanized on Day 3 post co-housing. At necropsy, the left lung was collected and placed in 10% neutral buffered formalin for histopathologic analysis. Tissue sections were trimmed and processed to hematoxylin and eosin (H&E) stained slides, all slides were examined by a board-certified pathologist and recorded using the Pristima 7.5.0 Build 8 version computer system.

Statistical analysis

Statistical analyses were performed using Prism version 9. Oral swab viral load was presented as area under curve (AUC) values. Mann-Whitney and Spearman analyses were used for group comparisons and correlations. All statistical tests were 2-tailed.

Data availability statement

The original contributions presented in the study are included in the article/Supplementary Material. Further inquiries can be directed to the corresponding author.

Ethics statement

The animal study was approved by the BIOQUAL Animal Care and Use Committee (Rockville, MD). The study was conducted in accordance with the local legislation and institutional requirements.

Author contributions

YS: Conceptualization, Data curation, Formal analysis, Investigation, Methodology, Supervision, Validation, Visualization, Writing – original draft, Writing – review & editing. SK: Data curation, Methodology, Writing – review & editing. BC: Data curation, Methodology, Writing – review & editing. TH: Methodology, Writing – review & editing. YY: Data curation, Methodology, Writing – review & editing. SW: Methodology, Writing – review & editing. HA: Conceptualization, Data curation, Methodology, Writing – review & editing. JB: Conceptualization, Funding acquisition, Supervision, Writing – review & editing.

Funding

The author(s) declare financial support was received for the research, authorship, and/or publication of this article. This work was supported by funding Z01 BC-011941 to JB from Intramural Research Program, Center for Cancer Research, National Cancer Institute, National Institutes of Health. The funders had no role in study design, data collection and analysis, decision to publish, or preparation of the manuscript.

Acknowledgments

We would like to thank Dr. Hyoyoung Choo-Wosoba, a statistician from office of collaborative biostatistics, CCR, NCI, for evaluating the data, and providing invaluable advice to validate the statements on statistics.

Conflict of interest

Authors SK, BC, and HA were employed by the company Bioqual Inc. Author SW was employed by the company Experimental Pathology Laboratories, Inc.

The remaining authors declare that the research was conducted in the absence of any commercial or financial relationships that could be construed as a potential conflict of interest.

The US government has filed the patent, NIH Ref. No. E-064-2021-0 on the adjuvanted mucosal subunit vaccine for preventing SARS-CoV-2 transmission and infection.

Generative AI statement

The author(s) declare that no Generative AI was used in the creation of this manuscript.

Publisher's note

All claims expressed in this article are solely those of the authors and do not necessarily represent those of their affiliated organizations, or those of the publisher, the editors and the reviewers. Any product that may be evaluated in this article, or claim that may be made by its manufacturer, is not guaranteed or endorsed by the publisher.

Supplementary material

The Supplementary Material for this article can be found online at: https://www.frontiersin.org/articles/10.3389/fimmu.2025.1514845/full#supplementary-material

References

1. Jung J, Kim JY, Park H, Park S, Lim JS, Lim SY, et al. Transmission and infectious SARS-coV-2 shedding kinetics in vaccinated and unvaccinated individuals. *JAMA Netw Open*. (2022) 5:e2213606. doi: 10.1001/jamanetworkopen.2022.13606

2. Riemersma KK, Haddock LA 3rd, Wilson NA, Minor N, Eickhoff J, Grogan BE, et al. Shedding of infectious SARS-CoV-2 despite vaccination. *PloS Pathog*. (2022) 18: e1010876. doi: 10.1371/journal.ppat.1010876

3. Salvatore PP, Lee CC, Sleweon S, McCormick DW, Nicolae L, Knipe K, et al. Transmission potential of vaccinated and unvaccinated persons infected with the SARS-CoV-2 Delta variant in a federal prison, July-August 2021. *Vaccine*. (2023) 41:1808–18. doi: 10.1016/j.vaccine.2022.11.045

4. Abu-Raddad LJ, Chemaitelly H, Ayoub HH, Tang P, Coyle P, Hasan MR, et al. Relative infectiousness of SARS-CoV-2 vaccine breakthrough infections, reinfections, and primary infections. *Nat Commun*. (2022) 13:532. doi: 10.1038/s41467-022-28199-7

5. Mostaghimi D, Valdez CN, Larson HT, Kalinich CC, Iwasaki A. Prevention of host-to-host transmission by SARS-CoV-2 vaccines. *Lancet Infect Dis*. (2022) 22:e52–8. doi: 10.1016/S1473-3099(21)00472-2

6. Cokaric Brdovcak M, Materljan J, Sustic M, Ravlic S, Ruzic T, Lisnic B, et al. ChAdOx1-S adenoviral vector vaccine applied intranasally elicits superior mucosal immunity compared to the intramuscular route of vaccination. *Eur J Immunol*. (2022) 52:936–45. doi: 10.1002/eji.202249823

7. Madhavan M, Ritchie AJ, Aboagye J, Jenkin D, Provstgaad-Morys S, Tarbet I, et al. Tolerability and immunogenicity of an intranasally-administered adenovirus-vectored COVID-19 vaccine: An open-label partially-randomised ascending dose phase I trial. *EBioMedicine*. (2022) 85:104298. doi: 10.1016/j.ebiom.2022.104298

8. Sui Y, Li J, Zhang R, Prabhu SK, Elyard HA, Venzon D, et al. Protection against SARS-CoV-2 infection by a mucosal vaccine in rhesus macaques. *JCI Insight*. (2021) 6:1–15. doi: 10.1172/jci.insight.148494

9. Sui Y, Li J, Andersen H, Zhang R, Prabhu SK, Hoang T, et al. An intranasally administrated SARS-CoV-2 beta variant subunit booster vaccine prevents beta variant replication in rhesus macaques. *PNAS Nexus*. (2022) 1:pgac091. doi: 10.1093/pnasnexus/pgac091

10. Sui Y, Andersen H, Li J, Hoang T, Bekele Y, Kar S, et al. Protection from COVID-19 disease in hamsters vaccinated with subunit SARS-CoV-2 S1 mucosal vaccines adjuvanted with different adjuvants. *Front Immunol*. (2023) 14:1154496. doi: 10.3389/fimmu.2023.1154496

11. Port JR, Yinda CK, Riopelle JC, Weishampel ZA, Saturday TA, Avanzato VA, et al. Infection- or vaccine mediated immunity reduces SARS-CoV-2 transmission, but increases competitiveness of Omicron in hamsters. *Nat Commun*. (2022) 14:6592. doi: 10.1101/2022.07.29.502072

12. Tan CW, Chia WN, Qin X, Liu P, Chen MI, Tiu C, et al. A SARS-CoV-2 surrogate virus neutralization test based on antibody-mediated blockage of ACE2-spike protein-protein interaction. *Nat Biotechnol*. (2020) 38:1073–8. doi: 10.1038/s41587-020-0631-z

13. Sui Y, Andersen H, Li J, Hoang T, Minai M, Nagata BM, et al. SARS-CoV-2 mucosal vaccine protects against clinical disease with sex bias in efficacy. *Vaccine*. (2024) 42:339–51. doi: 10.1016/j.vaccine.2023.11.059

14. Rovida F, Cassaniti I, Paolucci S, Percivalle E, Sarasini A, Piralla A, et al. SARS-CoV-2 vaccine breakthrough infections with the alpha variant are asymptomatic or mildly symptomatic among health care workers. *Nat Commun*. (2021) 12:6032. doi: 10.1038/s41467-021-26154-6

15. Puhach O, Meyer B, Eckerle I. SARS-CoV-2 viral load and shedding kinetics. *Nat Rev Microbiol*. (2023) 21:147–61. doi: 10.1038/s41579-022-00822-w

16. Li J, Hsu KS, Howe SE, Hoang T, Xia Z, Berzofsky JA, et al. Sex-biased immunogenicity of a mucosal subunit vaccine against SARS-CoV-2 in mice. *Front Immunol*. (2024) 15:1386243. doi: 10.3389/fimmu.2024.1386243

17. Langel SN, Johnson S, Martinez CI, Tedjakusuma SN, Peinovich N, Dora EG, et al. Adenovirus type 5 SARS-CoV-2 vaccines delivered orally or intranasally reduced disease severity and transmission in a hamster model. *Sci Transl Med*. (2022) 14: eabn6868. doi: 10.1126/scitranslmed.abn6868

frontiers | Frontiers in Immunology

TYPE Original Research
PUBLISHED 13 February 2025
DOI 10.3389/fimmu.2025.1513245

OPEN ACCESS

EDITED BY
Jiae Kim,
Henry M Jackson Foundation for the Advancement of Military Medicine (HJF), United States

REVIEWED BY
Rajesh Palanisamy,
University of Texas at San Antonio, United States
Anke Osterloh,
Research Center Borstel (LG), Germany

*CORRESPONDENCE
Rachita Sarangi
rachitapaedia@gmail.com
Anu Vinod Ranade
aranade@sharjah.ac.ae

RECEIVED 18 October 2024
ACCEPTED 02 January 2025
PUBLISHED 13 February 2025

CITATION
Panda S, Swain SK, Sahu BP, Mahapatra SR, Dey J, Sarangi R, Ranade AV and Mishra N (2025) Designing a potent multivalent epitope vaccine candidate against *Orientia tsutsugamushi* via reverse vaccinology technique - bioinformatics and immunoinformatic approach. *Front. Immunol.* 16:1513245. doi: 10.3389/fimmu.2025.1513245

Designing a potent multivalent epitope vaccine candidate against *Orientia tsutsugamushi* via reverse vaccinology technique - bioinformatics and immunoinformatic approach

Subhasmita Panda[1], Subrat Kumar Swain[1], Basanta Pravas Sahu[2], Soumya Ranjan Mahapatra[3], Jyotirmayee Dey[3], Rachita Sarangi[1]*, Anu Vinod Ranade[4]* and Namrata Mishra[3]

[1]Institute of Medical Sciences and SUM Hospital, Siksha O Anusandhan University, Bhubaneswar, India, [2]School of Biological Sciences, The University of Hong Kong, Hong Kong, Hong Kong SAR, China, [3]School of Biotechnology, Kalinga Institute of Information and Technology (KIIT) University, Bhubaneswar, India, [4]Department of Basic Medical Sciences, College of Medicine, University of Sharjah, Sharjah, United Arab Emirates

Scrub typhus is a life-threatening, undifferentiated febrile illness caused by a gram-negative bacterium, *Orientia tsutsugamushi*. The bacterial strain is a global health concern that should be considered. Despite several years of effort for the development of an effective immunogenic vaccine, no successful licensed vaccine is available. The aim of the study is to construct an epitope response using a reverse vaccinology approach. The TSA56 and ScaA proteins combined can be the most promising subunit vaccine candidates against *O. tsutsugamushi*. B-cell, CTL, and HTL epitopes were predicted, and subsequently, all the epitopes were linked by KK, AAY, and GPGPG linkers, respectively, along with an adjuvant at the N-terminal region. Furthermore, molecular docking and MD simulations were performed that exhibited a higher affinity towards TLR-2. A total of 16 linear B-cells, 6 CTL, and 2 HTL epitopes were identified and validated. The final vaccine construct showed high antigenicity, stability, and solubility. Molecular docking and MD simulations indicated strong binding interactions with TLR-2 and a stable vaccine-receptor complex. The expression of the vaccine in pET28a (+) vector was successfully implemented via in silico cloning as well as significant results from immune simulation demonstrated the efficacy of the vaccine in the immune cell interaction during the innate and adaptive immune responses immune simulation. In conclusion, the outcome suggested that the newly developed vaccine will be a promising candidate for controlling and providing definitive preventive measures against scrub typhus if further investigation is conducted experimentally.

KEYWORDS

multiplex vaccinology, scrub typhus, protein-protein docking, immune simulation, in-silico cloning, molecular dynamic simulation

1 Introduction

Scrub typhus, a neglected tropical disease, is caused by the gram-negative bacteria *Orientia tsutsugamushi* (*O. tsutsugamushi*), rising rapidly in various endemic countries and becoming a serious health concern (1, 2). Despite being recognized as early as 313 A.D. and causing a significant threat to billions of people across various regions of Asia and Australia, this disease remains underdiagnosed and underreported. Historically, it was confined to the "Tsutsugamushi triangle', an area covering 13 million km^2 that extends from Russia to Japan in the north, Northern Australia in the south, and Pakistan and Afghanistan in the west (3). However, confirmed cases have now emerged beyond the traditional countries, including Dubai, Chile, part of Africa, and Peru (4). The diversity in species and epidemic characteristics across other countries like China, Japan, Taiwan, Thailand, Hong Kong, and South Korea (1). Between January 2010 and December 2019, Taiwan reported 4,374 confirmed cases of scrub typhus, consisting of 4,352 domestic cases and 22 imported cases. Analysis of the epidemiological features revealed a significant male predominance (2,699 males vs. 1,675 females) (5). A study reported 6,338 reported ST cases, of which 304 were laboratory-confirmed. Incidence rates rose significantly over the years, from 0.03 per 100,000 in 2006 to 1.12 per 100,000 in 2021, with the highest rates occurring among farmers (6).

Vaccines have evolved over the years, directing from those that use the entire organism either killed or live-attenuated to those that are based on the smaller segments of the organism like toxins, purified antigens, subunits, and synthetic peptides. As genome sequencing became increasingly prevalent, it ushered in a new era in vaccinology known as reverse vaccinology (7). Multi-epitope subunit vaccines have been developed over the past few decades using reverse vaccinology techniques to combat a wide variety of infections such as *Acinetobacter baumannii* (8), *Pseudomonas aeruginosa* (9), *Klebsiella pneumonia* (10), *Helicobacter pylori* (11), *Mycobacterium tuberculosis* (12) and many more. These vaccines are effective in both *in vitro* and *in vivo* mouse model, making them viable alternatives to the cost and time-consuming process of developing vaccination in the trial-and-error process of the conventional way.

In the past few decades, demand for the use of active immunotherapy has increased, such as an epitope-based vaccination, for the treatment of different diseases (13). Prevailing epitope vaccination deficits can be mitigated by a variety of approaches including enhancing the number of antigenic epitopes that can be targeted by an immunogenic adjuvant or a carrier protein (14, 15).

Five autotransfer domain-containing proteins (ScaA-ScaE) and immunogenic surface antigen proteins such as TSA22, TSA47, and TSA56 are encoded by the 2.1Mbp genome of the gram-negative bacterium *O. tsutsugamushi*. ScaA facilitates bacterial adherence to the host cell and exhibits a high level of strain-specific conservation in its passenger domain (16). Patients develop strain-specific antibodies due to four variable domains of TSA56. Thus, potential vaccine candidates, including TSA47, TSA56, and ScaA, have been investigated (17, 18). Toll-like receptors are the most extensively researched Pathogen Recognition Receptors (PRRs); they are accountable for recognizing pathogen-associated molecular patterns (PAMPs). TLR2 is frequently used as a target for adjuvants because its activation can enhance both innate and adaptive immune responses. TLR2 activation can promote a strong antigen-presenting cell response and subsequent T-cell activation. In this research, the immunoinformatics and reverse vaccinology approach was applied to develop a potential multiepitope chimeric vaccine against the *O. tsutsugamushi* bacterium to prevent the spread of scrub typhus.

2 Materials and method

2.1 Sequence availability and proteome retrieval

Highly virulent TSA56 (accession no. SPR11258.1) and ScaA (accession no. SPR07654.1) proteins from all the available complete genome sequences of *O. tsutsugamushi* were retrieved from the NCBI database, among which the highly antigenic strain Gilliam was selected.

2.2 Screening of potent epitopes

B cell epitopes play a key role in generating long-term humoral immune response and memory cells by activating B lymphocytes. Linear B cell epitopes were predicted by using ABCPred (19) with a 10-mer window length. The NetMHCpan 4.1 server (20) was used to predict the MHC-I restricted CD8+ cytotoxic T-lymphocyte (CTL) epitopes of the chosen protein sequence. CTL epitope prediction was studied across 12 MHC class-I supertypes (HLA-A01:01, HLA-A02:01, HLA-A03:01, HLA-A24:02, HLA-A26:01, HLA-B07:02, HLA-B08:01, HLA-B27:05, HLA-B39:01, HLA-B40:01, HLA-B58:01, HLA-B15:01). In response to invading pathogens, helper T lymphocytes can activate either humoral or cellular immune responses. The IEDB server was used to predict HTL epitopes with human HLA cells as the default parameter. Scores below 50 nM for the IC50 indicate a strong binding affinity.

2.3 Evaluation of epitopes for vaccine construct and assessment

Antigen, non-allergen, non-toxic, and immunogenicity were all taken into account while selecting the epitopes by using VaxiJen v2.0 (21), AllerTop v2.0 (22), ToxinPred (23) and IEDB servers respectively. Cholera toxin subunit B (ACO36766.1), a potential adjuvant, was linked to the N-terminus of the construct with the help of EAAAK peptide linker to accelerate the immune response, followed by selected LBL, CTL, and HTL epitopes with appropriate linkers KK, AAY, and GPGPG to aid the amino acids in folding into appropriate conformations with maximum flexibility. The solubility of the vaccine design was calculated using the SolPro service (24). ExPASyProtParam server (25) was then used to evaluate the developed vaccine construct for its physicochemical characterization.

2.4 mRNA

With the help of the Mfold web server, the multi-epitope vaccine RNA secondary structure was anticipated (26). With minimal ΔG thermodynamics, this server provides true positive bps prediction.

2.5 Cluster analysis of MHC alleles

Similar binding specificities among MHC-I and MHC-II molecule alleles can be determined by cluster analysis which was done by using MHCcluster 2.0, a web-based server (27). All of the HLA supertype representatives were chosen during the analysis, and the number of peptides to be included was kept constant at 50,000.

2.6 Conservancy analysis and global population coverage

Conservancy analysis was performed on the anticipated epitope using the IEDB analysis resource (28) to predict the degree of similarity within the serotypes of *O. tsutsugamushi* at a sequence identity threshold of 60%. Due to polymorphism, MHC molecules may demonstrate substantial variations among populations. The IEDB population coverage server was used to determine whether or not the chosen CTL and HTL epitope alleles were represented in the general population (29).

2.7 Homology modelling, assessment and validation of vaccine construct

The PSIPRED 4.0 web server was employed to provide accurate predictions about the secondary structure of the vaccine construct (30). The tertiary structure of the vaccine sequence was obtained using the Robetta server (31). PyMol was used to display the 3D structure of the vaccine construct. GalaxyRefine2 (32) server was used to improve the final structure. The development of the Ramachandran plot using PROCHECK (33) and SWISS_MODEL (34) was used to check the model quality. The Ramachandran plot is used in this server to foresee the probability that amino acids form a secondary structure and to illustrate the quality of models by the proportion of amino acids in the favored, allowed preferred, and outlier ranges. The validation was additionally approved by the SAVES server using ERRAT (35) and Verify3D (36).

2.8 Discontinuous B-cell epitope prediction

Over 90% of B cell epitopes were found to be discontinuous. The confirmed three-dimensional structure of conformational B-cell epitopes is predicted by the web-based server Ellipro (37). Compared to other structure-based epitope prediction techniques, Ellipro came out on top, with an AUC value of 0.732 as the best computation for any protein.

2.9 Disulfide bond engineering

The DbD2 web server (38) was used to create a reasonable disulfide bond in the protein structure and assess whether they were consistent in terms of proximity and geometry. As the proteins are very dynamic, mutations can affect the structure and consequently the function of the protein.

2.10 Molecular docking

To predict the interaction and binding affinity between the designed vaccine and human Toll-like receptor-2 (TLR-2), molecular docking is an especially feasible and basic technique. To facilitate molecular docking, the crystal structure of TLR-2 (PDB id: 3a7c) was obtained from the protein data bank. The molecular docking was performed with ClusPro 2.0 employing novel FFT correlation, grouping the best energy conformations, and analyzing cluster stability with a short Monte Carlo simulation to predict the interaction between two proteins (39). The best-docked conformations of the proteins and peptides were visualized using the PyMol visualization tool.

2.11 Molecular dynamic simulation of the docked complex

Molecular dynamic (MD) simulation was used in the present study to better understand the protein-protein docking complex that performed most effectively. The MD simulation was carried out using GROMACS 2019 package (40) and OPLS-e force field, with the TIP3P water model used to solvate the protein complex. Sodium and chloride ions were introduced to get a neutral physiological salt content, and the system energy was minimized using the steepest descent technique. To keep the lengths of the covalent bonds constant during the simulation, the Linear Constraint Solver (LINCS) method was utilized. For the long-range electrostatic interactions, the Particle Mesh Ewald (PME) method was used, and for the short-range coulomb and Van der Waals interaction, we settled on a radius of 0.9 nm. After that, equilibrations were performed for both systems at 100 ps NVT [constant number of particles (N), volume (V), and temperature (T)] and 100 ps NPT [constant number of particles (N), pressure (P), and temperature (T)]. After running 50 ns of simulations using PBC, we analyzed the results with GROMACS modules and used xmgrace to create the relevant charts and figures.

2.12 Codon optimization and in silico cloning

To enable the production of the vaccine construct in a chosen expression vector, reverse translation and codon optimization was

carried out using the Java Codon Adaptation Tool (JCat) website (41). Since the final vaccine design derives its sequence from human DNA, it required some codon optimization so that it could be expressed in *E. coli* strain K12 host. Codon adaptation index (CAI) and GC content (%) are two measures of protein expression that are provided in JCat output. Adding HindIII and BamHI restriction sites to the N and C-terminus of the DNA sequences of the projected vaccines allowed for their cloning in the *E. coli* pET-28a (+) vector, yielding the final vaccine constructs with the optimal gene sequence. The final step in ensuring the expression of the vaccine was to use the SnapGene tool to insert the optimized DNA sequences with restriction sites into the pET-28a(+) vector.

2.13 Immune simulation of vaccine

Using the C-ImmSim server, in silico immune simulations were carried out to evaluate the immunogenic properties of a multi-epitope vaccine under real-world settings (42). The duration between doses 1 and 2 for vaccination should be at least 4 weeks. As a result, 3 injections containing one thousand vaccine proteins were administered 4 weeks apart at 1, 84, and 168 time-steps (each time-step equals 8 h in real life, and time-step 1 is injection at time = 0), for a total of 1050 simulation steps (parameters were set in the C-ImmSim immune simulator). Three injections of selected peptides were administrated at four-week intervals to simulate repeated antigen exposure and study clonal selection in a typical endemic area. The graph was used to determine the Simpson index (D), a metric of variety. Figure 1 depicts the entire process used in the reverse vaccinology analysis.

3 Results

3.1 Retrieval and phylogenetic analysis of target proteins

The complete proteome of the Gilliam strain was retrieved from NCBI to extract virulent TSA56 and ScaA proteins in FASTA format for peptide vaccine designing. The proteins were found to be antigen and non-allergen, with antigenicity scores of 0.79 and 0.82 for TSA56 and ScaA, respectively.

3.2 Evaluation of B-cell, CTL and HTL epitopes

Peptide mapping using ABCPred on the FASTA sequences of TSA56 and ScaA proteins revealed a total of 16 epitopes at the default threshold >0.51 and window length of 10. These peptides were selected by antigenicity and non-allergenicity. Among these, two 10mer peptides (TGAESTRLDS and SAEVEVGKGK of TSA56) with the most favorable ABCPred server score were chosen for additional assessment of antigenicity, toxicity, and allergenicity, shown in Table 1.

Antigenic determinants presented by MHC-I elicit a cellular immunological response. This kind of reaction often stimulates the production of cytotoxic cells. Table 2 summarizes the final selection of 6 epitopes for vaccine construction among the top 22 and 7 sequences of epitopes from TSA56 and ScaA protein. To determine HTL epitopes for all structural proteins, the IEDB server for human MHC-II alleles was used. Hence the epitopes

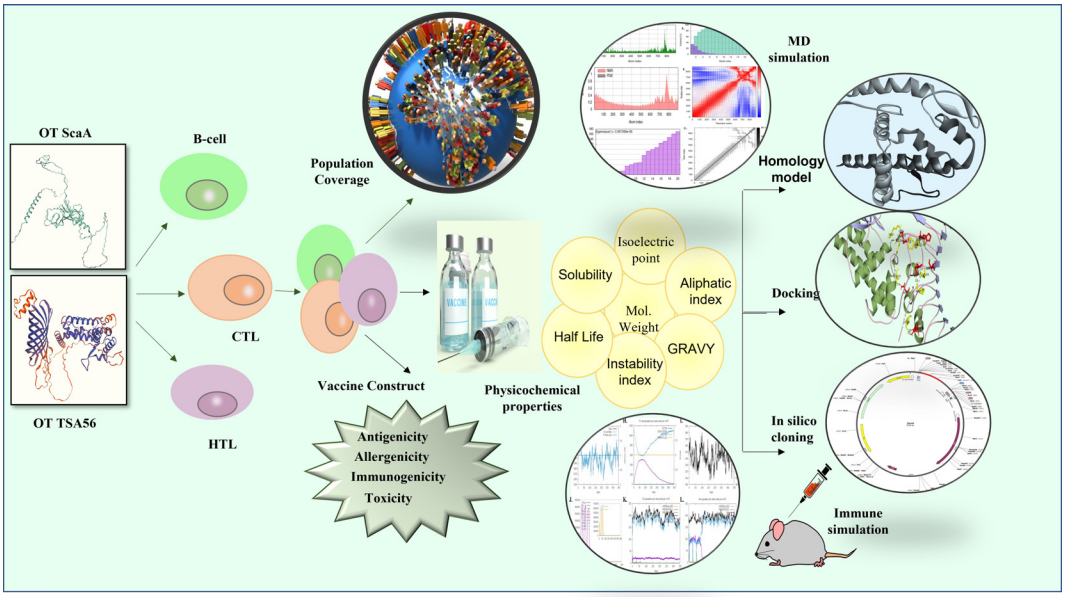

FIGURE 1
The complete hierarchy of the steps for the multi-epitope vaccine design used in the current study.

TABLE 1 B cell epitopes prediction for scrub typhus vaccine construct.

Sequence	Start position	Score	Predicted Antigenicity	Score	Predicted Allergenicity	ToxinPred Prediction
SAEVEVGKGK	100	0.78	Antigen	1.7382	Non allergen	Non-toxin
TGAESTRLDS	47	0.57	Antigen	2.0162	Non allergen	Non-toxin

TABLE 2 Shortlisted CTL epitopes for the final vaccine construct.

CTL	Peptide	Start	MHC	Affinity	Score	Predicted Allergenicity	Predicted Immunogenicity	Predicted Toxicity
TSA 56	KLQRHAGVK	375	HLA-A*03:01	28.15	1.0316	Non-allergen	0.13553	Non- toxin
	IYAGVGAGL	448	HLA-A*24:02	428.41	0.9248	Non-allergen	0.17172	Non- toxin
	ASVGVRYNF	516	HLA-B*58:01	84.91	1.8822	Non-allergen	0.12952	Non- toxin
ScaA	IFFTTLFTI	10	HLA-A*24:02	78.24	0.8279	Non allergen	0.2259	Non-toxic
	PTVGVRHSY	1378	HLA-A*26:01	1292.11	1.268	Non allergen	0.06706	Non-toxic
	SKFGGGNSL	741	HLA-B*39:01	40.78	1.3881	Non allergen	0.03488	Non-toxic

that had an SMM align IC50 value less than 50 and a percentile rank of 1 or lower were chosen. Based on the low percentile rank and a strong affinity concerning all the HLA supertypes, the epitopes YSINPLMASVGVRYN and RKRFKLTPPQPTIMP were appointed for consideration in the vaccine design (Table 3). All the candidate epitopes that passed the screening process were antigenic, non-allergen, and non-toxic.

3.3 Designing of vaccine construct and evaluation

Six CTLs, two HTLs, and two BCLs were used to create the final chimeric vaccine. EAAAK peptide linker is used to connect the N-terminus of the vaccine model to cholera toxin subunit B (ACO36766.1) adjuvant, and KK, AAY, GPGPG linkers are used

TABLE 3 Selected HTL epitopes for the final vaccine construct.

Alleles	Start	Peptide	ic50	Score	Predicted Allergenicity	Predicted Toxicity
HLA-DRB1*01:01 HLA-DRB1*13:02 HLA-DRB1*07:01 HLA-DRB1*09:01 HLA-DRB1*12:01 HLA-DRB1*03:01 HLA-DRB5*01:01 HLA-DRB1*15:01 HLA-DQA1*05:01/DQB1*03:01 HLA-DRB3*02:02 HLA-DRB1*11:01 HLA-DQA1*01:02/DQB1*06:02 HLA-DRB4*01:01 HLA-DRB1*08:02 HLA-DRB1*04:05 HLA-DPA1*03:01/DPB1*04:02 HLA-DRB1*04:01 HLA-DPA1*01:03/DPB1*04:01 HLA-DQA1*04:01/DQB1*04:02 HLA-DPA1*02:01/DPB1*01:01 HLA-DPA1*01:03/DPB1*02:01 HLA-DPA1*02:01/DPB1*14:01 HLA-DQA1*05:01/DQB1*02:01	509	YSINPLMASVGVRYN	7.6	1.0399	non-allergen	Non-toxin
HLA-DRB1*01:01 HLA-DRB1*04:05 HLA-DRB3*02:02	129	RKRFKLTPPQPTIMP	8.3	1.0248	non-allergen	Non-toxin

(Continued)

TABLE 3 Continued

Alleles	Start	Peptide	ic50	Score	Predicted Allergenicity	Predicted Toxicity
HLA-DRB1*07:01 HLA-DRB1*09:01 HLA-DRB5*01:01 HLA-DPA1*02:01/DPB1*14:01 HLA-DRB1*13:02 HLA-DRB1*11:01 HLA-DRB4*01:01 HLA-DRB1*04:01 HLA-DPA1*02:01/DPB1*01:01 HLA-DRB1*08:02 HLA-DQA1*05:01/DQB1*03:01 HLA-DRB3*01:01 HLA-DPA1*03:01/DPB1*04:02 HLA-DPA1*01:03/DPB1*04:01 HLA-DRB1*15:01 HLA-DRB1*03:01 HLA-DRB1*12:01						

to separate each BCL, CTL, and HTL epitopes respectively (Figure 2). The physicochemical property of the multi subunit vaccine is depicted in Supplementary Table 1.

3.4 Prediction and assessment of vaccine homology model

PSIPRED was used to make predictions about the secondary structure of the final vaccine construct based on its amino acid sequence (Supplementary Figure 1). It was found that the protein structure consists of 44.87% alpha helices, 26.24% random coils, 21.67% extended strands, and 7.22% beta turns. Robetta server created a 3D model of the vaccine construct (Figure 3), and model-2 was chosen merely because it had the greatest TMscore. If the TM-score was more than 0.5, signifying the model has been calibrated; the score was from 0 to 1. Using GalaxyRefine2, we were able to refine the projected 3D structure. The following factors were considered while selecting the optimal model for further study; Rama favored 95.5; RMSD, 0.327; GDT-HA, 0.98; Mol probability, 1.75; Clash score, 8.0; Poor rotamer, 0.5. When compared to the initial structure created by the Robetta server, an examination of the Ramachandran Plot of the refined protein acquired by GalaxyRefine indicated improved findings. Similarly, the model obtained via GalaxyRefine exhibits superior stereochemical quality as determined by further structural validation methods like ERRAT (92.43%) and verify 3D (81.73%) shown in Supplementary Figure 2.

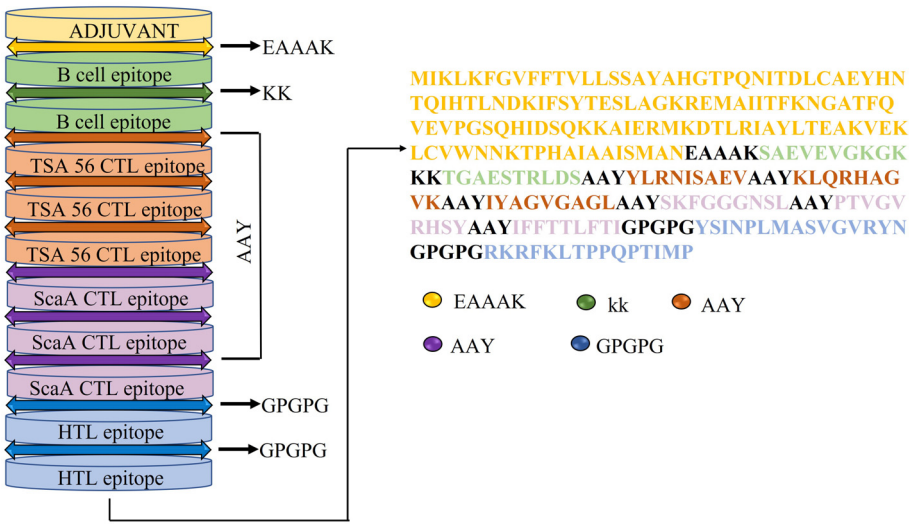

FIGURE 2
Schematic representation of the final vaccine construct that includes adjuvant, LBL, CTL, and HTL epitopes shown in different colors (top to bottom) linked by EAAAK, KK, AAY, GPGPG linkers respectively.

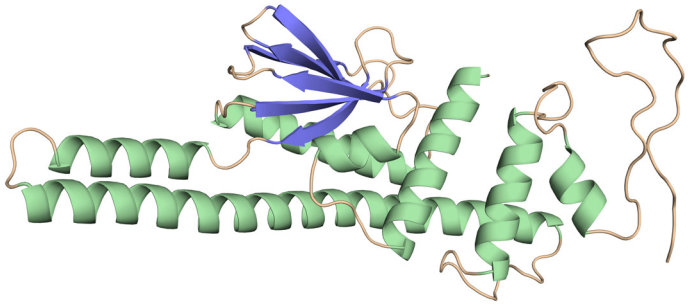

FIGURE 3
Tertiary structure of the vaccine construct.

3.5 mRNA structure

As the secondary structure of mRNA plays a crucial role in translation initiation, elongation, and mRNA synthesis, its prediction is of paramount importance. Using the Mfold web server, the free energy associated with the whole mRNA structure was calculated. As shown in Supplementary Figure 3, the secondary RNA structure has a minimum free energy of G= 105.27 kcal/mol. This value represents the proteins' host-based stability and translation efficiency. Enhanced mRNA stability correlates with a higher rate of expression.

3.6 Cluster prediction of MHC alleles

MHCcluster 2.0, a web-based program, analyzed clusters of MHC-I and MHC-II alleles that may interact with the projected epitopes. Phylogenetic allele groupings are automatically generated by the program. The results of the experiments are depicted in Supplementary Figure 4, where the red areas denote particularly robust interactions and yellow areas, relatively weak interactions.

3.8 Discontinuous B-cell epitope analysis

The discontinuous or conformational B-cell epitopes in the engineered vaccines were predicted using the Ellipro tool from the IEDB database with the basic parameters (maximum distance 6 Å and minimum score 0.5). The improved Thornton technique employing the residues clustering algorithm is the basis of these findings. As demonstrated in Figure 4 and Table 4, the prediction is

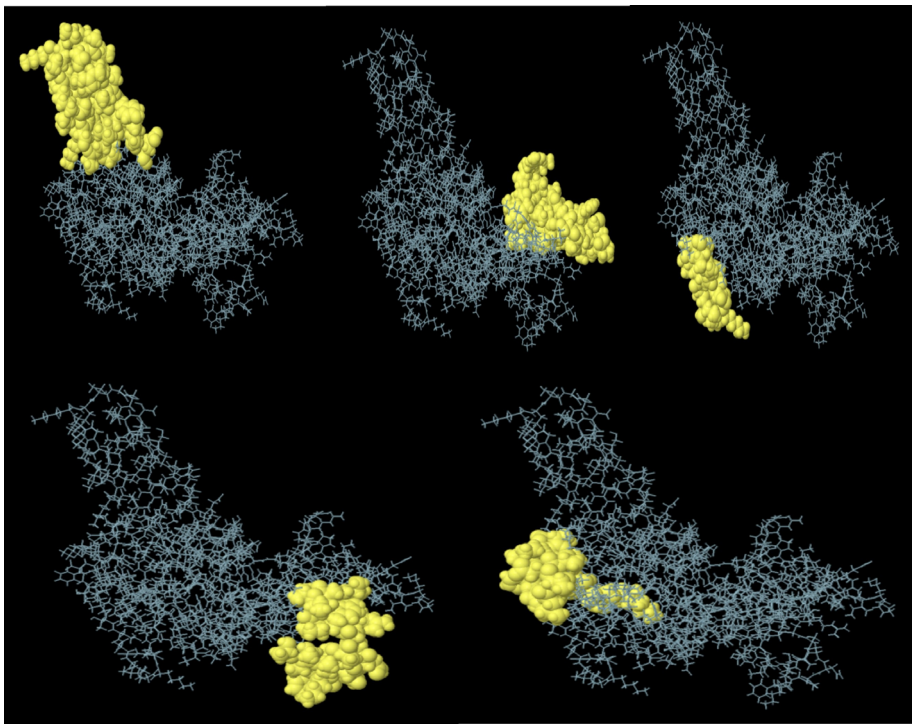

FIGURE 4
Conformational B-cell epitopes present in the vaccine where the light yellow spheres show the epitopes.

10.3389/fimmu.2025.1513245

TABLE 4 Predicted conformational B-cell epitopes of the constructed vaccine.

Number	Rresidues	No. of residues	Score
1	N124, A126, A127, A128, K129, S130, A131, E132, V133, E134, V135, G136, K137, G138, K139, K140, K141, T142, G143, A144, E145, S146, T147, R148, L149, D150, S151, A152, A153, Y154, Y155, L156, R157, N158, I159, E162	36	0.787
2	G224, P225, G226, P227, G228, Y229, S230, I231, N232, P233, L234, M235, A236, S237, V238, G239, V240, R241, Y242, N243, G244, P245, G246, P247, G248, R249, K250, F252, K253, L254, T255, P256, P257, Q258, P259, T260, I261, M262, P263	39	0.787
3	Y48, T49, E50, S51, L52, A53, G54, K55, R56, E57, M58, I60, R94	13	0.732
4	A185, A188, A189, S191, K192, F193, G194, G195, G196, N197, S198, L199, A200, A201, Y202, P203, T204, V205, G206, V207, R208	21	0.699
5	D43, K44, F46, S47, T62, K64, N65, G66, A67, T68, Y97, L98, T99, E100, A101, K112, T113, P114	18	0.589

made by taking into account the residual protein index (PI), neighbor residue clustering, and protein shape.

3.9 Disulfide bond engineering

By using certain geometric conformations, disulfide engineering was used to stabilize the vaccine construct. It was projected that 60 pairs of amino acid residues may create a disulfide bond through the DbD3 server. Two of them TYR18- ALA176, and CYS107-ALA118, which were substituted by cysteine residues, could form disulfide bonds after being assessed by $\chi 3$ and Beta-factor energy parameters (Figure 5). Based on the chi3 value of -73.37 and – 85, the energy values are 2.45 and 2.41, respectively.

3.10 Conservancy analysis and population coverage of vaccine construct

To create a universal broad-spectrum vaccination, conserved epitopes against many strains are required. Epitope conservation study about the other OT variants was performed using the IEDB conservation analysis program. All BCL, CTL, and HTL epitopes demonstrated 100% conservation at a sequence identity threshold >60%. Each of the six CD8+ (CTL) and two CD+ (HTL) epitopes was assigned to an allele by the MHC-I and MHC-II prediction server at IEDB. Hence the best binders for the population coverage study were chosen from alleles with IC50 values below 50. In a global examination of MHC-I and MHC-II epitope coverage, an average coverage of 94.35% was found. On the other hand, combining MHC-I and MHC-II epitope coverage was highest in Europe (96.36%), East Asia (94.44%), West Indies (86.52%), Oceania (85.50%), and South Asia (85.50%) shown in Figure 6.

3.11 Molecular docking

The assimilation of bacterial proteins and their stimulation of interferon and interleukin production in the immune system defense against infections are largely controlled by Toll-like receptors. The ability of the engineered vaccination to bind to the human Toll-like receptor was investigated in the current study. The interaction between the immune cells and the vaccine component is essential for the development of a robust immune response. ClusPro generates 30 unique clusters with increased interaction energies. The first cluster, with the lowest energy value (-1079.2 Kcal/mol) was chosen for further study. Table 5 lists the nine residues in the vaccine TLR-2 docked complex that form hydrogen bonds with one another (Figure 7).

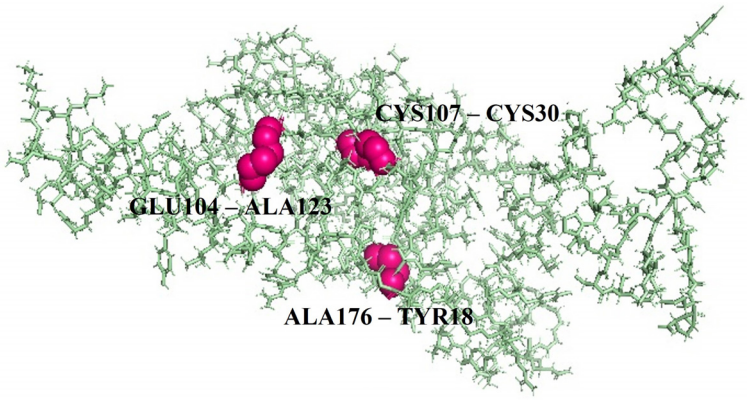

FIGURE 5
Figure showing the mutant form of vaccine construct by disulfide bond engineering for stability where three pairs of amino acids are represented in pink color.

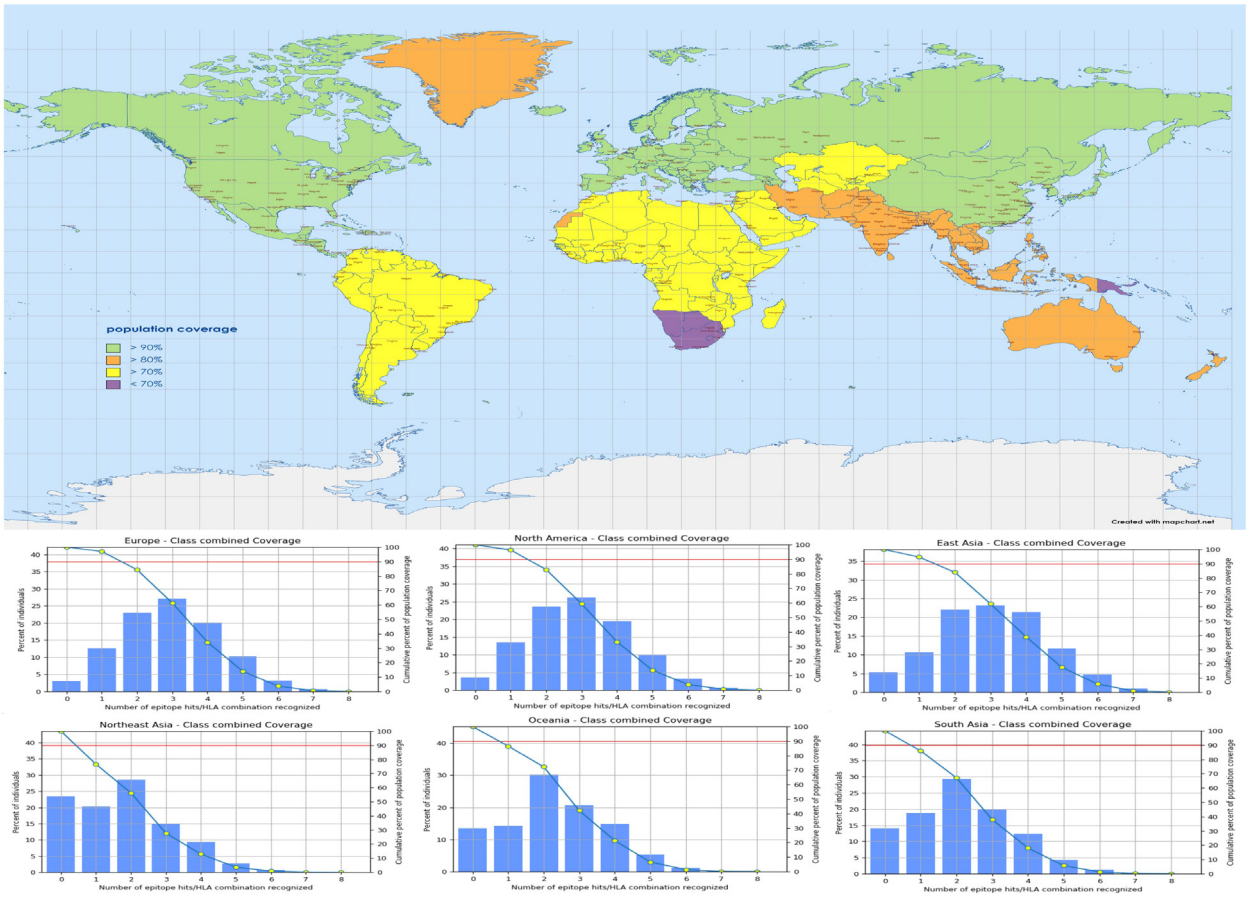

FIGURE 6
The map represents the worldwide population coverage with combined MHC epitopes based on their respective HLA binding alleles.

3.12 MD simulation of vaccine-receptor docking complex

As an input for the MD simulation, the best molecular docking complex was chosen. The complex was then subjected to a 50ns MD simulation, with the analysis focusing on key metrics such as root mean square deviation (RMSD), root mean square fluctuation (RMSF), the number of hydrogen bonds (H-bonds), and radius of gyration (Rg). The average RMSD of the receptor-vaccine combination, calculated for all atoms was 0.45 (Figure 8). As a result of these favorable interactions, a persistent vaccine-receptor complex may develop. The RMSF describes the residue-by-residue dynamics of a protein about its starting location. The RMSF of the protein atoms was analyzed to determine the conformational behavior of the ligand-receptor complex at the residual level. The average RMSF value was 0.26nm (Figure 8). Hydrogen bond interaction plays an essential role in both protein structural stabilization and protein-ligand identification. H-bond formation in the vaccine-receptor complex was also studied using MD simulation to shed light on the possibility of selective intermolecular interactions and the specificity of interactions. On average, nine H-bonds were formed in the vaccine-receptor complex (Figure 8). During the simulation, the average radius of gyration (Rg) for the vaccine-TLR2 complex was determined to be 3 nm. The findings demonstrated that the complex's compactness is enhanced after positive contact between the vaccine protein and the TLR-2 receptor.

TABLE 5 Results of the molecular docking analysis of the selected epitopes with TLR2 receptor interaction.

TLR-2	Vaccine	Distance
ARG400	ILE261	1.9
ASN376	THR219	2.1
LYS347	PRO257	1.8
LYS347	THR255	1.7
ASN345	THR255	2.8
HIS318	PHE252	1.9
ASP327	LYS3	1.8
ASP327	MET1	2.1
SER329	MET1	2.6

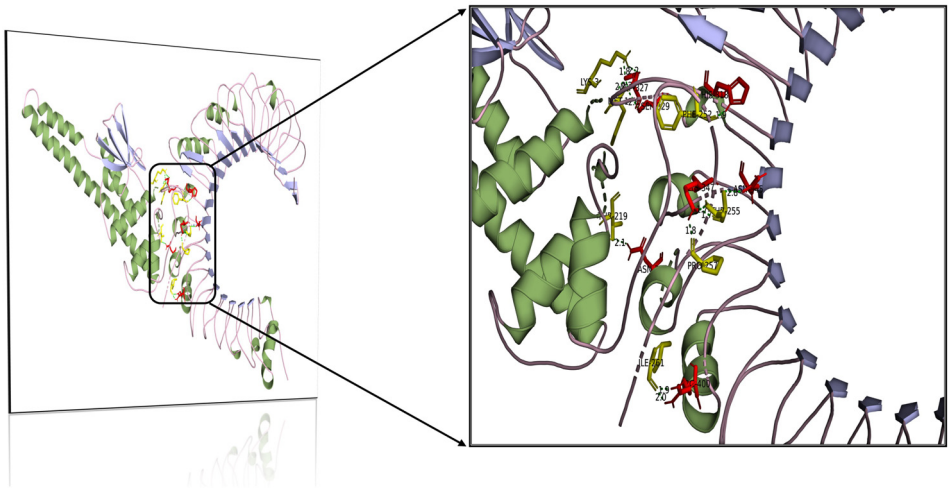

FIGURE 7
Molecular interaction of multi-epitope vaccine construct docked with TLR-2.

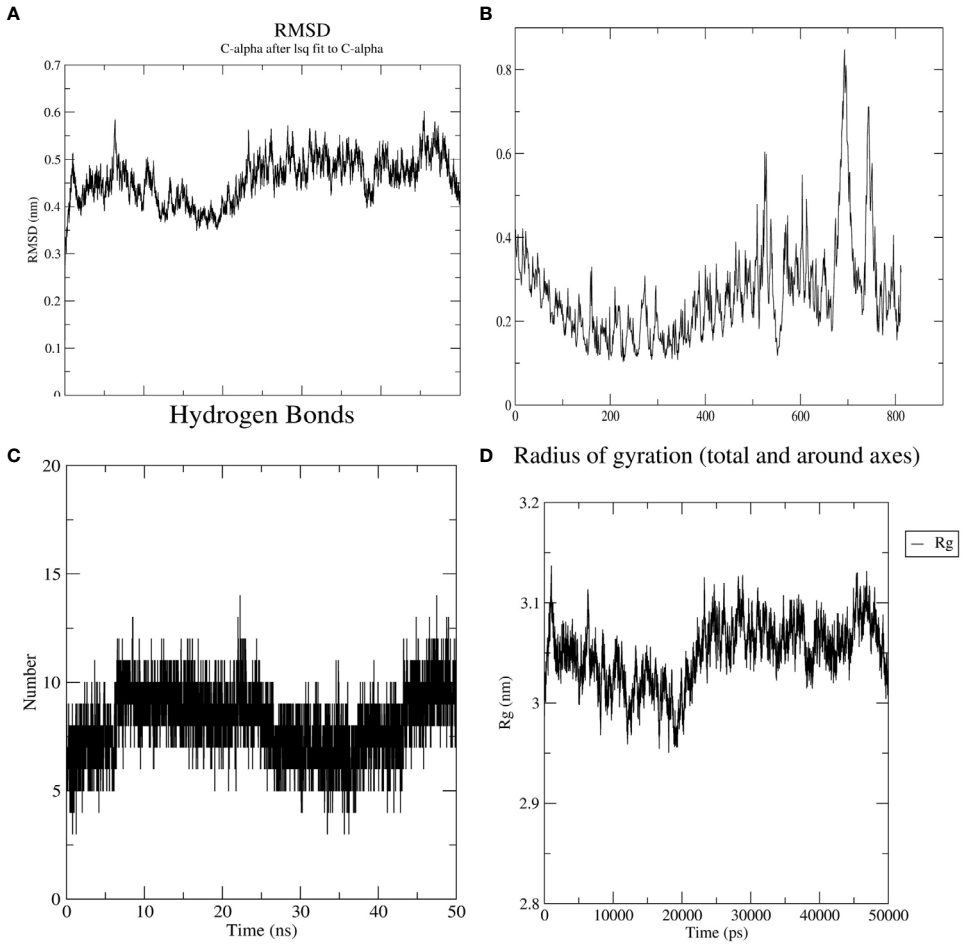

FIGURE 8
The MD simulation plot represents the interaction and the stability of the atoms and molecules between vaccine construct and TLR2 **(A)** root mean square deviation (RMSD) of the receptor–ligand complex shows infinitesimal deviation and becomes stable at the period of 6 ns, **(B)** Root mean square fluctuation plot (RMSF) representing the fluctuation of side chain residues. **(C, D)** Pressure and temperature plots concerning the time.

3.13 Codon optimization and in silico cloning

The serological analysis is the first stage in inspecting a vaccine candidate, and this needs the expression of the vaccine in an appropriate expression system. As an expression system, we settled on *E. coli* optimized cloning, and expression in the *E. coli* K12 strain is made easier with the help of the Java Codon adaptation tool (JCAT). The GC content of the modified sequence was predicted to be 50.19, and the codon adaptation index (CAI) was 0.97. Codon use in the optimal multi-epitope vaccine gene is depicted graphically in Figure 9. To execute in silico cloning, restriction enzyme sites were screened in the codon-optimized vaccine construct sequence; HindIII and BamHI were added at the N and C-terminals. After inserting the vaccine construct into pET-28a (+) vector, the functional clone was 6139bp (Figure 9).

3.14 Immune simulation

The immune simulation for the designed vaccine was conducted using the C-ImmSim server. This server models the immune response generated by key mammalian immune components, including the thymus (T cells), bone marrow (lymph and bone marrow cells), and lymphoid organs. The simulation results provide valuable insights into the potential immunogenicity of the vaccine and the type of immune response it might elicit in humans. After each of the three vaccination injections, the modeling research predicted that the major immune response to the antigenic pieces would expand dramatically, as seen by the gradual increase in concentrations of different immunoglobulins. Once again, it was demonstrated that primary immunological activation boosted subsequent immune responses. The immune simulation study was conducted for the vaccine complexes to explore the generation of adaptive immunity and also the immune interactions. The immune simulation study illustrated that after every injection dose, the primary immune response was increased significantly as gradual elevation or decrease rates of the different immunoglobulins were observed. Moreover, the secondary immune response was also increased (Figure 10A). The increasing rate of active B-cells (Figures 10B, C), plasma B-cell (Figure 10D), helper T-cells (Figures 10E, F), and regulatory and cytotoxic T-cells (Figures 10G–I) was observed. The vaccine protein was also capable of forming a vast number of different types of cytokines. Figure 10J shows the concentration of different cytokines and interleukins. These results indicated after every injection, a strong secondary immune response, increasing clearance of antigens, and strong immune memory generation occur. Moreover, good antigen presentation was also observed by these antigen-presenting cells from dendritic cell and macrophage cell concentrations (Figures 10K, L).

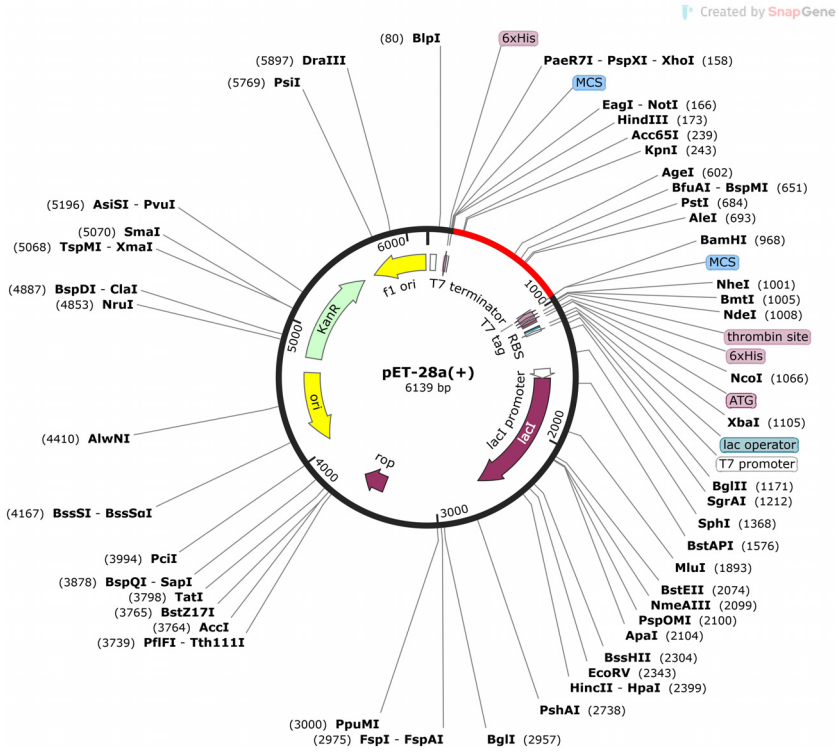

FIGURE 9
Restriction cloning of final multi-epitope vaccine by using pET28a (+) expression vector in the *in silico* space. The black circle indicates the vector and the red part is the place where the vaccine is inserted.

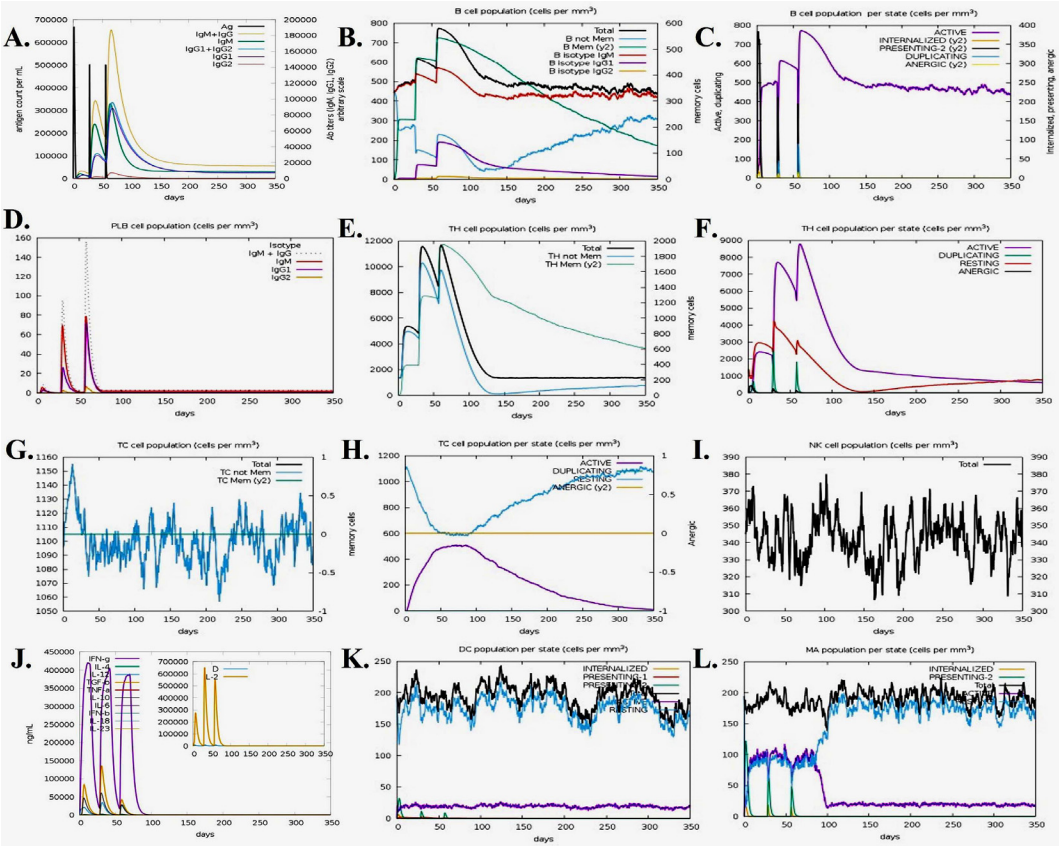

FIGURE 10
Immune simulation of the predicted vaccine; **(A)** Immunoglobulin and immune complex response to the antigen, **(B)** B lymphocyte population count, **(C)** B lymphocyte population per entity state, **(D)** plasma B lymphocyte count, **(E)** CD4 T helper lymphocyte count, **(F)** CD4 helper lymphocyte count by entity state, **(G)** CD8 T-cytotoxic lymphocyte count, **(H)** CD8 T-cytotoxic lymphocyte count per entity state, **(I)** natural killer cell population, **(J)** different cytokine and interleukin concentration, **(K)** dendritic cells per state and **(L)** macrophage population per state.

4 Discussion

Immunotherapy has emerged as a leading method for combating infectious diseases and saving lives. Bioinformatics, vaccinomics, and immunoinformatics are the new methodologies and technologies used in vaccine production that reduce the time and resources required to create a vaccine (43). Potential negative aspects of conventional vaccine production techniques include challenges with adequate culture of the microorganisms and undesirable immune responses arising from improper attenuation. The scientific community has generally warmed up to these software and database techniques (44, 45). As a result of this, research took advantage of the widely used in silico-based methodologies to build possible vaccines against *O. tsutsugamushi* for combating Scrub typhus disease. Antigens of *O. tsutsugamushi* that promote both humoral and T cell-mediated defense would be ideal for vaccination against scrub typhus. Another possibility that can be developed and evaluated is a multiplex subunit vaccine that induces substantial humoral and T cell-mediated protection.

To the greatest extent of our understanding, this is the first paper to detail the *in silico* development of a multi-epitope vaccine against scrub typhus. Antigenic epitopes from two surface-exposed highly pathogenic proteins like TSA56 and ScaA were used to create the vaccine design. According to research by Ha NY et al., ScaA acts as an adhesion factor for bacteria and an anti-ScaA antibody effectively blocks bacterial infection of host cells. When coupled with TSA58, a key outer membrane protein of *O. tsutsugamushi*, immunization with ScaA not only offers considerable protection against heterogeneous strains but additionally confers immunity against fatal challenges with the homologous strain (17). Supplementary Table 2 Provides the servers used in the analysis.

Another important immune cell is the CD4+ T cell (HTL), which may switch between the Th1 and Th2 phenotypes to elicit different types of immunological responses (46). The Th1 response stimulates the production of CD8+ T cells, natural killer cells, and macrophages. Antibody synthesis and the elimination of external pathogens are hallmarks of the Th2 immune response (47), which is involved in the activation of B cells, the differentiation of B cells, affinity maturation, and antibody production. The vaccine was docked with the TLR-2 receptor to evaluate the significance of the immune response it might produce. Finally, MD simulation was performed on the docked vaccine-receptor complex up to 50ns to

verify the stability of the interaction. The expression of the vaccine construct in the *E. coli* K12 host strain was studied by in silico cloning. The results of the immunological simulation showed that a high level of antibacterial cytokines, as well as humoral and innate immune responses, may be triggered by employing this multi-epitope vaccine. It might therefore be a promising vaccine candidate similar to a comparable multi-epitope vaccine against Pseudomonas infection (9). Finally, this multi-epitope construct certainly contributes to the future development of a broad-spectrum peptide vaccine against *O. tsutsugamushi* bacteria. Vaccine research has shifted its focus in recent years to utilize novel platforms such as virus-like particles (VLPs), DNA, and messenger RNA (48, 49). However, with high production costs and limited manufacturing yield, VLPs do not prefer mammalian expression systems for subunit vaccines (50). When it comes to DNA vaccines, however, adenoviral vectors have been the focus of a great deal of research and extensively evaluated (51, 52).

5 Conclusion

In conclusion, there has been a lack of successful strategy in developing a vaccine for 80 years. Insufficient knowledge of immunity to *O. tsutsugamushi*, in particular the criteria for vaccine-induced immunity, limited understanding of immunological memory in scrub typhus, and a failure to address the issue of cross-protection between strains, all contributed to the failure of previous efforts. In sum, our results backed up the ability of the construct to govern promising immune responses against this infectious disease, and this next-generation strategy offered a fresh perspective on creating a highly immunogenic vaccine for scrub typhus.

Data availability statement

The original contributions presented in the study are included in the article/Supplementary Material, further inquiries can be directed to the corresponding author/s.

Author contributions

SP: Methodology, Software, Validation, Writing – original draft, Writing – review & editing. SS: Conceptualization, Data curation, Supervision, Writing – original draft. BS: Data curation, Methodology, Visualization, Writing – review & editing, Writing – original draft. SM: Formal analysis, Software, Validation, Writing – review & editing. JD: Formal analysis, Validation, Visualization, Writing – review & editing. RS: Conceptualization, Validation, Writing – review & editing. AR: Conceptualization, Funding acquisition, Project administration, Writing – review & editing. NM: Supervision, Visualization, Writing – review & editing.

Funding

The author(s) declare that no financial support was received for the research, authorship, and/or publication of this article.

Acknowledgments

The authors would like to acknowledge Siksha O Anusandhana (deemed to be) University to provide the PhD fellowship.

Conflict of interest

The authors declare that the research was conducted in the absence of any commercial or financial relationships that could be construed as a potential conflict of interest.

Generative AI statement

The author(s) declare that no Generative AI was used in the creation of this manuscript.

Publisher's note

Supplementary material

The Supplementary Material for this article can be found online at: https://www.frontiersin.org/articles/10.3389/fimmu.2025.1513245/full#supplementary-material

SUPPLEMENTARY FIGURE 1
Prediction of the secondary structure of the multi-epitope vaccine construct.

SUPPLEMENTARY FIGURE 2
(A) Ramachandran plot for the validation of the designed structure **(B, C)** Quality assessment by ERRAT and Verify 3D.

SUPPLEMENTARY FIGURE 3
Prediction of RNA secondary structure of vaccine construct gene by Mfold.

SUPPLEMENTARY FIGURE 4
MHC cluster analysis tree map and heat map of both MHC-I and MHC-II epitopes.

References

1. Xu G, Walker DH, Jupiter D, Melby PC, Arcari CM. A review of the global epidemiology of scrub typhus. *PloS Negl Trop Dis*. (2017) 11:e0006062. doi: 10.1371/journal.pntd.0006062

2. Paris DH, Stephan F, Bulder I, Wouters D, van der Poll T, Newton PN, et al. Increased nucleosomes and neutrophil activation link to disease progression in patients with scrub typhus but not murine typhus in Laos. *PloS Negl Trop Dis*. (2015) 9: e0003990. doi: 10.1371/journal.pntd.0003990

3. Blacksell SD, Tanganuchitcharnchai A, Nawtaisong P, Kantipong P, Laongnualpanich A, Day NP, et al. Diagnostic accuracy of the InBios scrub typhus detect enzyme-linked immunoassay for the detection of IgM antibodies in northern Thailand. *Clin Vaccine Immunol*. (2016) 23:148–54. doi: 10.1128/CVI.00553-15

4. Luce-Fedrow A, Lehman ML, Kelly DJ, Mullins K, Maina AN, Stewart RL, et al. A review of scrub typhus (Orientia tsutsugamushi and related organisms): then, now, and tomorrow. *Trop Med Infect Dis*. (2018) 3:8. doi: 10.3390/tropicalmed3010008

5. Lin FH, Chou YC, Chien WC, Chung CH, Hsieh CJ, Yu CP. Epidemiology and risk factors for notifiable scrub typhus in Taiwan during the period 2010-2019. *Healthc (Basel)*. (2021) 9:1619. doi: 10.3390/healthcare9121619

6. Zhang Y, Zhang M, Qin Y, Zhang L, Kang D, Wei R, et al. Epidemiological analysis and risk prediction of scrub typhus from 2006 to 2021 in Sichuan, China. *Front Public Health*. (2023) 11:1177578. doi: 10.3389/fpubh.2023.1177578

7. Karch CP, Burkhard P. Vaccine technologies: From whole organisms to rationally designed protein assemblies. *Biochem Pharmacol*. (2016) 15:120. doi: 10.1016/j.bcp.2016.05.001

8. Xu Y, Zhu F, Zhou Z, Ma S, Zhang P, Tan C, et al. A novel mRNA multi-epitope vaccine of Acinetobacter baumannii based on multi-target protein design in immunoinformatic approach. *BMC Genomics*. (2024) 25:791. doi: 10.1186/s12864-024-10691-7

9. Dey J, Mahapatra SR, Patnaik S, Lata S, Kushwaha GS, Panda RK, et al. Molecular characterization and designing of a novel multiepitope vaccine construct against Pseudomonas aeruginosa. *Int J Pept Res Ther*. (2022) 28:49. doi: 10.1007/s10989-021-10356-z

10. Farhani I, Nezafat N, Mahmoodi S. Designing a novel multi-epitope peptide vaccine against pathogenic Shigella spp. based immunoinformatics approaches. *Int J Pept Res Ther*. (2019) 25:541–53. doi: 10.1007/s10989-018-9698-5

11. Ghosh P, Bhakta S, Bhattacharya M, Sharma AR, Sharma G, Lee SS, et al. A novel multi-epitopic peptide vaccine candidate against Helicobacter pylori: in-silico identification, design, cloning and validation through molecular dynamics. *Int J Pept Res Ther*. (2021) 27:1149–66. doi: 10.1007/s10989-020-10157-w

12. Bibi S, Ullah I, Zhu B, Adnan M, Liaqat R, Kong WB, et al. In silico analysis of epitope-based vaccine candidate against tuberculosis using reverse vaccinology. *Sci Rep*. (2021) 11:1249. doi: 10.1038/s41598-020-80899-6

13. Yang X, Yu X. An introduction to epitope prediction methods and software. *Rev Med Virol*. (2009) 19:77–96. doi: 10.1002/rmv.v19:2

14. Yi JZ, Liu MQ, Zhu CZ, Zhang Q, Sheng ZT, Du QY, et al. Recombinant bivalent vaccine against foot-and-mouth disease virus serotype O/A infection in Guinea pig. *Acta Biochim Biophys Sinica*. (2004) 36:589–96. doi: 10.1093/abbs/36.9.589

15. Coban C, Kobiyama K, Aoshi T, Takeshita F, Horii T, Akira S, et al. Novel strategies to improve DNA vaccine immunogenicity. *Curr Gene Ther*. (2011) 11:479–84. doi: 10.2174/156652311798192815

16. Ha NY, Kim Y, Choi JH, Choi MS, Kim IS, Kim YS, et al. Detection of antibodies against Orientia tsutsugamushi Sca proteins in scrub typhus patients and genetic variation of sca genes of different strains. *Clin Vaccine Immunol*. (2012) 19:1442–51. doi: 10.1128/CVI.00285-12

17. Ha NY, Sharma P, Kim G, Kim Y, Min CK, Choi MS, et al. Immunization with an autotransporter protein of Orientia tsutsugamushi provides protective immunity against scrub typhus. *PloS Negl Trop Dis*. (2015) 9:e0003585. doi: 10.1371/journal.pntd.0003585

18. Ha NY, Shin HM, Sharma P, Cho HA, Min CK, Kim HI, et al. Generation of protective immunity against Orientia tsutsugamushi infection by immunization with a zinc oxide nanoparticle combined with ScaA antigen. *J Nanobiotechnol*. (2016) 14:1–2. doi: 10.1186/s12951-016-0229-2

19. Saha S, Raghava GP. Prediction of continuous B-cell epitopes in an antigen using recurrent neural network. *Proteins: Struct Funct Bioinf*. (2006) 65:40–8. doi: 10.1002/prot.21078

20. Reynisson B, Alvarez B, Paul S, Peters B, Nielsen M. NetMHCpan-4.1 and NetMHCIIpan-4.0: improved predictions of MHC antigen presentation by concurrent motif deconvolution and integration of MS MHC eluted ligand data. *Nucleic Acids Res*. (2020) 48:W449–54.

21. Doytchinova IA, Flower DR. VaxiJen: a server for prediction of protective antigens, tumour antigens and subunit vaccines. *BMC Bioinf*. (2007) 8:1–7. doi: 10.1186/1471-2105-8-4

22. Dimitrov I, Bangov I, Flower DR, Doytchinova I. AllerTOP v. 2—a server for in silico prediction of allergens. *J Mol Model*. (2014) 20:1–6. doi: 10.1007/s00894-014-2278-5

23. Gupta S, Kapoor P, Chaudhary K, Gautam A, Kumar R, Open Source Drug Discovery Consortium, et al. In silico approach for predicting toxicity of peptides and proteins. *PloS One*. (2013) 8:e73957. doi: 10.1371/journal.pone.0073957

24. Hebditch M, Carballo-Amador MA, Charonis S, Curtis R, Warwicker J. Protein–Sol: a web tool for predicting protein solubility from sequence. *Bioinformatics*. (2017) 33:3098–100. doi: 10.1093/bioinformatics/btx345

25. Gasteiger E, Hoogland C, Gattiker A, Duvaud SE, Wilkins MR, Appel RD, et al. *Protein identification and analysis tools on the ExPASy server*. Humana press (2005).

26. Zuker M. Mfold web server for nucleic acid folding and hybridization prediction. *Nucleic Acids Res*. (2003) 31:3406–15. doi: 10.1093/nar/gkg595

27. Thomsen M, Lundegaard C, Buus S, Lund O, Nielsen M. MHCcluster, a method for functional clustering of MHC molecules. *Immunogenetics*. (2013) 65:655–65. doi: 10.1007/s00251-013-0714-9

28. Vita R, Mahajan S, Overton JA, Dhanda SK, Martini S, Cantrell JR, et al. The immune epitope database (IEDB): 2018 update. *Nucleic Acids Res*. (2019) 47:D339–43. doi: 10.1093/nar/gky1006

29. Bui HH, Sidney J, Dinh K, Southwood S, Newman MJ, Sette A. Predicting population coverage of T-cell epitope-based diagnostics and vaccines. *BMC Bioinf*. (2006) 7:1–5. doi: 10.1186/1471-2105-7-153

30. Buchan DW, Jones DT. The PSIPRED protein analysis workbench: 20 years on. *Nucleic Acids Res*. (2019) 47:W402–7. doi: 10.1093/nar/gkz297

31. Kim DE, Chivian D, Baker D. Protein structure prediction and analysis using the Robetta server. *Nucleic Acids Res*. (2004) 32:W526–31. doi: 10.1093/nar/gkh468

32. Lee GR, Won J, Heo L, Seok C. GalaxyRefine2: simultaneous refinement of inaccurate local regions and overall protein structure. *Nucleic Acids Res*. (2019) 47: W451–5. doi: 10.1093/nar/gkz288

33. Laskowski RA, MacArthur MW, Moss DS, Thornton JM. PROCHECK: a program to check the stereochemical quality of protein structures. *J Appl Crystallogr*. (1993) 26:283–91. doi: 10.1107/S0021889892009944

34. Waterhouse A, Bertoni M, Bienert S, Studer G, Tauriello G, Gumienny R, et al. SWISS-MODEL: homology modelling of protein structures and complexes. *Nucleic Acids Res*. (2018) 46:W296–303. doi: 10.1093/nar/gky427

35. Colovos C, Yeates TO. Verification of protein structures: patterns of nonbonded atomic interactions. *Protein Sci*. (1993) 2:1511–9. doi: 10.1002/pro.5560020916

36. Eisenberg D, Lüthy R, Bowie JU. [20] VERIFY3D: assessment of protein models with three-dimensional profiles. In: *Methods in enzymology*, vol. Vol. 277. Academic Press (1997). p. 396–404.

37. Ponomarenko JV, Bui H, Li W, Fusseder N, Bourne PE, Sette A, et al. ElliPro: a new structure-based tool for the prediction of antibody epitopes. *BMC Bioinf*. (2008) 9:514). doi: 10.1186/1471-2105-9-514

38. Craig DB, Dombkowski AA. Disulfide by Design 2.0: a web-based tool for disulfide engineering in proteins. *BMC Bioinf*. (2013) 14:1–7. doi: 10.1186/1471-2105-14-S19-S1

39. Kozakov D, Hall DR, Xia B, Porter KA, Padhorny D, Yueh C, et al. The ClusPro web server for protein–protein docking. *Nat Protoc*. (2017) 12:255–78. doi: 10.1038/nprot.2016.169

40. Hess B, Kutzner C, Spoel D, van der Lindahl E. GROMACS 4: algorithms for highly efficient, load-balanced, and scalable molecular simulation. *J Chem Theory Comput*. (2008) 435–47. doi: 10.1021/ct700301q

41. Grote A, Hiller K, Scheer M, Münch R, Nörtemann B, Hempel DC, et al. JCat: a novel tool to adapt codon usage of a target gene to its potential expression host. *Nucleic Acids Res*. (2005) 33:W526–31. doi: 10.1093/nar/gki376

42. Rapin N, Lund O, Bernaschi M, Castiglione F. Computational immunology meets bioinformatics: the use of prediction tools for molecular binding in the simulation of the immune system. *PloS One*. (2010) 5:e9862. doi: 10.1371/journal.pone.0009862

43. Hasan M, Ghosh PP, Azim KF, Mukta S, Abir RA, Nahar J, et al. Reverse vaccinology approach to design a novel multi-epitope subunit vaccine against avian influenza A (H7N9) virus. *Microb Pathogen*. (2019) 130:19–37. doi: 10.1016/j.micpath.2019.02.023

44. Pandey RK, Bhatt TK, Prajapati VK. Novel immunoinformatics approaches to design multi-epitope subunit vaccine for malaria by investigating anopheles salivary protein. *Sci Rep*. (2018) 8:1125. doi: 10.1038/s41598-018-19456-1

45. Maria RR, Arturo CJ, Alicia JA, Paulina MG, Gerardo AO. The impact of bioinformatics on vaccine design and development. *Vaccines*. (2017) 2:3–6.

46. Rappuoli R, Bottomley MJ, D'Oro U, Finco O, De Gregorio E. Reverse vaccinology 2.0: Human immunology instructs vaccine antigen design. *J Exp Med*. (2016) 213:469–81. doi: 10.1084/jem.20151960

47. Purcell AW, McCluskey J, Rossjohn J. More than one reason to rethink the use of peptides in vaccine design. *Nat Rev Drug Discov*. (2007) 6:404–14. doi: 10.1038/nrd2224

48. Mosmann T, Coffman RL. TH1 and TH2 cells: different patterns of lymphokine secretion lead to different functional properties. *Annu Rev Immunol*. (1989) 7:145–73. doi: 10.1146/annurev.iy.07.040189.001045

49. Ghaderi D, Zhang M, Hurtado-Ziola N, Varki A. Production platforms for biotherapeutic glycoproteins. Occurrence, impact, and challenges of non-human sialylation. *Biotechnol Genet Eng Rev*. (2012) 28:147–76. doi: 10.5661/bger-28-147

50. Dai S, Wang H, Deng F. Advances and challenges in enveloped virus-like particle (VLP)-based vaccines. *J Immunol Sci*. (2018) 2. doi: 10.29245/2578-3009/2018/2.1118

51. Xiang K, Ying G, Yan Z, Shanshan Y, Lei Z, Hongjun L, et al. Progress on adenovirus-vectored universal influenza vaccines. *Hum Vaccines Immunother*. (2015) 11:1209–22. doi: 10.1080/21645515.2015.1016674

52. Kallel H, Kamen AA. Large-scale adenovirus and poxvirus-vectored vaccine manufacturing to enable clinical trials. *Biotechnol J*. (2015) 10:741–7. doi: 10.1002/biot.201400390

frontiers | Frontiers in Immunology

TYPE Brief Research Report
PUBLISHED 04 April 2025
DOI 10.3389/fimmu.2025.1470034

OPEN ACCESS

EDITED BY
Ousman Jobe,
Henry M. Jackson Foundation for the Advancement of Military Medicine (HJF), United States

REVIEWED BY
Larry Ellingsworth,
Novavax, Inc., United States
Hongchen Shen,
Virginia Tech, United States

*CORRESPONDENCE
Paul H. Davis
pdavis@unomaha.edu

†PRESENT ADDRESS
Mackenzie E. Conrin,
Department of Environmental Health and Safety, University of Nebraska Medical Center, Omaha, NE, United States

RECEIVED 24 July 2024
ACCEPTED 18 March 2025
PUBLISHED 04 April 2025

CITATION
Neville AJ, Conrin ME, Schulze TT and Davis PH (2025) A selective C5a-derived peptidomimetic enhances IgG response following inactivated SARS-CoV-2 immunization and confers rapid disease resolution following murine coronavirus infection.
Front. Immunol. 16:1470034.
doi: 10.3389/fimmu.2025.1470034

A selective C5a-derived peptidomimetic enhances IgG response following inactivated SARS-CoV-2 immunization and confers rapid disease resolution following murine coronavirus infection

Andrew J. Neville[1], Mackenzie E. Conrin[1†], Thomas T. Schulze[1,2] and Paul H. Davis[1*]

[1]Department of Biology, University of Nebraska at Omaha, Omaha, NE, United States, [2]Department of Pathology, Microbiology, and Immunology, University of Nebraska Medical Center, Omaha, NE, United States

The host complement system is a critical component of innate immunity and serves as a principal mechanism of pathogen defense in mammals. EP67 is an engineered decapeptide derived from the C terminus of human complement protein C5a, which displays selective immunostimulatory activity. EP67 preferentially activates phagocyte mononuclear cells but shows minimal activity towards inflammatory granulocytes, including neutrophils. Previous studies of viral infection showed that EP67 possessed antiviral efficacy when used following infection and enhanced antibody responses to antigen challenges when used as an adjuvant. Here, we show in a rodent model that immunization with inactivated γ-irradiated SARS-CoV-2 in combination with EP67 can produce elevated nucleocapsid-specific IgG antibodies compared to viral lysate alone, supporting an enhanced adaptive immune response. Additionally, intranasal administration of EP67 following infection with live MHV-A59 coronavirus resulted in a rapid health improvement in symptomatic infections compared to PBS vehicle controls. Taken together, these results suggest EP67 shows efficacy towards betacoronaviruses when used as an adjuvant during immunization or as a therapeutic during active infections. Moreover, these findings continue to support the capability of EP67 as an antiviral agent and a useful immunostimulatory peptide.

KEYWORDS

coronavirus, MHV, peptide therapeutics, adjuvant, EP67, complement pathway, C5a, SARS-CoV-2

10.3389/fimmu.2025.1470034

Introduction

The complement system is an innate immune mechanism largely conserved across mammalian species and acts against infectious agents. Components of the complement system work in an orchestrated manner to subdue pathogens. This is achieved in myriad ways, including the deposition on the target pathogen, which leads to membrane disruption or opsonization, and the recruitment of immune cells to the area of activity through complement mediators. One such mediator is the complement subunit C5a, which is produced via proteolysis of the parent C5 molecule. Human C5a is 74 amino acids in length and acts in a chemotactic manner to recruit and activate immune cells bearing the C5a receptor (1). The native C5a molecule potently induces recruitment of phagocytes, including macrophages and monocytes, and less so inflammatory granulocytes, such as neutrophils and mast cells (2). Due to its ability to recruit, activate, and induce degranulation in the latter, full-length C5a is appropriately known for its inflammatory effects.

The C5aR1/CD88 interactive peptide, EP67, is a small decapeptide derived from the C terminus of human C5a with the sequence YSFKDMP[MeL]aR where "MeL" is N-methyl leucine and "a" is D-alanine. It was designed to act as a non-inflammatory immunostimulant and immune adjuvant by selectively recruiting and activating phagocytic antigen-presenting cells whilst reducing inflammatory effects that can occur with the recruitment of granulocytic cells (3–5). EP67 has demonstrated effectiveness in murine models of viral infection, such as protection against cytomegalovirus (CMV) infection via adjuvant activity (2). The antiviral activity may be partially due to EP67's ability to promote T_H1 immune activation via the C5aR1/CD88 receptor pathway (5). Additionally, EP67 has demonstrated efficacy as additional in bacterial and viral infections (6–8). Therefore, we posited that EP67 could work in a therapeutic manner against a potent, symptomatic coronavirus infection.

In 2020, the worldwide spread of SARS-CoV-2, a betacoronavirus, led to a pandemic with high morbidity and mortality. With the relative paucity of broad-spectrum antiviral agents, vaccine approaches were primarily employed to reduce spread and attenuate the more severe effects resulting from viral infection. Several animal models exist for modeling coronavirus infections; however, access barriers such as cost, availability, and housing requirements (e.g. BSL-3 facilities) can render these impractical for many laboratories (9). The betacoronavirus, Murine Hepatitis Virus (MHV), naturally infects mice and various disease pathologies of human SARS-CoV and SARS-CoV-2 infections can be modeled *in vivo* with varied animal and MHV strains (10–12). Specifically, C57BL/6 mice inoculated intranasally with MHV strain A59 (MHV-A59) have shown acute pneumonia and lung pathology due to viral spread in the lungs and leukocyte infiltration beginning as early as 2 days post-infection (2 dpi) (12). Using this model, we administered a single dose of EP67 intranasally after the onset of symptoms (3 days post-infection; 3 dpi) to evaluate the ability of EP67 treatment to alleviate severe health decline in infected mice. Mice receiving EP67 recovered quickly compared to untreated infected mice who significantly declined in health. This suggests that EP67 could serve as an effective antiviral therapeutic against the betacoronavirus MHV. Additionally, we show that EP67 increased long-term plasma IgG nucleocapsid antibodies when coadministered with inactivated SARS-CoV-2, with a similar increase in spike protein IgG. Together, these findings further support the antiviral efficacy of EP67 with potentially broader applications to additional viral diseases.

Materials and methods

Mouse hepatitis virus A59 propagation and preparation

17Cl-1 mouse fibroblasts and MHV-A59 viral stocks were graciously donated by Stanley Perlman, University of Iowa (13). Sanger sequencing confirmed the native MHV-A59 genotype. 17Cl-1 cells were cultured and used for MHV-A59 propagation, generation of high titer stocks, and quantification of plaque forming units (PFUs), as previously described (14). Briefly, 17Cl-1 cells were cultured in High-Glucose DMEM (Lonza BioWhittaker, cat# 12614F) supplemented with 4 mM L-alanyl-L-glutamine (Corning, cat# 25-015-CI), 1X penicillin-streptomycin (Hyclone, cat# SV30010), and 10% heat-inactivated fetal bovine serum (Gibco, cat# A3840001), further referred to as DME10. High-tier stocks were generated, plaque-purified, and stored at -80°C until use. Titers of viral stocks were quantified via plaque assays using 17Cl-1 cells inoculated with serially diluted viral stocks, followed by crystal violet staining to determine the number of plaques. PFU values were calculated as previously described (14).

Plasma IgG response following EP67-adjuvanted inactivated SARS-CoV-2 immunization

8-week-old female Swiss Webster (CFW) mice were purchased from Charles River Laboratories (Wilmington, Massachusetts, USA), housed in ventilated cages with a 12-hour light/dark cycle, and given water and food *ad libitum* as approved by IACUC 20-058-03. 11-week-old female Swiss Webster (CFW) mice were anesthetized via isoflurane inhalation and received a 20 µL intranasal (IN) inoculation (10 µL/nostril). On Day 0, mice received a mixture of either PBS (control; n=6 mice) or 100 µg EP67 adjuvant (n=3 mice) and 2.66 x 10^3 PFU of inactivated, γ-irradiated SARS-CoV-2, isolate USA-WA1/2020 infected Vero E6-heACE2 cell lysates (BEI Resources, cat# NR-53910). On Day 24, both groups of mice received the same inoculum as on Day 0. On Day 42, a 5 mm Goldenrod™ Animal Lancet (MEDIpoint, cat# GR-5MM) was used to puncture and collect blood via the submandibular bleeding method (15). Blood samples were collected directly into K_2EDTA Microvette CB 300 capillary blood collection tubes (Starstedt, cat# 16.444.100). Samples were then

centrifuged at room temperature at 2,000 x *g* for 6 minutes, and the plasma-containing supernatant was pipetted into 1.5 mL Protein LoBind tubes (Eppendorf, cat# 022431081) on ice. Plasma samples were immediately transferred and stored at -140°C until analysis. No hemolysis was observed in the plasma samples.

Enzyme-linked immunosorbent assays (ELISAs) were prepared using the Antigen-Down ELISA Development Kit (ImmunoChemistry Technologies, cat# 9101). All incubations were performed under light-protected conditions. Recombinant SARS-CoV-2 Nucleocapsid (N) protein (BEI Resources, cat# NR-53797, Lot# MF14JL0301; produced by Sino Biological, cat# 40588-V08B)) and Spike (S) glycoprotein (BEI Resources, cat# NR-55614, Lot# 70045340) were diluted to 2.0 µg/mL and 1.0 µg/mL, respectively, in 1X Antigen Coating Buffer (ImmunoChemistry Technologies, cat# 6247) and 50 µL was added per well in Nunc MaxiSorp flat-bottom 96-well plates (Thermo Scientific, cat# 44-2404-21), sealed with an adhesive plate sealer (R&D Systems, cat# DY992), and incubated at 4°C for 48 hours. Plates were equilibrated to room temperature, followed by aspiration of the antigen coating solution, and each well washed twice with 350 µL/wash of 1X ELISA Wash Buffer (ImmunoChemistry Technologies, cat# 651) using an ELx50 automated microplate washer (BioTek Instruments, cat# ELX50/8). 250 µL of General Block ELISA Blocking Buffer (ImmunoChemistry Technologies, cat# 632) was added per well, and the plate was sealed and blocked for 24 hours at room temperature, followed by an additional 16 hours at 4°C. Plates were equilibrated to room temperature before block buffer was aspirated. 50 µL of mouse plasma, pre-diluted 1:500 in General Serum Diluent (ImmunoChemistry Technologies, cat# 648), was added per well, plate sealed, and incubated for 8 hours at 4°C. A positive control anti-SARS-CoV-2 Nucleocapsid Antibody, Mouse IgG (Acro Biosystems, caat# NUN-S47A1), diluted in General Serum Diluent was used at 10.0 and 0.1 ng/mL. Rabbit IgG Polyclonal Anti-SARS-Related Coronavirus 2 Spike Glycoprotein (BEI Resources, cat# NR-52947) at 1:3000 and 1:30,000 dilutions in General Serum Diluent were used as the Spike glycoprotein positive control. Plates were returned to room temperature, samples aspirated, followed by five consecutive washes of each well using 350 µL/wash. 50 µL of Peroxidase-conjugated AffiniPure Goat Anti-Mouse IgG (H+L) (Jackson ImmunoResearch Labs, cat# 115-035-146; Lot# 158821) diluted 1:5,000 (160 ng/mL) in 1X Antigen-Down HRP Conjugate Stabilizer (ImmunoChemistry Technologies, cat# 6102) was added to each well. For the Rabbit IgG polyclonal anti-Spike glycoprotein positive control detection, a 1:10,000 dilution of 0.8 mg/mL Peroxidase-conjugated AffiniPure Mouse Anti-Rabbit IgG (H+L) (Jackson ImmunoResearch Labs, cat# 211-035-109) in General Serum Diluent. The plates were sealed, and incubated for 1 hour at room temperature., The plate was washed with seven consecutive washes using 350 µL per well, with the last wash including a 60-second soak before aspiration. 75 µL of TMB 1-Component HRP Microwell Substrate (ImmunoChemistry Technologies, cat# 6276) was added to each well and incubated for 10 minutes, followed by the addition of 75 µL of Stop Solution (ImmunoChemistry Technologies, cat# 6282) per well. Plates were gently tapped to ensure complete mixing, and absorbances were measured at 450 and 570 nm using a BioTek Synergy LX microplate reader (BioTek Instruments, cat# SLXFA). The corresponding absorbance measurements were reported as optical density (OD) values in the BioTek Gen5 software version 3.09 (BioTek Instruments, Winooski, Vermont, USA). OD_{570} nm readings were subtracted from the OD_{450} nm values to correct for optical imperfection background noise and to generate the corrected OD_{450} values used for statistical analyses. Each mouse plasma sample was assayed in technical duplicates. A two-tailed unpaired t-test for statistical significance was performed using GraphPad Prism version 10.4.1. Colored symbols represent the average corrected OD_{450} of two technical replicates measurements for each mouse, and the corrected OD_{450} group mean ± SEM are displayed as long and short bars, respectively. The background signal of the assay is displayed as a horizontal dotted line.

MHV-A59 mouse infection and treatment

Male C57BL/6J mice at six weeks of age were purchased from Jackson Labs (Bar Harbor, Maine, USA), housed in ventilated cages with a 12-hour light/dark cycle, and given water and food *ad libitum* in accordance with IACUC 20-058-03. Mice acclimated for one week before beginning the study. Throughout the study, individual weights were recorded daily, and mice were inspected twice daily for signs of illness. On Day 0 (0 dpi), 7-week-old male C57BL/6J mice (n=10 per group) were exposed to isoflurane via the drop method and received an intranasal (IN) inoculation. Each mouse was administered a total volume of 20 µL (10 µL/nostril) using a p200 pipette equipped with a 200 µL tip. The inoculum consisted of either 1.1×10^6 PFU of MHV-A59 mixed with 17-Cl1 cell lysate in DME10 for the two infected groups or 17Cl-1 lysate in DME10 as a mock infection for the uninfected control group.

On Day 3 post-infection (3 dpi), mice were anesthetized using isoflurane and IN administration of 20 µL (10 µL/nostril) of either 100 µg of EP67 (5 µg/µL) in sterile 1X phosphate-buffered saline (PBS) (Fisher BioReagents, cat# BP3994) or sterile 1X PBS only for the control group. On Day 5 post-infection, a random number generator was used to remove three mice from each group to preserve tissues. To account for any weight-related changes the EP67 treatment may have produced, the lysate mock-infected EP67-treated mice constituted the non-infected control group. Two-tailed unpaired t-tests were calculated using GraphPad Prism version 10.4.1 to determine statistical significance. Colored symbols represent individual mouse weights, and the group mean ± SEM are displayed as long and short bars, respectively.

Lungs were dissected from euthanized mice at two days post-treatment (5 days post-infection; n=3 per group) and seven days post-treatment (10 days post-infection; n=4 per group) and immediately placed in 3 mL of cold RNAlater™ Stabilization Solution (Invitrogen, cat# AM7020) and placed on ice. The mouse lungs in RNAlater solution were incubated overnight at 4° C. Lungs were thawed on ice, blotted with a Kimwipe to remove residual RNAlater solution, and the mass of each mouse lung was measured using an analytical balance.

EP67 synthesis

Using HCl as the counter ion, EP67 was commercially synthesized and validated via electrospray ionization mass spectrometry by CPC Scientific Inc. (Sunnyvale, CA, USA; lot #: CQ-10-00782). Reversed-phase high-performance liquid chromatography (RP-HPLC) analysis determined a purity of 96.5%, while amino acid analysis determined the peptide content to be 88%.

Murine macrophage exposure

RAW264.7 mouse macrophages (ATCC, cat# TIB-71) were grown in a humidified incubator at 37°C and 5% CO_2, and cultured in High-Glucose DMEM (Lonza BioWhittaker, cat# 12614F) supplemented with 4 mM L-alanyl-L-glutamine (Corning, cat# 25-015-CI), 1X penicillin-streptomycin (Hyclone, cat# SV30010), and 10% heat-inactivated fetal bovine serum (Gibco, cat# A3840001). Cells were plated at 0.5 x 10^6 cells/well (3 mL media/well) in 6-well cell culture-treated plates (Thermo Scientific, cat# 130184) and incubated for 24 hours to allow for cell attachment. Media was replaced with either fresh media only (control), or fresh media containing a final concentration of the following treatments: EP67 (50 µg/mL), recombinant human complement component C5a protein (100 ng/mL) (R&D Systems, cat# 2037-C5-025/CF), or lipopolysaccharide (LPS) (1 µg/mL) (Invitrogen, cat# 00-4976-93) and incubated for 16 hours. Each condition was tested in 3 separate wells (n=3 per condition). Supernatants were collected and secreted TNF-α protein levels were determined using the ELISA MAX™ Deluxe Set Mouse TNF-α Kit (BioLegend, cat# 430904) according to the manufacturer's instructions. The supernatant from each well was assayed via ELISA in technical duplicates. A two-tailed unpaired t-test for statistical significance was performed using GraphPad Prism version 10.4.1. The group mean ± SEM of supernatant TNF-α levels are displayed.

Results and discussion

To establish the capacity of EP67 to serve as a humoral immune adjuvant to SARS-CoV-2, mice were immunized with 2.7 x 10^3 PFU

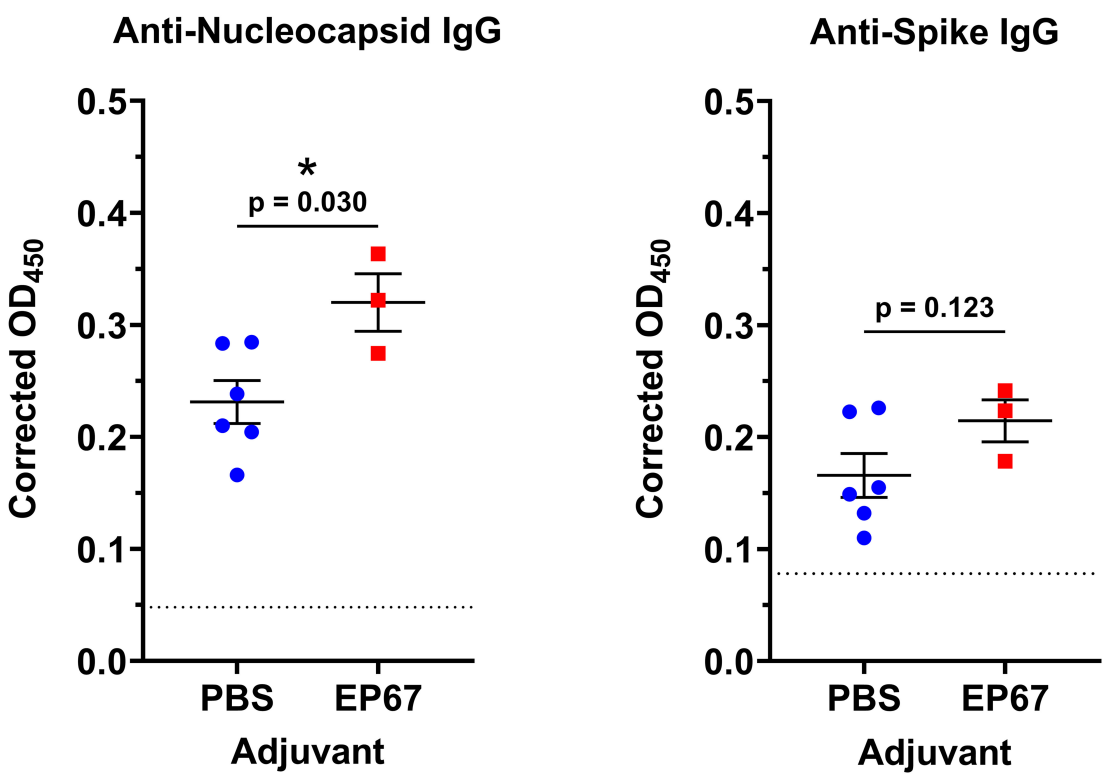

FIGURE 1
Mouse plasma anti-Nucleocapsid and anti-Spike IgG levels following intranasal immunizations with inactivated SARS-CoV-2 and adjuvant EP67. Mice received intranasal inoculations of either PBS vehicle (control; *n*=6) or 100 µg EP67 (*n*=3), co-administered with 2.7 x 10^3 PFU of γ-irradiated SARS-CoV-2 Vero cell lysate on days 0 and 24. On day 42, K_2EDTA plasma was obtained from submandibular bleeds, diluted 1:500, and an ELISA was performed to evaluate plasma IgG specific to SARS-CoV-2 Nucleocapsid (N) protein and Spike (S) glycoprotein. Mice receiving EP67-adjuvanted SARS-CoV-2 inactivated lysate demonstrated a significant increase in IgG levels toward Nucleocapsid protein, and an increase, though not significant, towards Spike glycoprotein, following immunizations compared to non-adjuvanted PBS vehicle controls. Each mouse plasma sample was tested in technical duplicates. A two-tailed unpaired t-test for statistical significance was performed using GraphPad Prism version 10.4.1. Colored symbols represent the average corrected OD_{450} of two technical replicates measurements for each mouse, and the corrected OD_{450} group mean ± SEM are displayed as long and short bars, respectively. The background signal of each assay is displayed as a horizontal dotted line. *p < 0.05.

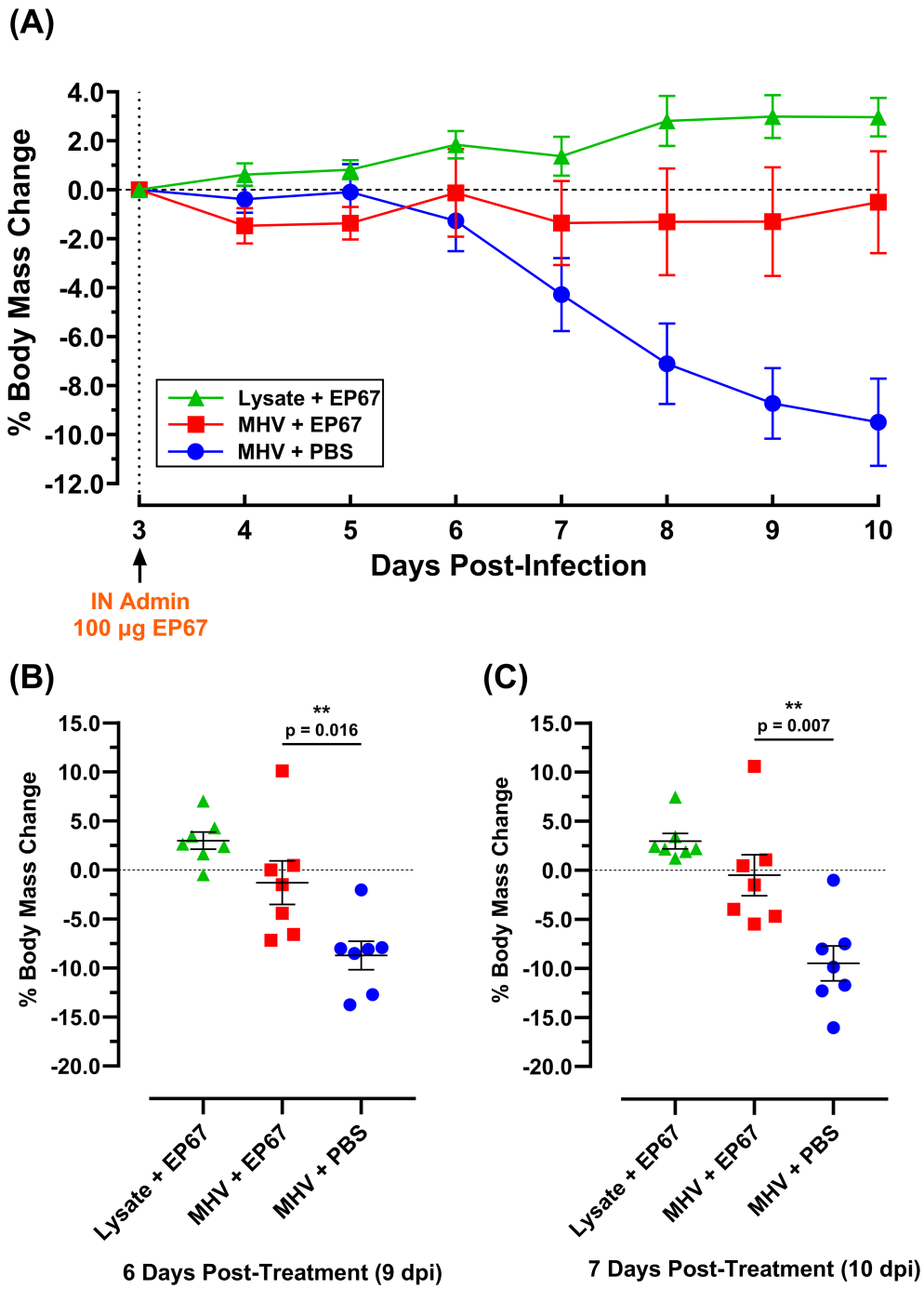

FIGURE 2
Body mass percent change of MHV-A59 infected and uninfected mice treated intranasally with PBS vehicle or immunostimulatory molecule EP67 three days post-infection. 7-week-old male C57BL/6J mice were infected intranasally (IN) with 17-Cl1 lysate containing 1.1 x 10^6 PFU of betacoronavirus MHV-A59 or mock-infected with only 17Cl-1 cell lysate as the uninfected control. Each group had an *n*=10 mice up to day 5 post-infection (5 dpi) and *n*=7 mice for the remainder of the study. Three days after infection (3 dpi), mice were intranasally administered either 100 µg EP67 dissolved in PBS or PBS vehicle alone. **(A)** EP67-treated infected mice (red) experienced a return to health and maintained body mass, while untreated infected mice (blue) declined in health and body mass. Data presented as the group mean ± SEM. **(B)** At day 9 post-infection ("9 dpi", 6 days post-treatment) and **(C)** day 10 post-infection ("10 dpi", 7 days post-treatment), infected mice that received EP67 treatment (*n*=7) had significantly more body mass than infected, untreated (PBS vehicle control) mice (*n*=7). Two-tailed unpaired t-tests were performed using GraphPad Prism version 10.4.1 to determine statistical significance. Colored symbols represent individual mouse weights, and the group mean ± SEM are displayed as long and short bars, respectively. **p < 0.05.

of γ-irradiated (inactivated) SARS-CoV-2 Vero cell lysate coadministered with either 100 μg EP67 or PBS (vehicle control group). The irradiated viral lysate was leveraged in place of infectious live virus; however, this approach limits the utilization of the T_H1 cell-mediated adaptive immune response, a known component of EP67 immune modulation (5). Nevertheless, following two immunizations spaced 24 days apart, mice receiving EP67-adjuvanted γ-irradiated SARS-CoV-2 lysate demonstrated significantly more viral nucleocapsid-specific IgG plasma antibodies compared to control mice receiving PBS and γ-irradiated SARS-CoV-2 lysate at Day 42 ($p = 0.030$). This suggests an apparent long-term, persistence in protection resulting from the immunizations at Days 0 and 24 (Figure 1).

To assess the ability of EP67 to serve as an effective treatment following the onset of illness from the related betacoronavirus Murine Hepatitis Virus (MHV), groups of 7-week-old male C57BL/6J mice were evaluated following infection. The C57BL/6 mouse strain has been previously used for infection with MHV strain A59 (MHV-A59), with disease progression correlated with observable illness and tissue pathology (12). Mouse body mass has been used extensively as a broad indicator of morbidity, and MHV infection in mice is known to significantly impact mouse health and weight loss, with higher doses proving lethal (12). In contrast, viral nucleic acid levels may persist in the tissues of animals with resolved infection for several days (16, 17). In the current study, each mouse received 1.1 x 10^6 PFU MHV-A59, or 17Cl-1 uninfected host cell lysate, delivered intranasally on day 0. By day 3 post-infection (3 dpi), infected mice demonstrated a disease state with changes in behavior associated with viral infection, in agreement with previously published observations (12). To evaluate EP67 for therapeutic treatment efficacy following initial signs of infection, 100 μg of EP67 or PBS vehicle control was delivered intranasally on day 3 post-infection, and mice were monitored daily thereafter. Infected control mice receiving PBS declined in body mass, notably from day 6 post-infection onward, while EP67-treated mice maintained their body mass from the day of treatment throughout the end of the study and rapidly increased in health (Figure 2). Symptomatically, EP67-treated mice returned to health by day 3 post-treatment (corresponding to day 6 post-infection) and resembled the uninfected EP67-treated control mice. Statistical significance in the body mass percentage loss, relative to initiation of treatment on day 3 post-infection (3 dpi), was observed for infected EP67-treated versus infected PBS control mice 6 days post-treatment (9 dpi; Figure 2B) and 7 days post-treatment (10 dpi; Figure 2C).

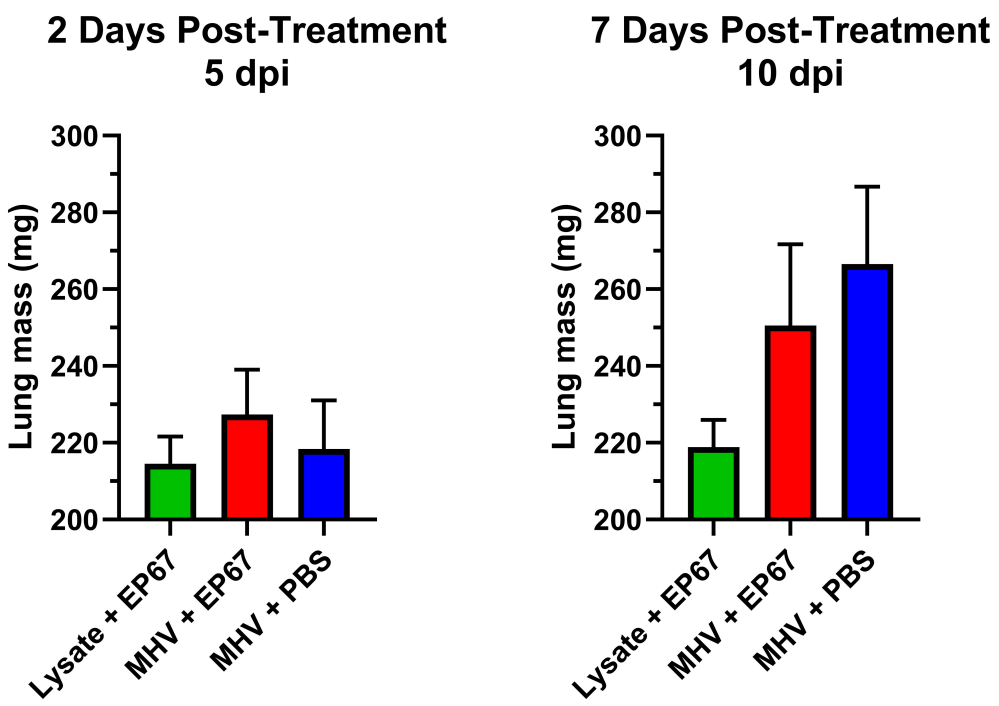

FIGURE 3
Lung masses of MHV-infected and uninfected mice treated intranasally with EP67 or PBS vehicle control. 7-week-old male C57BL/6J mice were infected intranasally (IN) with 17Cl-1 lysate containing 1.1 x 10^6 PFU of betacoronavirus MHV-A59 or mock-infected with only 17Cl-1 cell lysate as the uninfected control. Three days post-infection (3 dpi), mice were intranasally administered either EP67 (100 μg) dissolved in PBS or PBS vehicle alone (infected untreated control). Lungs were dissected from euthanized mice at two days post-treatment (n=3 per group) and seven days post-treatment (n=4 per group) and immediately placed in 3 mL preservative at 4°C overnight, briefly blotted with a Kimwipe, and the mass of each mouse lung was measured using an analytical balance. No significant difference in lung mass of the MHV-infected mice treated with EP67 versus untreated PBS vehicle was detected, though lungs from EP67-treated infected mice did show a slight increase at two days post-treatment (5 dpi) and a modest decrease compared to the infected untreated PBS control mice at seven days post-treatment (10 dpi). As expected, uninfected mice mock-infected with 17Cl-1 cell lysate alone at day 0 (0 dpi), followed by EP67 administration at 3 dpi, maintained consistent lung masses at two and seven days post-treatment. Two-tailed unpaired t-tests for statistical significance were performed and figures showing each group's mean lung mass ± SEM were generated using GraphPad Prism version 10.4.1.

Similar to SARS-CoV-2 infection in humans, intranasal infection of C57BL/6 mice by MHV strains (e.g. MHV-A59) is known to induce pathology by substantial recruitment of granulocytic cells to the lungs (12, 18, 19). The mean lung mass of EP67-treated infected mice (Figure 3) showed a slight increase at two days post-treatment (5 dpi) and a modest decrease compared to the infected untreated PBS control mice at seven days post-treatment (10 dpi). As expected, uninfected mice mock-infected with 17Cl-1 cell lysate alone at day 0 (0 dpi), followed by EP67 administration at 3 dpi, maintained consistent lung masses at two and seven days post-treatment, supporting the hypothesis that EP67 treatment did not aggravate the disease state further, but instead reduced disease severity within 24 hours based on behavior and measured weights. This suggests that in the context of this study, EP67, in contrast to its parent protein human C5a, does not appear to exacerbate host-mediated innate immune cascades (i.e. granulocyte effector functions) (6). Altogether, this evidence supports that EP67 treatment results in a significant decrease in morbidity following intranasal treatment at 3 days post-infection.

The ability of EP67 to rapidly cause restored health following administration in symptomatic models of viral infection supports the view of this peptide as a potent and selective immunostimulant. It is theorized that EP67 invokes recruitment and activation of antigen-presenting cells (APCs) and enhances their antigen processing time and/or display levels, thereby driving the adaptive immune response a more rapid opportunity to develop B and T cell-mediated defenses against viral infection and propagation. Such bridging of the innate and adaptive immune responses is believed to underlie the observed rapid return to health. Previous studies with EP67 and its compositional predecessor EP54 support this hypothesis: murine dendritic cells internalized the peptide, upregulated selected activation-associated cytokines, and increased MHC expression compared to control (4). Similarly, murine splenic cells demonstrated marked increases in activation-related cytokines, and promoted enhanced cellular and humoral immune responses against the ovalbumin (OVA) antigen (5). In line with these previous findings, we show that EP67 is a significant ($p < 0.0001$) inducer of TNF-alpha (TNF-α) secretion from another APC: mouse RAW 264.7 macrophages (Figure 4). As seen in Figure 4, EP67 resulted in nearly the same magnitude as its parental protein, human C5a. The anti-viral capabilities of TNF-α are well-established, and patients who asymptomatically clear SARS-CoV-2 have been found with slightly higher expression compared to symptomatic patients (20). While high levels of TNF-α may contribute to deleterious inflammatory responses in some diseases, it often does so only in the context of other co-expressed inflammatory cytokines: such is the case with SARS-CoV-2, where TNF-α alone did not contribute to cell damage (21). Taken together, the EP67 molecule used here demonstrates an ability to directly activate murine antigen-presenting cells, and

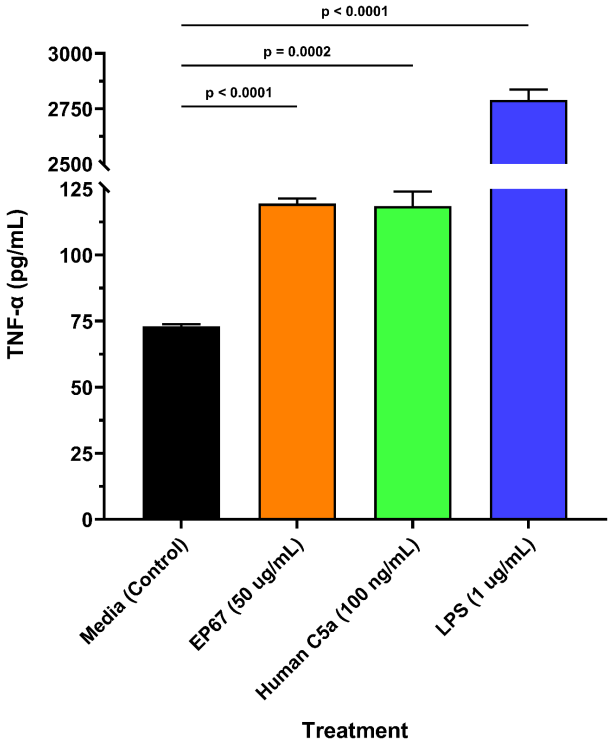

FIGURE 4
Murine macrophage release of TNF-α following EP67 exposure. Freshly prepared murine-derived RAW 264.7 macrophages were exposed to media only (control), human-derived C5a decapeptide EP67 (50 μg/mL), recombinant human parental complement molecule C5a (100 ng/mL), or lipopolysaccharide (LPS; 1 μg/mL) for 16 hours. Supernatants were collected to measure the release of TNF-α, a known anti-viral cytokine. Three wells per treatment ($n=3$) were assayed and each supernatant sample was tested in technical duplicates. A two-tailed unpaired t-test for statistical significance was performed using GraphPad Prism version 10.4.1. The group mean ± SEM of supernatant TNF-α levels are displayed.

provide effective therapy for symptomatically infected mice, supporting its role as a selective immunostimulatory bio-mimetic of the parent C5a molecule.

Conclusions

The SARS-CoV-2 global pandemic reiterated the urgent need for broad-spectrum antiviral agents, ideally with a capacity to treat individuals already infected. This brief study showed that the immunostimulant decapeptide, EP67, derived from human complement protein C5a, used in a single dose reduced disease severity of infection from mouse-native MHV, a betacoronavirus. EP67's ability to return treated mice to a healthy state emphasizes its potential for safe application in the case of viral infections known to otherwise promote tissue destruction through elevated inflammatory responses. While used as a prophylactic adjuvant or as a treatment for symptomatic disease in this study, a greater understanding of EP67's ideal therapeutic window will likely be an important element in future study designs (8). Finally, it would be valuable to advance the understanding on the molecular mechanisms responsible for this non-inflammatory immunostimulatory activity of EP67 and how it may bridge the innate and adaptive immune responses.

Data availability statement

The original contributions presented in the study are included in the article/supplementary material. Further inquiries can be directed to the corresponding author.

Ethics statement

The animal study was approved by University of Nebraska at Omaha Institutional Animal Care and Use Committee (IACUC), under the IACUC protocol #: 20-058-03. The study was conducted in accordance with the local legislation and institutional requirements.

Author contributions

AN: Conceptualization, Data curation, Formal Analysis, Investigation, Methodology, Visualization, Writing – original draft, Writing – review & editing. MC: Data curation, Investigation, Writing – review & editing. TS: Investigation, Writing – original draft, Writing – review & editing. PD: Conceptualization, Funding acquisition, Resources, Supervision, Writing – original draft, Writing – review & editing.

Funding

The author(s) declare that financial support was received for the research and/or publication of this article. This research was conducted at the University of Nebraska at Omaha. This work was supported by the National Institute for General Medical Science grant P20GM103427 and NIH SBIR 272201600038C, with additional support from National Strategic Research Institute and the University of Nebraska.

Acknowledgments

17Cl-1 mouse fibroblasts and MHV-A59 viral stocks were graciously donated by Stanley Perlman, University of Iowa. The following reagents were obtained through BEI Resources, NIAID, NIH: Whole Cell Antigen, SARS-Related Coronavirus 2, Isolate USA-WA1/2020 with Uninfected Control Vero E6 Cells with High Expression of Angiotensin-Converting Enzyme 2, Gamma-Irradiated, NR-53911; Nucleocapsid Protein from SARS-Related Coronavirus 2, Recombinant from Baculovirus, NR-53797; Spike Glycoprotein (Stabilized) from SARS-Related Coronavirus 2, Delta Variant, Recombinant from HEK293 Cells, NR-55614; Rabbit IgG Polyclonal Anti-SARS-Related Coronavirus 2 Spike Glycoprotein, NR-52947.

Conflict of interest

The authors declare that the research was conducted in the absence of any commercial or financial relationships that could be construed as a potential conflict of interest.

Publisher's note

References

1. Fernandez HN, Hugli TE. Primary structural analysis of the polypeptide portion of human C5a anaphylatoxin. Polypeptide sequence determination and assignment of the oligosaccharide attachment site in C5a. *J Biol Chem*. (1978) 253:6955–64. doi: 10.1016/S0021-9258(17)38013-4

2. Karuturi BV, Tallapaka SB, Phillips JA, Sanderson SD, Vetro JA. Preliminary evidence that the novel host-derived immunostimulant ep67 can act as a mucosal adjuvant. *Clin Immunol*. (2015) 161:251–9. doi: 10.1016/j.clim.2015.06.006

3. Alshammari AM, Smith DD, Parriott J, Stewart JP, Curran SM, McCulloh RJ, et al. Targeted amino acid substitution overcomes scale-up challenges with the human C5a-derived decapeptide immunostimulant ep67. *ACS Infect Dis.* (2020) 6:1169–81. doi: 10.1021/acsinfecdis.0c00005

4. Hegde GV, Meyers-Clark E, Joshi SS, Sanderson SD. A conformationally-biased, response-selective agonist of C5a acts as a molecular adjuvant by modulating antigen processing and presentation activities of human dendritic cells. *Int Immunopharmacol.* (2008) 8:819–27. doi: 10.1016/j.intimp.2008.01.031

5. Morgan EL, Morgan BN, Stein EA, Vitrs EL, Thoman ML, Sanderson SD, et al. Enhancement of *in vivo* and *in vitro* immune functions by a conformationally biased, response-selective agonist of human C5a: implications for a novel adjuvant in vaccine design. *Vaccine*. (2009) 28:463–9. doi: 10.1016/j.vaccine.2009.10.029

6. Cavaco CK, Patras KA, Zlamal JE, Thoman ML, Morgan EL, Sanderson SD, et al. A novel C5a-derived immunobiotic peptide reduces streptococcus agalactiae colonization through targeted bacterial killing. *Antimicrob Agents Chemother*. (2013) 57:5492–9. doi: 10.1128/AAC.01590-13

7. Hanke ML, Heim CE, Angle A, Sanderson SD, Kielian T. Targeting macrophage activation for the prevention and treatment of staphylococcus aureus biofilm infections. *J Immunol.* (2013) 190:2159–68. doi: 10.4049/jimmunol.1202348

8. Sanderson SD, Thoman ML, Kis K, Virts EL, Herrera EB, Widmann S, et al. Innate immune induction and influenza protection elicited by a response-selective agonist of human C5a. *PloS One*. (2012) 7:e40303. doi: 10.1371/journal.pone.0040303

9. Andrade A, Campolina-Silva GH, Queiroz-Junior CM, de Oliveira LC, Lacerda LSB, Pimenta JC, et al. A biosafety level 2 mouse model for studying betacoronavirus-induced acute lung damage and systemic manifestations. *J Virol.* (2021) 95:e0127621. doi: 10.1128/JVI.01276-21

10. Coley SE, Lavi E, Sawicki SG, Fu L, Schelle B, Karl N, et al. Recombinant mouse hepatitis virus strain A59 from cloned, full-length cdna replicates to high titers *in vitro* and is fully pathogenic *in vivo*. *J Virol.* (2005) 79:3097–106. doi: 10.1128/JVI.79.5.3097-3106.2005

11. Korner RW, Majjouti M, Alcazar MAA, Mahabir E. Of mice and men: the coronavirus mhv and mouse models as a translational approach to understand sars-cov-2. *Viruses*. (2020) 12. doi: 10.3390/v12080880

12. Yang Z, Du J, Chen G, Zhao J, Yang X, Su L, et al. Coronavirus mhv-A59 infects the lung and causes severe pneumonia in C57bl/6 mice. *Virol Sin*. (2014) 29:393–402. doi: 10.1007/s12250-014-3530-y

13. Grunewald ME, Shaban MG, Mackin SR, Fehr AR, Perlman S. Murine coronavirus infection activates the aryl hydrocarbon receptor in an indoleamine 2,3-dioxygenase-independent manner, contributing to cytokine modulation and proviral tcdd-inducible-parp expression. *J Virol.* (2020) 94. doi: 10.1128/JVI.01743-19

14. Leibowitz J, Kaufman G, Liu P. Coronaviruses: propagation, quantification, storage, and construction of recombinant mouse hepatitis virus. *Curr Protoc Microbiol.* (2011) Chapter 15:Unit 15E 1. doi: 10.1002/9780471729259.mc15e01s21

15. Golde WT, Gollobin P, Rodriguez LL. A rapid, simple, and humane method for submandibular bleeding of mice using a lancet. *Lab Anim (NY)*. (2005) 34:39–43. doi: 10.1038/laban1005-39

16. Chen Z, Yuan Y, Hu Q, Zhu A, Chen F, Li S, et al. Sars-cov-2 immunity in animal models. *Cell Mol Immunol.* (2024) 21:119–33. doi: 10.1038/s41423-023-01122-w

17. Valkenburg SA, Cheng SMS, Hachim A, Peiris M, Nicholls J. Postmortem stability of sars-cov-2 in mouse lung tissue. *Emerg Infect Dis.* (2021) 27:3173–5. doi: 10.3201/eid2712.211621

18. Sivaraman V, Parker D, Zhang R, Jones MM, Onyenwoke RU. Vaping exacerbates coronavirus-related pulmonary infection in a murine model. *Front Physiol.* (2021) 12:634839. doi: 10.3389/fphys.2021.634839

19. Lavi E, Gilden DH, Highkin MK, Weiss SR. Mhv-A59 pathogenesis in mice. *Adv Exp Med Biol.* (1984) 173:237–45. doi: 10.1007/978-1-4615-9373-7_24

20. Han H, Xu Z, Cheng X, Zhong Y, Yuan L, Wang F, et al. Descriptive, retrospective study of the clinical characteristics of asymptomatic covid-19 patients. *mSphere*. (2020) 5. doi: 10.1128/mSphere.00922-20

21. Karki R, Sharma BR, Tuladhar S, Williams EP, Zalduondo L, Samir P, et al. Synergism of tnf-alpha and ifn-gamma triggers inflammatory cell death, tissue damage, and mortality in sars-cov-2 infection and cytokine shock syndromes. *Cell.* (2021) 184:149–68.e17. doi: 10.1016/j.cell.2020.11.025

Frontiers in Immunology

Explores novel approaches and diagnoses to treat immune disorders.

The official journal of the International Union of Immunological Societies (IUIS) and the most cited in its field, leading the way for research across basic, translational and clinical immunology.

Discover the latest Research Topics

See more →

Frontiers

Avenue du Tribunal-Fédéral 34
1005 Lausanne, Switzerland
frontiersin.org

Contact us

+41 (0)21 510 17 00
frontiersin.org/about/contact